



*International Relativistic Astrophysics PhD
IRAP Ph.D.*



Sapienza University of Rome

Kuantay Boshkayev

Ph.D. Thesis

**Rotating White Dwarfs and Neutron Stars
in General Relativity**

Thesis Adviser:
Prof. Remo Ruffini

Co-Adviser:
Dr. Jorge A. Rueda

Academic year 2012-2013

Contents

General Introduction	iv
1 Gravitational field of compact objects in general relativity	5
1.1 Introduction	5
1.2 The Hartle-Thorne metrics	7
1.2.1 The interior solution	8
1.2.2 The exterior solution	10
1.3 The Fock's approach	11
1.3.1 The interior solution	11
1.3.2 The exterior solution	12
1.3.3 The Kerr metric	13
1.4 A solution with quadrupole moment	15
1.4.1 The exterior Fock solution	15
1.4.2 The exterior Quevedo-Mashhoon solution	19
1.5 Conclusions	23
1.6 Perspectives	24
2 Equatorial circular geodesics in the Hartle-Thorne spacetime	25
2.1 Introduction	25
2.2 The domain of validity of the Hartle-Thorne approximation	26
2.3 Equations for the equatorial circular geodesics	27
2.3.1 The Orbital Angular Velocity	27
2.3.2 Radii of marginally stable and marginally bound orbits	30
2.4 Conclusions	30
2.5 Perspectives	31
3 Tidal indicators in the field of a rotating deformed mass	33
3.1 Introduction	33
3.2 The gravitational field of a rotating deformed mass	34
3.2.1 Limiting cases	36
3.3 Circular orbits on the symmetry plane	37
3.4 Tidal indicators	39
3.4.1 Super-energy density and super-Poynting vector	40

3.4.2	Discussion	42
3.4.3	Limit of slow rotation and small deformation	44
3.5	Multipole moments and tidal Love numbers	49
3.6	Conclusions	50
3.7	Perspectives	51
4	On general relativistic uniformly rotating white dwarfs	53
4.1	Introduction	53
4.2	Spacetime geometry and Hartle's formalism	55
4.3	Limits on the stability of rotating white dwarfs	55
4.3.1	The mass-shedding limit	55
4.3.2	The turning-point criterion	56
4.3.3	Inverse beta-decay instability	57
4.3.4	Pycnonuclear fusion reactions	57
4.4	WD structure and stability boundaries	60
4.5	The maximum mass	60
4.6	The minimum rotation period	65
4.7	Occurrence of secular axisymmetric instability	66
4.8	Spin-up and spin-down evolution	70
4.9	Astrophysical implications	70
4.10	Conclusions	73
4.11	Perspectives	74
5	SGRs and AXPs as fast rotating white dwarfs	75
5.1	Introduction	75
5.2	Rotation powered white dwarfs	76
5.3	Structure and stability of rotating white dwarfs	77
5.4	SGR 0418+5729	79
5.4.1	Bounds on the WD parameters	79
5.4.2	Solidification and glitches	79
5.4.3	Rotation power and magnetic field	80
5.4.4	Prediction of the spin-down rate	81
5.4.5	Optical spectrum and luminosity	81
5.5	Swift J1822.3-1606	84
5.5.1	Bounds of the WD parameters	84
5.5.2	Solidification and glitches	84
5.5.3	Rotation power and magnetic field	85
5.5.4	Optical spectrum and luminosity	85
5.6	Conclusions	87
5.7	Perspectives	87
6	Magnetic Fields in Rotating Nuclear Matter Cores	89
6.1	Introduction	89

6.2	The relativistic Thomas-Fermi equation	90
6.3	The ultra-relativistic analytic solutions	94
6.4	Rotating nuclear matter cores of stellar dimensions	95
6.5	Stability of rotating nuclear matter cores of stellar dimensions	101
6.6	Conclusions	104
6.7	Perspectives	104
7	Neutron star equilibrium configurations	105
7.1	Introduction	105
7.2	The Constitutive Relativistic Equations	107
7.2.1	Core Equations	107
7.2.2	Core-crust transition layer equations	112
7.2.3	Crust equations	117
7.3	Neutron star structure	118
7.4	Observational constraints on the mass-radius relation	119
7.5	Comparison with the traditional TOV treatment	121
7.6	Rotating neutron stars	122
7.7	Conclusions	125
7.8	Perspectives	127
A	Derivation of the Fock extended metric	129
B	Relevant frame components of tidal tensors	131
C	The Hartle-Thorne solution and equatorial circular orbits	133
C.0.1	The Hartle-Thorne vacuum solution	133
C.0.2	Angular velocity of equatorial circular orbits	134
C.0.3	Weak field limit	135
C.1	Pycnonuclear fusion reaction rates	136
C.2	Comparison with the Newtonian treatment and other works	137
C.3	Accuracy of the Hartle's approach	139
D	Spherical Capacitor	145
E	Rotating neutron stars	147
	Bibliography	153

General Introduction

White dwarfs and neutron stars are formed when normal (main sequence) stars end their thermonuclear evolution. They differ from normal stars in two fundamental ways. First, since they do not burn nuclear fuel, they cannot support themselves against gravitational collapse by generating thermal pressure. Instead, white dwarfs are supported by the pressure of degenerate electrons, while neutron stars are supported largely by the pressure of degenerate neutrons. The second characteristic, distinguishing compact objects from normal stars, is their exceedingly small size. Relative to normal stars of comparable mass, compact objects have much smaller radii and hence, much stronger surface gravitational fields [235].

Because of the enormous density range spanned by compact objects, their analysis requires a deep physical understanding of the structure of matter and the nature of interparticle forces over a vast range of parameter space. All four fundamental interactions (the strong and weak nuclear forces, electromagnetism, and gravitation) play a crucial role in compact objects [95, 101, 18]. Particularly noteworthy are the large surface potentials encountered in compact objects, which imply that general relativity is important in determining their structure. Even for white dwarfs, where Newtonian gravitation is adequate to describe their equilibrium structure, general relativity turns out to be important for a proper understanding of their stability [235, 96, 45].

Because of their small radii, luminous white dwarfs, radiating away their residual thermal energy, are characterized by much higher effective temperatures than normal stars even though they have lower luminosities. In other words, white dwarfs are much “whiter” than normal stars, hence their name. Neutron stars derive their name from the predominance of neutrons in their interior, following the mutual elimination of electrons and protons by inverse β -decay [235]. Because their densities are comparable to nuclear values, neutron stars are essentially “giant nuclei” (10^{57} baryons!), held together by self-gravity [137, 222].

The main objective of this work is to investigate the equilibrium configuration of uniformly rotating white dwarfs and neutron stars. To this end in Chapter 1 we study some exact and approximate solutions of Einstein’s equations that can be used to describe the gravitational field of astrophysical compact objects in the limiting case of slow rotation and slight deformation. First, we show that none of the standard models obtained by using Fock’s method can be used as an interior source for the approximate exterior Kerr solution. We then use Fock’s method to derive a generalized interior solution, and also an exterior solution that turns out to be equivalent to the exterior Hartle-Thorne approximate

solution that, in turn, is equivalent to an approximate limiting case of the exact Quevedo-Mashhoon solution. As a result we obtain an analytic approximate solution that describes the interior and exterior gravitational field of a slowly rotating and slightly deformed astrophysical object [41].

In Chapter 2 we investigate the influence of the quadrupole moment of a rotating body on the motion of a test particle in the strong field regime. For this purpose we use the Hartle-Thorne (HT) metric, that is an approximate solution of the vacuum Einstein field equations which describes the exterior of any slowly rotating, stationary and axially symmetric body. The metric is given with accuracy up to the second order terms in the body's angular momentum, and first order terms in its quadrupole moment. We analyze the domain of validity of the HT metric then we give, with the same accuracy, the analytic equations for the equatorial circular geodesics and integrate them numerically [24]. In addition we derive the radii for marginally bound, marginally stable and photon orbits. We show that these radii are in agreement with the results of Bardeen et al. [13].

In Chapter 3 we consider tidal indicators, that are commonly associated with the electric and magnetic parts of the Riemann tensor (and its covariant derivatives), with respect to a given family of observers in a given spacetime. The observer-dependent tidal effects have been extensively investigated with respect to a variety of special observers in the equatorial plane of the Kerr spacetime. This analysis is extended here by considering a more general background solution (Quevedo-Mashhoon solution) to include the case of matter which is also endowed with an arbitrary mass quadrupole moment. Relation with curvature invariants and Bel-Robinson tensor, i.e., observer-dependent super-energy density and super-Poynting vector, are investigated too [23].

In Chapter 4 the properties of uniformly rotating white dwarfs (RWDs) are analyzed within the framework of general relativity. Hartle's formalism is applied to construct the internal and external solutions to the Einstein equations. The WD matter is described by the relativistic Feynman-Metropolis-Teller equation of state which generalizes the Salpeter's one by taking into account the finite size of the nuclei, the Coulomb interactions as well as electroweak equilibrium in a self-consistent relativistic fashion. The mass M , radius R , angular momentum J , eccentricity ϵ , and quadrupole moment Q of RWDs are calculated as a function of the central density ρ_c and rotation angular velocity Ω . We construct the region of stability of RWDs (J - M plane) taking into account the mass-shedding limit, inverse β -decay instability, and the boundary established by the turning-points of constant J sequences which separates stable from secularly unstable configurations. We found the minimum rotation periods $\sim 0.3, 0.5, 0.7$ and 2.2 seconds and maximum masses $\sim 1.500, 1.474, 1.467, 1.202 M_\odot$ for ${}^4\text{He}$, ${}^{12}\text{C}$, ${}^{16}\text{O}$, and ${}^{56}\text{Fe}$ WDs respectively. By using the turning-point method we found that RWDs can indeed be axisymmetrically unstable and we give the range of WD parameters where it occurs. We also construct constant rest-mass evolution tracks of RWDs at fixed chemical composition and show that, by losing angular momentum, sub-Chandrasekhar RWDs (mass smaller than maximum static one) can experience both spin-up and spin-down epochs depending on their initial mass and rotation period while, super-Chandrasekhar RWDs (mass larger than maximum static one), only spin-up [45].

In Chapter 5 we consider the astrophysical implication of RWDs. Following the work of Malheiro et al. (2012) we describe so-called *low magnetic field magnetars*, Swift J18822.3-1606 and SGR 0418+5729, as massive fast rotating highly magnetized white dwarfs. We give bounds for the mass, radius, moment of inertia, and magnetic field for these sources, by requesting the stability of realistic general relativistic uniformly rotating configurations. Based on these parameters, we improve the theoretical prediction of the lower limit of the spin-down rate of SGR 0418+5729. We also present the theoretical expectation of the infrared, optical and ultraviolet emission and show their consistency with the current available observational data. In addition, we compute the electron cyclotron frequencies corresponding to the predicted surface magnetic field [40].

In Chapter 6 we consider a globally neutral system of stellar dimensions consisting of degenerate N_n neutrons, N_p protons and N_e electrons in beta equilibrium. Such a system at nuclear density having mass numbers $A \approx 10^{57}$ can exhibit a charge distribution different from zero. We present the analysis in the framework of classical electrodynamics to investigate the magnetic field induced by this charge distribution when the system is allowed to rotate as a rigid body with a constant angular velocity around the axis of symmetry [43, 42]. In addition, we investigate the stability of these nuclear matter cores of stellar dimensions against centrifugal repulsion and magnetic energies extending the work of [222, 213]. These cores represent inner parts (cores) of neutron stars.

Natural generalization of non-rotating nuclear matter cores of stellar dimensions in general relativity taking into consideration weak, strong, electromagnetic and gravitational interactions has been presented by Belvedere et al. (2012) in [211, 193, 18]. Thus in Chapter 7, we construct uniformly rotating configurations for a new model of neutron stars making use of Hartle's formalism analogously to what we have already performed for RWDs [45]. We investigate the stability of the system against general relativistic instabilities and axisymmetric secular instabilities. As a result for globally and locally neutral configurations we have obtained the maximum mass $2.76M_\odot$ and $2.79M_\odot$, and the minimum rotation period 0.51 and 0.53 milliseconds, respectively.

Chapter 1

Gravitational field of compact objects in general relativity

1.1 Introduction

In astrophysics, the term compact object is used to refer to objects which are small for their mass. In a wider sense, the class of compact objects is often defined to contain collectively planet-like objects, white dwarfs, neutron stars, other exotic dense stars, and black holes. It is well known that Newtonian theory of gravitation provides an adequate description of the gravitational field of conventional astrophysical objects. However, the discovery of exotic compact objects such as quasars and pulsars together with the possibility of continued gravitational collapse to a black hole points to the importance of relativistic gravitation in astrophysics. Moreover, advances in space exploration and the development of modern measuring techniques have made it necessary to take relativistic effects into account even in the Solar system. Probably the simplest way to study the relativistic gravitational field of astrophysical compact objects is by expressing it in terms of their multipole moments, in close analogy with the Newtonian theory, taking into account the rotation and the internal structure of the source.

In this context, the first exterior solution with only a monopole moment was discovered by Schwarzschild [233], soon after the formulation of Einstein's theory of gravity. In 1917, Weyl [271] showed that the problem of finding static axisymmetric vacuum solutions can generically be reduced to a single linear differential equation whose general solution can be represented as an infinite series. The explicit form of this solution resembles the corresponding solution in Newtonian's gravity, indicating the possibility of describing the gravitational field by means of multipole moments. In 1918, Lense and Thirring [144] discovered an approximate exterior solution which, apart from the mass monopole, contains an additional parameter that can be interpreted as representing the angular momentum of the massive body. From this solution it became clear that, in Einstein's relativistic theory, rotation generates a gravitational field that leads to the dragging of inertial frames (Lense-Thirring effect). This is the so-called gravitomagnetic field which is of especial importance in the case of rapidly rotating compact objects. The case of a static axisym-

metric solution with monopole and quadrupole moment was analyzed in 1959 by Erez and Rosen [74] by using spheroidal coordinates which are specially adapted to describe the gravitational field of non-spherically symmetric bodies. The exact exterior solution which considers arbitrary values for the angular momentum was found by Kerr [124] only in 1963. The problem of finding exact solutions changed dramatically after Ernst [75] discovered in 1968 a new representation of the field equations for stationary axisymmetric vacuum solutions. In fact, this new representation was the starting point to investigate the Lie symmetries of the field equations. Today, it is known that for this special case the field equations are completely integrable and solutions can be obtained by using the modern solution generating techniques [66]. A comprehensive review on solution generating techniques and stationary axisymmetric global solutions of Einstein and Einstein-Maxwell equations is given in [120]. There are several solutions with higher multipole moments [52, 155, 157, 156, 179] with very interesting physical properties. In this work, we will analyze a particular class of solutions, derived by Quevedo and Mashhoon [199] in 1991, which in the most general case contains infinite sets of gravitational and electromagnetic multipole moments. Hereafter this solution will be denoted as the QM solution.

As for the interior gravitational field of compact objects, the situation is more complicated. There exists in the literature a reasonable number of interior spherically symmetric solutions [10] that can be matched with the exterior Schwarzschild metric. Nevertheless, a major problem of classical general relativity consists in finding a physically reasonable interior solution for the exterior Kerr metric. Although it is possible to match numerically the Kerr solution with the interior field of an infinitely tiny rotating disk of dust [173], such a solution cannot be used in general to describe astrophysical compact objects. It is now widely believed that the Kerr solution is not appropriate to describe the exterior field of rapidly rotating compact objects. Indeed, the Kerr metric takes into account the total mass and the angular momentum of the body. However, the quadrupole moment is an additional characteristic of any realistic body which should be considered in order to correctly describe the gravitational field. As a consequence, the multipole moments of the field created by a rapidly rotating compact object are different from the multipole moments of the Kerr metric [246]. For this reason a solution with arbitrary sets of multipole moments, such as the QM solution, can be used to describe the exterior field of arbitrarily rotating mass distributions.

In the case of slowly rotating compact objects it is possible to find approximate interior solutions with physically meaningful energy-momentum tensors and state equations. Because of its physical importance, in this work we will review the Hartle-Thorne [105, 108] interior solution which are coupled to an approximate exterior metric. Hereafter this solution will be denoted as the HT solution. One of the most important characteristics of this family of solutions is that the corresponding equation of state has been constructed using realistic models for the internal structure of relativistic stars. Semi-analytical and numerical generalizations of the HT metrics with more sophisticated equations of state have been proposed by different authors [8]. A comprehensive review of these solutions is given in [246]. In all these cases, however, it is assumed that the multipole moments (quadrupole and octupole) are relatively small and that the rotation is slow.

To study the physical properties of solutions of Einstein's equations, Fock [82] proposed an alternative method in which the parameters entering the exterior metric are derived by using physical models for the internal structure of the body. In this manner, the significance of the exterior parameters become more plausible and the possibility appear of determining certain aspects of the interior structure of the object by using observations performed in the exterior region of the body. Fock's metric in its first-order approximation was recently generalized in 1985 by Abdildin [2, 4] (for details see Appendix A).

In this work, we review the main exact and approximate metrics which can be used to study the interior and exterior gravitational field of compact objects and find the relationships between them. We will show that the exterior HT approximate solution is equivalent to a special case of the QM solution in the limit of a slowly rotating slightly deformed compact object (first order in the quadrupole and second order in the angular momentum). Moreover, we will show that a particular case of the extended Fock metric is equivalent to the approximate exterior HT solution. Furthermore, since those particular cases of the exterior HT metric that possess internal counterparts with plausible equations of state are also special cases of the exterior QM metric, we conclude that at least in those particular cases it should be possible to match the QM solution with an exact interior still unknown solution so that it describes globally the gravitational field of astrophysical compact bodies.

This work is organized as follows. In Section 1.2 we review the HT solutions and briefly comment on their most important properties. In Section 1.3 we present Fock's extended metric, as first derived by Abdildin [2, 4] in harmonic coordinates, and introduce a set of new coordinates which makes it suitable for comparison with other exterior metrics. Moreover, we find explicitly the coordinate transformation that relates Fock's extended metric with the exterior HT solution.

In Section 1.4.2 we present a particular case of the QM metric which contains, in addition to the mass and angular momentum parameters, an additional parameter related to the mass quadrupole of the source. Here we show explicitly that a limiting case of the QM metric contains the HT metric. Finally, Section 1.5 contains discussions of our results and suggestions for further research.

1.2 The Hartle-Thorne metrics

To second order in the angular velocity, the structure of compact objects can be approximately described by the mass, angular momentum and quadrupole moment. An important consequence of this approximation is that the equilibrium equations reduce to a set of ordinary differential equations. Hartle and Thorne [105, 108] explored the gravitational field of rotating stars in this slow rotation approximation. This formalism can be applied to most compact objects including pulsars with millisecond rotational periods, but it shows "large" discrepancies in the case of rapidly rotating relativistic objects near the mass-shedding limit according to [246], i. e., when the angular velocity of the object reaches the angular velocity of a particle in a circular Keplerian orbit at the equator. In

fact, recently in [20] and [21] it was shown that the second order rotation corrections of the HT metric are sufficient to describe the properties of stars with intermediate rotation rates. These results were generalized in [19] to include third order corrections. It turns out that third order corrections are irrelevant at the mass-shedding limit; however, they are important to study the moment of inertia of rapidly rotating neutron stars. Moreover, in [179] an analytical solution was derived that can be matched accurately with interior numerical solutions. On the other hand, an alternative numerical study [150] shows that in the case of uniformly rotating neutron stars the dimensionless specific angular momentum cannot exceed the value 0.7. An additional property of this formalism is that it can be used to match an interior solution with an approximate exterior solution. In this connection, it is worth noticing that the problem of matching interior and exterior solutions implies many mathematical and physical issues [186, 184, 187, 185, 180, 197], including the performance of the metric functions and the coordinates at the matching surface as well as the physical behavior of the internal parameters like the density and pressure of the matter distribution. In the following subsections we will present the interior and the exterior metrics and introduce notations which will be used throughout this work.

1.2.1 The interior solution

If a compact object is rotating slowly, the calculation of its equilibrium properties reduces drastically because it can be considered as a linear perturbation of an already-known non-rotating configuration. This is the main idea of Hartle's formalism [105]. To simplify the computation the following conditions are assumed to be satisfied.

- 1) Equation of state: the matter in equilibrium configuration is assumed to satisfy a one-parameter equation of state, $\mathcal{P} = \mathcal{P}(\mathcal{E})$, where \mathcal{P} is the pressure and \mathcal{E} is the mass-energy density.
- 2) Axial and reflection symmetry: the configuration is symmetric with respect to an arbitrary axis which can be taken as the rotation axis. Furthermore, the rotating object should be invariant with respect to reflections about a plane perpendicular to the axis of rotation.
- 3) Uniform rotation: only uniformly rotating configurations are considered since it is known that configurations that minimize the total mass-energy (e.g., all stable configurations) must rotate uniformly [107]¹.
- 4) Slow rotation: this means that angular velocities Ω are small enough so that the fractional changes in pressure, energy density and gravitational field due to the rotation are all less than unity, i.e.

$$\Omega^2 \ll \left(\frac{c}{R'}\right)^2 \frac{GM'}{c^2 R'} \quad (1.1)$$

where M' is the mass and R' is the radius of the non-rotating configuration. The above condition is equivalent to the physical requirement $\Omega \ll c/R'$.

¹ Notice, however, that stability is also possible in the case differentially rotating configurations. See, for instance, [127, 128]

When the equilibrium configuration described above is set into slow rotation, the geometry of space-time around it and its interior distribution of stress-energy are changed. With an appropriate choice of coordinates, the perturbed geometry is described by

$$ds^2 = e^\nu [1 + 2(h_0 + h_2 P_2)] dt^2 - \frac{[1 + 2(m_0 + m_2 P_2)/(R - 2M')]}{1 - 2M'/R} dR^2 - R^2 [1 + 2(v_2 - h_2) P_2] [d\Theta^2 + \sin^2 \Theta (d\phi - \omega dt)^2] + O(\Omega^3) \quad (1.2)$$

Here M' is the mass of the non-rotating star, $P_2 = P_2(\cos \Theta)$ is the Legendre polynomial of second order, ω is the angular velocity of the local inertial frame, which is a function of R and is proportional to the star's angular velocity Ω , and, finally, h_0, h_2, m_0, m_2, v_2 are all functions of R that are proportional to Ω^2 .

In the above coordinate system the fluid inside the star moves with a 4-velocity corresponding to a uniform and rigid rotation [257]. The contravariant components are

$$u^t = (g_{tt} + 2\Omega g_{t\phi} + \Omega^2 g_{\phi\phi})^{-1/2}, \quad u^\phi = \Omega u^t, \quad u^R = u^\Theta = 0. \quad (1.3)$$

The quantity Ω that appears in the expression for u^t is so defined that $\bar{\omega} \equiv \Omega - \omega$ is the angular velocity of the fluid relative to the local inertial frame.

The energy density \mathcal{E} and the pressure \mathcal{P} of the fluid are affected by the rotation because it deforms the compact object. In the interior of the object at a given (R, Θ) , in a reference frame that is momentarily moving with the fluid, the pressure and the density of mass-energy are

$$\mathcal{P} \equiv P + (E + P)(p_0^* + p_2^* P_2) = P + \Delta P \quad (1.4)$$

$$\mathcal{E} \equiv E + (E + P)(dE/dP)(p_0^* + p_2^* P_2) = E + \Delta E. \quad (1.5)$$

Here, p_0^* and p_2^* are dimensionless functions of R that are proportional to Ω^2 , and describe the pressure perturbation, P is the pressure and E is the energy density of the non-rotating configuration. The stress-energy tensor for the fluid of the rotating object is

$$T_\mu^\nu = (\mathcal{E} + \mathcal{P})u_\mu u^\nu - \mathcal{P}\delta_\mu^\nu. \quad (1.6)$$

The rotational perturbations of the objects's structure are described by the functions $\bar{\omega}, h_0, m_0, p_0^*, h_2, m_2, v_2, p_2^*$. These functions are calculated from Einstein's field equations (for details see [105, 108]).

1.2.2 The exterior solution

The HT metric describing the exterior field of a slowly rotating slightly deformed object is given by

$$\begin{aligned}
 ds^2 = & \left(1 - \frac{2\mathcal{M}}{R}\right) \left[1 + 2k_1 P_2(\cos \Theta) + 2 \left(1 - \frac{2\mathcal{M}}{R}\right)^{-1} \frac{J^2}{R^4} (2 \cos^2 \Theta - 1)\right] dt^2 \\
 & - \left(1 - \frac{2\mathcal{M}}{R}\right)^{-1} \left[1 - 2k_2 P_2(\cos \Theta) - 2 \left(1 - \frac{2\mathcal{M}}{R}\right)^{-1} \frac{J^2}{R^4}\right] dR^2 \\
 & - R^2 [1 - 2k_3 P_2(\cos \Theta)] (d\Theta^2 + \sin^2 \Theta d\phi^2) + 4 \frac{J}{R} \sin^2 \Theta dt d\phi
 \end{aligned} \tag{1.7}$$

with

$$\begin{aligned}
 k_1 &= \frac{J^2}{\mathcal{M}R^3} \left(1 + \frac{\mathcal{M}}{R}\right) + \frac{5Q - J^2/\mathcal{M}}{8\mathcal{M}^3} Q_2^2 \left(\frac{R}{\mathcal{M}} - 1\right), \quad k_2 = k_1 - \frac{6J^2}{R^4}, \\
 k_3 &= k_1 + \frac{J^2}{R^4} + \frac{5Q - J^2/\mathcal{M}}{4\mathcal{M}^2 R} \left(1 - \frac{2\mathcal{M}}{R}\right)^{-1/2} Q_2^1 \left(\frac{R}{\mathcal{M}} - 1\right),
 \end{aligned}$$

where

$$\begin{aligned}
 Q_2^1(x) &= (x^2 - 1)^{1/2} \left[\frac{3x}{2} \ln \frac{x+1}{x-1} - \frac{3x^2 - 2}{x^2 - 1} \right], \\
 Q_2^2(x) &= (x^2 - 1) \left[\frac{3}{2} \ln \frac{x+1}{x-1} - \frac{3x^3 - 5x}{(x^2 - 1)^2} \right],
 \end{aligned} \tag{1.8}$$

are the associated Legendre functions of the second kind. The constants \mathcal{M} , J and Q are related to the total mass, angular momentum and mass quadrupole moment of the rotating object, respectively. This form of the metric corrects some misprints of the original paper by Hartle and Thorne [108] (see also [30] and [21]).

The total mass of a rotating configuration is defined as $\mathcal{M} = M' + \delta M$, where M' is the mass of non-rotating configuration and δM is the change in mass of the rotating from the non-rotating configuration with the same central density. It should be stressed that in the terms involving J^2 and Q the total mass \mathcal{M} can be substituted by M' since δM is already a second order term in the angular velocity.

In general, the HT metric represents an approximate vacuum solution, accurate to second order in the angular momentum J and to first order in the quadrupole parameter Q . In the case of ordinary stars, such as the Sun, considering the gravitational constant G and the speed of light c , the metric (1.7) can be further simplified due to the smallness of the parameters:

$$\frac{G\mathcal{M}_{Sun}}{c^2\mathcal{R}_{Sun}} \approx 2 \times 10^{-6}, \quad \frac{GJ_{Sun}}{c^3\mathcal{R}_{Sun}^2} \approx 10^{-12}, \quad \frac{GQ_{Sun}}{c^2\mathcal{R}_{Sun}^3} \approx 10^{-10}. \tag{1.9}$$

For this special case one can calculate the corresponding approximate metric from (1.7) in the limit $c \rightarrow \infty$. The computations are straightforward and lead to

$$\begin{aligned}
 ds^2 = & \left[1 - \frac{2GM}{c^2 R} + \frac{2GQ}{c^2 R^3} P_2(\cos \Theta) + \frac{2G^2 M Q}{c^4 R^4} P_2(\cos \Theta) \right] c^2 dt^2 \\
 & - \left[1 + \frac{2GM}{c^2 R} - \frac{2GQ}{c^2 R^3} P_2(\cos \Theta) \right] dR^2 \\
 & - \left[1 - \frac{2GQ}{c^2 R^3} P_2(\cos \Theta) \right] R^2 (d\Theta^2 + \sin^2 \Theta d\phi^2) + \frac{4GJ}{c^2 R} \sin^2 \Theta dt d\phi . \quad (1.10)
 \end{aligned}$$

This metric describes the gravitational field for a wide range of compact objects, and only in the case of very dense ($GM \sim c^2 \mathcal{R}$) or very rapidly rotating ($GJ \sim c^3 \mathcal{R}^2$) objects large discrepancies will appear.

1.3 The Fock's approach

Fock proposed in [82] a method to analyze Einstein's equations in the presence of matter and to derive approximate interior and exterior solutions. This approach takes into account the internal properties of the gravitational source, and reduces the problem of finding interior approximate solutions to the computation of some integrals that depend explicitly on the physical characteristics of the object. In this section, we present the main results of this approach, derive a particular interior approximate solution, and investigate the possibility of matching it with an exterior counterpart.

1.3.1 The interior solution

Fock's first-order approximation metric was recently re-derived and investigated by Abdildin [3] in a simple manner. Initially, this metric was written in its original form in a harmonic coordinate system [62, 136] as follows (a derivation of this metric is presented in the Appendix)

$$\begin{aligned}
 ds^2 = & \left[c^2 - 2U + \frac{2U^2}{c^2} - \frac{2G}{c^2} \int \frac{\rho \left(\frac{3}{2} v^2 + \Pi - U \right) + 3p}{|\vec{r} - \vec{r}'|} (dx')^3 \right] dt^2 \\
 & - \left(1 + \frac{2U}{c^2} \right) (dx_1^2 + dx_2^2 + dx_3^2) + \frac{8}{c^2} (U_1 dx_1 + U_2 dx_2 + U_3 dx_3) dt, \quad (1.11)
 \end{aligned}$$

where U is the Newtonian gravitational potential, ρ is the mass density of the body, v is the speed of the particles inside the body, Π is the elastic energy per unit mass, p is the pressure, \vec{U} is the gravitational vector potential. Notice that the quantities ρ , v , Π and U that characterize the inner structure of the source depend only on the "inner" coordinates x'_i , which are defined inside the body only. To simplify the notations we

omit the arguments that define this coordinate dependence. The corresponding energy-momentum tensor is given as

$$T^{00} = \frac{\rho}{c^2} \left[1 + \frac{1}{c^2} \left(\frac{v^2}{2} + \Pi - U \right) \right], \quad T^{0i} = \frac{\rho}{c^2} v^i, \quad T^{ij} = \frac{1}{c^2} (\rho v^i v^j + p \delta^{ij}), \quad (1.12)$$

where δ^{ij} is the Kronecker delta and $i, j = 1, 2, 3$. Newton's potential satisfies the equation $\nabla^2 U = -4\pi G \rho$. The solution of this equation that satisfies the asymptotically flatness condition at infinity can be written in the form of a volume integral:

$$U = G \int \frac{\rho}{|\vec{r} - \vec{r}'|} dx'_1 dx'_2 dx'_3. \quad (1.13)$$

Furthermore, the vector potential must satisfy the equation $\nabla^2 U_i = -4\pi G \rho v_i$ whose general asymptotically flat solution can be represented as

$$U_i = G \int \frac{\rho v_i}{|\vec{r} - \vec{r}'|} dx'_1 dx'_2 dx'_3. \quad (1.14)$$

Additional details about this metric can be found in [5] and [6].

It is worth noticing that Chandrasekhar, using the Fock method, obtained in [54] a solution similar to (1.11) that later on was used by Hartle and Sharp in [107]. However, it is not difficult to show that Chandrasekhar's solution is equivalent to (1.11). Indeed, the identification of the density

$$\rho = \rho_{Fock} = \rho_{Chandra} \left[1 + \frac{1}{c^2} \left(3U + \frac{v^2}{2} \right) \right] \quad (1.15)$$

at the level of the energy-momentum tensor allows one to calculate the corresponding metric functions that show the equivalence of the metrics. Moreover, it has been shown in [54] that the solution for the non-rotating case can be matched with the well-known Schwarzschild solution, appropriately specialized to the case of spherical symmetry and hydrostatic equilibrium in the post Newtonian approximation.

1.3.2 The exterior solution

In order to completely determine the metric, it is necessary to calculate the above integrals. Clearly, the result will depend on the internal structure of the body which is determined by the density ρ , pressure p and velocity v_i distributions. Once these functions are given, the calculation of the integrals can be performed in accordance with the detailed formalism developed by Fock [82] and then extended and continued by Abdildin [2, 4] and Brumberg [49]. Consider, for instance, the case of a slowly rotating sphere with total mass M . Then, the corresponding exterior metric in spherical-like (non harmonic) coordinates

can be written as [2]

$$ds^2 = \left[c^2 - \frac{2GM}{r} - \kappa \frac{GS_0^2}{c^2 Mr^3} (1 - 3 \cos^2 \theta) \right] dt^2 - \left(1 + \frac{2GM}{c^2 r} \right) dr^2 - r^2 (d\theta^2 + \sin^2 \theta d\phi^2) + \frac{4GS_0}{c^2 r} \sin^2 \theta d\phi dt, \quad (1.16)$$

where S_0 is the angular momentum of the body². Here we added the constant κ and verified that in fact the above metric is an approximate solution for any arbitrary real value of κ . This simple observation allows us to interpret Fock's procedure as a method to find out how the internal structure of the object influences the values of the external parameters. For instance, the total mass in the above metric is M but it can be decomposed as

$$M = m + \frac{\zeta}{c^2}, \quad (1.17)$$

where m is the static mass of the body (for details see [82, 49, 107]), and ζ is an arbitrary real constant which, as the constant κ , depends on the internal properties of the body. In particular, the cases of a liquid and a solid sphere have been analyzed in detail in [2, 4, 6] with the result

$$\zeta = \begin{cases} \frac{8}{3}K + \frac{2}{3}\varepsilon, & \text{for a liquid sphere,} \\ 4K + \frac{2}{3}\varepsilon, & \text{for a solid sphere,} \end{cases} \quad \kappa = \begin{cases} \frac{4}{7}, & \text{for a liquid sphere,} \\ \frac{15}{28}, & \text{for a solid sphere.} \end{cases} \quad (1.18)$$

where K is the rotational kinetic energy of the body and ε is the energy of the mutual gravitational attraction of the particles inside the body. In Sec. 1.4.1, we will briefly explain how to obtain the above values.

1.3.3 The Kerr metric

To describe the gravitational field of the rotating sphere outside the source, it seems physically reasonable to assume that the exterior vacuum metric be asymptotically flat. In this case, the first obvious candidate is the Kerr solution in the corresponding limit. The Kerr metric [124] in Boyer-Lindquist coordinates [48, 49] can be written as

$$ds^2 = \left(1 - \frac{2\mu\varrho}{\varrho^2 + a^2 \cos^2 \vartheta} \right) c^2 dt^2 - \frac{\varrho^2 + a^2 \cos^2 \vartheta}{\varrho^2 - 2\mu\varrho + a^2} d\varrho^2 - (\varrho^2 + a^2 \cos^2 \vartheta) d\vartheta^2 - \left(\varrho^2 + a^2 + \frac{2\mu\varrho a^2 \sin^2 \vartheta}{\varrho^2 + a^2 \cos^2 \vartheta} \right) \sin^2 \vartheta d\phi^2 - \frac{4\mu\varrho a \sin^2 \vartheta}{\varrho^2 + a^2 \cos^2 \vartheta} c dt d\phi, \quad (1.19)$$

where

$$\mu = \frac{GM}{c^2}, \quad a = -\frac{S_0}{Mc}. \quad (1.20)$$

²Notice the typos in the sign in front of S_0^2 in Eqs. (1.78) and (1.79) of [4]

Expanding this metric to the order $\frac{1}{c^2}$, one obtains

$$ds^2 = \left[c^2 - \frac{2GM}{\varrho} + \frac{2GMa^2}{\varrho^3} \cos^2 \vartheta \right] dt^2 - \left(1 + \frac{2GM}{\varrho c^2} - \frac{a^2}{\varrho^2} \sin^2 \vartheta \right) d\varrho^2 - \varrho^2 \left(1 + \frac{a^2}{\varrho^2} \cos^2 \vartheta \right) d\vartheta^2 - \varrho^2 \left(1 + \frac{a^2}{\varrho^2} \right) \sin^2 \vartheta d\phi^2 - \frac{4GMa}{\varrho c} \sin^2 \vartheta d\phi dt . \quad (1.21)$$

Furthermore, if we introduce new coordinates $\varrho = \varrho(r, \theta)$, $\vartheta = \vartheta(r, \theta)$ by means of the equations

$$\varrho = r - \frac{a^2 \sin^2 \theta}{2r}, \quad \vartheta = \theta - \frac{a^2 \sin \theta \cos \theta}{2r^2}, \quad (1.22)$$

then the approximate Kerr metric (1.21) can be reduced to the following form

$$ds^2 = \left[c^2 - \frac{2GM}{r} - \frac{GS_0^2}{c^2 M r^3} (1 - 3 \cos^2 \theta) \right] dt^2 - \left(1 + \frac{2GM}{c^2 r} \right) dr^2 - r^2 (d\theta^2 + \sin^2 \theta d\phi^2) + \frac{4GS_0}{c^2 r} \sin^2 \theta d\phi dt , \quad (1.23)$$

which coincides with the metric (1.16) with $\kappa = 1$. Consequently, the extended Fock metric (1.16) can be interpreted as describing the exterior field of a rotating body to second order in the angular velocity. The advantage of using Fock's method to derive this approximate solution is that it allows the determination of the arbitrary constant κ . In fact, whereas $\kappa = \kappa_L = 4/7$ for a liquid sphere and $\kappa = \kappa_S = 15/28$ for a solid sphere, the value for the Kerr metric $\kappa = \kappa_K = 1$ does not seem to correspond to a concrete internal model. On the other hand, all the attempts to find a physically meaningful interior Kerr solution have been unsuccessful. Perhaps the relationship with Fock's formalism we have established here could shed some light into the structure of the interior counterpart of the Kerr metric.

Furthermore, the coordinate transformation [108]

$$\begin{aligned} \varrho &= R - \frac{a^2}{2R} \left[\left(1 + \frac{2GM}{c^2 R} \right) \left(1 - \frac{GM}{c^2 R} \right) - \cos^2 \Theta \left(1 - \frac{2GM}{c^2 R} \right) \left(1 + \frac{3GM}{c^2 R} \right) \right] , \\ \vartheta &= \Theta - \frac{a^2}{2R^2} \left(1 + \frac{2GM}{c^2 R} \right) \cos \Theta \sin \Theta , \end{aligned} \quad (1.24)$$

transforms the Kerr solution (1.19), expanded to second order in the angular momentum, (here one should set $G = c = 1$) into the HT solution (1.7) with $J = -\mathcal{M}a$, $M = \mathcal{M}$ and a particular quadrupole parameter $Q = J^2/\mathcal{M}$.

In this way, we have shown that the extended Fock metric coincides for $\kappa = 1$ with the approximate Kerr solution which, in turn, is equivalent to the exterior HT solution with a particular value of the quadrupole parameter. The fact that in the Kerr solution the quadrupole moment is completely specified by the angular momentum is an indication that it can be applied only to describe the gravitational field of a particular class of compact objects. A physically meaningful generalization of the Kerr solution should include a

set of arbitrary multipole moments which are not completely determined by the angular momentum. In the next section, we present a particular exact solution characterized by an arbitrary quadrupole moment.

1.4 A solution with quadrupole moment

In this section, we will consider the case of deformed objects as, for example, a rotating ellipsoid. It is obvious that if the form of the body slightly deviates from spherical symmetry, it acquires multipole moments, in particular, a quadrupole moment; the moments of higher order are negligible, especially, for a slowly rotating ellipsoid. We will generalize Fock's metric so that the quadrupole moment appears explicitly from the integration of (1.11) and in the Newtonian potential. It should be mentioned that finding external and internal Newtonian potentials for a rotating ellipsoid is one of the classic problems of both physics and mathematical physics. Some examples for a homogeneous ellipsoid are considered in [138], but the most comprehensive details on this matter are given in [55] and more recently in [162]. As for the exterior counterpart, there are several exact solutions [52, 155, 157, 156, 179] with quadrupole moment and rotation parameter that could be used as possible candidates to be matched with the interior approximate solution. In this work, we limit ourselves to the study of a particular solution first proposed in [198] and then generalized in [194, 199].

1.4.1 The exterior Fock solution

Let us consider the first-order approximation metric (1.11). It is convenient to use the notation $x'_1 = x$, $x'_2 = y$, and $x'_3 = z$. In general, the fact that the mass density $\rho = \rho(x, y, z)$ is a function of the coordinates does not allow us to find explicit expression for the internal Newtonian potential. It is possible only by numerical integration. However, for the case of uniform density there is in the literature a reasonable number of exact solutions for rotating ellipsoids. Since we consider slow rotation and the weak field approximation, we can use the expansion for the Newtonian potential [138], [139]

$$U(r, \theta) = G \int \frac{\rho}{|\vec{r} - \vec{r}'|} dx dy dz = \frac{Gm}{r} + \frac{GD}{2r^3} P_2(\cos \theta), \quad (1.25)$$

where m is the rest mass of the ellipsoid, D is the Newtonian quadrupole moment, θ is the angle between $r' = \sqrt{x^2 + y^2 + z^2}$ and z — axis. The first term in the expression above is the potential of a sphere and the second one is responsible for the deviation from spherical symmetry. If one takes the z axis as a rotating axis then the quadrupole moment is defined by

$$D = \int \rho(2z^2 - x^2 - y^2) dx dy dz. \quad (1.26)$$

For the rotating ellipsoid with uniform density the quadrupole moment is well-known $D = 2m(r_p^2 - r_e^2)/5$, where r_p and r_e are the polar and equatorial radii of the ellipsoid,

respectively. The mass of the ellipsoid is defined as the integral $m = \int \rho dx dy dz$ that in the case of an ellipsoid with uniform density yields $m = 4\pi\rho r_e^2 r_p/3$. Note that the integration is carried out in the ranges of $0 \leq x, y \leq r_e$ and $0 \leq z \leq r_p$. Using the same procedure one may write the integral in Fock's metric as follows

$$\int \frac{\rho \left(\frac{3}{2}v^2 + \Pi - U \right) + 3p}{|\vec{r} - \vec{r}'|} dx dy dz = \frac{\zeta}{r} + \frac{\mathcal{D}}{2r^3} P_2(\cos \theta), \quad (1.27)$$

where

$$\zeta = \int \left[\rho \left(\frac{3}{2}v^2 + \Pi - U \right) + 3p \right] dx dy dz, \quad (1.28)$$

$$\mathcal{D} = \int \left[\rho \left(\frac{3}{2}v^2 + \Pi - U \right) + 3p \right] (2z^2 - x^2 - y^2) dx dy dz. \quad (1.29)$$

The quantity \mathcal{D}/c^2 is the relativistic correction to the Newtonian quadrupole moment D , i. e., the quadrupole moment due to rotation. To evaluate the integrals we use the relation for a compressible elastic medium [82]

$$\rho\Pi - \rho U + p = \rho W, \quad (1.30)$$

where W is the potential of the centrifugal forces determined by

$$W = \frac{(x^2 + y^2)}{2} \Omega^2, \quad (1.31)$$

for rigid rotation the angular velocity of the body $\vec{\Omega} = \{0, 0, \Omega\}$ has only one component along z axis and $v^2 = 2W$. Taking into account these expressions, the above shown equations reduce to the simple form

$$\zeta = 2 \int [2\rho W + p] dx dy dz, \quad (1.32)$$

$$\mathcal{D} = 2 \int [2\rho W + p] (2z^2 - x^2 - y^2) dx dy dz. \quad (1.33)$$

Furthermore, to evaluate these integrals we consider the following two cases that determine the inner structure of the body:

- 1) A liquid body with following the equation of internal motion [82]

$$\rho \frac{\partial}{\partial x_i} (U + W) = \frac{\partial p}{\partial x_i}. \quad (1.34)$$

- 2) An absolute solid body with the following equation of internal motion [49]

$$\rho \frac{\partial U}{\partial x_i} = \frac{\partial p}{\partial x_i}. \quad (1.35)$$

These are the equations of hydrostatic equilibrium which are adopted by Fock [82] and Brumberg [49] to describe the internal structure of the object. We limit ourselves to consider those cases in which the body rotates as a whole, in the manner of a rigid body. Then, for both liquid and solid bodies the rotational kinetic energy takes the form

$$K = \int \rho W dx dy dz = \frac{I_{zz} \Omega^2}{2} , \quad (1.36)$$

where I_{zz} is the moment of inertia of the ellipsoid, which for a uniform density distribution, is equal to

$$I_{zz} = \int \rho (x^2 + y^2) dx dy dz = \frac{2}{5} m r_e^2 . \quad (1.37)$$

The pressure can be expressed as

$$\int p dx dy dz = \begin{cases} \frac{1}{3} (\varepsilon - 2K) , & \text{for a liquid body,} \\ \frac{1}{3} \varepsilon , & \text{for a solid body,} \end{cases} \quad (1.38)$$

where

$$\varepsilon = \frac{1}{2} \int \rho U dx dy dz , \quad (1.39)$$

represents the negative of the energy of mutual attraction of the constituent particles of the body. For a uniform density it has form

$$\varepsilon = \frac{3Gm^2}{5\sqrt{r_e^2 - r_p^2}} \arccos \frac{r_p}{r_e} . \quad (1.40)$$

The second moments

$$K_{ik} = \int \rho W x'_i x'_k dx dy dz , \quad (1.41)$$

can be computed by using the above expressions. Then, for the second moments of the pressure we obtain (see [3])

$$\int p x'_i x'_k dx dy dz = \begin{cases} \frac{1}{2} \chi_{ik} - \frac{2}{5} K_{ik} , & \text{for a liquid body,} \\ -\frac{1}{2} K_{ik} , & \text{for a solid body,} \end{cases} \quad (1.42)$$

where (more details can be found in [3])

$$\chi_{ik} = -\frac{2}{5} \int \rho x'_i x'_k x'_j \frac{\partial U}{\partial x'_j} dx dy dz . \quad (1.43)$$

After calculating all the integrals we have

$$\zeta = \begin{cases} \frac{8}{3} K + \frac{2}{3} \varepsilon , & \text{for a liquid body,} \\ 4K + \frac{2}{3} \varepsilon , & \text{for a solid body,} \end{cases} \quad (1.44)$$

$$\mathcal{D} = \begin{cases} \frac{28}{5} \frac{\kappa_L S_0^2}{I_{zz}^2} \left[\int \rho(x^2 + y^2)(z^2 - x^2) dx dy dz \right] - \frac{4}{5} \int \rho(z^2 - x^2) x'_j \frac{\partial U}{\partial x'_j} dx dy dz, & \text{liquid,} \\ \frac{28}{5} \frac{\kappa_S S_0^2}{I_{zz}^2} \left[\int \rho(x^2 + y^2)(z^2 - x^2) dx dy dz \right], & \text{solid,} \end{cases} \quad (1.45)$$

where S_0 is the angular momentum of the body, which is found from

$$\vec{S}_0 = I_{zz} \vec{\Omega}, \quad (1.46)$$

and the numerical factors are

$$\kappa = \begin{cases} \kappa_L = \frac{4}{7}, & \text{for a liquid body,} \\ \kappa_S = \frac{15}{28}, & \text{for a solid body.} \end{cases} \quad (1.47)$$

Unlike the Newtonian scalar potential, the vector potential can be easily calculated from

$$\vec{U} = \frac{G}{2r^3} \left[\vec{S}_0 \times \vec{r} \right]. \quad (1.48)$$

Introducing the effective (total) mass as

$$M = m + \frac{\zeta}{c^2}, \quad (1.49)$$

for the Fock metric we obtain the following expression

$$ds^2 = \left[c^2 - 2 \left(\frac{GM}{r} + \frac{GD}{2r^3} P_2(\cos \theta) \right) + \frac{2}{c^2} \left(\frac{GM}{r} + \frac{GD}{2r^3} P_2(\cos \theta) \right)^2 - \frac{GD}{c^2 r^3} P_2(\cos \theta) \right] dt^2 \\ - \left[1 + \frac{2GM}{c^2 r} + \frac{GD}{c^2 r^3} P_2(\cos \theta) \right] \left[dr^2 + r^2 (d\theta^2 + \sin^2 \theta d\phi^2) \right] + \frac{4GS_0}{c^2 r} \sin^2 \theta d\phi dt, \quad (1.50)$$

in harmonic coordinates. In order to write it in Schwarzschild like (standard) spherical coordinates one should use the coordinate transformation

$$r \rightarrow R - \frac{GM}{c^2}, \quad \theta \rightarrow \Theta. \quad (1.51)$$

which transforms the metric (1.50) into

$$ds^2 = \left[c^2 - \frac{2GM}{R} - \left(D + \frac{\mathcal{D}}{c^2} \right) \frac{G}{R^3} P_2(\cos \Theta) - \frac{G^2 DM}{c^2 R^4} P_2(\cos \Theta) \right] dt^2 + \frac{4GS_0}{c^2 R} \sin^2 \Theta d\phi dt \\ - \left[1 + \frac{2GM}{c^2 R} + \frac{GD}{c^2 R^3} P_2(\cos \Theta) \right] dR^2 - \left[1 + \frac{GD}{c^2 R^3} P_2(\cos \Theta) \right] R^2 (d\Theta^2 + \sin^2 \Theta d\phi^2), \quad (1.52)$$

where we have neglected quadratic terms in the quadrupole parameter D . In the limiting case with vanishing rotation $S_0 = 0$ and vanishing quadrupole moment $D = \mathcal{D} = 0$, this metric represents the approximate Schwarzschild solution.

An examination of the metric (1.50) shows that the rough approximation with $r_e \approx r_p \approx r_{sphere}$ and $S_0 \neq 0$ leads to the approximate Fock metric considered in Sec. 1.3 with the total mass M , for a slowly rotating spherically symmetric body with

$$D = 0, \quad \mathcal{D} = -\frac{2\kappa S_0^2}{M}. \quad (1.53)$$

It should be noted that an analogous result was obtained by Laarakkers and Poisson [133]. They numerically computed the scalar quadrupole moment \mathcal{Q} of rotating neutron stars for several equations of state (EoS). They found that for fixed gravitational mass M , the quadrupole moment is given as a simple quadratic fit

$$\mathcal{Q} = -\varkappa \frac{J^2}{Mc^2} \quad (1.54)$$

where J is the angular momentum of the star and \varkappa is a dimensionless quantity that depends on the EoS. Note that the scalar quadrupole moment \mathcal{Q} of Laarakkers and Poisson is related to the one of Hartle and Thorne as follows $\mathcal{Q} = -Q$. The above quadratic fit reproduces \mathcal{Q} with remarkable accuracy. The quantity \varkappa varies between $\varkappa \approx 2$ for very soft EoS's and $\varkappa \approx 7.4$ for very stiff EoS's, for $M = 1.4M_{Sun}$ as in neutron stars. This is considerably different from a Kerr black hole, for which $\varkappa = \kappa = 1$ (see [246, 258]). Recently, the results of [133] were modified taking into account the correct definition of multipole moments [187]. Therefore the value of the \varkappa parameter in the numerical fit (1.54) is slightly different from that given in [133]. In our case, we have similar, but not the same results, since the Fock solution is not valid in the limit of strong gravitational fields (like in neutron stars) and fast rotation. The values for the constant κ are obtained from qualitative analyses in the limit of weak field and slow rotation. In order to find exact values for κ one should specify the EoS's and perform numerical integrations. This task, however, is out of the scope of the present work.

1.4.2 The exterior Quevedo-Mashhoon solution

In this section, we study the general metric describing the gravitational field of a rotating deformed mass found by Quevedo and Mashhoon [198, 194, 195, 199], which is a stationary axisymmetric solution of the vacuum Einstein's equations belonging to the class of Weyl-Lewis-Papapetrou [271, 145, 183]. For the sake of simplicity we consider here a particular solution involving only four parameters: the mass parameter M , the angular momentum parameter a , the quadrupole parameter q , and the additional Zipoy-Voorhees [277, 266] constant δ . For brevity, in this section we use geometric units with $G = c = 1$. The corresponding line element in spheroidal coordinates (t, r, θ, ϕ) with $r \geq \sigma + M_0$, $0 \leq \theta \leq \frac{\pi}{2}$ is given by [198]

$$ds^2 = f(dt - \omega d\phi)^2 - \frac{1}{f} \left\{ e^{2\gamma} \left(d\theta^2 + \frac{dr^2}{r^2 - 2M_0r + a^2} \right) [(M_0 - r)^2 - (M_0^2 - a^2) \cos^2 \theta] + (r^2 - 2M_0r + a^2) \sin^2 \theta d\phi^2 \right\}, \quad (1.55)$$

where f , ω and γ are functions of r and θ only, and σ is a constant. They have the form [$x = (r - M_0)/\sigma$, $y = \cos \theta$]

$$\begin{aligned} f &= \frac{\tilde{R}}{L} e^{-2q\delta P_2 Q_2}, & \omega &= -2a - 2\sigma \frac{\mathfrak{M}}{\tilde{R}} e^{2q\delta P_2 Q_2}, \\ e^{2\gamma} &= \frac{1}{4} \left(1 + \frac{M}{\sigma}\right)^2 \frac{\tilde{R}}{(x^2 - 1)^\delta} e^{2\delta^2 \hat{\gamma}}, \end{aligned} \quad (1.56)$$

where

$$\tilde{R} = a_+ a_- + b_+ b_-, \quad L = a_+^2 + b_+^2, \quad (1.57)$$

$$\mathfrak{M} = (x+1)^{\delta-1} [x(1-y^2)(\lambda+\eta)a_+ + y(x^2-1)(1-\lambda\eta)b_+], \quad (1.58)$$

$$\begin{aligned} \hat{\gamma} &= \frac{1}{2}(1+q)^2 \ln \frac{x^2-1}{x^2-y^2} + 2q(1-P_2)Q_1 + q^2(1-P_2)[(1+P_2)(Q_1^2 - Q_2^2) \\ &\quad + \frac{1}{2}(x^2-1)(2Q_2^2 - 3xQ_1Q_2 + 3Q_0Q_2 - Q_2')]. \end{aligned} \quad (1.59)$$

Here $P_l(y)$ and $Q_l(x)$ are Legendre polynomials of the first and second kind, respectively. Furthermore

$$a_\pm = (x \pm 1)^{\delta-1} [x(1-\lambda\eta) \pm (1+\lambda\eta)], \quad (1.60)$$

$$b_\pm = (x \pm 1)^{\delta-1} [y(\lambda+\eta) \mp (\lambda-\eta)], \quad (1.61)$$

with

$$\lambda = \alpha(x^2-1)^{1-\delta}(x+y)^{2\delta-2} e^{2q\delta\delta_+}, \quad (1.62)$$

$$\eta = \alpha(x^2-1)^{1-\delta}(x-y)^{2\delta-2} e^{2q\delta\delta_-}, \quad (1.63)$$

$$\delta_\pm = \frac{1}{2} \ln \frac{(x \pm y)^2}{x^2-1} + \frac{3}{2}(1-y^2 \mp xy) + \frac{3}{4}[x(1-y^2) \mp y(x^2-1)] \ln \frac{x-1}{x+1}. \quad (1.64)$$

Moreover, α and σ are constants defined as

$$\alpha = \frac{\sigma - M}{a}, \quad \sigma = \sqrt{M^2 - a^2}. \quad (1.65)$$

The physical meaning of the parameters entering this metric can be investigated in an invariant manner by calculating the Geroch-Hansen [90, 103] moments:

$$M_{2k+1} = J_{2k} = 0, \quad k = 0, 1, 2, \dots, \quad (1.66)$$

$$M_0 = M + \sigma(\delta - 1), \quad J_1 = Ma + 2a\sigma(\delta - 1), \quad (1.67)$$

$$\begin{aligned} M_2 &= -Ma^2 + \frac{2}{15}q\sigma^3 \\ &\quad - \frac{1}{15}\sigma(\delta - 1) [45M^2 + 15M\sigma(\delta - 1) - (30 + 2q + 10\delta - 5\delta^2)\sigma^2], \end{aligned} \quad (1.68)$$

$$\begin{aligned} J_3 &= -Ma^3 + \frac{4}{15}aq\sigma^3 \\ &\quad - \frac{1}{15}a\sigma(\delta - 1) [60M^2 + 45M\sigma(\delta - 1) - 2\sigma^2(15 + 2q + 10\delta - 5\delta^2)]. \end{aligned} \quad (1.69)$$

The vanishing of the odd gravitoelectric (M_n) and even gravitomagnetic (J_n) multipole moments is a consequence of the reflection symmetry with respect to the equatorial plane $\theta = \pi/2$. Note that in the limiting case $\delta = 1$, $M_0 = M$ is the total mass of the body, a represents the specific angular momentum, and q is related to the deviation from spherical symmetry. All higher multipole moments can be shown to depend only on the parameters M , a , and q . In general, we see that the Zipoy-Voorhees parameter is related to the quadrupole moment of the source. In fact, even in the limiting static case with $a = 0$ and $q = 0$, the only non-vanishing parameters are $M = \sigma$ and δ so that all gravitomagnetic multipoles vanish and one obtains $M_0 = M\delta$ and $M_2 = -\frac{1}{3}M^3\delta(\delta^2 - 1)$ — the quadrupole moment that indicates a deviation from spherical symmetry. Some geometrical properties of (1.55) versus particle motion and tidal indicators in this spacetime were explored in [30] and [23], respectively.

Consider the limiting cases of the QM solution. For vanishing quadrupole parameter, $q = 0$, $\delta = 1$, and vanishing angular momentum $a = 0$, $\alpha = 0$, and $\sigma = M$, one recovers the Schwarzschild solution with the following metric functions:

$$f = 1 - \frac{2M}{r}, \quad \omega = 0, \quad \gamma = \frac{1}{2} \ln \frac{r(r - 2M)}{(M - r)^2 - M^2 \cos^2 \theta}. \quad (1.70)$$

For vanishing quadrupole parameter and $\delta = 1$, one recovers the Kerr solution (1.19) with $\vartheta \rightarrow \theta$ and $\varrho \rightarrow r$ and functions

$$\begin{aligned} f &= 1 - \frac{2Mr}{r^2 + a^2 \cos^2 \theta}, & \omega &= \frac{2aMr \sin^2 \theta}{r^2 - 2Mr + a^2 \cos^2 \theta}, \\ \gamma &= \frac{1}{2} \ln \frac{r(r - 2M) + a^2 \cos^2 \theta}{(M - r)^2 - (M^2 - a^2) \cos^2 \theta}. \end{aligned} \quad (1.71)$$

The above limiting cases show that this solution describes the exact exterior field a rotating deformed object. To compute the case of a slowly rotating and slightly deformed body we choose the Zipoy-Voorhees parameter as $\delta = 1 + sq$, where s is a real constant. Then, expanding the metric (1.55) to first order in the quadrupole parameter q and to second order in the rotation parameter a , we obtain

$$\begin{aligned} f &= 1 - \frac{2M}{r} + \frac{2a^2 M \cos^2 \theta}{r^3} + q(1 + s) \left(1 - \frac{2M}{r}\right) \ln \left(1 - \frac{2M}{r}\right) \\ &\quad + 3q \left(\frac{r}{2M} - 1\right) \left[\left(1 - \frac{M}{r}\right) (3 \cos^2 \theta - 1) \right. \\ &\quad \left. + \left\{ \left(\frac{r}{2M} - 1\right) (3 \cos^2 \theta - 1) - \frac{M}{r} \sin^2 \theta \right\} \ln \left(1 - \frac{2M}{r}\right) \right], \end{aligned} \quad (1.72)$$

$$\omega = \frac{2aMr \sin^2 \theta}{r - 2M}, \quad (1.73)$$

$$\begin{aligned} \gamma = & \frac{1}{2} \ln \frac{r(r-2M)}{(r-M)^2 - M^2 \cos^2 \theta} + \frac{a^2}{2} \left[\frac{M^2 \cos^2 \theta \sin^2 \theta}{r(r-2M)((r-M)^2 - M^2 \cos^2 \theta)} \right] \\ & + q(1+s) \ln \frac{r(r-2M)}{(r-M)^2 - M^2 \cos^2 \theta} \\ & - 3q \left[1 + \frac{1}{2} \left(\frac{r}{M} - 1 \right) \ln \left(1 - \frac{2M}{r} \right) \right] \sin^2 \theta. \end{aligned} \quad (1.74)$$

The further simplification $s = -1$, and the coordinate transformation [108, 30, 161]

$$\begin{aligned} r = R + \mathcal{M}q + \frac{3}{2} \mathcal{M}q \sin^2 \Theta \left[\frac{R}{\mathcal{M}} - 1 + \frac{R^2}{2\mathcal{M}^2} \left(1 - \frac{2\mathcal{M}}{R} \right) \ln \left(1 - \frac{2\mathcal{M}}{R} \right) \right] \\ - \frac{a^2}{2R} \left[\left(1 + \frac{2\mathcal{M}}{R} \right) \left(1 - \frac{\mathcal{M}}{R} \right) - \cos^2 \Theta \left(1 - \frac{2\mathcal{M}}{R} \right) \left(1 + \frac{3\mathcal{M}}{R} \right) \right] \end{aligned} \quad (1.75)$$

$$\theta = \Theta - \sin \Theta \cos \Theta \left\{ \frac{3}{2} q \left[2 + \left(\frac{R}{\mathcal{M}} - 1 \right) \ln \left(1 - \frac{2\mathcal{M}}{R} \right) \right] + \frac{a^2}{2R} \left(1 + \frac{2\mathcal{M}}{R} \right) \right\} \quad (1.76)$$

transforms the approximate QM solution (1.72)–(1.74) into

$$\begin{aligned} ds^2 = & \left[1 - \frac{2GM(1-q)}{c^2 R} + \frac{2G}{c^2 R^3} \left(\frac{J^2}{M} - \frac{4}{5} q M^3 \right) \left(1 + \frac{GM(1-q)}{c^2 R} \right) P_2(\cos \Theta) \right] c^2 dt^2 \\ & - \frac{4GMa}{c^2 R} \sin^2 \Theta dt d\phi - \left[1 + \frac{2GM(1-q)}{c^2 R} - \frac{2G}{c^2 R^3} \left(\frac{J^2}{M} - \frac{4}{5} q M^3 \right) P_2(\cos \Theta) \right] dR^2 \\ & - \left[1 - \frac{2G}{c^2 R^3} \left(\frac{J^2}{M} - \frac{4}{5} q M^3 \right) P_2(\cos \Theta) \right] R^2 (d\Theta^2 + \sin^2 \Theta d\phi^2). \end{aligned} \quad (1.77)$$

Here we introduced again all the necessary constants G and c in order to compare our results with previous metrics. Finally, if we redefine the parameters M , a , and q as

$$\mathcal{M} = M(1-q), \quad J = -Ma, \quad Q = \frac{J^2}{M} - \frac{4}{5} M^3 q, \quad (1.78)$$

the approximate metric (1.77) coincides with the exterior HT metric (1.10) and, consequently, can be matched with the interior HT metric discussed in 1.2.

The above metric is equivalent to the exterior extended Fock metric discussed in the previous subsection. To see this one has to consider the exterior solution (1.52) which is written in the same coordinates as the exterior solutions (1.77) and (1.10). It is convenient to show first the equivalence with the exterior HT solution (1.10) that yields the conditions

$$\mathcal{M} = M, \quad J = S_0, \quad Q = -\frac{1}{2} \left(D + \frac{\mathcal{D}}{c^2} \right). \quad (1.79)$$

The equivalence with the approximate QM solution (1.77) follows then from the comparison of Eqs.(1.78) and (1.79). We obtain

$$q = \frac{5}{8} \frac{c^4}{G^2} \frac{1}{M^3} \left[D + \frac{1}{c^2} \left(\mathcal{D} + \frac{2J^2}{M} \right) \right], \quad (1.80)$$

and for vanishing D

$$q = \frac{5}{4} \frac{c^2}{G^2} \frac{J^2}{M^4} (1 - \kappa). \quad (1.81)$$

This result is in accordance with the limiting case of the Kerr metric for which we obtained that $\kappa = 1$ and hence $q = 0$.

Thus we come to the conclusion that in the limit of a slowly rotating and slightly deformed body the QM approximate solution is equivalent to the exterior Fock solution.

1.5 Conclusions

In this work, we studied the gravitational field of slowly rotating, slightly deformed astrophysical compact objects. We presented the main exact and approximate solutions of Einstein's equations that can be used to describe the interior and the exterior gravitational field. In particular, we presented the method proposed by Hartle and Thorne to find interior and exterior approximate solutions, and the method proposed by Fock to derive approximate interior and exterior solutions. We derived an extension of the approximate exterior Fock metric that takes into account up to the first order the contribution of a quadrupole parameter that describes the deviation of the body from spherical symmetry. A particular parameter that enters the extended Fock metric turns out to have very specific values in the case of a liquid sphere and a solid sphere. In the case of the approximate Kerr metric, this parameter does not seem to correspond to any known interior model analyzed in the framework of Fock's formalism.

We found that a particular QM solution, which in general possesses an infinite set of gravitational and electromagnetic multipole moments, contains the exact Kerr metric and the approximate HT metric as special cases. Moreover, since the HT solution is endowed with its interior counterpart, we conclude that the approximate QM solution (to the second order in the angular momentum and to the first order in the quadrupole parameter) can be matched with the interior HT solution, indicating that it can be used to correctly describe the gravitational field of astrophysical compact objects. Moreover, we showed that the explicit form of the exterior Fock metric is equivalent to the approximate exterior QM solution.

To avoid the technical problems that are usually found in the process of matching solutions [197], we use the same set of coordinates inside and outside the body. In the cases presented here, this can be done in a relative easy way only because all the coordinate transformations are not calculated exactly, but with the same approximation as the metric functions. This approach allows us to reduce the matching problem to the comparison of the metrics on the matching surfaces in such a way that only algebraic conditions appear.

Using this method, we could show that the approximate Kerr metric cannot be matched with an interior Fock solution. However, if we take into account an additional quadrupole parameter, the matching of the extended Fock metric can be carried out by using as exterior counterpart a particular approximate QM solution that contains the Kerr metric as special case. We conclude that the quadrupole parameter offers an additional degree of freedom that allows the matching. A first step in this direction was recently taken forward in [196]. It would be interesting to see if this is also true in the case of exact solutions. This could shed some light into the problem of finding a realistic gravitational source for the Kerr metric, a long-standing problem of classical general relativity.

1.6 Perspectives

In view of recent works on white dwarfs [210, 209, 45] and neutron stars [18] it would be interesting to calculate the quadrupole moment for these objects and perform analyses of Laarakkers and Poisson [133], and Pappas and Apostolatos [187]. From our preliminary results we expect that the quadrupole moment for rotating white dwarfs and neutron stars will be larger than the Kerr quadrupole moment $Q = J^2/M$. To this end, it is appropriate to use the Hartle-Thorne solution, since it possesses both internal and external solutions unlike other exact solutions, in addition it works in the strong gravitational field regime whereas the Fock metric is valid only in the weak field regime.

Chapter 2

Equatorial circular geodesics in the Hartle-Thorne spacetime

2.1 Introduction

Astrophysical objects in general are characterized by a non-spherically symmetric distribution of mass. In many cases, like ordinary planets and satellites, it is possible to neglect the deviations from spherical symmetry: it seems instead reasonable to expect that deviations should be taken into account in case of strong gravitational fields (around compact objects). In this light we investigate the influence of the quadrupole parameter on the equatorial circular motion of a test particle in the field of a rotating deformed central object. To this end the metric, describing the exterior field of a slowly rotating slightly deformed object, found by Hartle and Thorne [105, 108] is of high importance. However in this chapter we use the form of the metric presented by Bini et al. [30], since it is always possible to show that by redefining the quadrupole parameter in [30] one can obtain the same metric form of Hartle and Thorne (HT) [108]. In geometrical units this metric is given by

$$\begin{aligned} ds^2 = & - \left(1 - \frac{2M}{r}\right) \left[1 + 2k_1 P_2(\cos \theta) + 2 \left(1 - \frac{2M}{r}\right)^{-1} \frac{J^2}{r^4} (2 \cos^2 \theta - 1) \right] dt^2 \\ & + \left(1 - \frac{2M}{r}\right)^{-1} \left[1 - 2k_2 P_2(\cos \theta) - 2 \left(1 - \frac{2M}{r}\right)^{-1} \frac{J^2}{r^4} \right] dr^2 \\ & + r^2 [1 - 2k_3 P_2(\cos \theta)] (d\theta^2 + \sin^2 \theta d\phi^2) - \frac{4J}{r} \sin^2 \theta dt d\phi \end{aligned} \quad (2.1)$$

where

$$k_1 = \frac{J^2}{Mr^3} \left(1 + \frac{M}{r}\right) - \frac{5Q - J^2/M}{8M^3} Q_2^2 \left(\frac{r}{M} - 1\right), \quad k_2 = k_1 - \frac{6J^2}{r^4},$$

$$k_3 = k_1 + \frac{J^2}{r^4} - \frac{5Q - J^2/M}{4M^2r} \left(1 - \frac{2M}{r}\right)^{-1/2} Q_2^1\left(\frac{r}{M} - 1\right),$$

$$P_2(x) = \frac{1}{2}(3x^2 - 1),$$

$$Q_2^1(x) = (x^2 - 1)^{1/2} \left[\frac{3x}{2} \ln \frac{x+1}{x-1} - \frac{3x^2 - 2}{x^2 - 1} \right],$$

$$Q_2^2(x) = (x^2 - 1) \left[\frac{3}{2} \ln \frac{x+1}{x-1} - \frac{3x^3 - 5x}{(x^2 - 1)^2} \right].$$

Here $P_2(x)$ is Legendre polynomials of the first kind, Q_l^m are the associated Legendre polynomials of the second kind and the constants M , J and Q are the total mass, angular momentum and quadrupole parameter of a rotating star respectively¹. The approximate Kerr metric [124] in the Boyer-Lindquist coordinates (t, R, Θ, ϕ) up to second order terms in the rotation parameter a can be obtained from (2.1) by setting

$$J = -Ma, \quad Q = J^2/M, \quad (2.2)$$

and making a coordinate transformation given by

$$r = R + \frac{a^2}{2R} \left[\left(1 + \frac{2M}{R}\right) \left(1 - \frac{M}{R}\right) - \cos^2 \Theta \left(1 - \frac{2M}{R}\right) \left(1 + \frac{3M}{R}\right) \right], \quad (2.3)$$

$$\theta = \Theta + \frac{a^2}{2R^2} \left(1 + \frac{2M}{R}\right) \sin \Theta \cos \Theta.$$

2.2 The domain of validity of the Hartle-Thorne approximation

Having on mind the applicability of the metric (2.1) to the exterior of a compact object, we demand that the energy-momentum tensor, which follows from (2.1), be much smaller than the corresponding tensor of the source object. The correct comparison of these tensors should be performed in terms of eigenvalues. Consider a surface of the object which generates the metric under consideration. According to the Einstein equations $G_\alpha^\beta = 8\pi T_\alpha^\beta$, where $\alpha, \beta = (t, r, \theta, \phi)$, the eigenvalues of the Einstein tensor inside the matter are equal to its density and pressure multiplied by 8π [249]. Due to the inequality $\rho > p$ which holds for all known types of matter, the maximum of eigenvalues can be estimated as $8\pi\rho$, where ρ represents the average density of the body:

$$|G_\alpha^\beta| \lesssim 8\pi\rho = \frac{8\pi M}{4\pi r^3/3} = \frac{6M}{r^3}. \quad (2.4)$$

¹We note here that the quadrupole parameter Q is related to the mass quadrupole moment Q defined by Hartle and Thorne [108] through $Q = 2J^2/M - Q_{HT}$.

On the other hand, the first non-vanishing terms in the expansion of the Einstein tensor of the Hartle-Thorne metric in powers of J and Q are G_0^4 and G_4^0 . Then the Einstein tensor has two purely imaginary eigenvalues different from zero $\lambda_{1,2} \neq 0$ and two exactly zero eigenvalues $\lambda_{3,4} = 0$. The first pair is diverging as $r \rightarrow 2M$. Near this radius we have, for $\delta r = r - 2M$ approaching 0, the leading terms equal to

$$\lambda_{1,2} \rightarrow \pm i \frac{15JQ(1 - 3\cos^2\theta)\sin\theta}{32\sqrt{2}M^{11/2}\delta r^{3/2}}. \quad (2.5)$$

Finally, by comparing the absolute values of (2.4) and (2.5) for $r \rightarrow 2M$, taking into account that $0 \leq (1 - 3\cos^2\theta)^2\sin^2\theta \leq 1$, we obtain the following inequality, describing the domain of validity of the Hartle-Thorne metric around the gravitating body

$$\delta r^3 \gg \frac{25J^2Q^2}{128M^7}. \quad (2.6)$$

If we take the extreme values of the parameters for neutron stars such as $J \simeq M^2$, $Q \simeq 10^{-2}M^3$ we obtain $\delta r \gg 3 \times 10^{-2}M$, that is certainly true for the exterior of neutron stars while their radii are more than $2.5M$ [101], i. e. $\delta r > 0.5M$.

2.3 Equations for the equatorial circular geodesics

2.3.1 The Orbital Angular Velocity

The 4-velocity U of a test particle on a circular orbit can be parametrized by the constant angular velocity ζ with respect to infinity

$$U = \Gamma[\partial_t + \zeta\partial_\phi], \quad (2.7)$$

where Γ is the normalization factor which assures that $U^\alpha U_\alpha = -1$. From the normalization and the geodesics conditions we obtain following expressions for Γ and $\zeta = U^\phi/U^t$

$$g_{tt} + 2\zeta g_{t\phi} + \zeta^2 g_{\phi\phi} = -1/\Gamma^2, \quad g_{tt,r} + 2\zeta g_{t\phi,r} + \zeta^2 g_{\phi\phi,r} = 0, \quad (2.8)$$

where $g_{\alpha\beta,r} = \partial g_{\alpha\beta}/\partial r$. Hence, ζ , the solution of (2.8)₂, is given by

$$\zeta_{\pm}(u) = \pm\zeta_0(u) [1 \mp j f_1(u) + j^2 f_2(u) + q f_3(u)] \quad (2.9)$$

where (+/-) stands for co-rotating/contra-rotating geodesics, $j = J/M^2$ and $q = Q/M^3$ are the dimensionless angular momentum and quadrupole parameter and $u = M/r$. The rest quantities are defined as follows

$$\begin{aligned} \zeta_0(u) &= \frac{u^{3/2}}{M}, \quad f_1(u) = u^{3/2}, \\ f_2(u) &= \frac{48u^7 - 80u^6 + 4u^5 + 42u^4 - 40u^3 - 10u^2 - 15u + 15}{16u^2(1-2u)} - f(u), \\ f_3(u) &= -\frac{5(6u^4 - 8u^3 - 2u^2 - 3u + 3)}{16u^2(1-2u)} + f(u), \\ f(u) &= \frac{15(1-2u^3)}{32u^3} \ln\left(\frac{1}{1-2u}\right). \end{aligned}$$

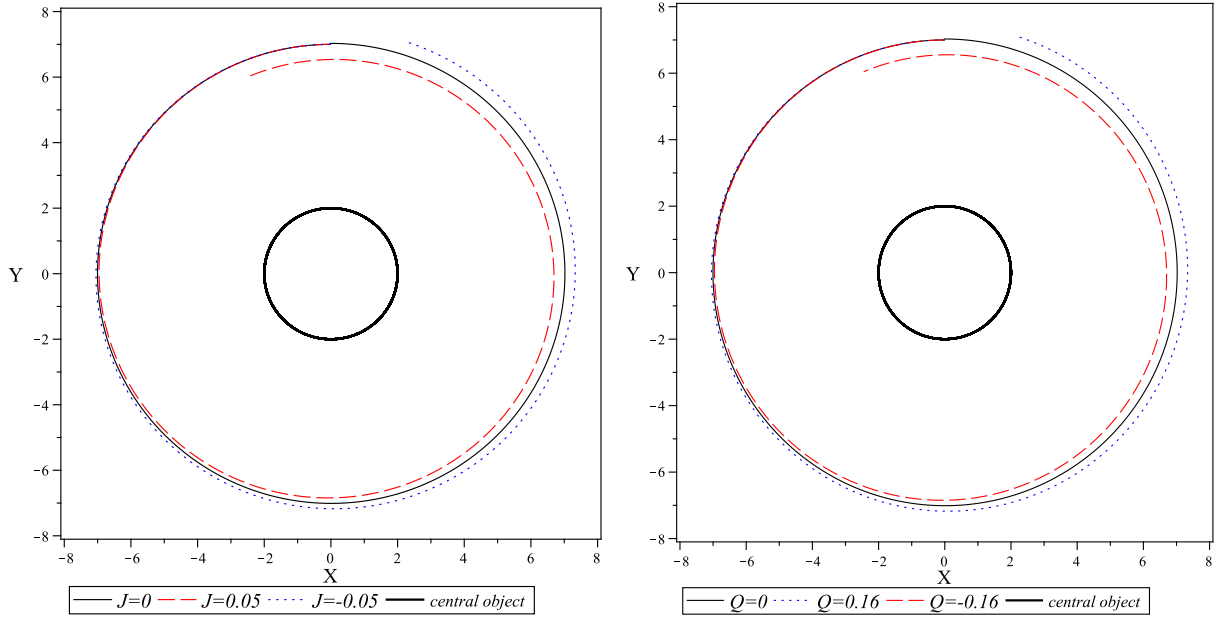


Figure 2.1: Left panel: one revolution of a test particle in the field of a rotating central body for $Q = 0$. Right panel: the motion of the test particle in the field of a non-rotating deformed object for $J = 0$. The common parameters are $M = 1$, $r = 7$, $dr/ds = 0$, $\phi = \pi/2$, and $d\phi/ds = 0.07145$.

In Fig. 2.1 left panel we show the differences among the geodesics with the same initial conditions arising due to the rotation of the central body i.e. the frame dragging effect in the strong field regime. The solid line for $J = 0$ corresponds to equatorial circular geodesics in the Schwarzschild spacetime. The dashed line for $J > 0$ corresponds to co-rotating and the dotted line for $J < 0$ corresponds to the contra-rotating orbits. In Fig. 2.1 right panel we show the differences between the geodesics with the same initial conditions arising due to the deformation of the source i.e. the oblateness of the central body. The solid line for $Q = 0$ corresponds to equatorial circular geodesics in the Schwarzschild spacetime. The dashed line for $Q < 0$ corresponds to the geodesics in the field of oblate and the dotted line for $Q > 0$ corresponds to the geodesics in the field of the prolate central body. It is easy to see that varying the quadrupole parameter Q one can recover the deviations from the Schwarzschild spacetime geodesics analogous to those caused by the frame dragging effect. By selecting the values of J and Q one can recover the circular orbits as in Fig. 2.2 left panel. In Fig.2.2 right panel and Figs. 2.3 we consider the geodesics with the same initial conditions in the field of non-rotating bodies with the increasing values of Q . As a result, we have obtained different spiraling and bound trajectories of the test particle.

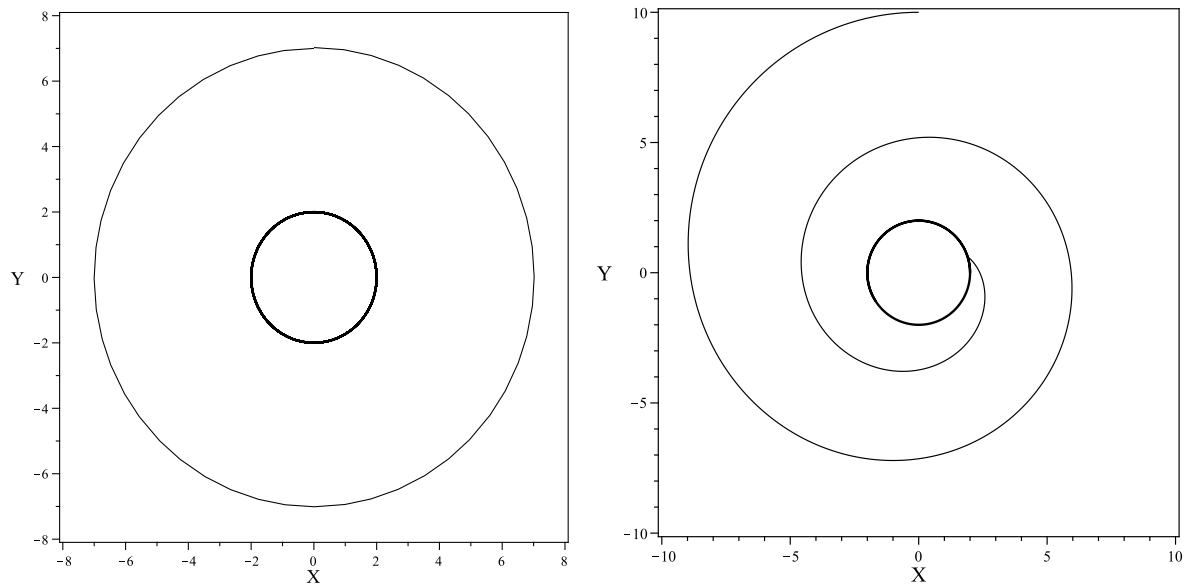


Figure 2.2: Left panel: circular orbit for $J = -0.05$, $Q = -0.1575$ and $r = 7$, $d\phi/ds = 0.07145$. Right panel: spiral orbit for $Q = -0.16$ and $J = 0$, $r = 10$, $d\phi/ds = 0.035355$. The common parameters are $M = 1$, $\phi = \pi/2$, and $dr/ds = 0$.

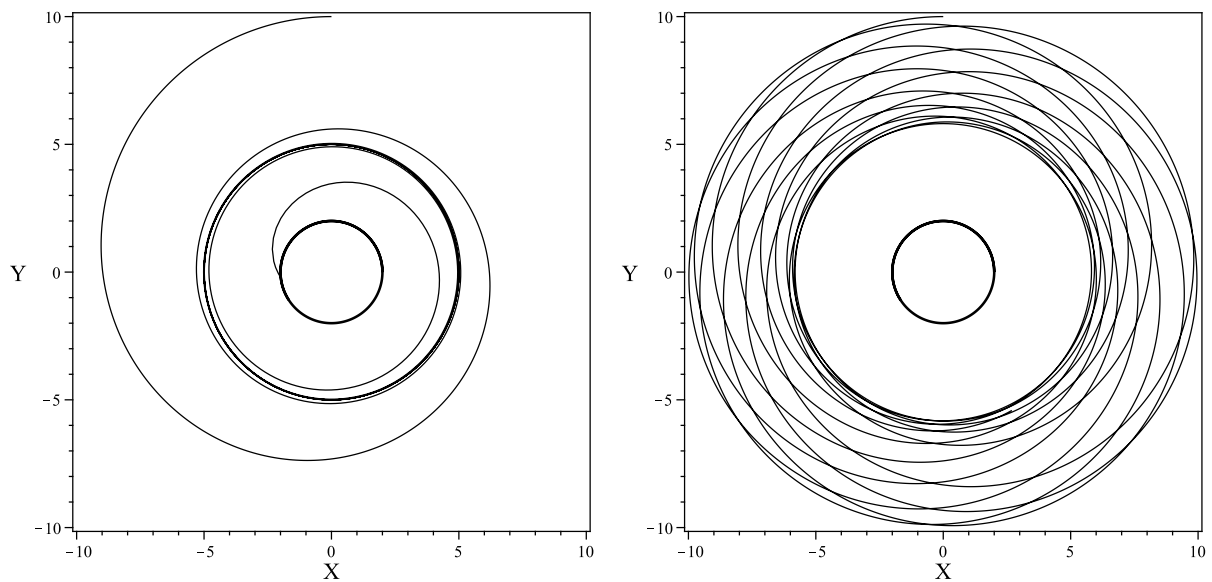


Figure 2.3: Left panel: spiral orbit for $Q = 0$. Right panel: bound orbit for $Q = 0.16$. The common parameters are $M = 1$, $J = 0$, $r = 10$, $dr/ds = 0$, $\phi = \pi/2$, and $d\phi/ds = 0.035355$.

2.3.2 Radii of marginally stable and marginally bound orbits

The condition $\varepsilon = -U_t = 1$ gives the radius of the marginally bound orbit r_{mb} , where ε is the conserved specific energy per unit mass of the particle and the normalization condition $P^\alpha P_\alpha = 0$ gives the photon orbit radius r_{ph} , where $P = \Gamma_{\text{ph}}[\partial_t + \zeta_{\text{ph}}\partial_\phi]$ is the photon 4-momentum. Note, that the normalization condition $P_\alpha P^\alpha = 0$ gives the orbital angular velocity for the photon ζ_{ph} , however Γ_{ph} remains arbitrary. In order to define the photon orbit radius r_{ph} , first, one has to define ζ_{ph} and evaluate the expression for the 4-acceleration a^α . For the circular geodesic the condition $a^\alpha = 0$ is enough to find r_{ph} . In addition, by setting $dl/dr = 0$ one can find the radius of the marginally stable orbit r_{ms} , where $l = -U_\phi/U_t$ is the specific angular momentum per unit energy of the particle.

$$\begin{aligned} r_{\text{mb}} &= 4M \left[1 \mp \frac{1}{2}j + \left(\frac{8033}{256} - 45 \ln 2 \right) j^2 + \left(-\frac{1005}{32} + 45 \ln 2 \right) q \right], \\ r_{\text{ph}} &= 3M \left[1 \pm \frac{2\sqrt{3}}{9}j + \left(\frac{1751}{324} - \frac{75}{16} \ln 3 \right) j^2 + \left(-\frac{65}{12} + \frac{75}{16} \ln 3 \right) q \right], \\ r_{\text{ms}} &= 6M \left[1 \pm \frac{2}{3}\sqrt{\frac{2}{3}}j + \left(-\frac{251903}{2592} + 240 \ln \frac{3}{2} \right) j^2 + \left(\frac{9325}{96} - 240 \ln \frac{3}{2} \right) q \right]. \end{aligned}$$

It is clear that the presence of both the rotation and quadrupole parameters can increase or decrease the values for r_{mb} , r_{ph} and r_{ms} . For the sake of comparison, if one writes these radii in the Boyer-Lindquist coordinates using the reverse of (2.3) for $\theta = \pi/2$, and the relation (2.2), then it is easy to obtain the following expressions for the Kerr solution with accuracy up to second order terms in the rotation parameter a :

$$\begin{aligned} R_{\text{mb}} &= 4M \left[1 \pm \frac{a}{2M} - \frac{a^2}{16M^2} \right], \\ R_{\text{ph}} &= 3M \left[1 \mp \frac{2\sqrt{3}}{9} \frac{a}{M} - \frac{2a^2}{27M^2} \right], \\ R_{\text{ms}} &= 6M \left[1 \mp \frac{2}{3}\sqrt{\frac{2}{3}} \frac{a}{M} - \frac{7a^2}{108M^2} \right]. \end{aligned}$$

These radii are exactly those radii, expanded in terms up to second order in a , given in the work of Bardeen et. al. [13] for the Kerr solution.

2.4 Conclusions

In this chapter we have explored the domain of validity of the Hartle-Thorne solution as well as the geodesics in this spacetime. We considered equatorial circular geodesics and investigated the role of the quadrupole parameter in the motion of a test particle. Besides, we have shown that the effects arisen from the rotation of the source can be

balanced (increased or decreased) by its oblateness (quadrupole moment). Moreover we derived the radii of innermost marginally stable, marginally bound and photon circular orbits with the same accuracy of the Hartle-Thorne solution. It has been shown that these results are approximately in agreement with those of Bardeen [13] for the Kerr solution.

2.5 Perspectives

The quadrupole moment of astrophysical compact objects plays a crucial role, as well as the frame dragging effect, in exploring the motion of test particles. As we can see from the previous part of this work, the quadrupole moment offers an additional degree of freedom that allows not only the matching of the different solutions but also the fitting of observational data. In this respect the Hartle-Thorne solutions, both internal and external, are of high importance. With the help of the HT solutions one can obtain analytic expressions for the orbital angular velocity, angular momentum, energy and epicyclic frequencies of test particles around compact objects. These quantities are relevant to several astrophysical phenomena, namely to the observed quasi periodic oscillations (QPOs) in the X-ray luminosity from black hole candidates and neutron star sources. It is believed that QPOs data may be used to test the strong field regime of Einstein's general relativity, and the physics of super dense matter which neutron stars are made of. This task will be treated in our forthcoming works.

Chapter 3

Tidal indicators in the field of a rotating deformed mass

3.1 Introduction

Relativistic tidal problems have been extensively studied in the literature in a variety of contexts. Tidal effects are responsible for deformations or even disruption of astrophysical objects (like ordinary stars but also compact objects like neutron stars) placed in strong gravitational fields. For instance, they play a central role in the merging of compact object binaries, which can be accurately modeled only by numerical simulations in full general relativity, solving the coupled Einstein-hydrodynamics equations needed to evolve relativistic, self-gravitating fluids [240, 69, 239]. Such tidal disruption events are expected to happen very frequently in the Universe, leading then to a possible detection of the associated emission of gravitational waves in the near future by ground-based detectors [1]. To this end, different analytical and semi-analytical approaches have been developed to properly describe at least part of the coalescence process and to study the associated gravitational wave signals [81, 113, 114, 60]. These approaches usually require either Post-Newtonian techniques or first order perturbation theory. In fact, in this limit the motion of each individual compact object in the binary system can be treated as the motion of an extended body in a given gravitational field due to its companion under the assumption that it causes only a small perturbation on the background [159, 160]. Finally, one can also be interested in studying the tidal disruption limit of ordinary stars and compact objects in the field of a black hole (see, e.g., Ref. [119] and references therein). Tidal problems of this kind can be treated within the so-called tidal approximation, i.e., by assuming that the mass of the star is much smaller than the black hole mass and that the stellar radius is smaller than the orbital radius, so that backreaction effects on the background field can be neglected. Therefore, the star is usually described as a self-gravitating Newtonian fluid and its center of mass is assumed to move around the black hole along a timelike geodesic path. The tidal field due to the black hole is then computed from the Riemann tensor in terms of the geodesic deviation equation.

The role of the observer in relativistic tidal problems has never received enough atten-

tion in the literature. Nevertheless, it is crucial in interpreting the results. In fact, if tidal forces are due to curvature, the latter is experienced by observers through the electric and magnetic parts of the Riemann tensor, which is the only true 4-dimensional invariant quantity. In contrast, its electric and magnetic parts depend by definition on the choice of the observers who perform the measurement. In a recent paper [29] we have addressed such an issue by providing all necessary tools to relate the measurement of tidal effects by different families of observers. We have considered two “tidal indicators” defined as the trace of the square of the electric and magnetic parts of the Riemann tensor, respectively. They are both curvature and observer dependent and we have investigated their properties by considering a number of special observer families in the equatorial plane of the Kerr spacetime. As an interesting feature we have shown that the electric-type indicator cannot be made as vanishing with respect to any such observers, whereas the family of Carter’s observers is the only one who measures zero tidal magnetic indicator. We have argued that the explanation for this effect relies on the absence of a quadrupole moment independent on the rotational parameter for the Kerr solution. To answer this question, as well as to extend the previous analysis to a more general context, we consider here a solution of the vacuum Einstein field equations due to Quevedo and Mashhoon [195, 199], which generalizes the Kerr spacetime to include the case of matter with arbitrary mass quadrupole moment and is specified by three parameters, the mass M , the angular momentum per unit mass a and the quadrupole parameter q . It is its genuine quadrupole moment content which makes this solution of particular interest here. We will thus investigate how the shape deformation of the rotating source affects the properties of tidal indicators with respect to special family of observers, including static observers, ZAMOs (i.e., zero angular momentum observers) and geodesic observers.

In this chapter latin indices run from 1 to 3 whereas greek indices run from 0 to 3 and geometrical units are assumed. The metric signature is chosen as $+2$.

3.2 The gravitational field of a rotating deformed mass

The exterior gravitational field of a rotating deformed mass can be described by the Quevedo-Mashhoon (hereafter QM) solution [195, 199]. This is a stationary axisymmetric solution of the vacuum Einstein’s equations belonging to the class of Weyl-Lewis-Papapetrou [271, 145, 183] and is characterized, in general, by the presence of a naked singularity. Although the general solution is characterized by an infinite set of gravitoelectric and gravitomagnetic multipoles, we consider here the special solution discussed in Ref. [198] that involves only three parameters: the mass M , the angular momentum per unit mass a and the mass quadrupole parameter q of the source.

The corresponding line element in prolate spheroidal coordinates (t, x, y, ϕ) with $x \geq 1$,

$-1 \leq y \leq 1$ is given by [245]

$$ds^2 = -f(dt - \omega d\phi)^2 + \frac{\sigma^2}{f} \left\{ e^{2\gamma} (x^2 - y^2) \left(\frac{dx^2}{x^2 - 1} + \frac{dy^2}{1 - y^2} \right) + (x^2 - 1)(1 - y^2) d\phi^2 \right\}, \quad (3.1)$$

where f , ω and γ are functions of x and y only and σ is a constant. They have the form

$$\begin{aligned} f &= \frac{R}{L} e^{-2qP_2Q_2}, \quad \omega = -2a - 2\sigma \frac{\mathfrak{M}}{R} e^{2qP_2Q_2}, \\ e^{2\gamma} &= \frac{1}{4} \left(1 + \frac{M}{\sigma} \right)^2 \frac{R}{x^2 - 1} e^{2\hat{\gamma}}, \end{aligned} \quad (3.2)$$

where

$$\begin{aligned} R &= a_+ a_- + b_+ b_-, \quad L = a_+^2 + b_+^2, \\ \mathfrak{M} &= \alpha x (1 - y^2) (e^{2q\delta_+} + e^{2q\delta_-}) a_+ + y (x^2 - 1) (1 - \alpha^2 e^{2q(\delta_+ + \delta_-)}) b_+, \\ \hat{\gamma} &= \frac{1}{2} (1 + q)^2 \ln \frac{x^2 - 1}{x^2 - y^2} + 2q(1 - P_2)Q_1 + q^2(1 - P_2) \left[(1 + P_2)(Q_1^2 - Q_2^2) \right. \\ &\quad \left. + \frac{1}{2}(x^2 - 1)(2Q_2^2 - 3xQ_1Q_2 + 3Q_0Q_2 - Q_2') \right]. \end{aligned} \quad (3.3)$$

Here $P_l(y)$ and $Q_l(x)$ are Legendre polynomials of the first and second kind respectively. Furthermore

$$\begin{aligned} a_{\pm} &= x(1 - \alpha^2 e^{2q(\delta_+ + \delta_-)}) \pm (1 + \alpha^2 e^{2q(\delta_+ + \delta_-)}), \\ b_{\pm} &= \alpha y (e^{2q\delta_+} + e^{2q\delta_-}) \mp \alpha (e^{2q\delta_+} - e^{2q\delta_-}), \\ \delta_{\pm} &= \frac{1}{2} \ln \frac{(x \pm y)^2}{x^2 - 1} + \frac{3}{2} (1 - y^2 \mp xy) + \frac{3}{4} [x(1 - y^2) \mp y(x^2 - 1)] \ln \frac{x - 1}{x + 1}, \end{aligned} \quad (3.4)$$

the quantity α being a constant

$$\alpha = \frac{\sigma - M}{a}, \quad \sigma = \sqrt{M^2 - a^2}. \quad (3.5)$$

We limit our analysis here to the case $\sigma > 0$, i.e. $M > a$. In the case $\sigma = 0$ the solution reduces to the extreme Kerr spacetime irrespective of the value of q [199].

The Geroch-Hansen [90, 103] moments are given by

$$M_{2k+1} = J_{2k} = 0, \quad k = 0, 1, 2, \dots \quad (3.6)$$

$$M_0 = M, \quad M_2 = -Ma^2 + \frac{2}{15} qM^3 \left(1 - \frac{a^2}{M^2} \right)^{3/2}, \dots \quad (3.7)$$

$$J_1 = Ma, \quad J_3 = -Ma^3 + \frac{4}{15} qM^3 a \left(1 - \frac{a^2}{M^2} \right)^{3/2}, \dots \quad (3.8)$$

The vanishing of the odd gravitoelectric (M_n) and even gravitomagnetic (J_n) multipole moments is a consequence of the reflection symmetry of the solution about the hyperplane $y = 0$, which we will refer to as “symmetry” (or equivalently “equatorial”) plane hereafter. Note that these expressions are limiting cases of (1.66) with the Zipoy-Voorhees parameter $\delta = 1$. From the above expressions we see that M is the total mass of the body, a represents the specific angular momentum, and q is related to the deviation from spherical symmetry. All higher multipole moments can be shown to depend only on the parameters M , a , and q [198].

Some geometric and physical properties of the QM solution have been analyzed in Ref. [30]. It turns out that the whole geometric structure of the QM spacetime is drastically changed in comparison with Kerr spacetime, leading to a number of previously unexplored physical effects strongly modifying the features of particle motion, especially near the gravitational source. In fact, the QM solution is characterized by a naked singularity at $x = 1$, whose existence critically depends on the value of the quadrupole parameter q . In the case $q = 0$ (Kerr solution) $x = 1$ represents instead an event horizon.

3.2.1 Limiting cases

The QM solution reduces to the Kerr spacetime in the limiting case $q \rightarrow 0$, to the Erez-Rosen spacetime when $a \rightarrow 0$ and to the Schwarzschild solution when both parameters vanish. Furthermore, it has been shown in Ref. [30] that the general form of the QM solution is equivalent, up to a coordinate transformation, to the exterior vacuum Hartle-Thorne solution once linearized to first order in the quadrupole parameter and to second order in the rotation parameter. The limiting cases contained in the general solution thus suggest that it can be used to describe the exterior asymptotically flat gravitational field of a rotating body with arbitrary quadrupole moment.

Kerr solution

For vanishing quadrupole parameter we recover the Kerr solution, with functions [245]

$$\begin{aligned} f_K &= \frac{c^2 x^2 + d^2 y^2 - 1}{(cx + 1)^2 + d^2 y^2}, & \omega_K &= 2a \frac{(cx + 1)(1 - y^2)}{c^2 x^2 + d^2 y^2 - 1}, \\ \gamma_K &= \frac{1}{2} \ln \left(\frac{c^2 x^2 + d^2 y^2 - 1}{c^2 (x^2 - y^2)} \right), \end{aligned} \quad (3.9)$$

where

$$c = \frac{\sigma}{M}, \quad d = \frac{a}{M}, \quad c^2 + d^2 = 1, \quad (3.10)$$

so that $\alpha = (\sigma - M)/a = (c - 1)/d$. Transition of this form of Kerr metric to the more familiar one associated with Boyer-Lindquist coordinates is accomplished by the map

$$t = t, \quad x = \frac{r - M}{\sigma}, \quad y = \cos \theta, \quad \phi = \phi, \quad (3.11)$$

so that $x = 1$ corresponds to the outer horizon $r = r_+ = M + \sigma$.

Erez-Rosen solution

Similarly, for vanishing rotation parameter we recover the Erez-Rosen solution [74, 67, 275]. It is a solution of the static Weyl class of solutions (i.e. $\omega \equiv 0$) with functions

$$f_{ER} = \frac{x-1}{x+1} e^{-2qP_2Q_2}, \quad \gamma_{ER} = \hat{\gamma}, \quad (3.12)$$

which reduce to the Schwarzschild solution

$$f_S = \frac{x-1}{x+1}, \quad \gamma_S = \frac{1}{2} \ln \left(\frac{x^2-1}{x^2-y^2} \right) \quad (3.13)$$

when $q = 0$ too.

Hartle-Thorne solution

The Hartle-Thorne solution is associated with the exterior field of a slowly rotating slightly deformed object [105, 108]. It is an approximate solution of the vacuum Einstein equations accurate to second order in the rotation parameter a/M and to first order in the quadrupole parameter q , generalizing the Lense-Thirring spacetime [144]. The corresponding metric functions are given by

$$\begin{aligned} f_{HT} &\simeq \frac{x-1}{x+1} \left[1 - q \left(2P_2Q_2 - \ln \frac{x-1}{x+1} \right) \right] - \frac{x^2+x-2y^2}{(x+1)^3} \left(\frac{a}{M} \right)^2, \\ \omega_{HT} &\simeq 2M \frac{1-y^2}{x-1} \left(\frac{a}{M} \right), \\ \gamma_{HT} &\simeq \frac{1}{2} \ln \left(\frac{x^2-1}{x^2-y^2} \right) + 2q(1-P_2)Q_1 - \frac{1}{2} \frac{1-y^2}{x^2-1} \left(\frac{a}{M} \right)^2, \end{aligned} \quad (3.14)$$

where terms of the order of $q(a/M)$ have also been neglected.

3.3 Circular orbits on the symmetry plane

Let us introduce the ZAMO family of fiducial observers, with four velocity

$$n = N^{-1}(\partial_t - N^\phi \partial_\phi), \quad (3.15)$$

where $N = (-g^{tt})^{-1/2}$ and $N^\phi = g_{t\phi}/g_{\phi\phi}$ are the lapse and shift functions respectively. A suitable orthonormal frame adapted to ZAMOs is given by

$$e_{\hat{t}} = n, \quad e_{\hat{x}} = \frac{1}{\sqrt{g_{xx}}} \partial_x, \quad e_{\hat{y}} = \frac{1}{\sqrt{g_{yy}}} \partial_y, \quad e_{\hat{\phi}} = \frac{1}{\sqrt{g_{\phi\phi}}} \partial_\phi, \quad (3.16)$$

with dual

$$\omega^{\hat{t}} = N dt, \quad \omega^{\hat{x}} = \sqrt{g_{xx}} dx, \quad \omega^{\hat{y}} = \sqrt{g_{yy}} dy, \quad \omega^{\hat{\phi}} = \sqrt{g_{\phi\phi}} (d\phi + N^\phi dt). \quad (3.17)$$

The 4-velocity U of uniformly rotating circular orbits can be parametrized either by the (constant) angular velocity with respect to infinity ζ or, equivalently, by the (constant) linear velocity ν with respect to ZAMOs

$$U = \Gamma[\partial_t + \zeta\partial_\phi] = \gamma[e_{\hat{t}} + \nu e_{\hat{\phi}}], \quad \gamma = (1 - \nu^2)^{-1/2}, \quad (3.18)$$

where Γ is a normalization factor which assures that $U_\alpha U^\alpha = -1$ given by

$$\Gamma = [N^2 - g_{\phi\phi}(\zeta + N^\phi)^2]^{-1/2} = \frac{\gamma}{N} \quad (3.19)$$

and

$$\zeta = -N^\phi + \frac{N}{\sqrt{g_{\phi\phi}}}\nu. \quad (3.20)$$

We limit our analysis to the motion on the symmetry plane ($y = 0$) of the solution (3.1)–(3.5), where there exists a large variety of special circular orbits [28, 25, 26, 31].

The prolate spheroidal coordinates in which the metric (3.1) is written are adapted to the Killing symmetries of the spacetime itself and automatically select the family of static or “threading” observers, i.e. those at rest with respect to the coordinates, following the time coordinate lines. Threading observers have zero angular velocity, whereas their relative velocity with respect to ZAMOs is

$$\zeta_{(\text{thd})} = 0, \quad \nu_{(\text{thd})} = \frac{f\omega}{\sigma\sqrt{x^2 - 1}}. \quad (3.21)$$

ZAMOs are instead characterized by

$$\zeta_{(\text{zamo})} = -\frac{f^2\omega}{\sigma^2(x^2 - 1) - f^2\omega^2}, \quad \nu_{(\text{zamo})} = 0. \quad (3.22)$$

Co-rotating (+) and counter-rotating (−) timelike circular geodesics are characterized by the following linear velocities

$$\nu_{(\text{geo})\pm} \equiv \nu_\pm = \frac{fC \pm [f^2\omega^2 - \sigma^2(x^2 - 1)]\sqrt{D}}{\sqrt{x^2 - 1}\sigma\{f_x[f^2\omega^2 + \sigma^2(x^2 - 1)] + 2f(f^2\omega\omega_x - \sigma^2x)\}}, \quad (3.23)$$

where

$$\begin{aligned} C &= -2\sigma^2(x^2 - 1)\omega f_x - f\{\omega_x[f^2\omega^2 + \sigma^2(x^2 - 1)] - 2\sigma^2x\omega\}, \\ D &= f^4\omega_x^2 - \sigma^2 f_x[f_x(x^2 - 1) - 2xf]. \end{aligned} \quad (3.24)$$

All quantities in the previous expressions are meant to be evaluated at $y = 0$. The corresponding timelike conditions $|\nu_\pm| < 1$ together with the reality condition $D \geq 0$ identify the allowed regions for the “radial” coordinate where co/counter-rotating geodesics exist. We refer to Ref. [30] for a detailed discussion about the effect of the quadrupole moment on the causality condition. There exists a finite range of values of q wherein timelike circular geodesics are allowed: $q_1 < q < q_3$ for co-rotating and $q_2 < q < q_3$ for counter-rotating circular geodesics. The critical values q_1 , q_2 and q_3 of the quadrupole parameter can be (numerically) determined from Eq. (3.23). For instance, for a fixed distance parameter $x = 4$ from the source and the choice of the rotation parameter $a/M = 0.5$ we find $q_1 \approx -105.59$, $q_2 \approx -36.29$ and $q_3 \approx 87.68$.

3.4 Tidal indicators

We investigate here tidal forces, commonly associated with the Riemann tensor and more specifically with its electric and magnetic parts with respect to a generic timelike congruence. Let us denote by u the corresponding unit tangent vector.

The electric and magnetic parts of the Weyl tensor $C_{\alpha\beta\gamma\delta}$ with respect to a generic timelike congruence with unit tangent vector u are defined as [63]

$$E(u)_{\alpha\beta} = C_{\alpha\mu\beta\nu}u^\mu u^\nu, \quad H(u)_{\alpha\beta} = -C_{\alpha\mu\beta\nu}^*u^\mu u^\nu. \quad (3.25)$$

These spatial fields are both symmetric and tracefree. The electric part is associated with tidal gravity, whereas the magnetic part describes differential dragging of inertial frames. Some tools for visualizing the spacetime curvature through the electric and magnetic parts of the Weyl tensor have been recently introduced in Ref. [178], where the nonlinear dynamics of curved spacetime in merging black hole binaries has been investigated by using numerical simulations. We recall that in a vacuum spacetime, which is just the case we are considering, the Weyl and Riemann tensors coincide.

The simplest way to built up scalar quantities through the electric and magnetic parts of the Riemann tensor which are representative of them and serve as “tidal indicators” in the study of tidal effects is to take the trace of their square. One can then consider the following electric and magnetic tidal indicators [29]

$$\mathcal{J}_E(u) = \text{Tr}[E(u)^2], \quad \mathcal{J}_H(u) = \text{Tr}[H(u)^2]. \quad (3.26)$$

They are related to the curvature tensor as well as to the particle/observer undergoing tidal deformations. One could also consider other more involved tidal invariants constructed from the covariant derivative of the curvature tensor. Such invariants have received some attention in the recent literature in order to investigate both geometrical and topological properties of certain classes of static as well as stationary spacetimes (see, e.g., Refs. [134, 169, 228]). However, in the context of tidal problems differential invariants are of interest only when using Fermi coordinate tidal potential, as discussed in Ref. [119]. We will not address this problem in the present work.

Let $u = n$ be the unit tangent vector to the ZAMO family of observer given by Eq. (3.15) with adapted frame (3.16). The relevant nonvanishing frame components of the electric and magnetic parts of the Riemann tensor are given by $E(n)_{11}$, $E(n)_{33}$ and $H(n)_{12}$ with

$$E(n)_{11} + E(n)_{22} = -E(n)_{33}. \quad (3.27)$$

They are listed in Appendix B. The tidal indicators (3.26) then turn out to be given by

$$\begin{aligned} \mathcal{J}_E(n) &= 2\{[E(n)_{11}]^2 + [E(n)_{22}]^2 + E(n)_{11}E(n)_{22}\}, \\ \mathcal{J}_H(n) &= 2[H(n)_{12}]^2. \end{aligned} \quad (3.28)$$

Let now U be tangent to a uniformly rotating timelike circular orbit on the symmetry

plane. We find ¹

$$\begin{aligned}\mathcal{T}_E(U) &= \gamma^4 \left\{ \mathcal{T}_E(n)(\nu^4 + 1) - 4H(n)_{12}(E(n)_{11} - E(n)_{22})\nu(\nu^2 + 1) \right. \\ &\quad \left. - 2\nu^2([E(n)_{11}]^2 + [E(n)_{22}]^2 + 4E(n)_{11}E(n)_{22} - 4[H(n)_{12}]^2) \right\}, \\ \mathcal{T}_H(U) &= \mathcal{T}_H(n)\gamma^4(\nu - \nu_*)^2(\nu - \bar{\nu}_*)^2,\end{aligned}\quad (3.29)$$

where

$$\nu_* = W - \sqrt{W^2 - 1}, \quad W = \frac{E(n)_{11} - E(n)_{22}}{2H(n)_{12}}, \quad (3.30)$$

and we have used the notation $\bar{\nu}_* = 1/\nu_*$. After expliciting the Lorentz factor $\gamma^4 = 1/(1 - \nu^2)^2$ and rearranging terms we can derive from Eq. (3.29) the following relation

$$\mathcal{T}_E(U) = \mathcal{T}_E(n) - \mathcal{T}_H(n) + \mathcal{T}_H(U). \quad (3.31)$$

This is actually an invariance relation also involving the curvature invariants. In fact, it is possible to show that

$$\mathcal{T}_E(U) - \mathcal{T}_H(U) = \frac{K}{8} = \mathcal{T}_E(n) - \mathcal{T}_H(n), \quad (3.32)$$

where K is the Kretschmann invariant of the spacetime (evaluated on the equatorial plane $y = 0$, see Appendix B), i.e.,

$$K = C_{\alpha\beta\gamma\delta}C^{\alpha\beta\gamma\delta}|_{y=0}. \quad (3.33)$$

Its behavior as a function of the distance parameter is shown in Fig. 3.1(a) for a fixed value of the rotation parameter and different values of the quadrupole parameter. As a consequence, since K does not depend on ν , all along the family of circular orbits parametrized by ν both tidal indicators have their extremal values simultaneously, i.e.,

$$\frac{d\mathcal{T}_E(U)}{d\nu} = \frac{d\mathcal{T}_H(U)}{d\nu}. \quad (3.34)$$

3.4.1 Super-energy density and super-Poynting vector

Bel [17] and Robinson [206] first introduced the Bel-Robinson super-energy-momentum tensor for the gravitational field in vacuum in terms of the Weyl curvature tensor in analogy with electromagnetism (see also Refs. [153, 39])

$$T_{\alpha\beta}{}^{\gamma\delta} = \frac{1}{2}(C_{\alpha\rho\beta\sigma}C^{\gamma\rho\delta\sigma} + {}^*C_{\alpha\rho\beta\sigma}{}^*C^{\gamma\rho\delta\sigma}). \quad (3.35)$$

¹These relations were first derived in Ref. [29]. Note that the last line of Eq. (4.5) there was misprinted by an overall minus sign, corrected here. Such a misprint also affected the equivalent form (4.6), which was but never used.

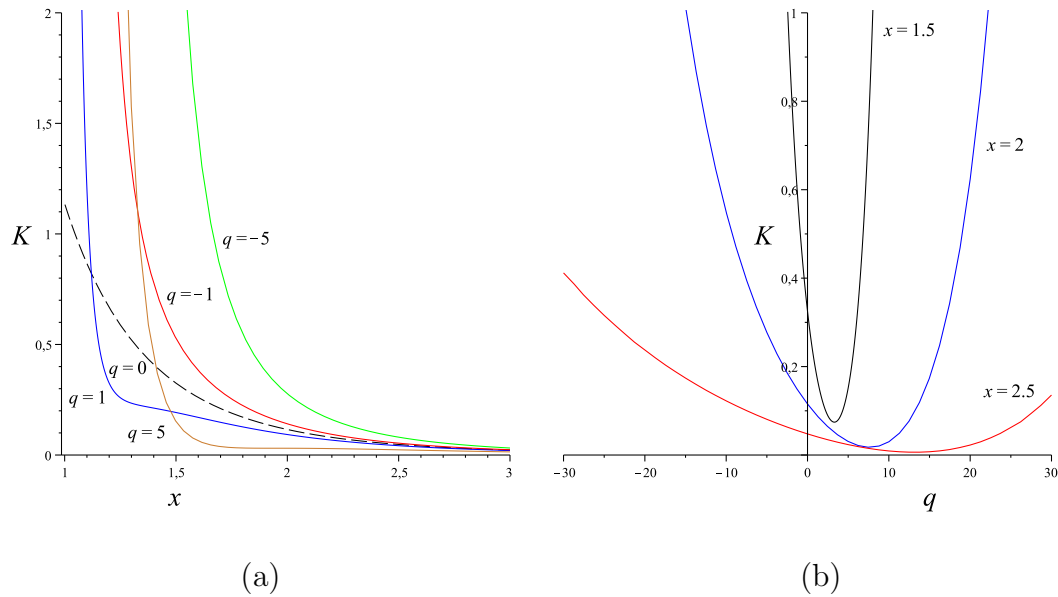


Figure 3.1: The behavior of the Kretschmann invariant K evaluated on the symmetry plane is shown as a function of the distance parameter for the choice $a/M = 0.5$ and different values of $q = [-5, -1, 0, 1, 5]$ in panel (a). Panel (b) shows instead its behavior as a function of q for different values of $x = [1.5, 2, 2.5]$ Units on the vertical axis are chosen so that $M = 1$.

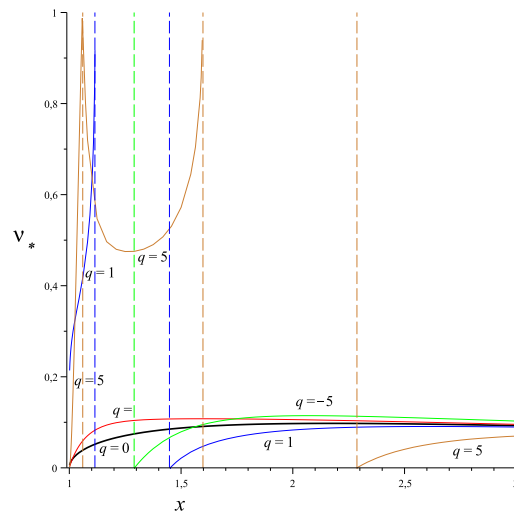


Figure 3.2: The behavior of the linear velocity ν_* as a function of the distance parameter is shown for the choice $a/M = 0.5$ and different values of the quadrupole $q = [-5, -1, 0, 1, 5]$. The thick black solid curve refers to the Kerr case ($q = 0$), i.e., to the Carter's 4-velocity. Dashed vertical lines correspond to observer horizons.

The super-energy density and the super-Poynting vector associated with a generic observer u are given by

$$\begin{aligned}\mathcal{E}^{(\text{g})}(u) &= T_{\alpha\beta\gamma\delta}u^\alpha u^\beta u^\gamma u^\delta = \frac{1}{2}[\mathcal{T}_E(u) + \mathcal{T}_H(u)] , \\ P^{(\text{g})}(u)_\alpha &= T_{\alpha\beta\gamma\delta}u^\beta u^\gamma u^\delta = [E(u) \times_u H(u)]_\alpha ,\end{aligned}\tag{3.36}$$

where

$$[E(u) \times_u H(u)]_\alpha = \eta(u)_{\alpha\beta\gamma} E(u)^\beta_\delta H(u)^{\delta\gamma}\tag{3.37}$$

and the spatial unit-volume 3-form has been introduced, i.e.,

$$\eta(u)_{\alpha\beta\gamma} = u^\mu \eta_{\mu\alpha\beta\gamma} .\tag{3.38}$$

Bel showed that for Petrov types I and D, an observer always exists for which the super-Poynting vector vanishes: this observer aligns the electric and magnetic parts of the Weyl tensor in the sense that they are both diagonalized and therefore commute. For black hole spacetimes, the Carter's observer family plays this role at each spacetime point. The same property is also shared by the observers ν_* in this more general context. In fact, the super-Poynting vector for a circularly rotating orbit U turns out to have a single nonvanishing frame component along $e_{\hat{\phi}}$ given by

$$P^{(\text{g})}(U)_{\hat{\phi}} = \frac{\gamma^4}{2\nu_*} \mathcal{T}_H(n)(\nu - \nu_*)(\nu - \bar{\nu}_*)[(1 + \nu_*^2)(1 + \nu^2) - 4\nu\nu_*] .\tag{3.39}$$

Furthermore, the orbit associated with ν_* is also characterized by the following relation involving the super-energy density (which can be easily evaluated from Eq. (3.29))

$$\frac{d\mathcal{E}^{(\text{g})}(U)}{d\nu} = -4\gamma^2 P^{(\text{g})}(U)_{\hat{\phi}} ,\tag{3.40}$$

or in terms of the rapidity parameter α such that $\nu = \tanh \alpha$

$$\frac{d\mathcal{E}^{(\text{g})}(U)}{d\alpha} = -4P^{(\text{g})}(U)_{\hat{\phi}} ,\tag{3.41}$$

so remembering the structure of Hamilton's equations for conjugate variables. The observers ν_* thus correspond to vanishing super-Poynting vector and minimal super-energy density.

3.4.2 Discussion

Eq. (3.29) implies that $\mathcal{T}_H(U)$ vanishes for $\nu = \nu_*$, regardless of the value of the quadrupole parameter q . The family of observers identified by this 4-velocity plays the role of Carter's family in such a generalized Kerr spacetime. In the Kerr case in Boyer-Lindquist coordinates Carter's observer velocity is given by

$$\nu_{(\text{car})} = \frac{a\sqrt{\Delta}}{r^2 + a^2} .\tag{3.42}$$

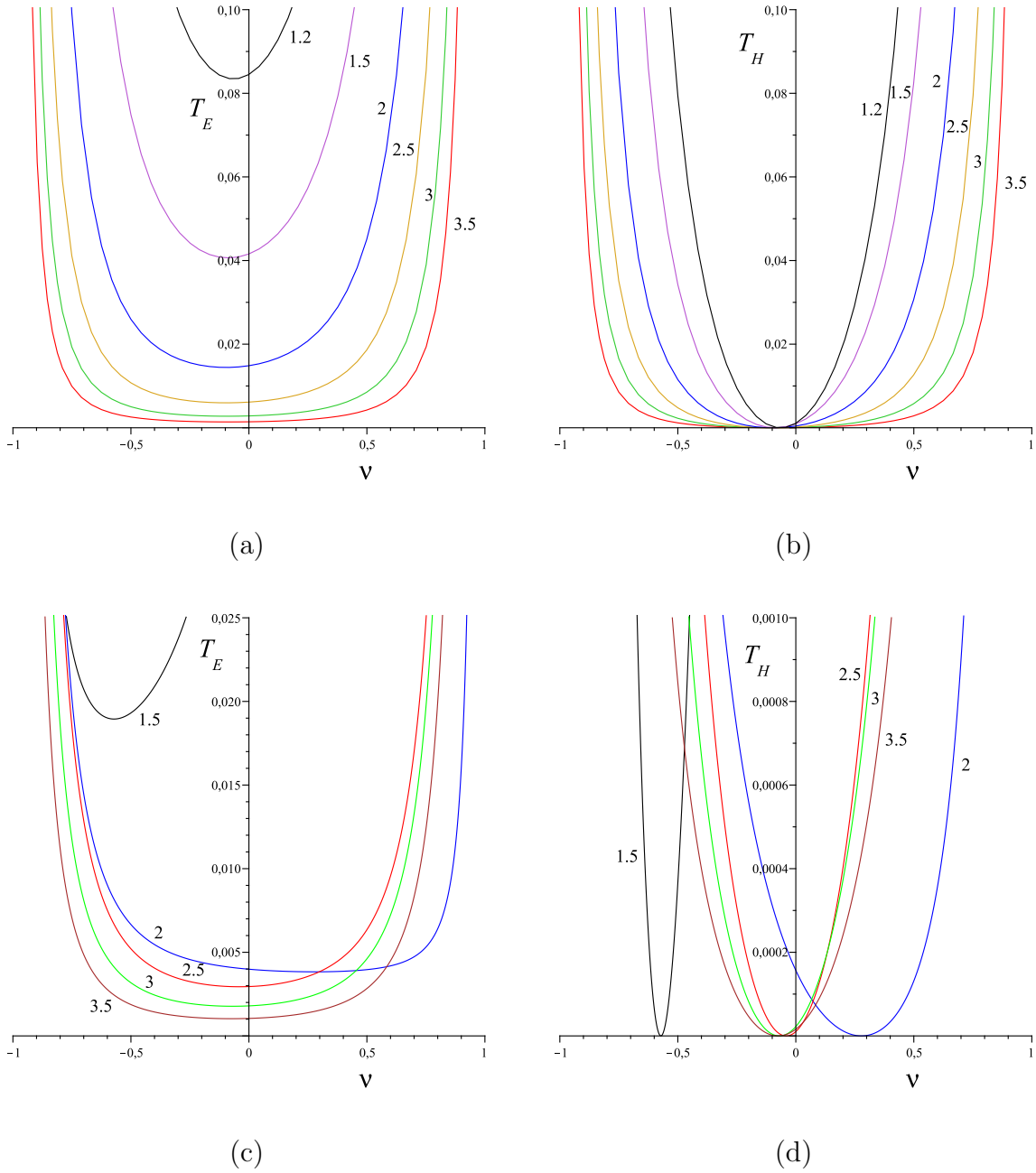


Figure 3.3: The behaviors of the tidal indicators $\mathcal{T}_E(U)$ and $\mathcal{T}_H(U)$ as functions of ν are shown in panels (a), (c) for $q = 0$ and (b), (d) for $q = 5$ respectively for the choice $a/M = 0.5$ and different values of the coordinate $x = [1.2, 1.5, 2, 2.5, 3, 3.5]$. For negative values of q the behaviors are very similar to the Kerr case. For q increasingly negative the values of $\mathcal{T}_E(U)$ at the minimum of each curve increase, whereas the curves corresponding to $\mathcal{T}_H(U)$ shrink to the vertical axis. Units on the vertical axis are chosen so that $M = 1$.

The main property of Carter's observers world lines is to be the unique timelike world lines belonging to the intersection of the Killing two-plane (t, ϕ) with the two-plane spanned by the two independent principal null directions of the Kerr spacetime. In contrast, the QM solution is Petrov type I with four independent principal null directions and hence the above property is lost.

Fig. 3.2 shows how the behavior of the generalized Carter's observer velocity ν_* as a function of the distance parameter modifies due to the presence of the quadrupole. Carter's observers are defined outside the outer event horizon of the Kerr spacetime, corresponding to $x = 1$. For negative values of q , the observer horizon associated with such generalized Carter's observers is located at a certain value $x > 1$, which increases as q becomes increasingly negative. A similar situation occurs also for positive values of q , but additional allowed branches also appear in the inner region.

In contrast with the Kerr case where Carter's observers are the only ones who measure zero magnetic tidal indicator, this property is shared here also by other observer families for special values of q . This is evident from Figs. 3.3 and 3.4, where the behaviors of the tidal indicators as functions of ν are shown for a fixed value of the quadrupole and different values of the distance parameter in comparison with the Kerr case (Fig. 3.3) and for a fixed value of x and different values of q (Fig. 3.4). In fact, we see that $\mathcal{T}_H(U)$ vanishes many times for different values of ν corresponding either to different x with fixed q , or to different q with fixed x .

Correspondingly the electric type tidal indicator takes its minimum value, which can be further reduced by suitably choosing the quadrupole parameter, but cannot be made vanishing. In fact, the invariant relation (3.32) implies for instance that $\mathcal{T}_E(U)$ is minimum when $\mathcal{T}_H(U) = 0$ and K is minimum as well. Fig. 3.1(b) shows the behavior of K as a function of q for different values of the distance parameter. K reaches an absolute minimum only for positive values of q , which increase for increasing x . The behaviors of the tidal indicators as measured by ZAMOs, static and geodesic observers are shown in Figs. 3.3–3.5, respectively, as functions of the distance parameter for different values of q . The behavior is Kerr-like for negative values of q . For positive values of q instead the situation significantly modifies with respect to the Kerr case, the magnetic tidal indicator vanishing many times and correspondingly the electric tidal indicator showing a damped oscillating behavior.

3.4.3 Limit of slow rotation and small deformation

Let us consider the limiting case of the Hartle-Thorne metric written in terms of the more familiar Boyer-Lindquist coordinates according to the transformation (3.11). Terms of the order a^3 , q^2 , aq and higher are then neglected in all formulas listed below. The relevant nonvanishing ZAMO frame components of the electric and magnetic parts of the

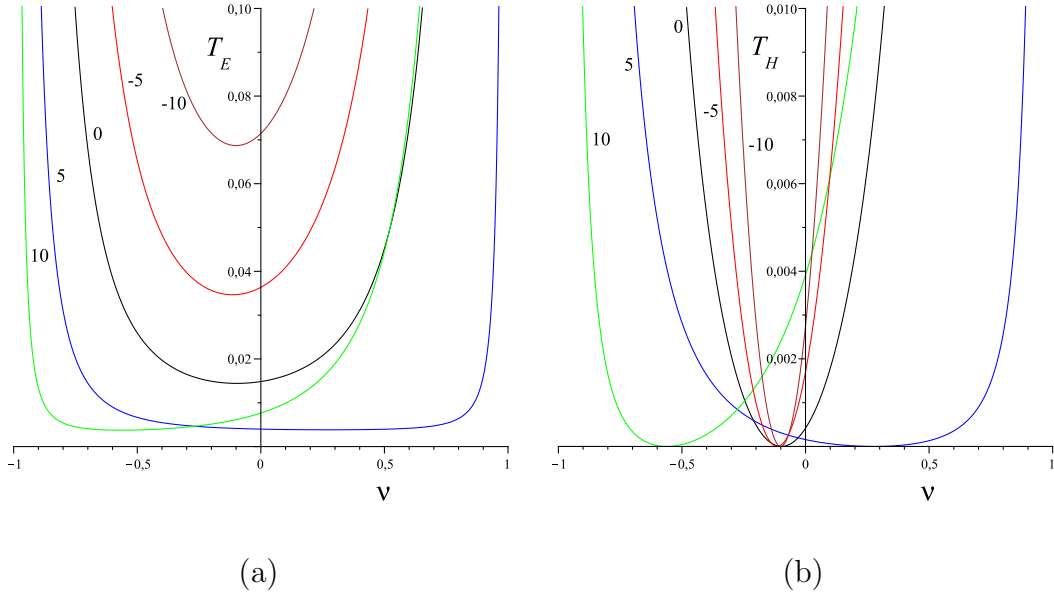


Figure 3.4: The behaviors of the tidal indicators $\mathcal{T}_E(U)$ and $\mathcal{T}_H(U)$ as functions of ν are shown in panels (a) and (b) respectively for the choice $a/M = 0.5$, with a fixed value $x = 2$ of the distance parameter and different values of $q = [-10, -5, 0, 5, 10]$. Units on the vertical axis are chosen so that $M = 1$.

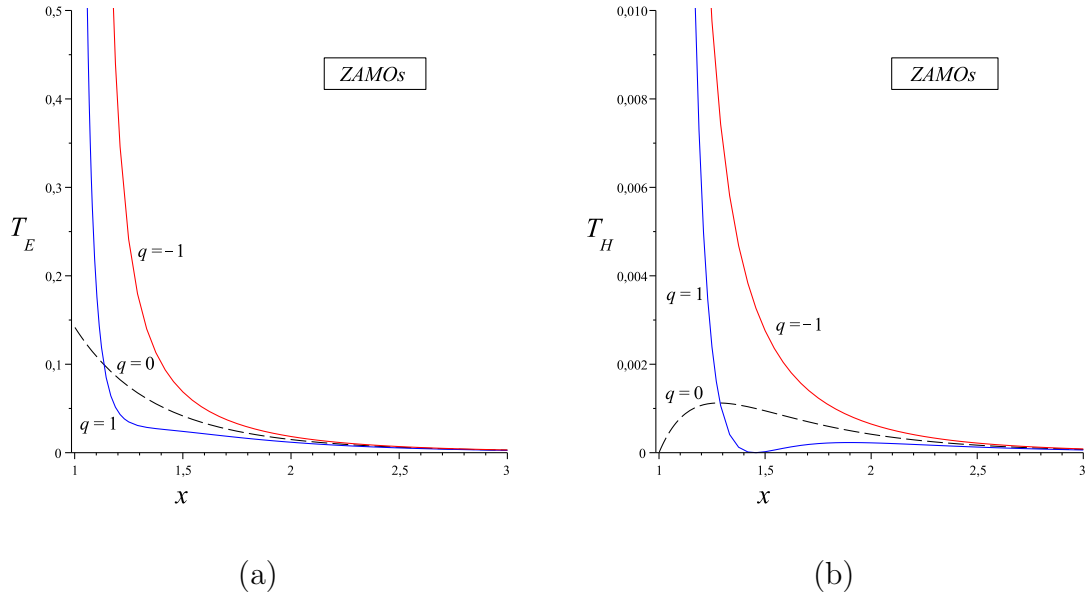


Figure 3.5: The behaviors of the tidal indicators $\mathcal{T}_E(U)$ and $\mathcal{T}_H(U)$ as measured by ZAMOs are shown as functions of the distance parameter for the choice $a/M = 0.5$ and different values of $q = [-1, 0, 1]$. Dashed curves correspond to the Kerr case (i.e., $q = 0$). Units on the vertical axis are chosen so that $M = 1$.

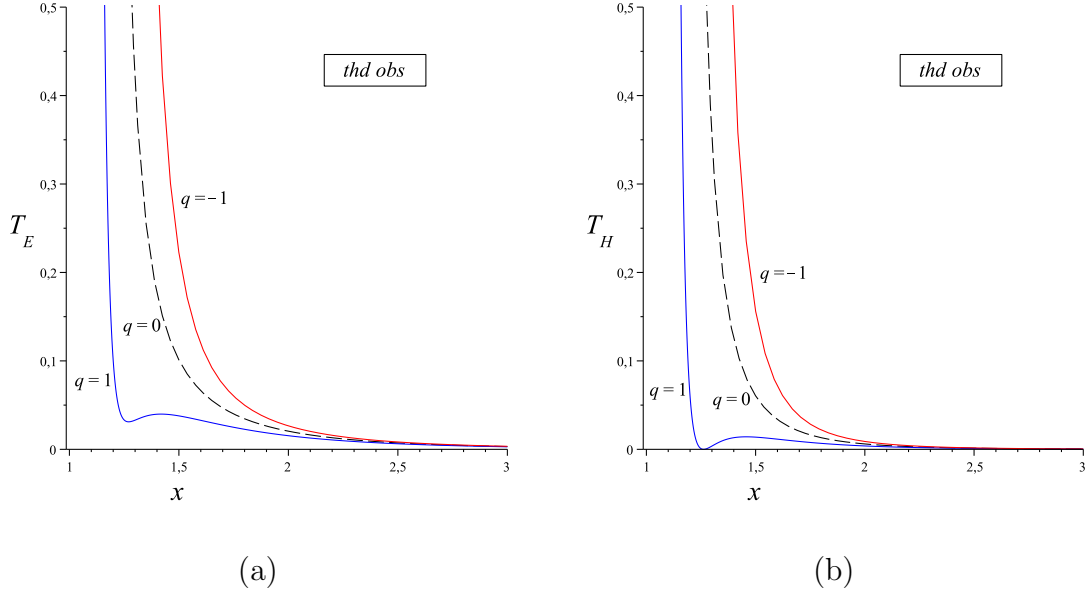


Figure 3.6: The behaviors of the tidal indicators $\mathcal{T}_E(U)$ and $\mathcal{T}_H(U)$ as measured by static observers are shown as functions of the distance parameter for the choice $a/M = 0.5$ and different values of $q = [-1, 0, 1]$. Dashed curves correspond to the Kerr case (i.e., $q = 0$). Units on the vertical axis are chosen so that $M = 1$.

Riemann tensor are given by

$$\begin{aligned}
 E(n)_{11} &= -\frac{2M}{r^3} - \frac{3a^2M}{r^5}N^2 + q \left[\frac{6(r^2 - 3Mr + 4M^2)}{Mr^3}Q_1 - \frac{3r - 10M}{r^3}Q_2 \right. \\
 &\quad \left. + \frac{4M}{r^3} \ln N \right], \\
 E(n)_{33} &= \frac{M}{r^3} + q \left[\frac{3(7M^3 - 9rM^2 + 5r^2M - r^3)}{Mr^3(r - 2M)}Q_1 + \frac{3r^2 - 11Mr + 7M^2}{r^3(r - 2M)}Q_2 \right. \\
 &\quad \left. - \frac{2M}{r^3} \ln N \right], \\
 H(n)_{12} &= -\frac{3aM}{r^4}N,
 \end{aligned} \tag{3.43}$$

where $N = \sqrt{1 - 2M/r}$ and $Q_1 = Q_1(r/M - 1)$ and $Q_2 = Q_2(r/M - 1)$ are Legendre functions. The Kretschmann invariant on the symmetry plane is

$$K = \frac{48M^2}{r^6} \left\{ 1 - q \left[\frac{6(r^2 - 3Mr + 4M^2)}{M^2}Q_1 - \frac{3r - 10M}{M}Q_2 + 4 \ln N \right] \right\}. \tag{3.44}$$

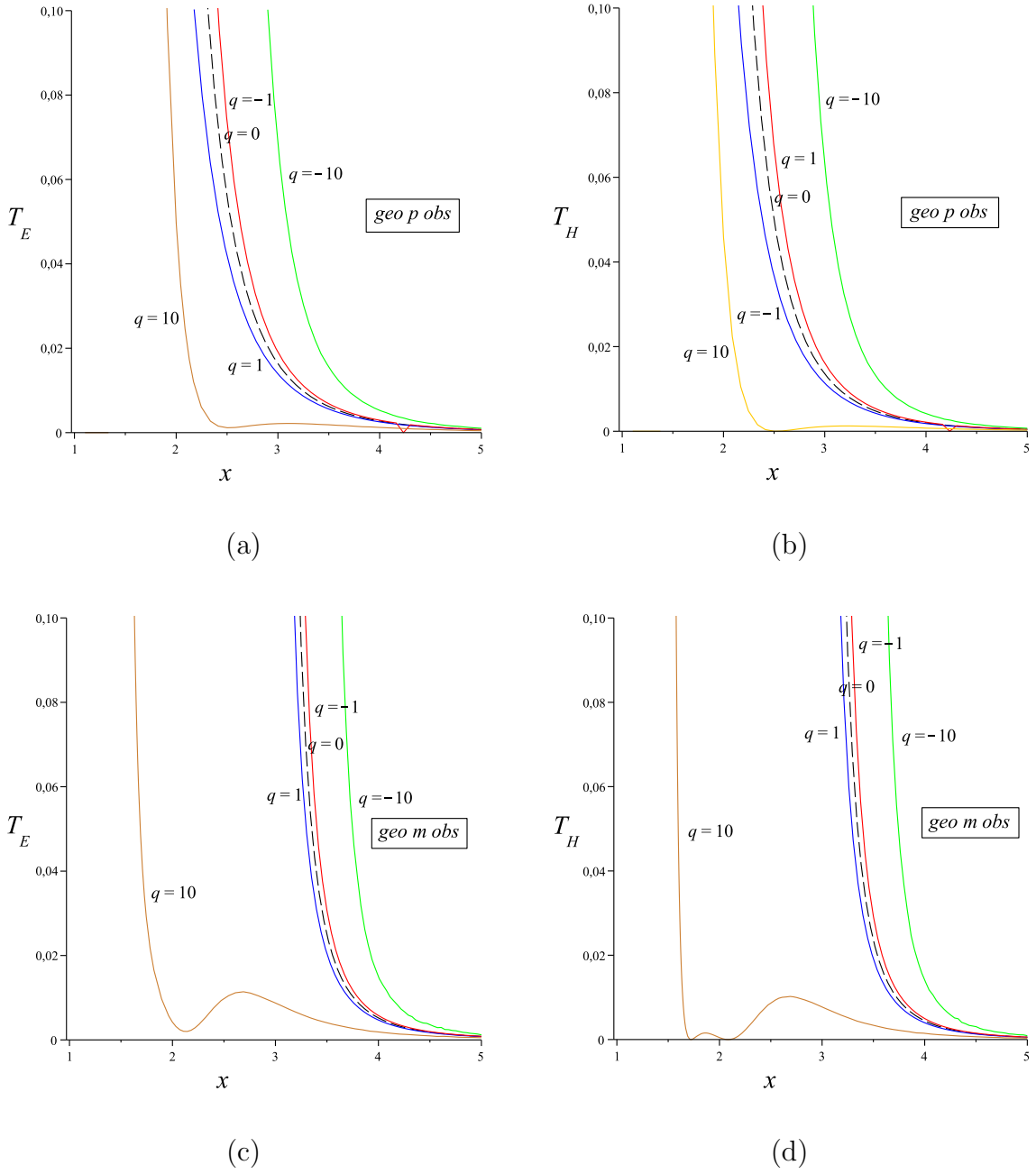


Figure 3.7: The behaviors of the tidal indicators $\mathcal{T}_E(U)$ and $\mathcal{T}_H(U)$ as measured by geodesic observers are shown as functions of the distance parameter for the choice $a/M = 0.5$ and different values of $q = [-10, -1, 0, 1, 10]$. Panels (a)–(b) and (c)–(d) correspond to the co-rotating and counter-rotating case respectively. Dashed curves correspond to the Kerr case (i.e., $q = 0$). Units on the vertical axis are chosen so that $M = 1$.

Generalized Carter's observers have 4-velocity $\nu_* = aN/r$, whereas static observers are characterized by $\nu_{(\text{thd})} = -2aM/r^2N$ and geodesics observers by

$$\begin{aligned} \nu_{(\text{geo})\pm} &= \pm \sqrt{\frac{M}{r}} \frac{1}{N} \left[1 + \frac{a^2}{2N^2 r^4} (r^2 + 2Mr - 12M^2) \right] - \frac{3aM}{r^2 N} \\ &\mp \frac{3}{2} q \frac{(r-M)^2}{N^3 \sqrt{Mr^3}} \left[\left(\frac{r}{M} - 1 \right) Q_1 - Q_2 \right]. \end{aligned} \quad (3.45)$$

We list below the expression for $\mathcal{T}_H(U)$ corresponding to the different families of observers considered above:

$$\begin{aligned} \mathcal{T}_H(n) &= \frac{18a^2 M^2}{r^8} N^2, \\ \mathcal{T}_H(u_{(\text{thd})}) &= \frac{18a^2 M^2}{r^8} \frac{1}{N^2}, \\ \mathcal{T}_H(u_*) &= 0, \\ \mathcal{T}_H(u_{(\text{geo})\pm}) &= \frac{18M^3}{r^5} \frac{N^2}{(r-3M)^2} \mp 36aM^2 \frac{N^2}{r^5} \sqrt{\frac{M}{r}} \frac{r-M}{(r-3M)^3} \\ &+ \frac{18a^2 M^2}{r^7} \frac{1}{(r-3M)^4} (r^3 + Mr^2 - 13M^2 r + 15M^3) \\ &- q \left[\frac{72M^3}{r^5} \frac{N^2}{(r-3M)^2} \ln N \right. \\ &+ \frac{18M}{r^6} \frac{1}{(r-3M)^3} (9r^4 - 60Mr^3 + 170M^2 r^2 - 248M^3 r + 153M^4) Q_1 \\ &\left. - \frac{18M^2}{r^6} \frac{1}{(r-3M)^3} (5r^3 - 29Mr^2 + 73M^2 r - 69M^3) Q_2 \right]. \end{aligned} \quad (3.46)$$

Note that $\mathcal{T}_H(n)$ and $\mathcal{T}_H(u_{(\text{thd})})$ do not depend on q , in this limit, in contrast to the general case. This is a consequence of the series expansion in the parameters a/M and q , so that terms of the order of $q(a/M)$ have also been neglected.

Finally, in the weak field limit $M/r \ll 1$ the previous expressions have the following asymptotic forms (up to the order $(M/r)^{10}$)

$$\begin{aligned} \mathcal{T}_H(n) &\simeq \frac{18a^2 M^2}{r^8} \left(1 - \frac{2M}{r} \right), \\ \mathcal{T}_H(u_{(\text{thd})}) &\simeq \frac{18a^2 M^2}{r^8} \left(1 + \frac{2M}{r} \right), \\ \mathcal{T}_H(u_{(\text{geo})\pm}) &\simeq \frac{18M^3}{r^7} \left\{ 1 - 3q + \frac{M}{r} \left(4 + \frac{a^2}{M^2} - 9q \right) + \frac{M^2}{r^2} \left(15 + 13 \frac{a^2}{M^2} - \frac{214}{5} q \right) \right. \\ &\left. \mp 2 \frac{a}{M} \sqrt{\frac{M}{r}} \left(1 + \frac{6M}{r} + 29 \frac{M^2}{r^2} \right) \right\}. \end{aligned} \quad (3.47)$$

3.5 Multipole moments and tidal Love numbers

Although the merging of compact objects can be accurately modeled only by numerical simulations in full general relativity, there is a variety of analytical and semi-analytical approaches which allow to properly describe at least part of the coalescence process and to study the associated gravitational wave signals (see, e.g., Refs. [81, 113, 114, 60]). The effect of the tidal interaction on the orbital motion and the gravitational wave signal is measured by a quantity known as the tidal Love number of each companion.

In Newtonian gravity, where it has been introduced [152], the Love number is a constant of proportionality between the external tidal field applied to the body and the resulting multipole moment of its mass distribution. In a relativistic context instead Flanagan and Hinderer [81, 113, 114] estimated the tidal responses of a neutron star to the external tidal solicitation of its companion, showing that the Love number is potentially measurable in gravitational wave signals from the early regime of the inspiral through Earth-based detectors.

The relativistic theory of Love numbers has been developed by Binnington and Poisson [32] and Damour and Nagar [59]. They classified tidal Love numbers into two types: an electric-type Love number having a direct analogy with the Newtonian one, and a magnetic-type Love number with no analogue in Newtonian gravity, already introduced in Post-Newtonian theory by Damour, Soffel and Xu [61]. Damour and Lecian [58] also defined a third class of Love numbers, i.e., the “shape” Love numbers, measuring the distortion of the shape of the surface of a star by an external gravito-electric tidal field. The relativistic Love numbers are defined within the context of linear perturbation theory, in which an initially spherical body is perturbed slightly by an applied tidal field. Tidal fields are assumed to change slowly with time, so that only stationary perturbations are considered. Computing the Love numbers requires the construction of the metric also in the interior of the body and its matching with the external metric at the perturbed boundary of the matter distribution. Therefore, the internal problem depends on the choice of the stellar model, i.e., on the selected equation of state, whereas the external problem applies to a body of any kind.

Consider a massive body placed in a static, external tidal gravitational field, which is characterized by the electric part of the associated Riemann tensor. This tidal field will deform the body which will develop in response a gravitational mass quadrupole moment (and higher moments). The components of the tidal field, quadrupole moment and total mass of the body will enter as coefficients the power series expansion of the spacetime metric in the body local asymptotic rest frame [259, 113, 114]. For an isolated body in a static situation these moments are uniquely defined. They are just the coordinate-independent moments defined by Geroch and Hansen [90, 103] for stationary, asymptotically flat spacetimes (see Eqs. (3.7)–(3.8)).

Tidal effects in relativistic binary system dynamics have been recently investigated in the framework of Post-Newtonian theory (see Ref. [27] and references therein). They have computed tidal indicators of both electric and magnetic types within the so called “effective one body approach” suitably modified to include tidal effects in the formalism,

so improving the analytical description of the late inspiral dynamics with respect to previous works (see, e.g., Ref. [60]). In order to relate our results with the analysis done in Ref. [27], consider, for instance, the electric-type tidal indicator. In the case of geodesic orbits and in absence of rotation we find in the weak field limit the following approximate expression (up to terms of the order $(M/r)^8$)

$$\mathcal{T}_E(u_{(\text{geo})\pm}) \simeq \frac{6M^2}{r^6} \left[1 - 2q + \frac{3M}{r}(1 - q) \right], \quad (3.48)$$

which can then be rewritten passing to harmonic coordinates $r = r_h + M$ and restoring the physical mass parameter [105, 108], i.e., $\mathcal{M} = M(1 - q)$, as

$$\mathcal{T}_E(u_{(\text{geo})\pm}) \simeq \frac{6\mathcal{M}^2}{r_h^6} \left[1 - \frac{3\mathcal{M}}{r_h} \right]. \quad (3.49)$$

The same quantity (termed J_a in Ref. [27], see Eq. (4.14) there) as above for the binary system at 1 PN order reads as

$$\mathcal{T}_E(u_{(\text{geo})\pm}) \simeq \frac{6\mathcal{M}^2 X_2^2}{r_h^6} \left[1 + \frac{(X_1 - 3)\mathcal{M}}{r_h} \right], \quad (3.50)$$

where evaluation is performed in the center of mass system using harmonic coordinates and the mass of the two bodies are encoded in the parameters $X_1 = m_1/\mathcal{M}$ and $X_2 = m_2/\mathcal{M}$, with $\mathcal{M} = m_1 + m_2$. In the limit $X_1 = 0$ ($X_2 = 1$) the two expressions coincide, as expected.

3.6 Conclusions

We have discussed the observer-dependent character of tidal effects associated with the electric and magnetic parts of the Riemann tensor with respect to an arbitrary family of observers in a generic spacetime. Our considerations have then been specialized to the Quevedo-Mashhoon solution describing the gravitational field of a rotating deformed mass and to the family of stationary circularly rotating observers on the equatorial plane. This family includes static, ZAMOs and geodesic observers and for each of them we have evaluated certain tidal indicators built up through the electric and magnetic parts of the Riemann tensor. The main difference from the Kerr case examined in a previous paper is due to the presence of a genuine quadrupolar structure of the background solution adopted here: the total quadrupole moment of the source is not depending on the rotation parameter only, but there is also a further contribution due to the shape deformation directly related to the mass through a new mass quadrupole parameter, q . The properties of tidal indicators strongly depend on this new parameter. We have found that there exists a family of circularly rotating orbits associated with $\nu = \nu_*$ along which the magnetic tidal indicator vanishes identically as in the Kerr case, playing the same role as Carter's observers there. For special values of q this property is also shared by other observer

families, a novelty in comparison with the Kerr case. However, still no observer family can be found for which the electric tidal indicator vanishes, a fact that can be explained in terms of curvature invariants. The tidal electric indicator can be but extremized several times close to the source, showing also a damped oscillating behavior.

We have also investigated the relation between tidal indicators and Bel-Robinson tensor, i.e., observer-dependent super-energy density and super-Poynting vector. We have shown that the super-Poynting vector identically vanishes for $\nu = \nu_*$ leading to minimal gravitational super-energy as seen by such a generalized Carter's observer within the family of all circularly rotating observers at each spacetime point, a property already known to characterize Carter's observers in the case of black hole spacetimes.

3.7 Perspectives

It is important to study relativistic tidal problems in different contexts and the possibility to apply the approach presented here, in order to better understand the role of the observers, measuring such a kind of effects. These effects result in deforming and even tidally disrupting astrophysical objects, like ordinary stars but also compact objects like neutron stars. It is also widely believed that such tidal disruption events occur very frequently in the Universe, leading then to a possible detection of the associated emission of gravitational waves in the near future by ground-based detectors such as LIGO or VIRGO and their advanced versions [1]. In this line, the further development of the current work is of high importance and relevance.

Chapter 4

On general relativistic uniformly rotating white dwarfs

4.1 Introduction

The relevance of rotation in enhancing the maximum stable mass of a white dwarf (WD) have been discussed for many years both for uniform rotation (see e.g. [121, 7, 215, 166, 91]) and differential rotation (see e.g. [176, 177, 252, 73]). Newtonian gravity and post-Newtonian approximation have been mainly used to compute the structure of the star, with the exception of the work of [11], where rotating white dwarfs (RWDs) were computed in full General Relativity (GR). From the microscopical point of view, the equation of state (EOS) of cold WD matter has been assumed to be either the one of a microscopically uniform degenerate electron fluid used by [53] in his classic work, or assumed to have a polytropic form.

However, as shown first by [229] in the Newtonian case and then by [210, 209] in General Relativity (GR), a detailed description of the EOS taking into account the effects of the Coulomb interaction are essential for the determination of the maximum stable mass of non-rotating WDs. Specific microphysics of the ion-electron system forming a Coulomb lattice, together with the detail computation of the inverse β -decays and the pycnonuclear reaction rates, play a fundamental role.

A new EOS taking into account the finite size of the nucleus, the Coulomb interactions, and the electroweak equilibrium in a self-consistent relativistic fashion has been recently obtained by [210]. This relativistic Feynman-Metropolis-Teller (RFMT) EOS generalizes both the [53] and [229] works in that a full treatment of the Coulomb interaction is given through the solution of a relativistic Thomas-Fermi model. This leads to a more accurate calculation of the energy and pressure of the Wigner-Seitz cells, hence a more accurate EOS. It has been shown how the Salpeter EOS overestimates at high densities and underestimates at low densities the electron pressure. The application of this new EOS to the structure of non-rotating ${}^4\text{He}$, ${}^{12}\text{C}$, ${}^{16}\text{O}$ and ${}^{56}\text{Fe}$ was recently done in [209]. The new mass-radius relations generalize the works of [53] and [102]; smaller maximum masses and a larger minimum radii are obtained. Both GR and inverse β -decay can be

relevant for the instability of non-rotating WDs depending on the nuclear composition, as we can see from Table 4.1, which summarizes some results of [209].

Composition	ρ_{crit} (g/cm ³)	Instability	$M_{\text{max}}^{J=0}/M_{\odot}$
⁴ He	1.56×10^{10}	GR	1.40906
¹² C	2.12×10^{10}	GR	1.38603
¹⁶ O	1.94×10^{10}	inverse β -decay	1.38024
⁵⁶ Fe	1.18×10^9	inverse β -decay	1.10618

Table 4.1: Critical density and mass for the gravitational collapse of non-rotating ⁴He, ¹²C, ¹⁶O and ⁵⁶Fe WDs in GR obtained by [209], based on the RFMT EOS [210]. We indicate in the third column if the critical density is due either to inverse β -decay or to general relativistic effects.

We here extend the previous results of [209] for uniformly RWDs at zero temperatures obeying the RFMT EOS. We use the Hartle’s approach [105] to solve the Einstein equations accurately up to second order approximation in the angular velocity of the star. We calculate the mass M , equatorial R_{eq} and polar R_p radii, angular momentum J , eccentricity ϵ , and quadrupole moment Q , as a function of the central density ρ_c and rotation angular velocity Ω of the WD. We construct also RWD models for the Chandrasekhar and Salpeter EOS and compare and contrast the differences with the RFMT ones.

We analyze in detail the stability of RWDs both from the microscopic and macroscopic point of view in Sec. 4.3. Besides the inverse β -decay instability, we also study the limits to the matter density imposed by zero-temperature pycnonuclear fusion reactions using up-to-date theoretical models [89, 274]. The mass-shedding limit as well as the secular axisymmetric instability boundary are calculated.

The general structure and stability boundaries of ⁴He, ¹²C, ¹⁶O and ⁵⁶Fe WDs are discussed in in Sec. 4.4. From the maximally rotating models (mass-shedding sequence), we calculate in Sec. 4.5 the maximum mass of uniformly rotating ⁴He, ¹²C, ¹⁶O and ⁵⁶Fe WDs for the Chandrasekhar, Salpeter, and RFMT EOS, and compare the results with the existing values in the literature. We calculate the minimum(maximum) rotation period(frequency) of a RWD for the above nuclear compositions, taking into account both inverse β -decay and pycnonuclear restrictions to the density; see Sec. 4.6.

We discuss in Sec. 4.7 the axisymmetric instabilities found in this work. A comparison of Newtonian and general relativistic WDs presented in App. C.2 show that this is indeed a general relativistic effect. Furthermore, we estimate in App. C.3 the accuracy of the “slow” rotation approximation (power-series solutions up to order Ω^2) for the determination of the maximally rotating sequence of WDs. In this line, we calculate the rotation to gravitational energy ratio and the deviations from spherical symmetry.

In addition, we construct in Sec. 4.8 constant rest-mass evolution tracks of RWDs at fixed chemical composition and show that RWDs may experience both spin-up and spin-down epochs while loosing angular momentum, depending on their initial mass and rotation period.

Finally, in Sec. 4.9 we outline some astrophysical implications of the results presented in this work, which we summarized in Sec. 4.10.

4.2 Spacetime geometry and Hartle’s formalism

[105] described for the first time the structure of rotating objects approximately up to second order terms in the angular velocity of the star Ω , within GR. In this “slow” rotation approximation, the solution of the Einstein equations in the exterior vacuum can be written in analytic closed form in terms of the total mass M , angular momentum J and quadrupole moment Q of the star (see App. C). The interior metric is constructed by solving numerically a system of ordinary differential equations for the perturbation functions (see for details [105, 108]).

The spacetime geometry up to order Ω^2 , with an appropriate choice of coordinates is, in geometrical units $c = G = 1$, described by [105]

$$\begin{aligned}
 ds^2 = & \left\{ e^{\nu(r)} [1 + 2h_0(r) + 2h_2(r)P_2(\cos\theta)] - \omega^2 r^2 \sin^2\theta \right\} dt^2 \\
 & + 2\omega r^2 \sin^2\theta dt d\phi - e^{\lambda(r)} \left[1 + 2 \frac{m_0(r) + m_2(r)P_2(\cos\theta)}{r - M^{J=0}(r)} \right] dr^2 \\
 & - r^2 [1 + 2k_2(r)P_2(\cos\theta)] (d\theta^2 + \sin^2\theta d\phi^2), \tag{4.1}
 \end{aligned}$$

where $P_2(\cos\theta)$ is the Legendre polynomial of second order, $e^{\nu(r)}$ and $e^{\lambda(r)} = [1 - 2M^{J=0}(r)/r]^{-1}$, and $M^{J=0}(r)$ are the metric functions and mass of the corresponding static (non-rotating) solution with the same central density as the rotating one. The angular velocity of local inertial frames $\omega(r)$, proportional to Ω , as well as the functions h_0 , h_2 , m_0 , m_2 , k_2 , proportional to Ω^2 , must be calculated from the Einstein equations (see for details [105, 108]); their analytic expressions in the vacuum case can be found in App. C.

The parameters M , J and Q , are then obtained for a given EOS from the matching procedure between the internal and external solutions at the surface of the rotating star. The total mass is defined by $M = M^{J \neq 0} = M^{J=0} + \delta M$, where $M^{J=0}$ is the mass of a static (non-rotating) WD with the same central density as $M^{J \neq 0}$, and δM is the contribution to the mass due to rotation.

4.3 Limits on the stability of rotating white dwarfs

4.3.1 The mass-shedding limit

The velocity of particles on the equator of the star cannot exceed the Keplerian velocity of “free” particles, computed at the same location. In this limit, particles on the star’s surface keep bound to the star only due to a balance between gravity and centrifugal forces. The evolution of a star rotating at this Keplerian rate is accompanied by loss of mass, becoming thus unstable (see e.g. see e.g. stergioulas). A procedure to obtain the maximum possible angular velocity of the star before reaching this limit was developed e.g. by [85]. However, in practice, it is less complicated to compute the mass-shedding (or Keplerian) angular velocity of a rotating star, $\Omega_K^{J \neq 0}$, by calculating the orbital angular velocity of a test particle in the external field of the star and corotating with it at its equatorial radius, $r = R_{eq}$.

For the Hartle-Thorne external solution, the Keplerian angular velocity can be written as (see e.g. [261, 24] and App. C.0.2, for details)

$$\Omega_K^{J \neq 0} = \sqrt{\frac{M}{R_{eq}^3}} [1 - jF_1(R_{eq}) + j^2F_2(R_{eq}) + qF_3(R_{eq})], \quad (4.2)$$

where $j = cJ/(GM^2)$ and $q = c^4Q/(G^2M^3)$ are the dimensionless angular momentum and quadrupole moment, and the functions $F_i(r)$ are defined in App. C.0.2. Thus, the numerical value of $\Omega_K^{J \neq 0}$ can be computed by gradually increasing the value of the angular velocity of the star, Ω , until it reaches the value $\Omega_K^{J \neq 0}$ expressed by Eq. (4.2).

It is important to analyze the issue of the accuracy of the slow rotation approximations, e.g. accurate up to second order in the rotation expansion parameter, for the description of maximally rotating stars as WDs and neutron stars (NSs). We have performed in App. C.3 a scrutiny of the actual physical request made by the slow rotation regime. Based on this analysis, we have checked that the accuracy of the slow rotation approximation increases with the density of the WD, and that the mass-shedding (Keplerian) sequence of RWDs can be accurately described by the Ω^2 approximation within an error smaller than the one found for rapidly rotating NSs, $\lesssim 6\%$.

4.3.2 The turning-point criterion

In a sequence of increasing central density the mass of non-rotating star is limited by the first maximum of the M - ρ_c curve, i.e. the turning-point given by the maximum mass, $\partial M/\partial \rho_c = 0$, marks the secular instability point and it coincides also with the dynamical instability point if the perturbation obeys the same EOS as of the equilibrium configuration (see e.g. [235] for details). The situation is, however, much more complicated in the case of rotating stars; the determination of axisymmetric dynamical instability points implies to find the perturbed solutions with zero frequency modes, that is, perturbed configurations whose energy (mass) is the same as the unperturbed (equilibrium) one, at second order. However, [84] formulated, based on the works of [241, 242], a turning-point method to locate the points where secular instability sets in for uniformly rotating relativistic stars: along a sequence of rotating stars with fixed angular momentum and increasing central density, the onset of secular axisymmetric instability is given by

$$\left(\frac{\partial M(\rho_c, J)}{\partial \rho_c} \right)_J = 0. \quad (4.3)$$

Thus, configurations on the right-side of the maximum mass of a J -constant sequence are secularly unstable. After the secular instability sets in, the configuration evolves quasi-stationarily until it reaches a point of dynamical instability where gravitational collapse should take place (see [246] and references therein). The secular instability boundary thus separates stable from unstable stars. It is worth stressing here that the turning-point of a constant J sequence is a sufficient but not a necessary condition for secular instability and therefore it establishes an absolute upper bound for the mass (at constant J). We

Decay	ϵ_Z^β (MeV)	ρ_{crit}^β (g/cm ³)
${}^4\text{He} \rightarrow {}^3\text{H} + n \rightarrow 4n$	20.596	1.39×10^{11}
${}^{12}\text{C} \rightarrow {}^{12}\text{B} \rightarrow {}^{12}\text{Be}$	13.370	3.97×10^{10}
${}^{16}\text{O} \rightarrow {}^{16}\text{N} \rightarrow {}^{16}\text{C}$	10.419	1.94×10^{10}
${}^{56}\text{Fe} \rightarrow {}^{56}\text{Mn} \rightarrow {}^{56}\text{Cr}$	3.695	1.18×10^9

Table 4.2: Onset for the inverse β -decay of ${}^4\text{He}$, ${}^{12}\text{C}$, ${}^{16}\text{O}$ and ${}^{56}\text{Fe}$. The experimental values of the threshold energies ϵ_Z^β have been taken from Table 1 of [12]; see also [268, 235]. The corresponding critical density ρ_{crit}^β are for the RFMT EOS [209]

construct the boundary given by the turning-points of constant angular momentum sequences as given by Eq. (4.3). The question whether dynamically unstable RWDs can exist or not on the left-side of the turning-point boundary remains an interesting problem and deserves further attention in view of the very recent results obtained by [250] for some models of rapidly rotating NSs.

4.3.3 Inverse beta-decay instability

It is known that a WD might become unstable against the inverse β -decay process $(Z, A) \rightarrow (Z - 1, A)$ through the capture of energetic electrons. In order to trigger such a process, the electron Fermi energy (with the rest-mass subtracted off) must be larger than the mass difference between the initial (Z, A) and final $(Z - 1, A)$ nucleus. We denote this threshold energy as ϵ_Z^β . Usually it is satisfied $\epsilon_{Z-1}^\beta < \epsilon_Z^\beta$ and therefore the initial nucleus undergoes two successive decays, i.e. $(Z, A) \rightarrow (Z - 1, A) \rightarrow (Z - 2, A)$ (see e.g. [229, 235]). Some of the possible decay channels in WDs with the corresponding known experimental threshold energies ϵ_Z^β are listed in Table 4.2. The electrons in the WD may eventually reach the threshold energy to trigger a given decay at some critical density ρ_{crit}^β . Since the electrons are responsible for the internal pressure of the WD, configurations with $\rho > \rho_{\text{crit}}^\beta$ become unstable due to the softening of the EOS as a result of the electron capture process (see [104, 229] for details). In Table 4.2, correspondingly to each threshold energy ϵ_Z^β , the critical density ρ_{crit}^β given by the RFMT EOS is shown; see [209] for details.

4.3.4 Pycnonuclear fusion reactions

In our WD model, we assume a unique nuclear composition (Z, A) throughout the star. We have just seen that inverse β -decay imposes a limit to the density of the WD over which the current nuclear composition changes from (Z, A) to $(Z - 1, A)$. There is an additional limit to the nuclear composition of a WD. Nuclear reactions proceed with the overcoming of the Coulomb barrier by the nuclei in the lattice. In the presence case of zero temperatures $T = 0$, the Coulomb barrier can be overcome because the zero-point

energy of the nuclei (see e.g. [235])

$$E_p = \hbar\omega_p, \quad \omega_p = \sqrt{\frac{4\pi e^2 Z^2 \rho}{A^2 M_u^2}}, \quad (4.4)$$

where e is the fundamental charge and $M_u = 1.6605 \times 10^{-24}$ g is the atomic mass unit.

Based on the pycnonuclear rates computed by [276] and [50], [229] estimated that in a time of 0.1 Myr, ^1H is converted into ^4He at $\rho \sim 5 \times 10^4$ g cm $^{-3}$, ^4He into ^{12}C at $\rho \sim 8 \times 10^8$ g cm $^{-3}$, and ^{12}C into ^{24}Mg at $\rho \sim 6 \times 10^9$ g cm $^{-3}$. The threshold density for the pycnonuclear fusion of ^{16}O occurs, for the same reaction time 0.1 Myr, at $\rho \sim 3 \times 10^{11}$ g cm $^{-3}$, and for 10 Gyr at $\sim 10^{11}$ g cm $^{-3}$. These densities are much higher than the corresponding density for inverse β -decay of ^{16}O , $\rho \sim 1.9 \times 10^{10}$ g cm $^{-3}$ (see Table 4.2). The same argument applies to heavier compositions e.g. ^{56}Fe ; so pycnonuclear reactions are not important for heavier than ^{12}C in WDs.

It is important to analyze the case of ^4He WDs in detail. At densities $\rho_{pyc} \sim 8 \times 10^8$ g cm $^{-3}$ a ^4He WD should have a mass $M \sim 1.35M_\odot$ (see e.g. Fig. 3 in [209]). However, the mass of ^4He WDs is constrained to lower values from their previous thermonuclear evolution: a cold star with mass $> 0.5M_\odot$ have already burned an appreciable part of its Helium content at earlier stages. Thus, WDs of $M > 0.5M_\odot$ with ^4He cores are very unlikely (see [102] for details). It should be stressed that ^4He WDs with $M \lesssim 0.5M_\odot$ have central densities $\rho \sim 10^6$ g cm $^{-3}$ [209] and at such densities pycnonuclear reaction times are longer than 10 Gyr, hence unimportant. However, we construct in this work ^4He RWDs configurations all the way up to their inverse β -decay limiting density for the sake of completeness, keeping in mind that the theoretical ^4He WDs configurations with $M \gtrsim 0.5M_\odot$ could actually not be present in any astrophysical system.

From the above discussion we conclude that pycnonuclear reactions can be relevant only for ^{12}C WDs. It is important to stress here that the reason for which the pycnonuclear reaction time, τ_{pyc}^{C+C} , determines the lifetime of a ^{12}C WD is that reaction times $\tau_{pyc}^{C+C} < 10$ Gyr are achieved at densities $\sim 10^{10}$ g cm $^{-3}$, lower than the inverse β decay threshold density of ^{24}Mg , $^{24}\text{Mg} \rightarrow ^{24}\text{Na} \rightarrow ^{24}\text{Ne}$, $\rho \sim 3.2 \times 10^9$ g cm $^{-3}$ (see e.g. [229, 235]). Thus, the pycnonuclear $^{12}\text{C}+^{12}\text{C}$ fusion produces unstable ^{24}Mg that almost instantaneously decay owing to electron captures, and so the WD becomes unstable as we discussed in Subsec. 4.3.1.

However, the pycnonuclear reaction rates are not known with precision due to theoretical and experimental uncertainties. [102] had already pointed out in their work that the above pycnonuclear density thresholds are reliable only within a factor 3 or 4. The uncertainties are related to the precise knowledge of the Coulomb tunneling in the high density low temperature regime relevant to astrophysical systems, e.g. WDs and NSs, as well as with the precise structure of the lattice; impurities, crystal imperfections, as well as the inhomogeneities of the local electron distribution and finite temperature effects, also affect the reaction rates. The energies for which the so-called astrophysical S -factors are known from experiments are larger with respect to the energies found in WD and NS crusts, and therefore the value of the S -factors have to be obtained theoretically from

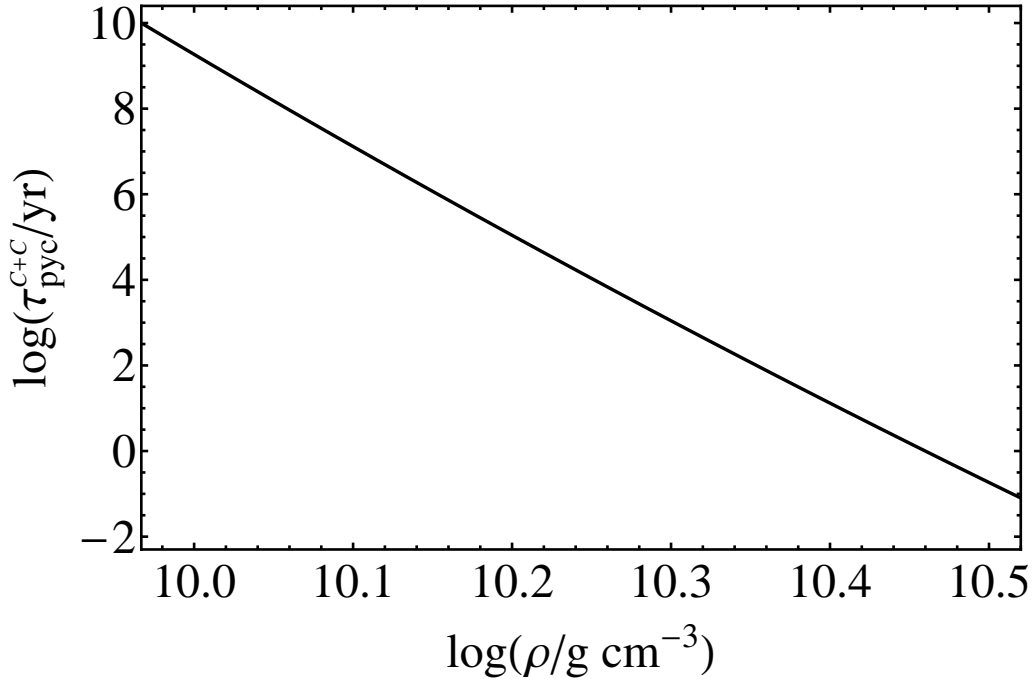


Figure 4.1: Pycnonuclear reaction times at zero temperature for C+C fusion as a function of the density.

the extrapolation of experimental values using appropriate nuclear models, which at the same time are poorly constrained. A detailed comparison between the different theoretical methods and approximations used for the computation of the pycnonuclear reaction rates can be found in [89, 274].

The S -factors have been computed in [89, 274] using up-to-date nuclear models. Following these works, we have computed the pycnonuclear reaction times for C+C fusion as a function of the density as given by Eq. (C.14), $\tau_{\text{pyc}}^{\text{C+C}}$, which we show in Fig. 4.1; we refer to App. C.1 for details.

We obtain that for $\tau_{\text{pyc}}^{\text{C+C}} = 10$ Gyr, $\rho_{\text{pyc}} \sim 9.26 \times 10^9 \text{ g cm}^{-3}$ while, for $\tau_{\text{pyc}}^{\text{C+C}} = 0.1$ Myr, $\rho_{\text{pyc}} \sim 1.59 \times 10^{10} \text{ g cm}^{-3}$, to be compared with the value $\rho \sim 6 \times 10^9 \text{ g cm}^{-3}$ estimated by [229]. In order to compare the threshold densities for inverse β -decay and pycnonuclear fusion rates, we shall indicate in our mass-density and mass-radius relations the above two density values corresponding to these two lifetimes. It is important to keep in mind that [89] estimated that the S -factors are reliable within a factor ~ 3.5 , so the density is reliable within the same factor. If three times larger, the above value of ρ_{pyc} for $\tau_{\text{pyc}}^{\text{C+C}} = 0.1$ Myr becomes $\rho_{\text{pyc}} \sim 4.8 \times 10^{10} \text{ g cm}^{-3}$, larger than the inverse β -decay threshold density $\rho_{\beta}^{\text{C}} \sim 3.97 \times 10^{10} \text{ g cm}^{-3}$ (see Table 4.2). As we will see, the turning-point construction leads to an axisymmetric instability boundary between $2.12 \times 10^{10} < \rho < \rho_{\beta}^{\text{C}}$ g cm^{-3} for a specific range of angular velocities; a range of densities particularly close to the above value of ρ_{pyc} .

4.4 WD structure and stability boundaries

The structure of uniformly RWDs have been studied by several authors (see [121, 7, 215, 166, 91]). The issue of the stability of both uniformly and differentially rotating WDs has been studied as well (see e.g. [176, 177, 252, 73]). All the above computations were carried out within Newtonian gravity or at the post-Newtonian approximation. The EOS of cold WD matter has been assumed to be either the one of a microscopically uniform degenerate electron fluid, which we refer hereafter as Chandrasekhar EOS [53], or assuming a polytropic EOS. However, microscopic screening caused by Coulomb interactions as well as the process of inverse β -decay of the composing nuclei cannot be properly studied within such EOS (see [210, 209] for details).

The role of general relativistic effects, shown in [209], has been neglected in all the above precedent literature. The only exception to this rule is, up to our knowledge, the work of [11], who investigated uniformly RWDs for the Chandrasekhar EOS within GR. They use an Ω^2 approximation following a method developed by [234], independently of the work of [105]. A detailed comparison of our results with the ones of [11] can be found in App. C.2.

In Figs. 4.2–4.3 we show the mass-central density relation and the mass-radius relation of general relativistic rotating ^{12}C and ^{16}O WDs. We explicitly show the boundaries of mass-shedding, secular axisymmetric instability, inverse β -decay, and pycnonuclear reactions.

Turning now to the rotation properties, in Fig. 4.4 we show the J - M plane especially focusing on RWDs with masses larger than the maximum non-rotating mass, hereafter Super-Chandrasekhar WDs (SCWDs). It becomes clear from this diagram that SCWDs can be stable only by virtue of their non-zero angular momentum: the lower-half of the stability line of Fig. 4.4, from $J = 0$ at $M/M_{max}^{J=0}$ all the way up to the value of J at $M_{max}^{J\neq 0} \sim 1.06M_{max}^{J=0}$, determines the critical (minimum) angular momentum under which a SCWDs becomes unstable. The upper half of the stability line determines, instead, the maximum angular momentum that SCWDs can have.

4.5 The maximum mass

The maximum masses of rotating WDs belongs to the Keplerian sequence (see Figs. 4.2–4.4) and it can be expressed as

$$M_{max}^{J\neq 0} = k M_{max}^{J=0}, \quad (4.5)$$

where $M_{max}^{J=0}$ is the maximum stable mass of non-rotating WDs and k is a numerical factor that depends on the chemical composition, see Table 4.3 for details. For ^4He , ^{12}C , ^{16}O , and ^{56}Fe RWDs, we found $M_{max}^{J\neq 0} \sim 1.500, 1.474, 1.467, 1.202 M_{\odot}$, respectively.

In Table 4.4 we compare the properties of the configuration with maximum mass using different EOS, namely Chandrasekhar $\mu = 2$ (see e.g. [44]), Salpeter, and RFMT EOS. A comparison with classical results obtained with different treatments and EOS can be found in App. C.2.

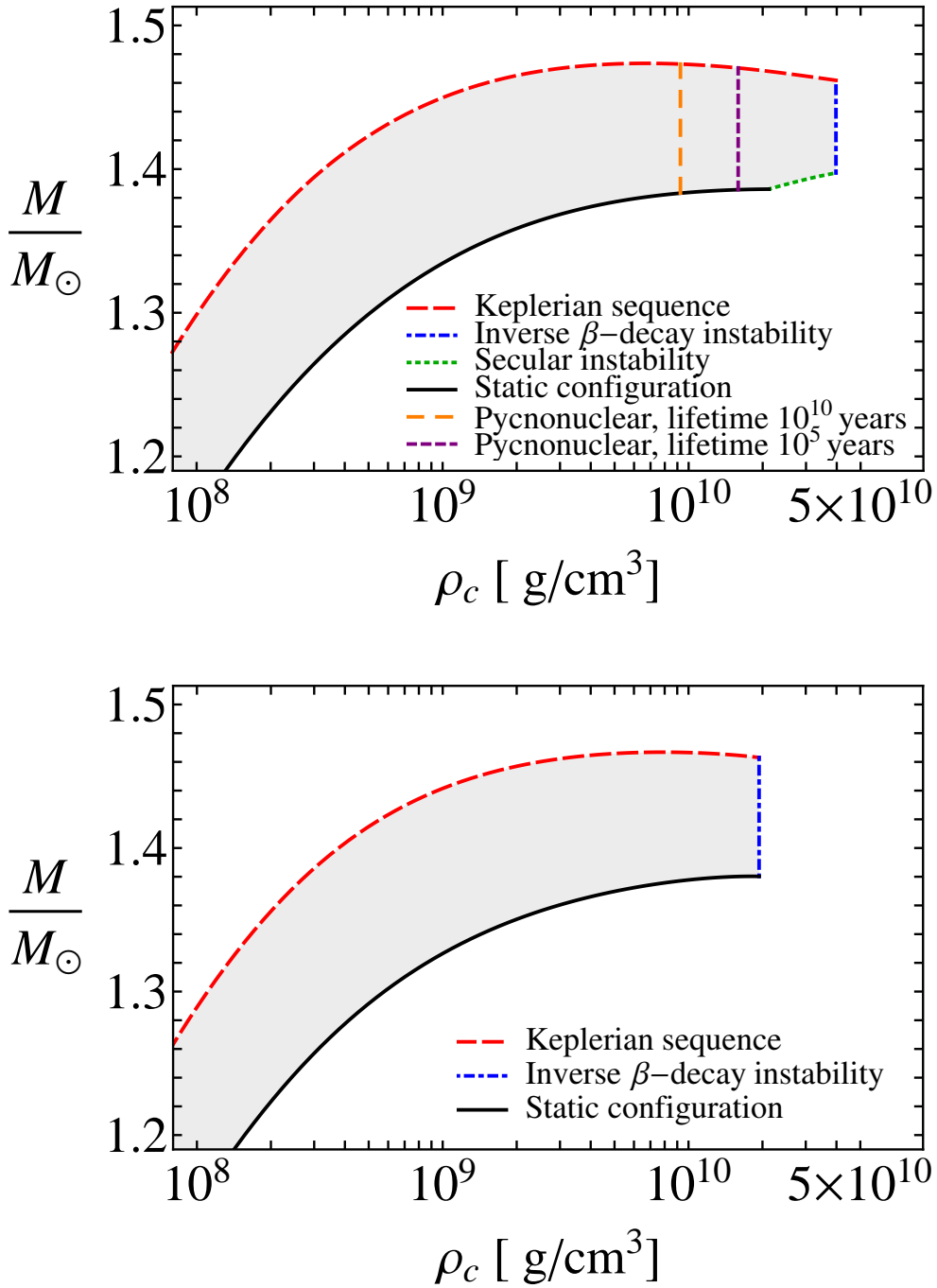


Figure 4.2: Mass in solar masses versus the central density for ^{12}C (top panel) and for ^{16}O (bottom panel) WDs. The solid curve corresponds to the mass of non-rotating WDs, the Keplerian sequence is the red thick dashed curve, the blue thick dotted-dashed curve is the inverse β instability boundary, and the green thick solid curve is the axisymmetric secular instability boundary. The orange and purple dashed boundaries correspond to the pycnonuclear densities for reaction times $\tau_{pyc} = 10$ Gyr and 0.1 Myr, respectively. All rotating stable WDs are in the shaded region.

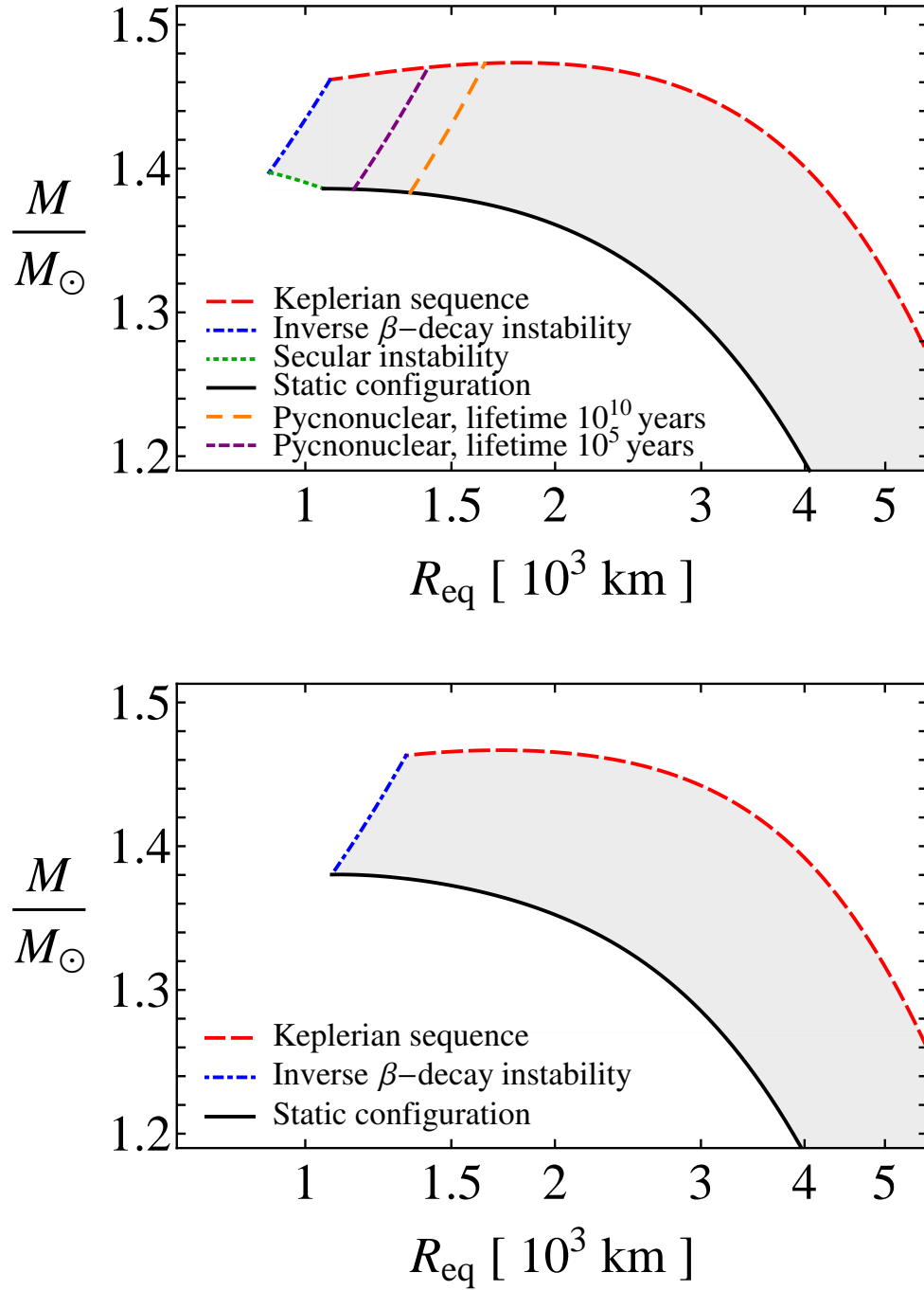


Figure 4.3: Mass in solar masses versus the equatorial radius in units of 10^3 km for ^{12}C (top panel) and for ^{16}O (bottom panel) WDs. The left and right panels show the configurations for the same range of central densities of the corresponding panels of Fig. 4.2.

Comp.	$\rho_{M_{max}^{J \neq 0}}$	k	$M_{max}^{J=0}/M_{\odot}$	$R_{M_{max}^{J=0}}$	P_{min}	$R_p^{P_{min}}$	$R_{eq}^{P_{min}}$	$(T/ W)^{P_{min}}$	$\epsilon^{P_{min}}$
^4He	5.46×10^9	1.0646	1.40906	1163	0.284	564	736	0.0163	0.642
^{12}C	6.95×10^9	1.0632	1.38603	1051	0.501	817	1071	0.0181	0.647
^{16}O	7.68×10^9	1.0626	1.38024	1076	0.687	1005	1323	0.0194	0.651
^{56}Fe	1.18×10^9	1.0864	1.10618	2181	2.195	2000	2686	0.0278	0.667

Table 4.3: Properties of uniformly rotating general relativistic ^4He , ^{12}C , ^{16}O and ^{56}Fe WDs: Comp. stands for nuclear composition, $\rho_{M_{max}^{J \neq 0}}$ is the central density in g cm^{-3} corresponding to the rotating maximum mass $M_{max}^{J \neq 0}$; k is the dimensionless factor used to express the rotating maximum mass $M_{max}^{J \neq 0}$ as a function of the non-rotating maximum mass $M_{max}^{J=0}$ of WDs, in solar masses, obtained in [209], as defined in Eq. (4.5); the corresponding minimum radius is $R_{M_{max}^{J=0}}$, in km; P_{min} is the minimum rotation period in seconds. It is worth recalling that the configuration with P_{min} is obtained for a WD rotating at the mass-shedding limit and with central density equal to the critical density for inverse β -decay (see Table 4.2 and the right panel of Fig. 4.6). The polar $R_p^{P_{min}}$ and equatorial $R_{eq}^{P_{min}}$ radii of the configuration with P_{min} are also given in km. The quantity $(T/|W|)^{P_{min}}$ is the ratio between the kinetic and binding energies, the parameter $\epsilon^{P_{min}}$ is the eccentricity of the star, rotating at P_{min} .

Comp.	EOS	$\rho_{M_{max}^{J \neq 0}}$ (g/cm^3)	$R_p^{M_{max}^{J \neq 0}}$ (km)	$R_{eq}^{M_{max}^{J \neq 0}}$ (km)	$M_{max}^{J \neq 0}/M_{\odot}$	$P^{M_{max}^{J \neq 0}}$ (sec)
$\mu = 2$	Chandra	1.07×10^{10}	1198.91	1583.47	1.5159	0.884
	Salpeter	1.07×10^{10}	1193.08	1575.94	1.4996	0.883
^4He	RFMT	5.46×10^9	1458.58	1932.59	1.5001	1.199
	Salpeter	1.08×10^{10}	1183.99	1564.16	1.4833	0.878
^{12}C	RFMT	6.95×10^9	1349.15	1785.98	1.4736	1.074
	Salpeter	1.09×10^{10}	1178.88	1556.68	1.4773	0.875
^{16}O	RFMT	7.68×10^9	1308.09	1730.65	1.4667	1.027
	Salpeter	1.14×10^9	2002.43	2693.17	1.2050	2.202
^{56}Fe	RFMT	1.18×10^9	2000.11	2686.06	1.2017	2.195

Table 4.4: The maximum rotating mass of general relativistic uniformly rotating ^4He , ^{12}C , ^{16}O and ^{56}Fe WDs for different EoS. $\rho_{M_{max}^{J \neq 0}}$, $R_p^{M_{max}^{J \neq 0}}$, $R_{eq}^{M_{max}^{J \neq 0}}$, and $P^{M_{max}^{J \neq 0}}$ are central density, polar and equatorial radii, and rotation period of the configuration with the maximum mass, $M_{max}^{J \neq 0}$.

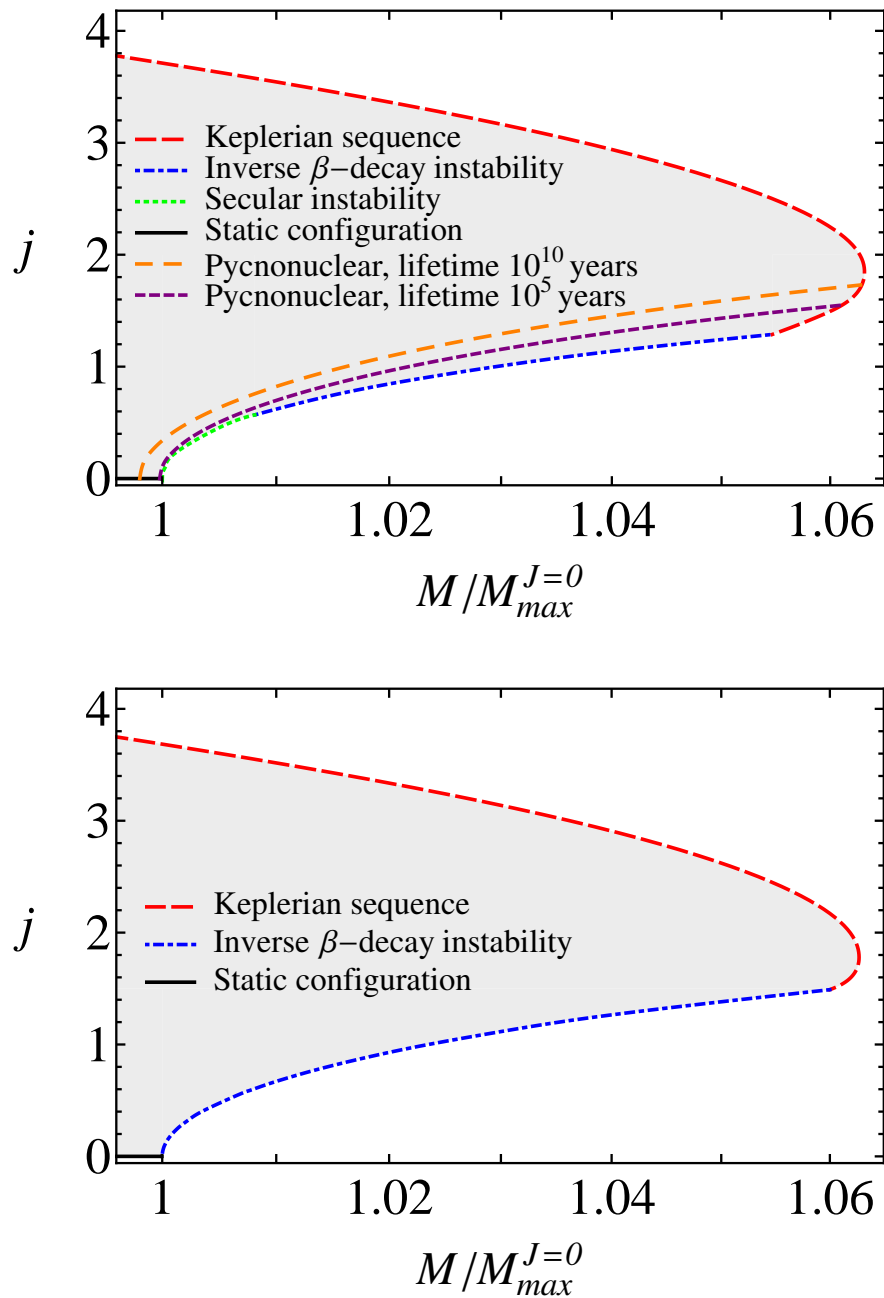


Figure 4.4: Dimensionless angular momentum $j \equiv cJ/(GM^2)$ versus the mass of rotating ^{12}C (top panel) and ^{16}O (bottom panel) WDs, normalized to the maximum non-rotating mass. All rotating stable WDs are in the shaded region.

It is worth mentioning that the maximum mass of RWDs is not associated with a critical maximum density for gravitational collapse. This is in contrast with the non-rotating case where the configuration of maximum mass (turning-point) corresponds to a critical maximum density over which the WD is unstable against gravitational collapse.

The angular momentum J along the mass-shedding sequence is not constant and thus the turning-point criterion (4.3) does not apply to this sequence. Therefore the configuration of maximum rotating mass (4.5) does not separate stable from secular axisymmetrically unstable WDs. We have also verified that none of the RWDs belonging to the mass-shedding sequence is a turning-point of some $J = \text{constant}$ sequence, and therefore they are indeed secularly stable. We therefore extend the Keplerian sequence all the way up to the critical density for inverse β decay, $\rho_{\text{crit}}^{\beta}$, see Table 4.2 and Fig. 4.2.

4.6 The minimum rotation period

The minimum rotation period P_{min} of WDs is obtained for a configuration rotating at Keplerian angular velocity, at the critical inverse β -decay density; i.e. is the configuration lying at the crossing point between the mass-shedding and inverse β -decay boundaries, see Figs. 4.2 and 4.4. For ${}^4\text{He}$, ${}^{12}\text{C}$, ${}^{16}\text{O}$, and ${}^{56}\text{Fe}$ RWDs we found the minimum rotation periods ~ 0.28 , 0.50 , 0.69 and 2.19 seconds, respectively (see Table 4.3 for details). In Table 4.4 we compare the properties of the configuration with minimum rotation period using different EOS, namely Chandrasekhar $\mu = 2$, Salpeter, and RFMT EOS.

In the case of ${}^{12}\text{C}$ WDs, the minimum period 0.50 seconds have to be compared with the value obtained assuming as critical density the threshold for pycnonuclear reactions. Assuming lifetimes $\tau_{\text{pyc}}^{\text{C+C}} = 10$ Gyr and 0.1 Myr, corresponding to critical densities $\rho_{\text{pyc}} \sim 9.26 \times 10^9 \text{ g cm}^{-3}$ and $\rho_{\text{pyc}} \sim 1.59 \times 10^{10} \text{ g cm}^{-3}$, we obtain minimum periods $P_{\text{min}}^{\text{pyc}} = 0.95$ and 0.75 seconds, respectively.

It is interesting to compare and contrast some classical results with the ones presented in this work. Using post-Newtonian approximation, [215] analyzed the problem of dynamical stability of maximally rotating RWDs, i.e. WDs rotating at the mass-shedding limit. The result was a minimum polar radius of 363 km, assuming the Chandrasekhar EOS with $\mu = 2$. The Roxburgh critical radius is rather small with respect to our minimum polar radii, see Table 4.3. It is clear that such a small radius would lead to a configuration with the central density over the limit established by inverse β -decay: the average density obtained for the Roxburgh's critical configuration is $\sim 1.47 \times 10^{10} \text{ g/cm}^3$, assuming the maximum mass $1.48M_{\odot}$ obtained in the same work (see Table C.2 in App. C.2). A configuration with this mean density will certainly have a central density larger than the inverse β -decay density of ${}^{12}\text{C}$ and ${}^{16}\text{O}$, $3.97 \times 10^{10} \text{ g/cm}^3$ and $1.94 \times 10^{10} \text{ g/cm}^3$, respectively (see Table 4.2). The rotation period of the WD at the point of dynamical instability of Roxburgh must be certainly shorter than the minimum values presented here.

The above comparison is in line with the fact that we did not find any turning-point that cross the mass-shedding sequence (see Figs. 4.2–4.3). Presumably, ignoring the limits imposed by inverse β -decay and pycnonuclear reactions, the boundary determined

Composition	EOS	$\rho_{\text{crit}}^{\beta}$ (g/cm ³)	$R_p^{P_{\text{min}}}$ (km)	$R_{\text{eq}}^{P_{\text{min}}}$ (km)	$M_{P_{\text{min}}}^{J \neq 0} / M_{\odot}$	P_{min} (sec)
$\mu = 2$	Chandra	1.37×10^{11}	562.79	734.54	1.4963	0.281
⁴ He	Salpeter	1.37×10^{11}	560.41	731.51	1.4803	0.281
	RFMT	1.39×10^{11}	563.71	735.55	1.4623	0.285
¹² C	Salpeter	3.88×10^{10}	815.98	1070.87	1.4775	0.498
	RFMT	3.97×10^{10}	816.55	1071.10	1.4618	0.501
¹⁶ O	Salpeter	1.89×10^{10}	1005.62	1324.43	1.4761	0.686
	RFMT	1.94×10^{10}	1005.03	1323.04	1.4630	0.687
⁵⁶ Fe	Salpeter	1.14×10^9	2002.43	2693.17	1.2050	2.202
	RFMT	1.18×10^9	2000.11	2686.06	1.2018	2.195

Table 4.5: The minimum rotation period of general relativistic rotating ⁴He, ¹²C, ¹⁶O and ⁵⁶Fe WDs. $\rho_{\text{crit}}^{\beta}$ is the critical density for inverse β decay. $M_{P_{\text{min}}}^{J \neq 0}$, $R_p^{P_{\text{min}}}$, and $R_{\text{eq}}^{P_{\text{min}}}$ are the mass, polar, and equatorial radii corresponding to the configuration with minimum rotation period, P_{min} .

by the turning-points could cross at some higher density the Keplerian sequence. Such a configuration should have a central density very similar to the one found by [215].

In the work of [11] the problem of the minimum rotation period of a WD was not considered. However, they showed their results for a range of central densities covering the range of interest of our analysis. Thus, we have interpolated their numerical values of the rotation period of WDs in the Keplerian sequence and calculated the precise values at the inverse β -decay threshold for ⁴He, ¹²C, and ¹⁶O that have $\mu = 2$ and therefore in principle comparable to the Chandrasekhar EOS results with the same mean molecular weight. We thus obtained minimum periods $\sim 0.31, 0.55, 0.77$ seconds, in agreement with our results (see Table 4.5).

It is important to stress that, although it is possible to compare the results using the Chandrasekhar EOS $\mu = 2$ with the ones obtained for the RFMT EOS, both qualitative and quantitative differences exist between the two treatments. In the former a universal mass-density and mass-radius relation is obtained assuming $\mu = 2$ while, in reality, the configurations of equilibrium depend on the specific values of Z and A in non-trivial way. For instance, ⁴He, ¹²C, and ¹⁶O have $\mu = 2$ but the configurations of equilibrium are rather different. This fact was emphasized by [102] in the Newtonian case and further in GR by [209], for non-rotating configurations. In Fig. 4.5 we present a comparison of the mass-density and mass-radius for the universal Chandrasekhar $\mu = 2$ and the RFMT EOS for specific nuclear compositions.

4.7 Occurrence of secular axisymmetric instability

Regarding the stability of rotating WDs, [176, 177, 73] showed that uniformly rotating Newtonian polytropes and WDs described by the uniform degenerate electron fluid EOS are axisymmetrically stable at any rotation rate. In clear contrast with these results, we have shown here that uniformly RWDs can be indeed be secularly axisymmetric unstable as can be seen from Figs. 4.2–4.4 (green boundary). We have constructed in

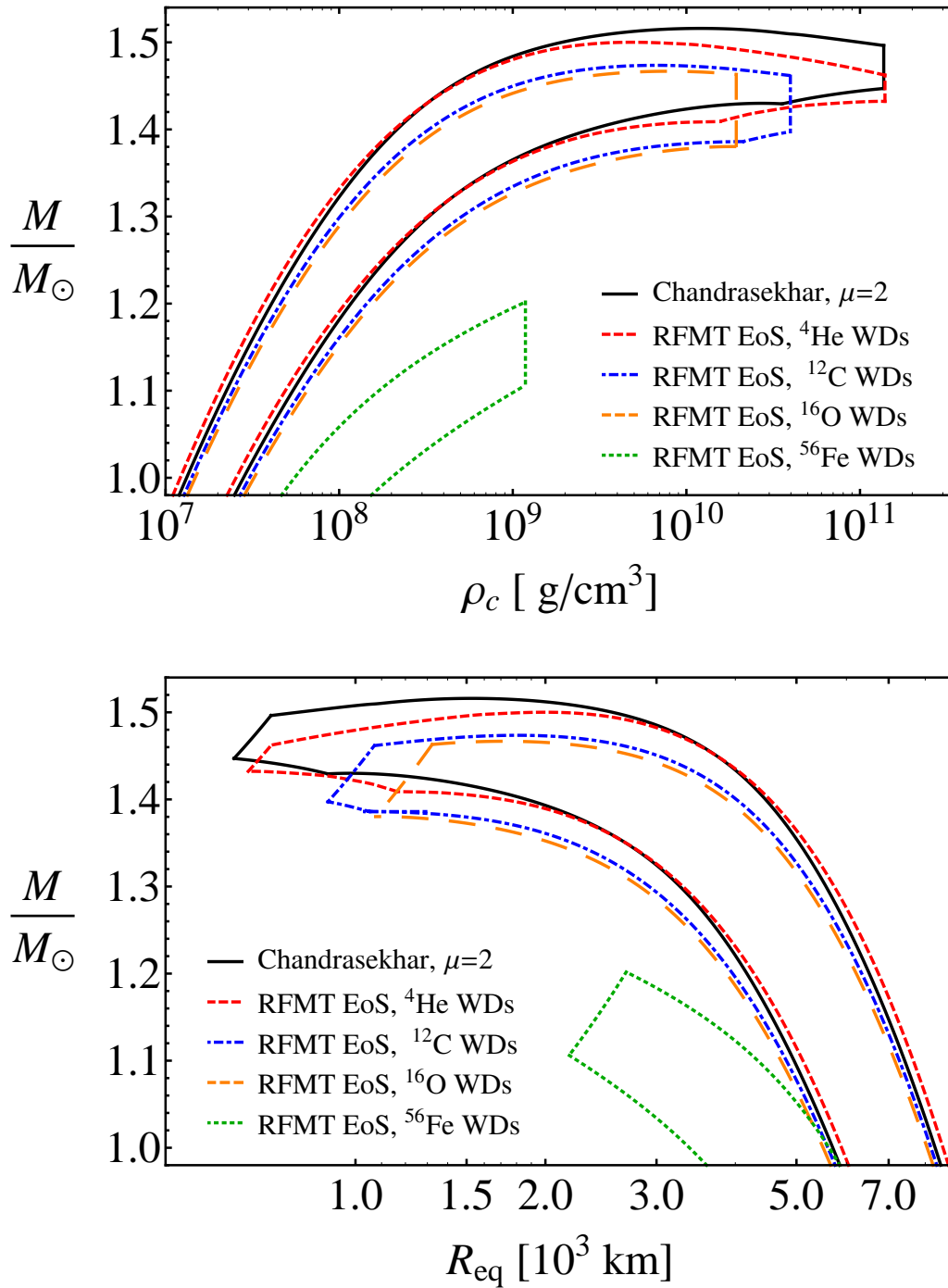


Figure 4.5: Mass versus central density (top panel) and mass versus equatorial radius (bottom panel) for general relativistic WDs using the Chandrasekhar and the RFMT EOS.

App. C.2 Newtonian RWDs for the Chandrasekhar EOS and compare the differences with the general relativistic counterpart. Apart from the quantitative differences for the determination of the mass at high densities, it can be seen from Fig. C.1 (left panel) the absence of turning-points in the Newtonian mass-density relation. This can be understood from the fact that the maximum stable mass of non-rotating WDs is, in the Newtonian case, reached formally at infinite central density. We should then expect that turning-points will appear only from a post-Newtonian approximation, where the critical mass is shifted to finite densities (see e.g. [215] for the calculation of dynamical instability for post-Newtonian RWDs obeying the Chandrasekhar EOS).

In this respect the Fig. 4.4 is of particular astrophysical relevance. Configurations lying in the filled region are stable against mass-shedding, inverse β -decay and secular axisymmetric instabilities. RWDs with masses smaller than the maximum non-rotating mass (Sub-Chandrasekhar WDs), i.e. $M^{J \neq 0} < M_{max}^{J=0}$, can have angular momenta ranging from a maximum at the mass-shedding limit all the way down to the non-rotating limit $J = 0$. SCWDs, however, are stabilized due to rotation and therefore there exist a minimum angular momentum, $J_{min} > 0$, to guarantee their stability. We have shown above that secular axisymmetric instability is relevant for the determination of this minimum angular momentum of SCWDs (see green boundary in Fig. 4.4). It is interesting to note in this respect that from our results it turns out that SCWDs with *light chemical compositions* such as ${}^4\text{He}$ and ${}^{12}\text{C}$, are unstable against *axisymmetric*, inverse β -decay and mass-shedding instabilities. On the opposite, in SCWDs with *heavier chemical compositions*, such as ${}^{16}\text{O}$ and ${}^{56}\text{Fe}$, the secular axisymmetric instability does not take place; see Fig. 4.4. The existence of the new boundary due to secular axisymmetric instability is a critical issue for the evolution of SCWDs since their lifetime might be reduced depending on their initial mass and angular momentum.

From the quantitative point of view, we have found that axisymmetric instability sets in for ${}^{12}\text{C}$ SCWDs in the range of masses $M_{max}^{J=0} < M \lesssim 1.397M_{\odot}$, for some specific range of rotation periods $\gtrsim 1.24$ seconds. We can express the minimum rotation period that a SCWD with a mass M within the above mass range can have through the fitting formula

$$P_{axi} = 0.062 \left(\frac{M - M_{max}^{J=0}}{M_{\odot}} \right)^{-0.67} \text{ seconds}, \quad (4.6)$$

where $M_{max}^{J=0}$ is the maximum mass of general relativistic non-rotating ${}^{12}\text{C}$ WDs, $M_{max}^{J=0} \approx 1.386M_{\odot}$ (see Table 4.1 and [209]). Thus, Eq. (4.6) describes the rotation periods of the configurations along the green-dotted boundary in Figs. 4.2, 4.3, and 4.4. Correspondingly, the central density along this instability boundary varies from the critical density of static ${}^{12}\text{C}$ WDs, $\rho_{crit}^{C,J=0} = 2.12 \times 10^{10} \text{ g cm}^{-3}$ (see Table 4.1), up to the inverse β -decay density, $\rho_{\beta}^C = 3.97 \times 10^{10} \text{ g cm}^{-3}$ (see Table 4.2).

It is important to note that at the lower edge of the density range for axisymmetric instability, $\rho_{crit}^{C,J=0}$, the timescale of C+C pycnonuclear reactions are $\tau_{pyc}^{C+C} \approx 339 \text{ yr}$ (see Fig. 4.1). It becomes then of interest to compare this timescale with the corresponding one of the secular axisymmetric instability that sets in at the same density.

The growing time of the secular instability is given by the dissipation time that can be

driven either by gravitational radiation or viscosity [56]. However, gravitational radiation reaction is expected to drive secular instabilities for systems with rotational to gravitational energy ratio $T/|W| \sim 0.14$, the bifurcation point between McClaurin spheroids and Jacobi ellipsoids (see [56] for details). Therefore, we expect gravitational radiation to become important only for differentially rotating WDs, which can attain more mass and more angular momentum [176]. In the present case of general relativistic uniformly RWDs, only the viscosity timescale τ_v is relevant. A rotating star that becomes secularly unstable first evolve with a characteristic time τ_v and eventually reach a point of dynamical instability, thus collapsing within a time $\tau_{dyn} \approx \Omega_K^{-1} \sim \sqrt{R^3/GM} \lesssim 1$ s, where R is the radius of the star (see e.g. [246]).

The viscosity timescale can be estimated as $\tau_v = R^2 \rho / \eta$ (see e.g. [149]), where ρ and η are the density and viscosity of the star. The viscosity of a WD assuming degenerate relativistic electrons is given by [72]

$$\eta_{fluid} = 4.74 \times 10^{-2} \frac{H_\Gamma(Z)}{Z} \rho^{5/3} \left[\left(\frac{\rho}{2 \times 10^6} \right)^{2/3} + 1 \right]^{-1}, \quad (4.7)$$

where $H_\Gamma(Z)$ is a slowly varying dimensionless constant that depends on the atomic number Z and the Coulomb to thermal energy ratio

$$\Gamma = \frac{e^2 Z^2}{k_B T} \left(\frac{4\pi}{3} \frac{\rho}{2ZMu} \right)^{1/3}, \quad (4.8)$$

where k_B is the Boltzmann constant and $A \simeq 2Z$ has been used.

The expression (4.7) is valid for values of Γ smaller than the critical value for crystallization Γ_{cry} . The critical Γ_{cry} is not well constrained but its value should be of the order of $\Gamma_{cry} \sim 100$ (see e.g. [72, 235]). The critical value Γ_{cry} defines a crystallization temperature T_{cry} under which the system behaves as a solid. For $\Gamma_{cry} \sim 100$, we have $T_{cry} \approx 8 \times 10^7 [\rho / (10^{10} \text{ g cm}^{-3})]^{1/3}$ K, for $Z = 6$. When Γ approaches Γ_{cry} the viscosity can increase drastically to values close to [265, 72]

$$\eta_{cry} = 4.0 \times 10^{-2} \left(\frac{Z}{7} \right)^{2/3} \rho^{5/6} \exp[0.1(\Gamma - \Gamma_{cry})]. \quad (4.9)$$

For instance, we find that at densities $\rho_{crit}^{C,J=0}$ and assuming a central temperature $T \gtrsim 0.5 T_{cry}$ with $T_{cry} \approx 10^8$ K, the viscous timescale is in the range $10 \lesssim \tau_v \lesssim 1000$ Myr, where the upper limit is obtained using Eq. (4.7) and the lower limit with Eq. (4.9). These timescales are longer than the pycnonuclear reaction timescale $\tau_{pyc}^{C+C} = 339$ yr at the same density. So, if the pycnonuclear reaction rates are accurate, it would imply that pycnonuclear reactions are more important to restrict the stability of RWDs with respect to the secular instability. However, we have to keep in mind that, as discussed in Sec. 4.3.4, the pycnonuclear critical densities are subjected to theoretical and experimental uncertainties, which could in principle shift them to higher values. For instance, a possible shift of the density for pycnonuclear instability with timescales $\tau_{pyc}^{C+C} \sim 1$ Myr to higher values $\rho_{pyc}^{C+C} > \rho_{crit}^{C,J=0}$, would suggest an interesting competition between secular and pycnonuclear instability in the density range $\rho_{crit}^{C,J=0} < \rho < \rho_\beta^C$.

4.8 Spin-up and spin-down evolution

It is known that at constant rest-mass M_0 , entropy S and chemical composition (Z, A) , the spin evolution of a RWD is given by (see [236] for details)

$$\dot{\Omega} = \frac{\dot{E}}{\Omega} \left(\frac{\partial \Omega}{\partial J} \right)_{M_0, S, Z, A}, \quad (4.10)$$

where $\dot{\Omega} \equiv d\Omega/dt$ and $\dot{E} \equiv dE/dt$, with E the energy of the star.

Thus, if a RWD is losing energy by some mechanism during its evolution, that is $\dot{E} < 0$, the change of the angular velocity Ω in time depends on the sign of $\partial\Omega/\partial J$; RWDs that evolve along a track with $\partial\Omega/\partial J > 0$, will spin-down ($\dot{\Omega} < 0$) and the ones following tracks with $\partial\Omega/\partial J < 0$ will spin-up ($\dot{\Omega} > 0$).

In Fig. 4.6 we show, in the left panel, the $\Omega = \text{constant}$ and $J = \text{constant}$ sequences in the mass-central density diagram and, in the right panel, contours of constant rest-mass in the $\Omega - J$ plane.

The sign of $\partial\Omega/\partial J$ can be analyzed from the left panel plot of Fig. 4.6 by joining two consecutive $J = \text{constant}$ sequences with an horizontal line and taking into account that J decreases from left to right and from up to down. The angular velocity Ω , instead, decreases from right to left and from up to down for SCWDs and, for sub-Chandrasekhar WDs, from left to right and from up to down. We note that, in the SCWDs region $\Omega = \text{constant}$ sequences satisfy $\partial\Omega/\partial\rho_c < 0$ while, in the sub-Chandrasekhar region, both $\partial\Omega/\partial\rho_c < 0$ and $\partial\Omega/\partial\rho_c > 0$ appear (see minima). SCWDs can only either spin-up by angular momentum loss or spin-down by gaining angular momentum. In the latter case, the RWD becomes decompressed with time increasing its radius and moment of inertia, and then SCWDs following this evolution track will end at the mass-shedding limit (see Fig. 4.6). Some evolutionary tracks of sub-Chandrasekhar WDs and SCWDs are shown in the right panel of Fig. 4.6. It is appropriate to recall here that [236] showed that spin-up behavior by angular momentum loss occurs for rapidly rotating Newtonian polytropes if the polytropic index is very close to $n = 3$, namely for an adiabatic index $\Gamma \approx 4/3$. It was shown explicitly by [92] that these conditions are achieved only by Super-Chandrasekhar polytropes.

Besides the confirmation of the above known result for SCWDs in the general relativistic case, we report here the presence of minima $\partial\Omega/\partial\rho_c = 0$ for some sub-Chandrasekhar masses (see e.g. the evolution track of the RWD with $M = 1.38M_\odot$ in the right panel of Fig. 4.6) which raises the possibility that sub-Chandrasekhar WDs can experience, by angular momentum loss, not only the intuitively spin-down evolution, but also spin-up epochs.

4.9 Astrophysical implications

It is appropriate to analyze the astrophysical consequences of the general relativistic RWDs presented in this work.

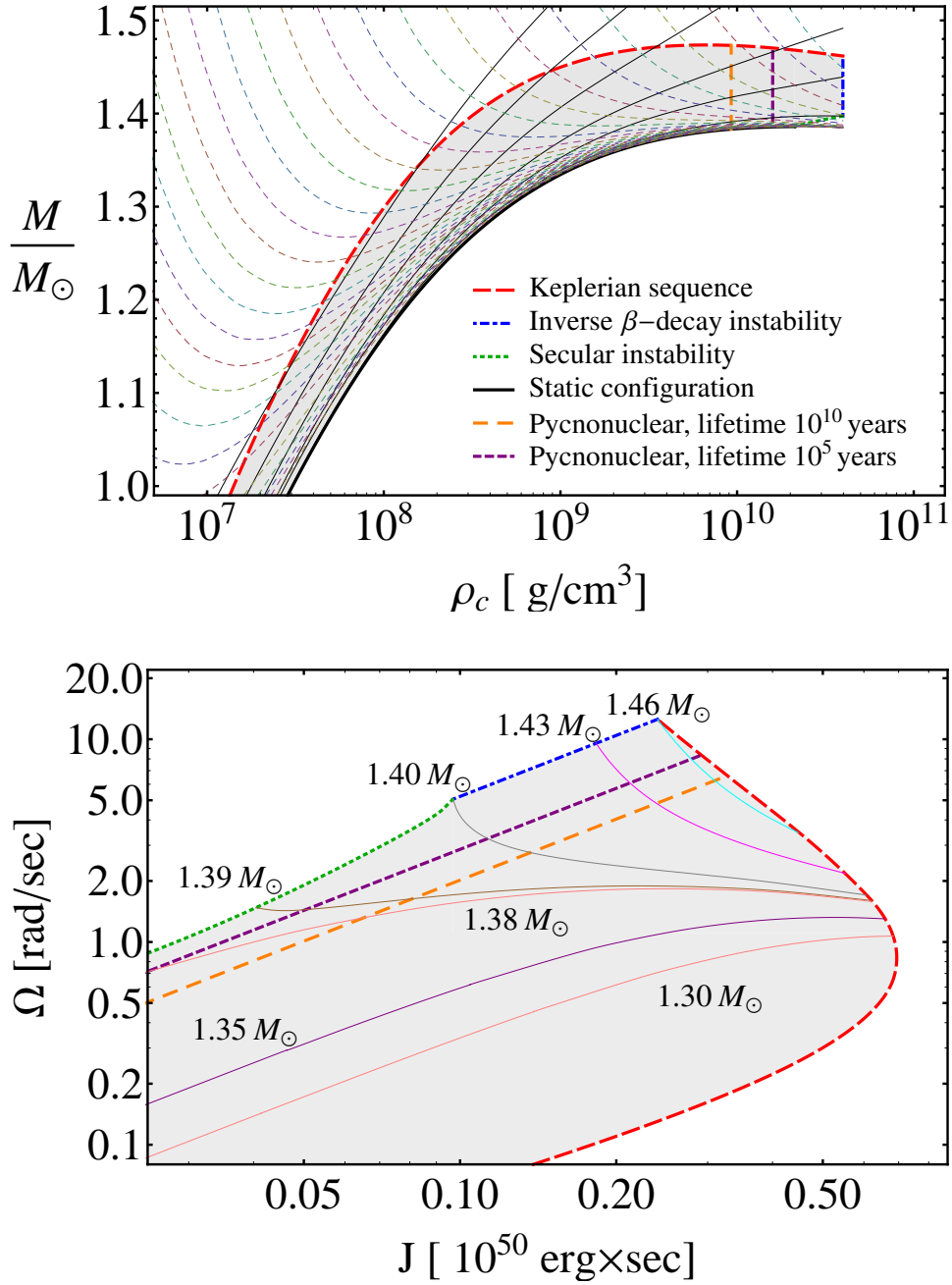


Figure 4.6: Top panel: mass versus the central density for ^{12}C RWDs. The solid black curves correspond to $J=\text{constant}$ sequences, where the static case $J = 0$ the thickest one. The color thin-dashed curves correspond to $\Omega=\text{constant}$ sequences. The Keplerian sequence is the red thick dashed curve, the blue thick dotted-dashed curve is the inverse β -decay instability boundary, and the green thick dotted curve is the axisymmetric secular instability boundary. Bottom panel: contours of constant rest-mass in the $\Omega - J$ plane; RWDs that evolve along a track with $\partial\Omega/\partial J > 0$ spin-down by losing angular momentum while, the ones with $\partial\Omega/\partial J < 0$, spin-up.

Most of the observed magnetic WDs are massive; for instance REJ 0317-853 with $M \sim 1.35M_\odot$ and $B \sim (1.7\text{--}6.6) \times 10^8$ G (see e.g. [14, 132]); PG 1658+441 with $M \sim 1.31M_\odot$ and $B \sim 2.3 \times 10^6$ G (see e.g. [148, 231]); and PG 1031+234 with the highest magnetic field $\sim 10^9$ G (see e.g. [232, 131]). However, they are generally found to be slow rotators (see e.g. [272]). It is worth mentioning that it has been recently shown by [87] that such a magnetic WDs can be indeed the result of the merger of double degenerate binaries; the misalignment of the final magnetic dipole moment of the newly born RWD with the rotation axis of the star depends on the difference of the masses of the WD components of the binary.

The precise computation of the evolution of the rotation period have to account for the actual value at each time of the moment of inertia and the equatorial and polar radii of the WD. Whether magnetic and gravitational radiation braking can explain or not the current relatively long rotation periods of some observed magnetic WDs is an important issue that deserves the appropriate attention and will be addressed elsewhere.

Magnetic braking of SCWDs has been recently invoked as a possible mechanism to explain the delayed time distribution of type Ia supernovae (SNe) (see [118] for details): a type Ia SN explosion is delayed for a time typical of the spin-down time scale τ_B due to magnetic braking, providing the result of the merging process of a WD binary system is a magnetic SCWD rather than a sub-Chandrasekhar one. The characteristic timescale τ_B of SCWD has been estimated to be $10^7 \lesssim \tau_B \lesssim 10^{10}$ yr for magnetic fields comprised in the range $10^6 \lesssim B \lesssim 10^8$ G. A constant moment of inertia $\sim 10^{49}$ g cm² and a fixed critical(maximum) rotation angular velocity

$$\Omega_{\text{crit}} \sim 0.7\Omega_K^{J=0} = 0.7\sqrt{\frac{GM^{J=0}}{R_{M^{J=0}}^3}}, \quad (4.11)$$

have been adopted [118].

It is important to recall here that, as discussed in Sec. 4.8, SCWDs spin-up by angular momentum loss, and therefore the reference to a “spin-down” time scale for them is just historical. SCWDs then evolve toward the mass-shedding limit, which determines in this case the critical angular velocity for rotational instability.

If we express $\Omega_K^{J \neq 0}$ in terms of $\Omega_K^{J=0}$ (see App. C.0.2), taking into account the values of j and q from the numerical integration, we find for RWDs

$$\Omega_K^{J \neq 0} = \sigma\Omega_K^{J=0}, \quad (4.12)$$

where the coefficient σ varies in the interval [0.78,0.75] in the range of central densities [$10^5, 10^{11}$] g cm⁻³. It is important to mention that the above range of σ hold approximately the same independently on the chemical composition of the WD. However, the actual numerical value of the critical angular velocity, $\Omega_K^{J \neq 0}$, is different for different compositions owing to the dependence on (Z, A) of mass-radius relation of non-rotating WDs.

Furthermore, as we have shown, the evolution track followed by a SCWD depends strongly on the initial conditions of mass and angular momentum as well as on chemical composition, and evolution of the moment of inertia (see Fig. 4.6 and Sec. 4.8 for details).

It is clear that the assumption of fixed moment of inertia $I \sim 10^{49}$ g cm², leads to a spin-down time scale depending only on the magnetic field strength. A detailed computation will lead to a strong dependence on the mass of the SCWD; resulting in a two-parameter family of delayed times $\tau_B(M, B)$. Detailed calculations of the lifetime of SCWDs braking-down due to magnetic dipole radiation are then needed to shed light on this important matter. Theoretical work along these lines is currently in progress and the results will be presented in a forthcoming publication.

Massive fast rotating and highly magnetized WDs have been proposed as an alternative scenario of Soft Gamma Ray Repeaters (SGRs) and Anomalous X-ray Pulsars (AXPs); see [154] for details. Within such scenario, the range of minimum rotation periods of massive WDs found in this work, $0.3 \lesssim P_{min} \lesssim 2.2$ seconds, depending on the nuclear composition (see Table 4.5), implies the rotational stability of SGRs and AXPs, which possess observed rotation periods $2 \lesssim P \lesssim 12$ seconds. The relatively long minimum period of ⁵⁶Fe RWDs ~ 2.2 seconds, implies that RWDs describing SGRs and AXPs have to be composed of nuclear compositions lighter than ⁵⁶Fe, e.g. ¹²C or ¹⁶O.

4.10 Conclusions

We have calculated the properties of uniformly RWDs within the framework of GR using the Hartle formalism and our new EOS for cold WD matter based on the relativistic Feynman-Metropolis-Teller treatment [210], which generalizes previous approaches including the EOS of [229]. A detailed comparison with RWDs described by the Chandrasekhar and the Salpeter EOS has been performed.

We constructed the region of stability of RWDs taking into account the mass-shedding limit, secular axisymmetric instability, inverse β -decay, and pycnonuclear reaction lifetimes. The latter have been computed using the updated theoretical models of [89, 274]. We found that the minimum rotation periods for ⁴He, ¹²C, ¹⁶O, and ⁵⁶Fe RWDs are ~ 0.3 , 0.5, 0.7 and 2.2 seconds, respectively (see Table 4.5). For ¹²C WDs, the minimum period 0.5 seconds needs to be compared with the values $P_{min}^{pyc} = 0.75$ and 0.95 seconds, obtained assuming as critical density the threshold for pycnonuclear reactions for lifetimes $\tau_{pyc}^{C+C} = 0.1$ Myr and 10 Gyr, respectively. For the same chemical compositions, the maximum masses are $\sim 1.500, 1.474, 1.467, 1.202 M_{\odot}$ (see Table 4.4). These results and additional properties of RWDs can be found in Table 4.3.

We have presented a new instability boundary of general relativistic SCWDs, over which they become axisymmetrically unstable. We have expressed the range of masses and rotation periods where this occurs through a fitting formula given by Eq. (4.6). A comparison with Newtonian RWDs in App. C.2 show to the conclusion that this new boundary of instability for uniformly rotating WDs is a general relativistic effect.

We showed that, by losing angular momentum, sub-Chandrasekhar RWDs can experience both spin-up and spin-down epochs while, SCWDs, can only spin-up. These results are particularly important for the evolution of WDs whose masses approach, either from above or from below, the maximum non-rotating mass. The knowledge of the actual

values of the mass, radii, and moment of inertia of massive RWDs are relevant for the computation of delay collapse times in the models of type Ia SN explosions. A careful analysis of all the possible instability boundaries as the one presented here have to be taken into account during the evolution of the WD at pre-SN stages.

We have indicated specific astrophysical systems where the results of this work are relevant; for instance the long rotation periods of observed massive magnetic WDs; the delayed collapse of SCWDs as progenitors of type Ia SNe; and the alternative scenario for SGRs and AXPs based on massive RWDs.

4.11 Perspectives

Recently magnetic braking of SCWDs has been invoked as a possible mechanism to explain the delayed time distribution of type Ia supernovae (SNe) (see [118] for details): a type Ia SN explosion is delayed for a time typical of the spin-down time scale t due to magnetic braking, providing that the result of the merging process of a WD binary system is a magnetic SCWD rather than a sub-Chandrasekhar one. The characteristic timescale t of SCWD has been estimated to be $10^7 \lesssim t \lesssim 10^{10}$ yr for magnetic fields comprised in the range $10^6 \lesssim B \lesssim 10^8$ G. We have performed similar computations to estimate the characteristic timescale for the realistic EoS of white dwarfs presented in [209] relaxing the constancy of the moment of inertia, the radius and other parameters of WDs. Indeed we have shown here that all parameters are the functions of the central density and rotation period. Hence we performed more refined analyses, that can be seen from Fig. 4.7, taking into consideration all the stability criteria. The details will be addressed in our forthcoming works.

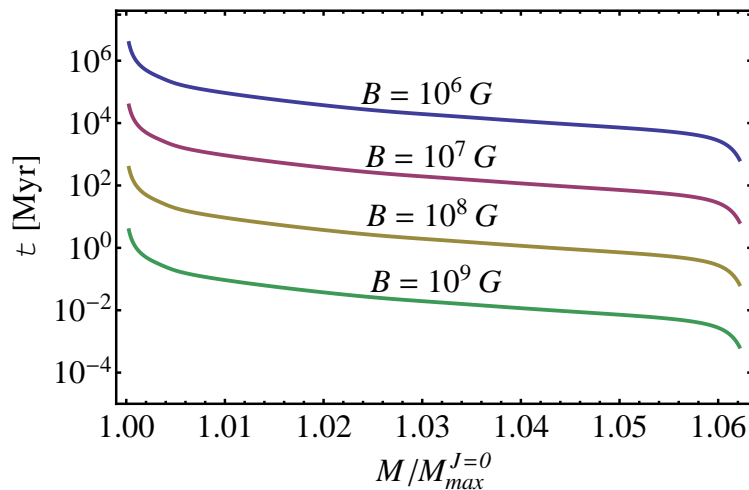


Figure 4.7: The characteristic t (life time, in Myr) versus WD mass in units of $M_{max}^{J=0}$ for ^{12}C RWDs. The magnetic field B is in Gauss.

Chapter 5

SGRs and AXPs as fast rotating white dwarfs

5.1 Introduction

Soft Gamma Ray Repeaters (SGRs) and Anomalous X-ray Pulsars (AXPs) are a class of compact objects that show interesting observational properties (see e.g. [163]): rotational periods in the range $P \sim (2\text{--}12)$ s, a narrow range with respect to the wide range of ordinary pulsars $P \sim (0.001\text{--}10)$ s; spin-down rates $\dot{P} \sim (10^{-13}\text{--}10^{-10})$, larger than ordinary pulsars $\dot{P} \sim 10^{-15}$; strong outburst of energies $\sim (10^{41}\text{--}10^{43})$ erg, and for the case of SGRs, giant flares of even large energies $\sim (10^{44}\text{--}10^{47})$ erg, not observed in ordinary pulsars.

The observation of SGR 0418+5729 with a rotational period of $P = 9.08$ s, an upper limit of the first time derivative of the rotational period $\dot{P} < 6.0 \times 10^{-15}$ [200], and an X-ray luminosity of $L_X = 6.2 \times 10^{31}$ erg s $^{-1}$ can be considered as the Rosetta Stone for alternative models of SGRs and AXPs.

The magnetar model, based on a neutron star of fiducial parameters $M = 1.4M_\odot$, $R = 10$ km and a moment of inertia $I = 10^{45}$ g cm 2 , needs a magnetic field larger than the critical field for vacuum polarization $B_c = m_e^2 c^3 / (e \hbar) = 4.4 \times 10^{13}$ G in order to explain the observed X-ray luminosity in terms of the release of magnetic energy (see [70, 255] for details). The inferred upper limit of the surface magnetic field of SGR 0418+5729 $B < 7.5 \times 10^{12}$ G describing it as a neutron star (see [200] for details), is well below the critical field, which has challenged the power mechanism based on magnetic field decay in the magnetar scenario.

Alternatively, it has been recently pointed out how the pioneering works of [167] and [181] on the description of 1E 2259+586 as a white dwarf (WD) can be indeed extended to all SGRs and AXPs. These WDs were assumed to have fiducial parameters $M = 1.4M_\odot$, $R = 10^3$ km, $I = 10^{49}$ g cm 2 , and magnetic fields $B \gtrsim 10^7$ G (see [154] for details) inferred from the observed rotation periods and spin-down rates.

The energetics of SGRs and AXPs including their steady emission, glitches, and their subsequent outburst activities have been shown to be powered by the rotational energy of

the WD [154]. The occurrence of a glitch, the associated sudden shortening of the period, as well as the corresponding gain of rotational energy, can be explained by the release of gravitational energy associated with a sudden contraction and decrease of the moment of inertia of the uniformly rotating WD, consistent with the conservation of their angular momentum.

By describing SGR 0418+5729 as a WD, [154] calculated an upper limit for the magnetic field $B < 7.5 \times 10^8$ G and show that the X-ray luminosity observed from SGR 0418+5729 can be well explained as originating from the loss of rotational energy of the WD leading to a theoretical prediction for the spin-down rate

$$\frac{L_X P^3}{4\pi^2 I} = 1.18 \times 10^{-16} \leq \dot{P}_{\text{SGR0418+5729}} < 6.0 \times 10^{-15}, \quad (5.1)$$

where the lower limit was established by assuming that the observed X-ray luminosity of SGR 0418+5729 coincides with the rotational energy loss of the WD. As we will show below, these predictions can be still improved by considering realistic WD parameters [45] instead of fiducial ones.

The situation has become even more striking considering the recent X-ray timing monitoring with Swift, RXTE, Suzaku, and XMM-Newton satellites of the recently discovered SGR Swift J1822.3–1606 [201]. The rotation period $P = 8.437$ s, and the spin-down rate $\dot{P} = 9.1 \times 10^{-14}$ have been obtained. Assuming a NS of fiducial parameters, a magnetic field $B = 2.8 \times 10^{13}$ G is inferred, which is again in contradiction with a magnetar explanation for this source.

We have recently computed in [45] general relativistic configurations of uniformly rotating white dwarfs within Hartle’s formalism [105]. We have used the relativistic Feynman-Metropolis-Teller equation of state [210] for WD matter, which we have shown generalizes the traditionally used equation of state of [229]. It has been there shown that rotating WDs can be stable up to rotation periods of ~ 0.28 s (see [45] and Sec. 5.3 for details). This range of stable rotation periods for WDs amply covers the observed rotation rates of SGRs and AXPs $P \sim (2\text{--}12)$ s.

The aim of this work is to describe the so-called *low magnetic field magnetars*, SGR 0418+5729 and Swift J1822.3-1606, as massive fast rotating highly magnetized WDs. In doing so we extend the work of [154] by using precise WD parameters recently obtained by [45] for general relativistic uniformly rotating WDs. It is also performed an analysis of the expected Optical and near-Infrared emission from these sources within the WD model and confront the results with the observational data.

5.2 Rotation powered white dwarfs

The loss of rotational energy associated with the spin-down of the WD is given by

$$\dot{E}_{\text{rot}} = -4\pi^2 I \frac{\dot{P}}{P^3} = -3.95 \times 10^{50} I_{49} \frac{\dot{P}}{P^3} \text{ ergs}^{-1}, \quad (5.2)$$

where I_{49} is the moment of inertia of the WD in units of 10^{49} g cm². This rotational energy loss amply justifies the steady X-ray emission of all SGRs and AXPs (see [154] for details).

The upper limit on the magnetic field (see e.g. [77]) obtained by requesting that the rotational energy loss due to the dipole field be smaller than the electromagnetic emission of the magnetic dipole, is given by

$$B = \left(\frac{3c^3}{8\pi^2} \frac{I}{\bar{R}^6} P \dot{P} \right)^{1/2} = 3.2 \times 10^{15} \left(\frac{I_{49}}{\bar{R}_8^6} P \dot{P} \right)^{1/2} \text{ G}, \quad (5.3)$$

where \bar{R}_8 is the mean radius of the WD in units of 10^8 cm. The mean radius is given by $\bar{R} = (2R_{eq} + R_p)/3$ (see e.g. [108]) with R_{eq} and R_p the equatorial and polar radius of the star.

It is clear that the specific values of the rotational energy loss and the magnetic field depend on observed parameters, such as P and \dot{P} , as well as on model parameters, such as the mass, moment of inertia, and mean radius of the rotating WD.

5.3 Structure and stability of rotating white dwarfs

The rotational stability of fast rotating WDs was implicitly assumed by [154]. The crucial question of whether rotating WDs can or not attain rotation periods as short as the ones observed in SGRs and AXPs has been recently addressed by [45]. The properties of uniformly rotating WDs were computed within the framework of general relativity through Hartle's formalism [105]. The equation of state for cold WD matter is based on the relativistic Feynman-Metropolis-Teller treatment [210], which generalizes the equation of state of [229]. The stability of rotating WDs was analyzed taking into account the mass-shedding limit, inverse β -decay instability, and secular axisymmetric instability, with the latter determined by the turning point method of [84]; see Fig. 5.1 and [45], for details.

The minimum rotation period P_{min} of WDs is obtained for a configuration rotating at Keplerian angular velocity, at the critical inverse β -decay density, namely this is the configuration lying at the crossing point between the mass-shedding and inverse β -decay boundaries. The numerical values of the minimum rotation period $P_{min} \approx (0.3, 0.5, 0.7, 2.2)$ s and the maximum masses were found for Helium (He), Carbon (C), Oxygen (O), and Iron (Fe) WDs, respectively (see Table 5.1 and [45], for details). As a byproduct, these values show that indeed all SGRs and AXPs can be described as rotating WDs because their rotation periods are in the range $2 \lesssim P \lesssim 12$ s.

The relatively long minimum period of rotating Fe WDs, ~ 2.2 s, lying just at the lower edge of the observed range of rotation periods of SGRs and AXPs, reveals crucial information on the chemical composition of SGRs and AXPs, namely they are very likely made of elements lighter than Fe, such as C or O.

It can be seen from Fig. 5.1 that every Ω =constant sequence intersects the stability region of general relativistic uniformly rotating WDs (M - R_{eq} curves inside the shaded region of Fig. 5.1) in two points. These two points determine the minimum(maximum)

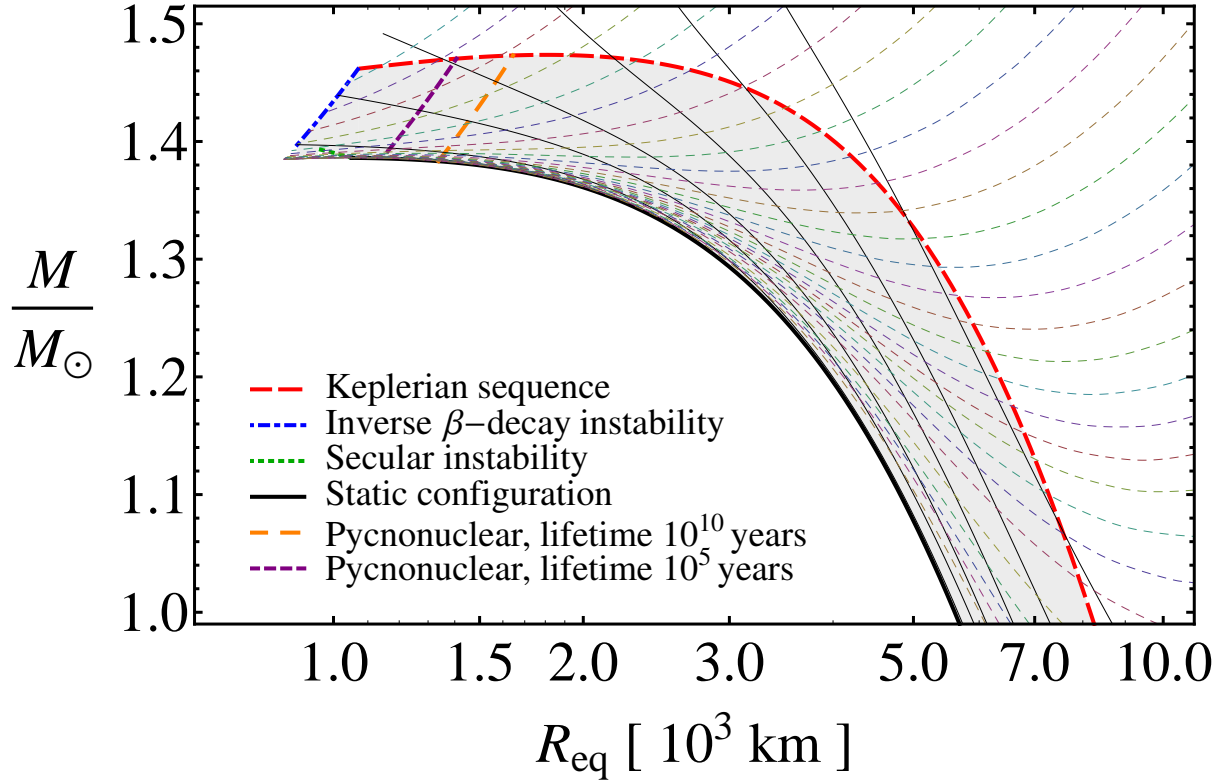


Figure 5.1: Mass versus equatorial radius of rotating Carbon WDs. The solid black curves correspond to J -constant sequences, where the static case $J = 0$ the thickest one. The color thin-dashed curves correspond to Ω -constant sequences. The Keplerian sequence is the red thick dashed curve, the blue thick dotted-dashed curve is the inverse β instability boundary, and the green thick dotted curve is the axisymmetric instability line. The gray-shaded region is the stability region of rotating white dwarfs [45].

Composition	P_{min} (s)	M_{max}/M_{\odot}
Helium	0.3	1.500
Carbon	0.5	1.474
Oxygen	0.7	1.467
Iron	2.2	1.202

Table 5.1: Minimum rotation period and maximum mass of general relativistic uniformly rotating WDs (see [45], for details).

Comp.	M_{min}	M_{max}	R_{eq}^{min}	R_{eq}^{max}	\bar{R}_{min}	\bar{R}_{max}	I_{48}^{min}	I_{50}^{max}	$B_{min}(10^7\text{G})$	$B_{max}(10^8\text{G})$
He	1.18	1.41	1.16	6.88	1.15	6.24	3.59	1.48	1.18	2.90
C	1.15	1.39	1.05	6.82	1.05	6.18	2.86	1.42	1.19	3.49
O	1.14	1.38	1.08	6.80	1.08	6.15	3.05	1.96	1.42	3.30
Fe	0.92	1.11	2.21	6.36	2.21	5.75	12.9	1.01	1.25	0.80

Table 5.2: Bounds for the mass M (in units of M_\odot), equatorial R_{eq} and mean \bar{R} radius (in units of 10^8 cm), moment of inertia I , and surface magnetic field B of SGR 0418+5729. I_{48} and I_{50} is the moment of inertia in units of 10^{48} and 10^{50} g cm², respectively.

and maximum(minimum) $M_{min,max}(R_{eq}^{max,min})$, respectively, for the stability of a WD with the given rotation angular velocity $\Omega = 2\pi/P$. Associated to the boundary values $M_{min,max}$ and $R_{eq}^{max,min}$, we can obtain the corresponding bounds for the moment of inertia of the WD, $I_{max,min}$, respectively.

We turn now to a specific analysis to each of the two sources SGR 0418+5729 and SGR 1822–1606.

5.4 SGR 0418+5729

5.4.1 Bounds on the WD parameters

SGR 0418+5729 has a rotational period of $P = 9.08$ s, and the upper limit of the spin-down rate $\dot{P} < 6.0 \times 10^{-15}$ was obtained by [200]. The corresponding rotation angular velocity of the source is $\Omega = 2\pi/P = 0.69$ rad s⁻¹. We show in Table 5.2 bounds for the mass, equatorial radius, mean radius, and moment of inertia of SGR 0418+5729 obtained by the request of the rotational stability of the rotating WD, as described in Section 5.4, for selected chemical compositions. Hereafter we shall consider general relativistic rotating Carbon WDs.

5.4.2 Solidification and glitches

It has been shown by [154] that the massive WDs consistent with SGRs and AXPs possibly behave as solids since the internal temperature of the WD ($\sim 10^7$) is very likely lower than the crystallization temperature (see e.g. [235, 264])

$$T_{\text{cry}} \simeq 2.28 \times 10^5 \frac{Z^2}{A^{1/3}} \left(\frac{\bar{\rho}}{10^6 \text{g/cm}^3} \right)^{1/3} \text{ K}, \quad (5.4)$$

where (Z, A) and $\bar{\rho}$ denote the chemical composition and mean density, respectively.

This fact introduces the possibility in the WD to observe sudden changes in the period of rotation, namely glitches. The expected theoretical values of the fractional change of periods of massive WDs have been shown to be consistent with the values observed in many SGRs and AXPs (see [154] for details).

From the bounds of M and R_{eq} we obtain that the mean density of SGR 0418+5729 must be in the range $1.72 \times 10^6 \lesssim \bar{\rho} \lesssim 5.70 \times 10^8$ g cm³. Correspondingly, the crystalliza-

tion temperature is comprised in the range $4.3 \times 10^6 \text{ K} \lesssim T_{\text{cry}} \lesssim 2.97 \times 10^7 \text{ K}$, where the lower and upper limits correspond to the configuration of minimum and maximum mass configurations, respectively.

The crystallization temperature obtained here indicates that SGR 0418+5729 should behave as a rigid solid body and therefore glitches during the rotational energy loss, accompanied by radiative events, are expected. Starquakes leading to glitches in the WD may occur with a recurrence time (see e.g. [16, 264, 154])

$$\delta t_q = \frac{2D^2}{B} \frac{|\Delta P|/P}{|\dot{E}_{\text{rot}}|}, \quad (5.5)$$

where \dot{E}_{rot} is the loss of rotational energy (5.2), $D = (3/25) GM_c^2/R_c$,

$B = 0.33 (4\pi/3) R_c^3 e^2 Z^2 [\bar{\rho}_c / (A m_p)]^{4/3}$, M_c , R_c and $\bar{\rho}_c$ are the mass, the radius and the mean density of the solid core, and m_p is the proton mass.

For the minimum and maximum mass configurations and the upper limit of the spin-down rate $\dot{P} < 6 \times 10^{-15}$, we obtain a lower limit for recurrence time of starquakes

$$\delta t_q > \begin{cases} 4 \times 10^9 (|\Delta P|/P) \text{ yr}, & M = M_{\text{min}} \\ 2 \times 10^{12} (|\Delta P|/P) \text{ yr}, & M = M_{\text{max}} \end{cases}, \quad (5.6)$$

which for a typical fractional change of period $|\Delta P|/P \sim 10^{-6}$ observed in SGRs and AXPs we obtain $\delta t_q > 4 \times 10^3 \text{ yr}$ and $\delta t_q > 2 \times 10^6 \text{ yr}$, for M_{min} and M_{max} respectively. These very long starquake recurrent times are in agreement with the possibility that SGR 0418+5729 is an old WD whose magnetospheric activity is settling down, in agreement with its relatively low spin-down rate, magnetic field, and high efficiency parameter L_X/\dot{E}_{rot} , with respect to the values of other SGRs and AXPs (see e.g. Fig. 9 in [154]).

5.4.3 Rotation power and magnetic field

Introducing the values of P and the upper limit \dot{P} into Eq. (5.2) we obtain an upper limit for the rotational energy loss

$$\dot{E}_{\text{rot}} < \begin{cases} -9.05 \times 10^{32} \text{ erg s}^{-1}, & M = M_{\text{max}} \\ -4.49 \times 10^{34} \text{ erg s}^{-1}, & M = M_{\text{min}} \end{cases}, \quad (5.7)$$

which for any possible mass is larger than the observed X-ray luminosity of SGR 0418+5729, $L_X = 6.2 \times 10^{31} \text{ erg s}^{-1}$, assuming a distance of 2 kpc [200].

The corresponding upper limits on the surface magnetic field of SGR 0418+5729, obtained from Eq. (5.3) are (see also Table 5.2)

$$B < \begin{cases} 1.19 \times 10^7 \text{ G}, & M = M_{\text{min}} \\ 3.49 \times 10^8 \text{ G}, & M = M_{\text{max}} \end{cases}. \quad (5.8)$$

It is worth noting that the above maximum possible value of the surface magnetic field of SGR 0418+5729 obtained for the maximum possible mass of a WD with rotation period 9.08 s, $B < 3.49 \times 10^8$ G, is even more stringent and improves the previously value given by [154], $B < 7.5 \times 10^8$ G, based on fiducial WD parameters.

The electron cyclotron frequency expected from such a magnetic field is

$$f_{cyc,e} = \frac{eB}{2\pi m_e c} = \begin{cases} 3.33 \times 10^{13} & \text{Hz, } M = M_{min} \\ 9.76 \times 10^{14} & \text{Hz, } M = M_{max} \end{cases}, \quad (5.9)$$

corresponding to wavelengths 9.04 and 0.31 μm , respectively.

5.4.4 Prediction of the spin-down rate

Assuming that the observed X-ray luminosity of SGR 0418+5729 equals the rotational energy loss \dot{E}_{rot} , we obtain the lower limit for the spin-down rate

$$\dot{P} > \frac{L_X P^3}{4\pi^2 I} = \begin{cases} 8.28 \times 10^{-18}, & M = M_{min} \\ 4.11 \times 10^{-16}, & M = M_{max} \end{cases}, \quad (5.10)$$

which in the case of the WD with the maximum possible mass is more stringent than the value reported by [154], $\dot{P} = 1.18 \times 10^{-16}$, for a massive WD of fiducial parameters.

5.4.5 Optical spectrum and luminosity

[71] observed SGR 0418+5729 with the two wide filters F606W and F110W of the Hubble Space Telescope, and derive the upper limits of the apparent magnitudes, $m_{F606W} > 28.6$ and $m_{F110W} > 27.4$ (Vega system), within the positional error circle derived from Chandra observations of the field of SGR 0418+5729 [200]. The approximate distance to the source is $d = 2$ kpc (see [71] for details). Assuming an interstellar extinction obtained from the N_H column absorption value observed in the X-ray data, $A_V = 0.7$, [71] obtained the corresponding luminosity upper bounds $L_{F606W} < 5 \times 10^{28}$ erg s⁻¹ and $L_{F110W} < 6 \times 10^{28}$ erg s⁻¹, respectively.

We use here a similar technique, i.e. computing the interstellar extinction values for the V band from the N_H column absorption value observed in the X-ray data, $N_H = 1.5 \times 10^{21} \text{cm}^{-2}$ [200], and then using the empirical formula described in [192]. Then we have extrapolated the extinction to the other filters by using the method delineated in [51]. Since the F606W and the F110W are well approximated by the V and J band, we obtained for the extinction values $A_{F606W} = 0.83$ and $A_{F110W} = 0.235$ respectively. The corresponding luminosity upper bounds are, consequently, $L_{F606W} < 6.82 \times 10^{28}$ erg s⁻¹ and $L_{F110W} < 3.05 \times 10^{28}$ erg s⁻¹.

An estimate of the effective surface temperature can be obtained by approximating the spectral luminosity in these bands by the black body luminosity

$$L = 4\pi R^2 \sigma T^4, \quad (5.11)$$

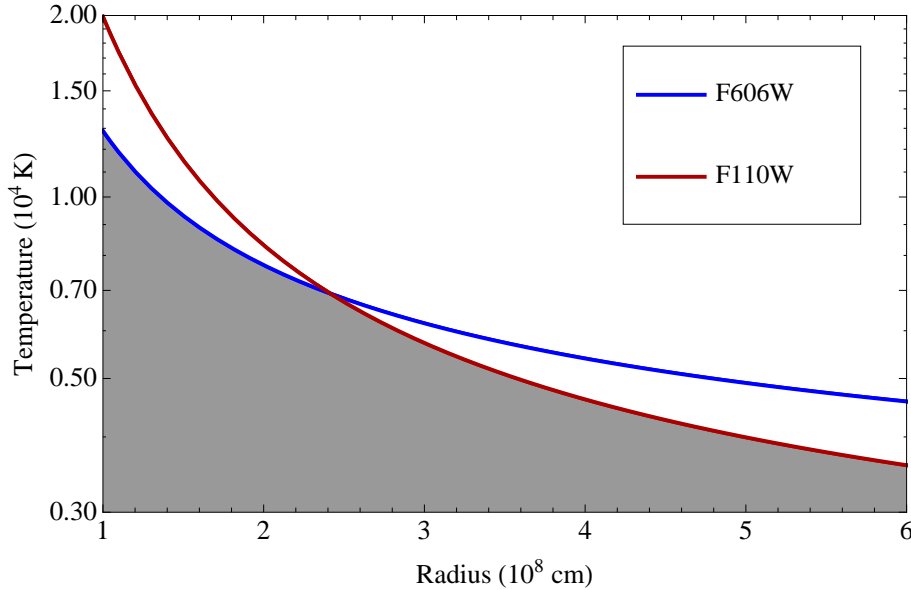


Figure 5.2: Temperature-Radius constraint given by Eq. (5.16). The gray region corresponds to the possible values for the temperature and the radius of the WD. The range of radii correspond to the one defined by the minimum and maximum radius of SGR 0418+5729 inferred from the WD stability analysis and summarized in Table 5.2, namely $R_{min} \leq R \leq R_{max}$.

where $\sigma = 5.67 \times 10^{-5} \text{ erg cm}^{-2} \text{ s}^{-1} \text{ K}^{-4}$ is the Stefan-Boltzmann constant. For a WD of fiducial radius $R = 10^8 \text{ cm}$, the upper limits for the WD surface temperature, $T < 9.58 \times 10^3 \text{ K}$ and $T < 9.15 \times 10^3 \text{ K}$, can be obtained for the F110W and F606W filters, replacing the upper limits for L_{F110W} and L_{F606W} in Eq. (5.11).

The above bounds of the surface temperature of the WD can be improved by using the explicit dependence on the radius of the black body surface temperature for each filter. The black body flux at a given frequency ν , in the source frame, is given by

$$\nu f_\nu = \pi \frac{2h}{c^2} \frac{\nu^4}{\exp[h\nu/(kT)] - 1}, \quad (5.12)$$

where h , k , and ν are the Planck constant, the Boltzmann constant, and the spectral frequency respectively. From this expression we can obtain the temperature as a function of the frequency, the observed flux, the distance d and radius R of the black body source

$$T = \frac{h\nu}{k \ln \left(1 + \frac{\pi 2h\nu^4 R^2}{c^2 d^2 F_{\nu, \text{obs}}} \right)}, \quad (5.13)$$

where we have used the relation between the flux in the observed and source frames, $F_{\nu, \text{obs}} = (R/d)^2 \nu f_\nu$.

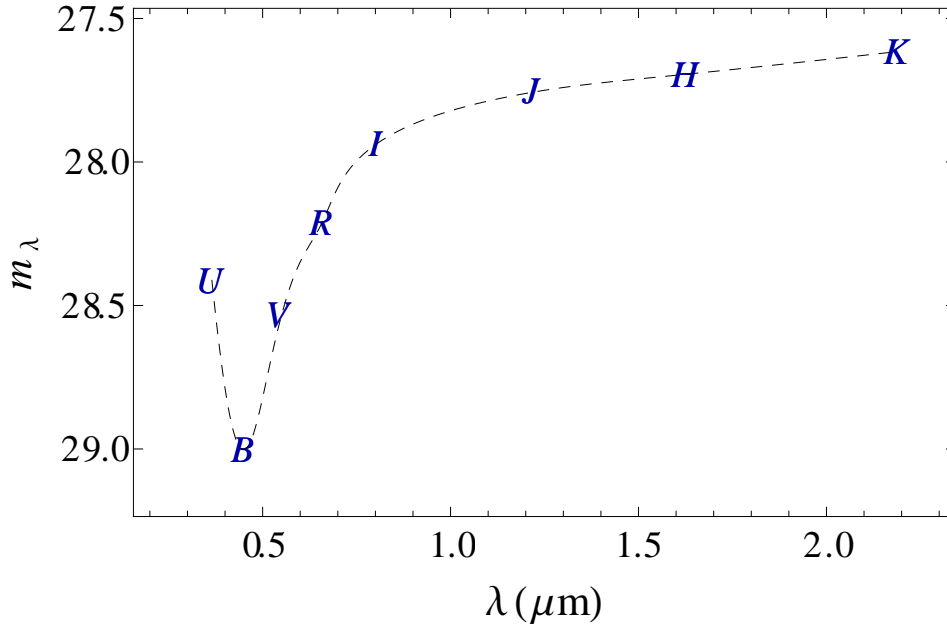


Figure 5.3: Expected optical magnitudes for the progenitor WD of SGR 0418+5729 obtained assuming a simple blackbody for the spectral emission from a WD with surface temperature $T = 10^4$ K and a radius of 1.5×10^8 cm, according to the constraints shown in Fig. 5.2.

The observed fluxes, in units of $\text{erg}, \text{cm}^{-2}, \text{s}^{-1}$, corrected for the extinction are given by

$$F_{\nu, \text{obs}}^{F606W} = 3.6 \times 10^{-20} \nu_{F606W} \times 10^{0.4(m_{F606W} - A_{F606W})}, \quad (5.14)$$

and

$$F_{\nu, \text{obs}}^{F110W} = 1.8 \times 10^{-20} \nu_{F110W} \times 10^{0.4(m_{F110W} - A_{F110W})}, \quad (5.15)$$

where $\nu_{F606W} = 5.07 \times 10^{14}$ Hz and $\nu_{F110W} = 2.60 \times 10^{14}$ Hz.

Introducing the upper limits of the apparent magnitudes of [71] with the extinction values computed in this work, Eq. (5.13) gives the upper bounds on the temperature

$$T < \begin{cases} \frac{1.25 \times 10^4}{\ln(1 + 0.44 R_8^2)} & \text{K, F110W} \\ \frac{2.43 \times 10^4}{\ln(1 + 6.35 R_8^2)} & \text{K, F606W} \end{cases}, \quad (5.16)$$

where R_8^2 is the radius of the WD in units of 10^8 cm and, following [71], we have approximated the band integrated flux as $\nu_c F_\nu$, with ν_c the pivot wavelength of the corresponding band filter.

In Fig. 5.2, we show the constraints on the T - R relation obtained from Eq. (5.16). We have used the range of radii defined by the minimum and maximum radius of SGR 0418+5729 inferred from the WD stability analysis and summarized in Table 5.2. It is clear that the optical observational constraints are in agreement with a model based on a massive fast rotating highly magnetic WD for SGR 0418+5729. It is appropriate

to recall in this respect the observed range of temperatures of massive isolated WDs $1.14 \times 10^4 \text{ K} \leq T \leq 5.52 \times 10^4 \text{ K}$; see Table 1 in [78].

[154] obtained for a WD of fiducial parameters the upper limits for the WD surface temperature, $T < 3.14 \times 10^4$. We now improve these bounds on the surface temperature using realistic WD parameters. From the minimum and maximum values we have obtained for the equatorial radius of SGR 0418+5729 (see Table 5.2) we obtain for the F110W filter

$$T_{F110W} < \begin{cases} 3.94 \times 10^3 & \text{K, } M = M_{min} \\ 2.90 \times 10^4 & \text{K, } M = M_{max} \end{cases}, \quad (5.17)$$

and for the F606W filter

$$T_{F606W} < \begin{cases} 4.22 \times 10^3 & \text{K, } M = M_{min} \\ 1.13 \times 10^4 & \text{K, } M = M_{max} \end{cases}. \quad (5.18)$$

These values are in agreement with a WD description of SGR 0418+5729. In this respect it is worth recalling the optical observations of 4U 0142+61 of [116] where the photometric results of the field of 4U 0142+61 at the 60-inch telescope on Palomar Mountain were found to be in agreement with a $1.3M_{\odot}$ WD with a surface temperature $\sim 4 \times 10^5$ K (see [116] for details).

We show in Fig. 5.3 the expected optical magnitudes of a WD with surface temperature $T = 10^4$ K and radius $R = 1.5 \times 10^8$ cm, located at a distance of 2 kpc. This radius corresponds to the upper limit given by the gray region shown in Fig. 5.2, for this specific value of the temperature.

5.5 Swift J1822.3–1606

5.5.1 Bounds of the WD parameters

Swift J1822.3–1606 (or SGR 1822–1606) was recently discovered in July 2011 by Swift Burst Alert Telescope (BAT). A recent X-ray timing monitoring with Swift, RXTE, Suzaku, and XMM-Newton satellites found that SGR 1822-1606 rotates with a period of $P = 8.44$ s and slows down at a rate $\dot{P} = 9.1 \times 10^{-14}$ (see [201] for details). The corresponding rotation angular velocity of the source is $\Omega = 2\pi/P = 0.74 \text{ rad s}^{-1}$. Bounds for the mass, equatorial radius, and moment of inertia of SGR 0418+5729 obtained by the request of the rotational stability of the rotating WD, as described in Section 5.4, are shown in Table 5.2.

5.5.2 Solidification and glitches

The mean density of SGR 1822–1606 is in the range $1.98 \times 10^6 \lesssim \bar{\rho} \lesssim 5.70 \times 10^8 \text{ g cm}^3$. The crystallization temperature for such a range following Eq. (5.4) is then in the range $4.51 \times 10^6 \text{ K} \lesssim T_{\text{cry}} \lesssim 2.97 \times 10^7 \text{ K}$, which indicates that SGR 1822-1606 will likely behave as a rigid solid body.

Comp.	M_{min}	M_{max}	R_{eq}^{min}	R_{eq}^{max}	\bar{R}_{min}	\bar{R}_{max}	I_{48}^{min}	I_{50}^{max}	$B_{min}(10^7 \text{G})$	$B_{max}(10^9 \text{G})$
He	1.21	1.41	1.16	6.61	1.15	5.99	3.59	1.38	4.84	1.09
C	1.17	1.39	1.05	6.55	1.05	5.93	2.86	1.32	4.87	1.31
O	1.16	1.38	1.08	6.53	1.08	5.91	3.05	1.83	5.80	1.24
Fe	0.95	1.11	2.21	6.11	2.20	5.53	12.9	0.94	5.09	0.30

Table 5.3: Bounds for the mass M (in units of M_\odot), equatorial R_{eq} and mean \bar{R} radius (in units of 10^8 cm), moment of inertia I , and surface magnetic field B of Swift J1822.3–1606. I_{48} and I_{50} is the moment of inertia in units of 10^{48} and 10^{50} g cm², respectively.

For the minimum and maximum mass configurations and the spin-down rate $\dot{P} = 9.1 \times 10^{-14}$, we obtain a lower limit for recurrence time of starquakes

$$\delta t_q > \begin{cases} 2 \times 10^8 (|\Delta P|/P) \text{ yr}, & M = M_{min} \\ 1 \times 10^{11} (|\Delta P|/P) \text{ yr}, & M = M_{max} \end{cases}, \quad (5.19)$$

which for a typical fractional change of period $|\Delta P|/P \sim 10^{-6}$ gives $\delta t_q > 2 \times 10^2$ yr and $\delta t_q > 1 \times 10^5$ yr, for M_{min} and M_{max} respectively. The long recurrence time for starquakes obtained in this case, confirms the similarities between SGR 1822–1606 and SGR 0418+5729 as old objects with a settling down magnetospheric activity.

5.5.3 Rotation power and magnetic field

Using the observed values of P and \dot{P} , we obtain from Eq. (5.2) a rotational energy loss

$$\dot{E}_{rot} < \begin{cases} -1.71 \times 10^{34} \text{ erg s}^{-1}, & M = M_{max} \\ -7.89 \times 10^{35} \text{ erg s}^{-1}, & M = M_{min} \end{cases}, \quad (5.20)$$

which amply justifies the observed X-ray luminosity of SGR 1822–1606, $L_X = 4 \times 10^{32}$ erg s⁻¹, obtained assuming a distance of 5 kpc (see [201] for details).

The surface magnetic field of SGR 1822.3-1606, as given by Eq. (5.3), is then between the values (see Table 5.3)

$$B = \begin{cases} 3.63 \times 10^7 \text{ G}, & M = M_{min} \\ 1.30 \times 10^9 \text{ G}, & M = M_{max} \end{cases}. \quad (5.21)$$

Corresponding to the above magnetic fields, the electron cyclotron frequencies are

$$f_{cyc,e} = \frac{eB}{2\pi m_e c} = \begin{cases} 1.01 \times 10^{14} \text{ Hz}, & M = M_{min} \\ 3.63 \times 10^{15} \text{ Hz}, & M = M_{max} \end{cases}, \quad (5.22)$$

that correspond to wavelengths 2.96 and 0.08 μm , respectively.

5.5.4 Optical spectrum and luminosity

[201] observed the field of SGR 1822–1606 with the Gran Telescopio Canarias (GranTe-Can) within the Swift-XRT position [182]. Three sources ($S1$, $S2$, and $S3$) were detected

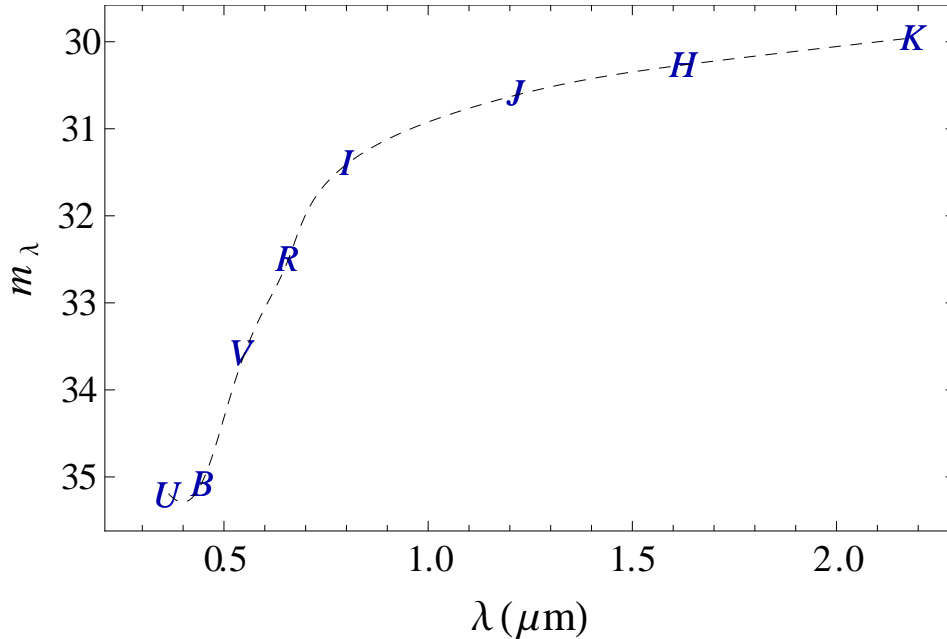


Figure 5.4: Expected optical magnitudes of SGR 1822–1606 assuming a blackbody spectral emission from a WD with surface temperature $T = 10^4$ K and a radius of 1.5×10^8 cm.

with the Sloan z filter with corresponding z -band magnitudes $m_{z,S1} = 18.13 \pm 0.16$, $m_{z,S2} = 20.05 \pm 0.04$, and $m_{z,S3} = 19.94 \pm 0.04$ (see [201] for details). No additional objects were found to be consistent with the Swift-XRT position up to a magnitude $m_z = 22.2 \pm 0.2$ (3σ).

In addition, data from the UK Infrared Deep Sky Survey (UKIDSS) for the field of SGR 1822–1606 were found to be available, giving the magnitudes of the three aforementioned sources in the J , H , and K bands; $m_{J,i} = (13.92, 16.62, 16.43)$, $m_{H,i} = (12.37, 15.75, 15.40)$, and $m_{K,i} = (11.62, 15.20, 14.88)$, where the index i indicates the values for the sources $S1$, $S2$, and $S3$. In addition to $S1$, $S2$, and $S3$, no sources were detected within the consistent position up to the limiting magnitudes $m_J = 19.3$, $m_H = 18.3$, and $m_K = 17.3$ (5σ).

We repeat the same analysis for SGR 0418+5729 to the case of SGR 1822–1606. We consider only the upper limits, since the three sources reported in [201], $S1$, $S2$ and $S3$, are very luminous to be a WD at the distance considered for the SGR, $d \approx 5$ kpc. From the NH column density value, $N_H = 7 \times 10^{21} \text{ cm}^{-2}$ we obtain an extinction in the V -band of $A_V = 3.89$. From the [51] relation we obtain the extinction values for the four bands considered, $A_z = 1.86$, $A_J = 1.10$, $A_H = 0.74$ and $A_K = 0.44$. The extinction corrected upper limits do not put very strong constraints to the temperature and the radius of the WD, due to the very large distance assumed for SGR 1822–1606. We show in Fig 5.4 the expected extinction-corrected magnitudes for a WD with a temperature $T = 10^4$ K and a radius $R = 1.5 \times 10^8$ cm at a distance of 5 kpc. We obtain a very deep value

for the K -band of ≈ 30 . We conclude that, if SGR 1822–1606 is at the distance of 5 kpc introduced by [201], it will be hard to detect the WD. On the contrary, a possible detection would lead to a more precise determination of the distance.

5.6 Conclusions

The recent observations of SGR 0418+5729 [200], $P = 9.08$ and $\dot{P} < 6.0 \times 10^{-15}$, and Swift J1822.3-1606 [201], $P = 8.44$ s and $\dot{P} = 9.1 \times 10^{-14}$, challenge the description of these sources as ultramagnetized NSs of the magnetar model of SGRs and AXPs. Based on the recent work of [154], we have shown here that, instead, both SGR 0418+5729 and Swift J1822.3-1606 are in full agreement with a description based on massive fast rotating highly magnetic WDs.

From an analysis of the rotational stability of the WD using the results of [45], we have predicted the WD parameters. In particular, bounds for the mass, radius, moment of inertia, and magnetic field of SGR 0418+5729 and Swift J1822.3-1606 have been presented (see Tables 5.2 and 5.3, for details).

We have improved the theoretical prediction of the lower limit for the spin-down rate of SGR 048+5729, for which only the upper limit, $\dot{P} < 6.0 \times 10^{-15}$ [200], is currently known. Based on a WD of fiducial parameters, [154] predicted for SGR 0418+5729 the lower limit $\dot{P} > 1.18 \times 10^{-16}$. Our present analysis based on realistic general relativistic rotating WDs allows us to improve such a prediction, see Eq. (5.10) for the new numerical values.

We have given in Eqs. (5.9) and (5.22) an additional prediction of the electron cyclotron frequencies of SGR 0418+5729 and Swift J1822.3-1606, respectively. The range we have obtained for such frequencies fall into the optical and infrared bands.

We have also presented the optical properties of SGR 0418+5729 and Swift J1822.3-1606 as expected from a model based on WDs. In particular, the surface temperature of the WD has been inferred and predictions for the emission fluxes in the UV, Optical, and Infrared bands have been given. Follow-on missions of Hubble and VLT are strongly recommended to establish the precise values of the luminosity in the Optical and in the near-Infrared bands, which will verify the WD nature of SGRs and AXPs.

5.7 Perspectives

It would be interesting to study possible progenitors of SGRs and AXPs which could be the mergers of WDs that lead to the formation of massive fast rotating highly magnetized WDs (see [117], [88] for details). In addition it is important to analyze the mechanisms of radiation of these WDs, specifically in the high-energy bands e.g. X and Gamma rays. This will be a natural extension of this work where we have showed the emission in the optical band. This issue will be considered in the forthcoming works.

Chapter 6

Magnetic Fields in Rotating Nuclear Matter Cores

6.1 Introduction

Neutron stars are mainly detected as pulsars, whose regular pulsations in the radio, X-ray, and optical bands are produced by constant, ordered magnetic fields that are the strongest known in the Universe. However the origin of the magnetic field in the neutron stars is not fully understood, so far. Nevertheless in the literature one may find various hypotheses explaining the formation of the magnetic field [93, 273, 216, 217, 202, 203, 204]. The simplest hypothesis to explain the presence of the strong fields observed in neutron stars is the conservation of the magnetic flux already present in the progenitor stars during the gravitational collapse. This idea is based on the assumption that all stars at all stages of their evolution have some magnetic field, due to electronic currents circulating in their interiors. Thus this argument led to the prediction of the fields $B \approx 10^{12} G$ in neutron stars a few years before the discovery of pulsars [93, 273]. However, there is no detailed physical picture of such a flux conserving collapse. Thompson and Duncan [254] put forward the hypothesis that newborn neutron stars are likely to combine vigorous convection and differential rotation making a dynamo process operate in them. They predicted fields up to $10^{15} - 10^{16} G$ in neutron stars with few millisecond initial periods, and suggested that such fields could explain much of the phenomenology associated with Soft Gamma Repeaters and Anomalous X-ray Pulsars [255, 256].

Probably, these processes are not mutually exclusive. A strong field might be present in the collapsing star, but later be deformed and perhaps amplified by some combination of convection, differential rotation, and magnetic instabilities [253, 243]. The relative importance of these ingredients depends on the initial field strength and rotation rate of the star. For both mechanisms, the field and its supporting currents are not likely to be confined to the solid crust of the star, but distributed in most of the stellar interior, which is mostly a fluid mixture of neutrons, protons, electrons, and other, more exotic particles.

Unlike aforementioned hypotheses which are based on the assumptions that all stars are magnetized or charged with some net charge different from zero, we explore the system

recently considered by Ruffini et al. [222]. According to that work the system consisting of degenerate neutrons, protons and electrons in beta equilibrium is globally neutral and expected to be kept at nuclear density by self gravity. In what follows these systems are termed as Nuclear Matter Cores of Stellar Dimensions. Despite the global neutrality the charge distribution turned out to be different from zero inside and outside (near the surface) the star. The magnitude of the net charge inside and outside the core is equal, but the sign is opposite. Such an effect takes place as a consequence of the beta equilibrium, the penetration of electrons into the core, hence the screening of the core charge and global charge neutrality. As a result of this effect, one can show the presence of an electric field close to the critical value $E_c = m_e^2 c^3 / e \hbar$ near the surface of the massive cores, although localized in a very narrow shell. Thus in this case the magnetic field of the neutron star may be generated only if it spins like pulsars, even though the progenitor star has not been magnetized or electrically charged. In addition the stability against the Coulomb repulsion of such configurations has been shown in [213] within the Newtonian theory of gravity and a new island of stability has been found. In the present work the special attention is given to the stability of such rotating nuclear matter cores of stellar dimensions extending the results for stability given in [213].

6.2 The relativistic Thomas-Fermi equation

The Thomas-Fermi equation is the exact theory for atoms, molecules and solids as $N_p \rightarrow \infty$ [147]. The relativistic Thomas-Fermi theory developed for the study of atoms for heavy nuclei with $N_p = 10^6$ (see for instance [189], [79, 223]) gives important basic new information on the study of nuclear matter in bulk in the limit of $A = (m_{Planck}/m_n)^3$ nucleons of mass m_n and on its electrodynamic properties. The analysis of nuclear matter bulk in neutron stars composed of degenerate gas of neutrons, protons and electrons, has traditionally been approached by implementing microscopically the charge neutrality condition by requiring the electron density $n_e(r)$ to coincide with the proton density $n_p(r)$,

$$n_e(r) = n_p(r). \quad (6.1)$$

It is clear however that especially when conditions close to the gravitational collapse occur, there is an ultra-relativistic component of degenerate electrons whose confinement requires the existence of very strong electromagnetic fields, in order to guarantee the overall charge neutrality of the neutron star. Under these conditions equation (6.1) will be necessarily violated.

Using the relativistic Thomas-Fermi equation, [79], and later [223] have analyzed the electron densities around an extended nucleus in a neutral atom all the way up to $N_p = 6000$. They have shown the effect of penetration of the electron orbital well inside the nucleus, leading to a screening of the nuclei positive charge and to the concept of an “effective” nuclear charge distribution.

In the work of [223] and [213] the relativistic Thomas-Fermi equation has been used to extrapolate the treatment of super heavy nuclei to the case of nuclear matter cores

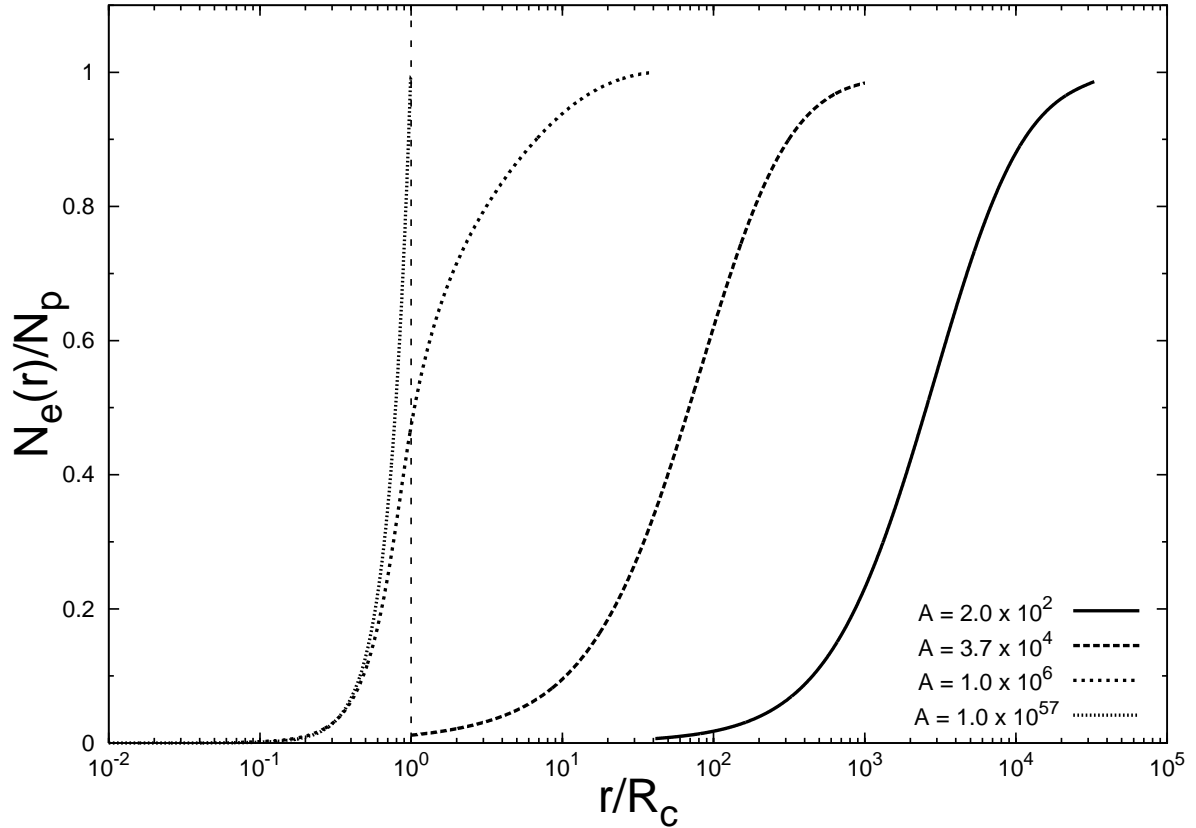


Figure 6.1: The electron number in the unit of the total proton number N_p , for selected values of A , as function of radial distance is shown in logarithmic scale. It is clear how by increasing the value of A the penetration of electrons inside the core increases (this figure is reproduced from [222]).

of stellar dimensions. These cores represent the inner part of neutron stars and are characterized by an atomic number of order of $A = (m_{Planck}/m_n)^3 \approx 10^{57}$, composed of degenerate neutrons, protons and electrons in beta equilibrium and expected to be kept at nuclear density by self gravity. It has been shown that near the surface of the massive cores it is possible to have an electric field close to the critical value E_c , although localized in a very narrow shell of the order of the λ_e electron Compton wavelength. Now let us review the main assumptions and results of those works.

According to [223] and [213] the protons are distributed at constant density n_p within a radius

$$R_c = \Delta \frac{\hbar}{m_\pi c} N_p^{1/3}, \quad (6.2)$$

where Δ is a parameter such that $\Delta \approx 1$ ($\Delta < 1$) corresponds to nuclear (supranuclear)

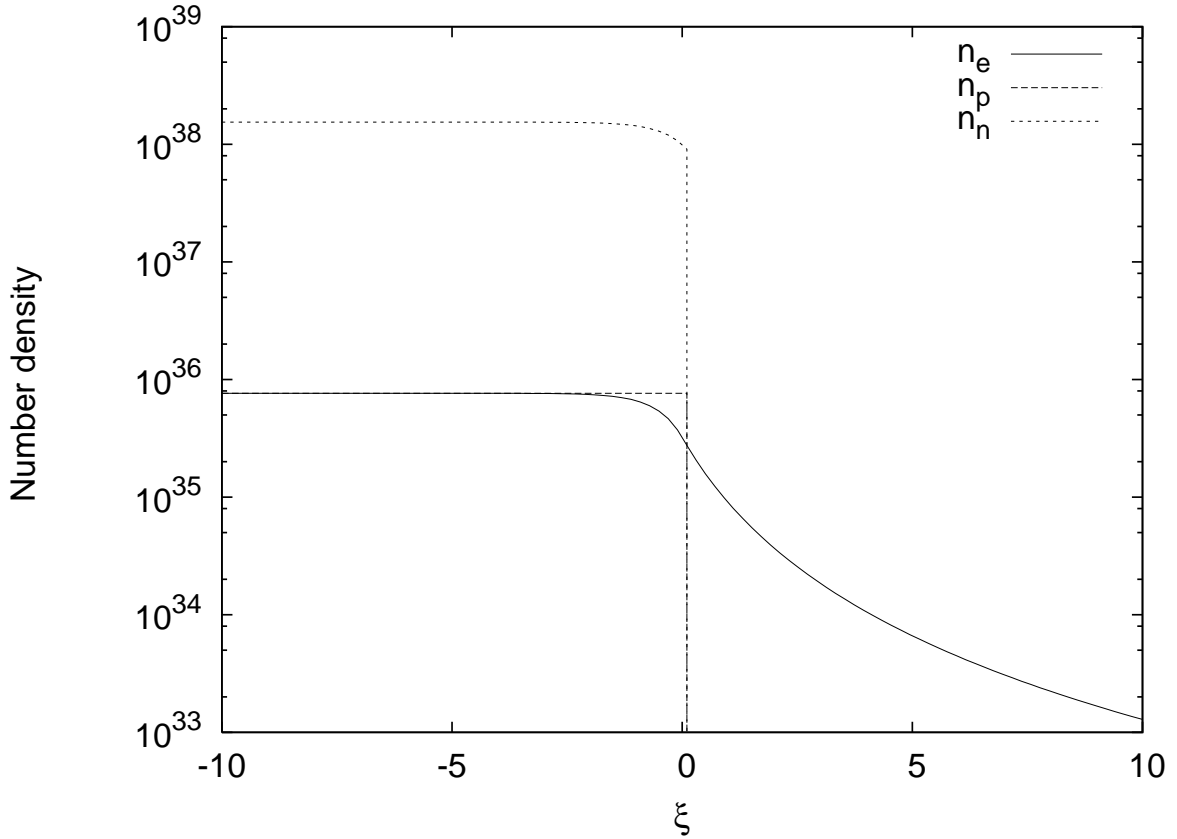


Figure 6.2: The neutron number density n_n , the proton number density n_p and the electron number density n_e , expressed in cm^{-3} , are plotted as functions of the dimensionless radial coordinate ξ . It is clear that near the surface of the core is located a transition layer of width $\approx \hbar/(\sqrt{\alpha}m_\pi c)$ with an uncompensated charge which generates an overcritical electric field (see Fig. 6.5).

densities when applied to ordinary nuclei. The proton number density is given by

$$n_p = \frac{1}{3\pi^2\hbar^3}(P_p^F)^3 = \frac{3N_p}{4\pi R_c^3}H(R_c - r), \quad (6.3)$$

where P_p^F is the Fermi momentum of a proton and $H(R_c - r)$ is the Heaviside step function (for details see [213]). The overall Coulomb potential satisfies the Poisson equation

$$\nabla^2 V(r) = -4\pi e [n_p(r) - n_e(r)], \quad (6.4)$$

with the boundary conditions $V(\infty) = 0$ (due to the global charge neutrality of the system) and finiteness of $V(0)$. The density $n_e(r)$ of the electrons of charge $-e$ is determined by the Fermi energy condition on their Fermi momentum P_e^F ; we assume here

$$E_e^F = [(P_e^F c)^2 + m_e^2 c^4]^{1/2} - m_e c^2 - eV(r) = 0, \quad (6.5)$$

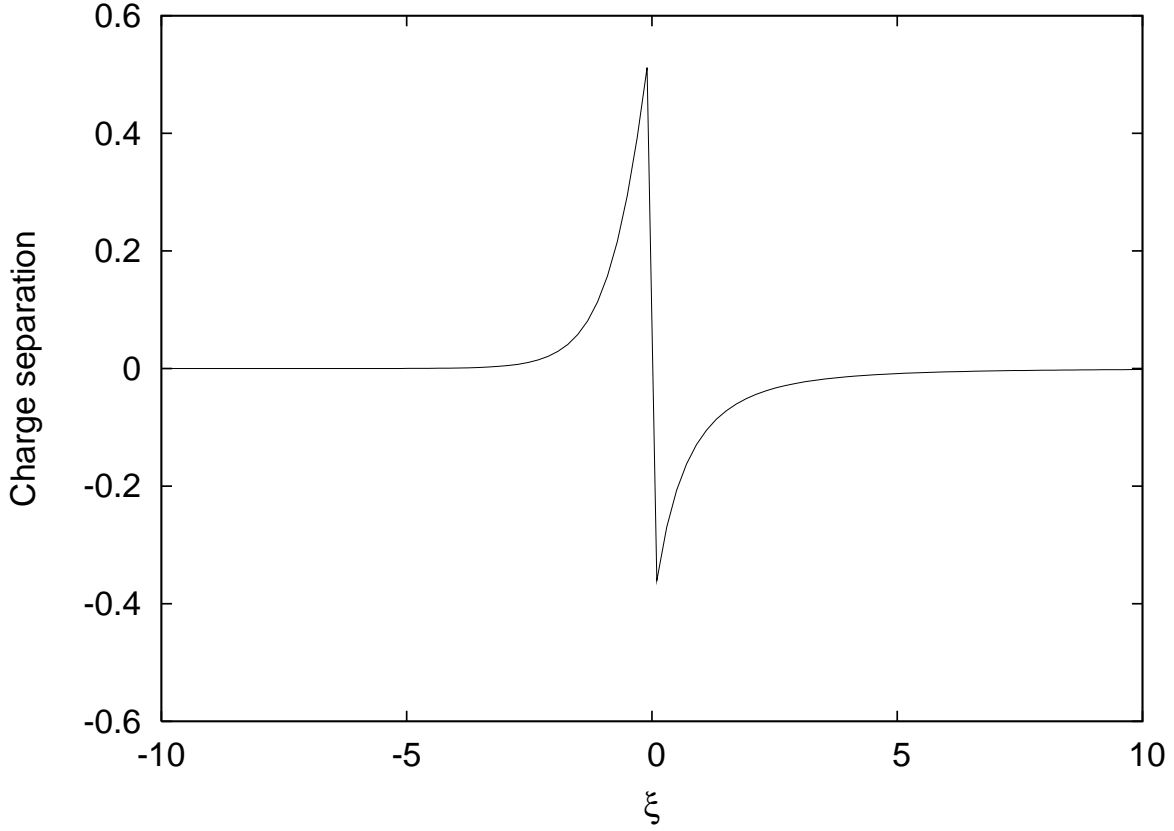


Figure 6.3: The normalized charge separation $(n_p - n_e)/n_p$ is plotted as function of the dimensionless radial coordinate ξ . The maximum charge separation happens near the surface of the core where a transition layer with an uncompensated charge is located (see Fig. 6.2).

which leads to

$$n_e(r) = \frac{(P_e^F)^3}{3\pi^2\hbar^3} = \frac{1}{3\pi^2\hbar^3 c^3} [e^2 V^2(r) + 2m_e c^2 eV(r)]^{3/2}. \quad (6.6)$$

By introducing the dimensionless quantities $x = r/[\hbar/m_\pi c]$, $x_c = R_c/[\hbar/m_\pi c]$ and $\chi/r = eV(r)/c\hbar$, the relativistic Thomas-Fermi equation takes the form

$$\frac{1}{3x} \frac{d^2\chi(x)}{dx^2} = -\frac{\alpha}{\Delta^3} H(x_c - x) + \frac{4\alpha}{9\pi} \left[\frac{\chi^2(x)}{x^2} + 2\frac{m_e}{m_\pi} \frac{\chi}{x} \right]^{3/2}, \quad (6.7)$$

where $\alpha = e^2/(\hbar c)$ is the fine structure constant and the boundary conditions for $\chi(x)$ are $\chi(0) = 0$, $\chi(\infty) = 0$ $N_e = \int_0^\infty 4\pi r^2 n_e(r) dr$. These equations together with the beta equilibrium, form a close set of non-linear boundary value problem for a unique solution for the Coulomb potential V and electron distribution n_e , as functions of the parameter Δ , i.e., the proton number-density n_p . A relevant quantity for exploring the physical

significance of the solution is given by the number of electrons within a given radius r , $N_e(r) = \int_0^r 4\pi(r')^2 n_e(r') dr'$. This allows to determine, for selected values of the mass number A , the distribution of the electrons within and outside the core and to follow the progressive penetration of the electrons in the core at increasing values of A (see Fig.6.1). We can then evaluate the net charge inside the core $N_{\text{net}} = N_p - N_e(R_c) < N_p$, and consequently determine the electric field at the core surface, as well as within and outside the core. The neutron density $n_n(r)$ is determined by the Fermi energy condition on their Fermi momentum P_n^F imposed by beta decay equilibrium

$$E_n^F = [(P_n^F c)^2 + m_n^2 c^4]^{1/2} - m_n c^2 = [(P_p^F c)^2 + m_p^2 c^4]^{1/2} - m_p c^2 + eV(r), \quad (6.8)$$

which in turn is related to the proton and electron densities by Eqs. (6.4), (6.6) and (6.7).

6.3 The ultra-relativistic analytic solutions

In the ultrarelativistic limit with the planar approximation the relativistic Thomas-Fermi equation admits an analytic solution. Introducing the new function ϕ defined by $\phi = 4^{1/3}(9\pi)^{-1/3}\Delta\chi/x$ and the new variables $\hat{x} = (12/\pi)^{1/6}\sqrt{\alpha}\Delta^{-1}x$, $\xi = \hat{x} - \hat{x}_c$, where $\hat{x}_c = (12/\pi)^{1/6}\sqrt{\alpha}\Delta^{-1}x_c$, then Eq. (6.7) becomes

$$\frac{d^2\hat{\phi}(\xi)}{d\xi^2} = -H(-\xi) + \hat{\phi}(\xi)^3, \quad (6.9)$$

where $\hat{\phi}(\xi) = \phi(\xi + \hat{x}_c)$. The boundary conditions on $\hat{\phi}$ are: $\hat{\phi}(\xi) \rightarrow 1$ as $\xi \rightarrow -\hat{x}_c \ll 0$ (at the nuclear matter core center) and $\hat{\phi}(\xi) \rightarrow 0$ as $\xi \rightarrow \infty$. The function $\hat{\phi}$ and its first derivative $\hat{\phi}'$ must be continuous at the surface $\xi = 0$ of the nuclear matter core of stellar dimensions.

Hence equation (6.9) admits an exact solution

$$\hat{\phi}(\xi) = \begin{cases} 1 - 3 [1 + 2^{-1/2} \sinh(a - \sqrt{3}\xi)]^{-1}, & \xi < 0, \\ \frac{\sqrt{2}}{(\xi + b)}, & \xi > 0, \end{cases} \quad (6.10)$$

where the integration constants a and b have the values $a = \text{arccosh}(9\sqrt{3}) \approx 3.439$, $b = (4/3)\sqrt{2} \approx 1.886$. The charge distribution inside and outside the core is defined by

$$\rho(\xi) = \begin{cases} \frac{3e}{4\pi} \left(\frac{\Delta\hbar}{m_\pi c}\right)^{-1} [1 - \hat{\phi}(\xi)^3], & \xi < 0, \\ \frac{3e}{4\pi} \left(\frac{\Delta\hbar}{m_\pi c}\right)^{-1} [-\hat{\phi}(\xi)^3], & \xi > 0, \end{cases} \quad (6.11)$$

details are given in Fig. 6.3. Hence the Coulomb potential and electric field functions

$$V(\xi) = \left(\frac{9\pi}{4}\right)^{1/3} \frac{m_\pi c^2}{\Delta e} \hat{\phi}(\xi), \quad E(\xi) = -\left(\frac{3^5\pi}{4}\right)^{1/6} \frac{\sqrt{\alpha} m_\pi^2 c^3}{\Delta^2 e\hbar} \hat{\phi}'(\xi). \quad (6.12)$$

Details are given in Figs. 6.4 and 6.5.

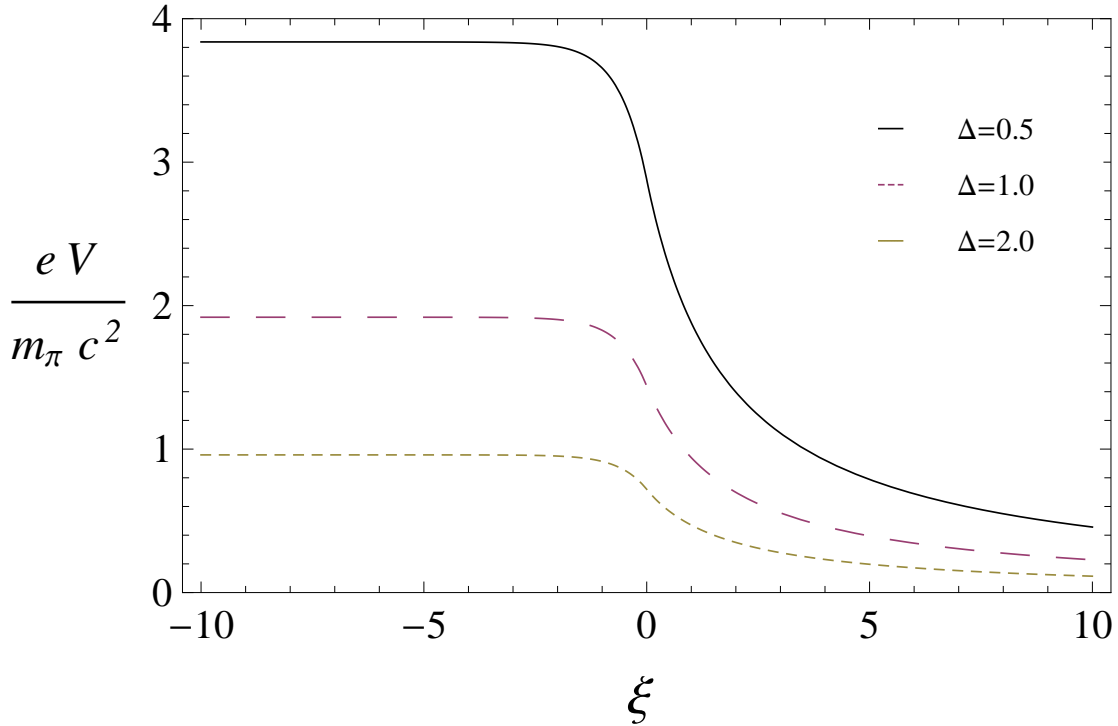


Figure 6.4: The proton Coulomb potential energy eV , in units of pion mass m_π is plotted as a function of the radial coordinate $\xi = \hat{x} - \hat{x}_c$, for selected values of the density parameter Δ .

6.4 Rotating nuclear matter cores of stellar dimensions

In section 6.2 and 6.3 we have seen that in the massive nuclear density cores the electric charge distribution is different from zero, although it is globally neutral (for details see *Table 6.4*). In this section we investigate the case when this charge distribution is allowed to rotate with the constant angular velocity $\vec{\omega} = \{0, 0, \omega\}$ around the axis of symmetry. Thus the magnetic field of the resultant current density is calculated in terms of the charge distribution. Consider a charge distribution moving in a such way that at every point in space the charge density and the current density remain constant. In this case the magnetic field is defined by

$$\vec{B}(\vec{r}) = \vec{\nabla} \times \vec{A}(\vec{r}), \quad \vec{A}(\vec{r}) = \frac{\vec{\omega}}{c^2} \times \vec{F}(\vec{r}), \quad \vec{F}(\vec{r}) = \frac{1}{4\pi\epsilon_0} \int \frac{r'^j \rho(r') d^3 r'}{|\vec{r} - \vec{r}'|}, \quad (6.13)$$

where \vec{A} is the vector potential of the magnetic field, $\vec{F}(\vec{r})$ is the "superpotential" in general form and ϵ_0 is the electric constant. In the case of spherical symmetry, $\vec{F}(\vec{r})$ may

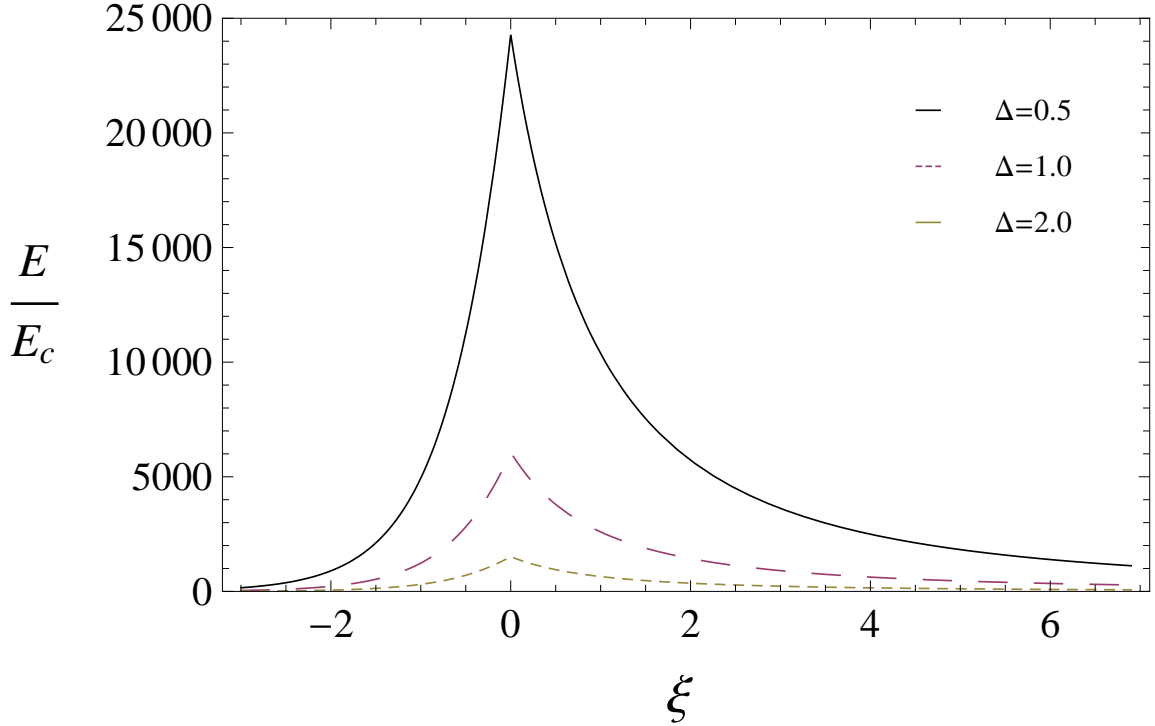


Figure 6.5: The electric field is plotted in units of the critical field E_c as a function of the radial coordinate ξ , showing a sharp peak at the core radius, for selected values of Δ .

be taken as radial (see [158]). Writing $\vec{F}(\vec{r}) = \vec{e}_r F(r)$, where \vec{e}_r is the unit radial vector, one has

$$F(r) = \frac{1}{r^2} \int_0^r r'^2 \frac{d}{dr'} [r' V(r')] dr'. \quad (6.14)$$

This expression allows to calculate the magnetic field induced due to rotation of any spherically symmetric distribution of charge in terms of its electrostatic Coulomb potential. Note that in fact due to rotation the shape of the neutron star must deviate from spherical symmetry. Since we are interested in the estimation of the order (magnitude) of the magnetic field, the distortions to the shape of the star can be neglected for the sake of simplicity. Thus the magnetic field is defined by

$$\vec{B}(\vec{r}) = B_r \vec{e}_r + B_\theta \vec{e}_\theta, \quad (6.15)$$

where

$$B_r = \frac{2\omega F}{c^2 r} \cos \theta, \quad B_\theta = -\frac{2\omega}{c^2} \left[\frac{F}{r} + \frac{r}{2} \frac{d}{dr} \left(\frac{F}{r} \right) \right] \sin \theta, \quad (6.16)$$

B_r is the radial component and B_θ is the angular component of the magnetic field, θ is the angle between r and z axis, and \vec{e}_θ is the unit vector along θ . Consequently the

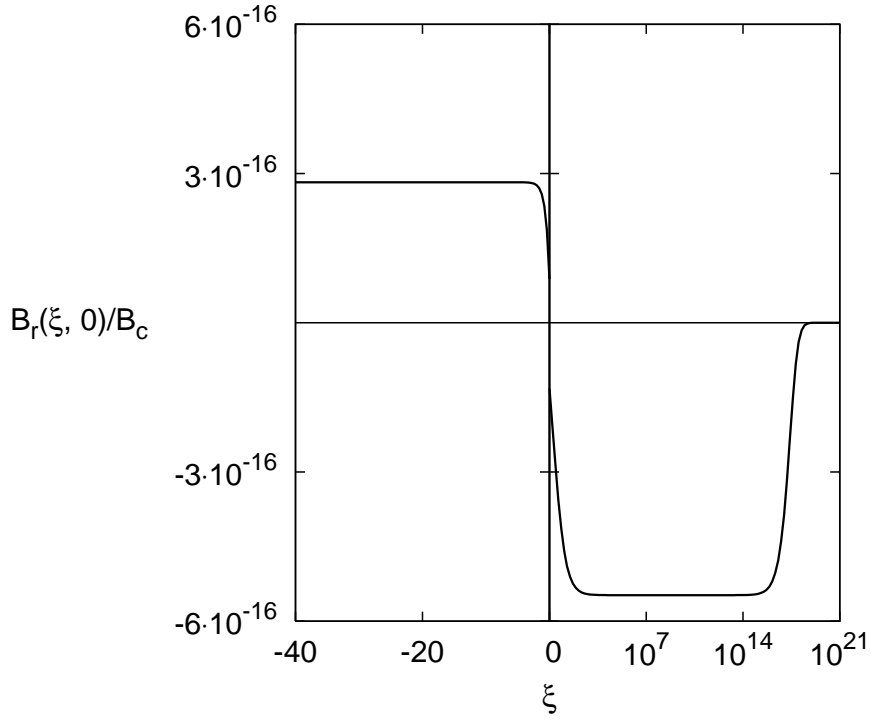


Figure 6.6: The radial component of the magnetic field B_r is plotted as a function of the radial coordinate ξ in units of the critical field $B_c = m_e^2 c^3 / e \hbar \approx 4.5 \times 10^{13} \text{ G}$. Here the period is taken to be $P = 10 \text{ ms}$, $\theta = 0$, $\Delta = 1$ and the radius of the core $R_c = 10 \text{ km}$. Note that B_r is considered at the poles of star, where it has maximum value. Outside the star B_r has very small negative value and it tends to zero.

expression for the magnitude (the absolute value) of the magnetic field can be written as

$$B(r, \theta) = \frac{\omega r}{c^2} \sqrt{\left(\frac{2F}{r^2}\right)^2 + \left\{ \frac{4F}{r^2} \frac{d}{dr} \left(\frac{F}{r}\right) + \left[\frac{d}{dr} \left(\frac{F}{r}\right) \right]^2 \right\} \sin^2 \theta}. \quad (6.17)$$

Using the relation between r and ξ

$$r = R_c + \left(\frac{\pi}{12}\right)^{1/6} \frac{\Delta}{\sqrt{\alpha}} \frac{\hbar}{m_\pi c} \xi, \quad (6.18)$$

one may estimate the value of the magnetic field. Details are given in Figs. 6.6, 6.7, 6.10 and 6.9.

Examining Fig. 6.6 one can see very small value of B_r which almost does not make a significant contribution to the magnitude of the field, except for the poles of the star. On the contrary, B_θ has values exceeding the critical magnetic field near the surface of the core although localized in a narrow region between positively and negatively charged

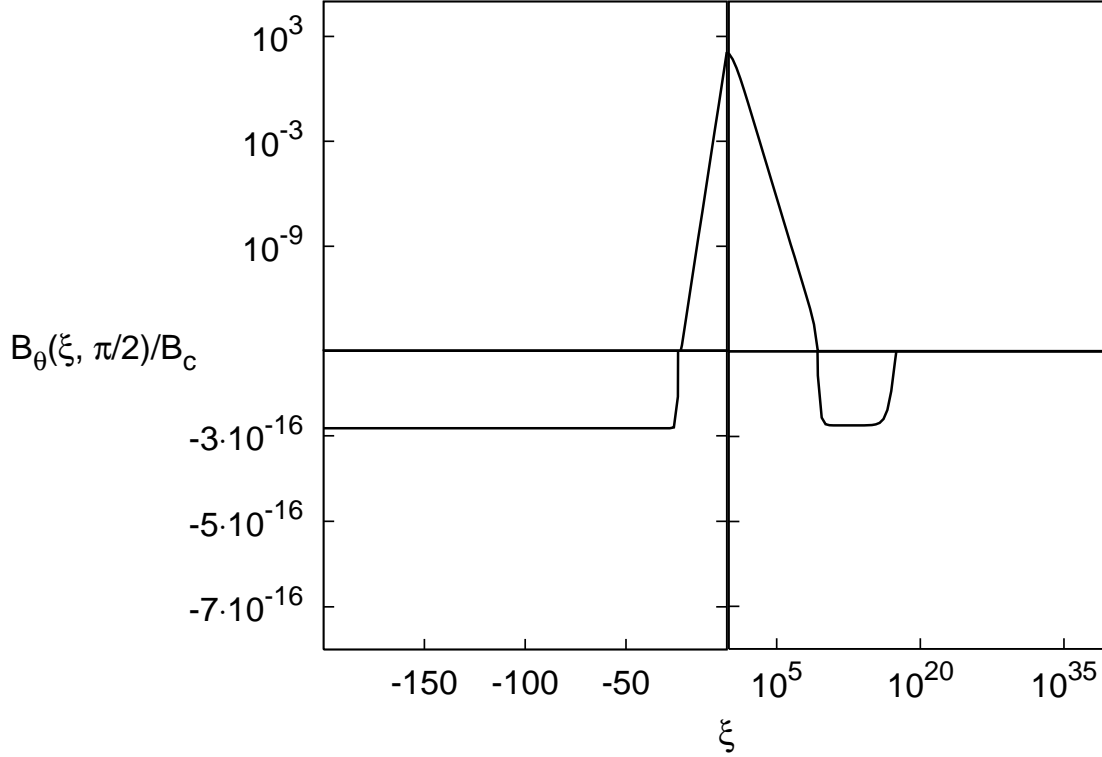


Figure 6.7: The angular component of the magnetic field B_θ is plotted in units of the B_c . Here $P = 10 \text{ ms}$, $\theta = \pi/2$, $\Delta = 1$ and $R_c = 10 \text{ km}$. Note that B_θ is considered at the equator, where it has maximum value. Inside the star it has very small constant negative value. Outside the star first it becomes negative (the value is very small) then it tends to zero.

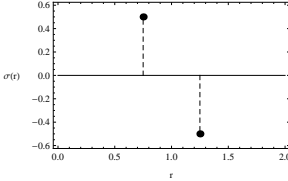
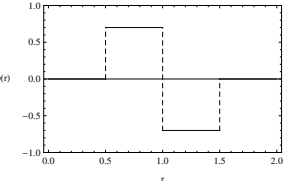
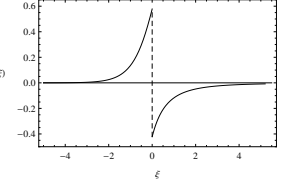
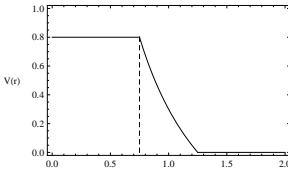
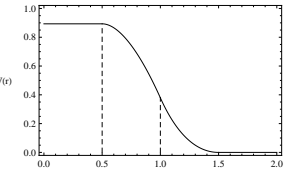
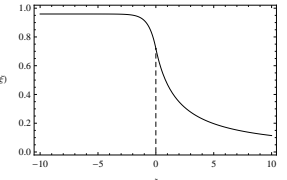
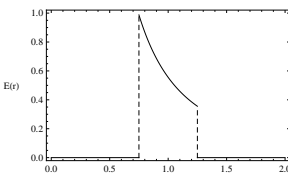
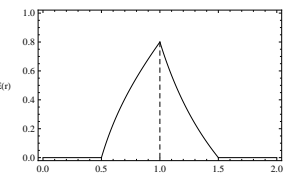
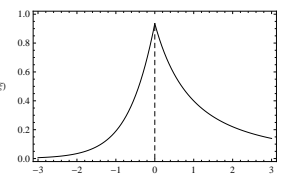
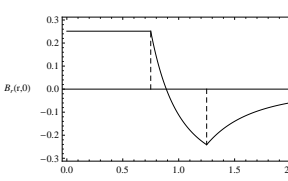
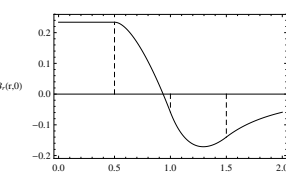
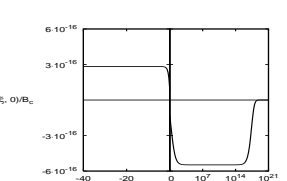
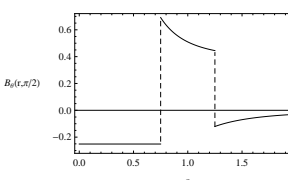
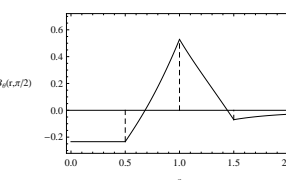
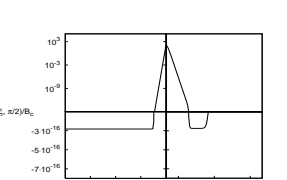
shells as expected Fig. 6.7. Outside the core the magnetic field becomes negative. The magnitude of the field has very small and eventually vanishing values.

In Fig. 6.8 shows spacial distribution of the magnetic field on the surface of the nuclear matter core. According to the figure the magnetic field has its maximum value at the equatorial plane and minimum at the poles. Fig. 6.9 represents magnetic lines of force inside, outside and on the surface of the star. It turned out that the lines of force of the overcritical magnetic field are appressed between two shells along the surface of the core.

In Table 6.4. electrodynamic properties of the globally neutral configurations with different charge distribution are presented schematically. All parameters are chosen in a such way to show the general features of the systems. Analyzing the magnetic fields of the configurations one can easily see the resemblance between the Coulomb potential V and B_r , plus between the electric field E and B_θ for both idealized and real configurations. In our case the magnetic field shares common properties with the previous configurations although it has its own peculiarities representing the smooth changes in the regions close

*

Table 6.1: Electrodynamics properties of the globally neutral configurations with different charge distribution are demonstrated schematically. The dashed lines correspond to the radii of the spheres.

Configuration	A spherical capacitor of radii $R_1 < R_2$	Concentric spherical layers of radii $R_1 < R_2 < R_3$	Our case (the solution of the Thomas-Fermi equation)
Charge distribution ρ			
Coulomb potential V			
Electric field E			
Radial component of the magnetic field $B_r(r, 0)$			
Angular component of the magnetic field $B_\theta(r, \frac{\pi}{2})$			

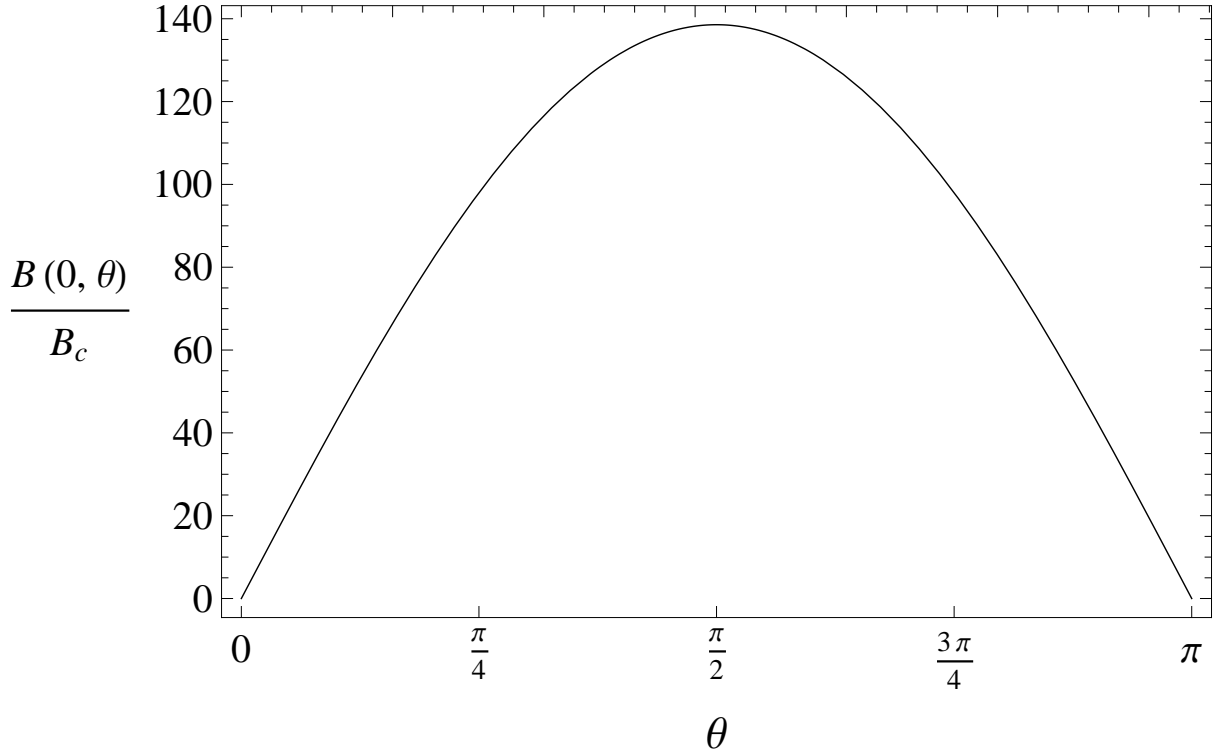


Figure 6.8: The magnitude of the magnetic field $B(\xi = 0, \theta)$ as given by (6.17) in the units of the critical magnetic field B_c is shown as a function of the angular variable θ . It is seen from the picture that the magnetic field has its maximum at the equatorial plane and minimum at the poles.

to the surface of the core. In order to check the validity of our results we have considered similar examples. First thing when one deals with the positively and negatively charged spherical shells with the thickness of order of λ_e in contrast with a radius of $10km$ neutron star, the natural idea that comes to one's mind is to assume a spherical surface charge distribution. Since there are two spherical shells the closest example has been to explore electrodynamic properties of a spherical capacitor. As matter of fact this example showed the similar behavior of the Coulomb potential V and B_r with the solution of Thomas-Fermi equation plus a huge difference in the orders between B_r and B_θ , however the electric field E and B_θ had completely different features from our results. Moreover the spherical capacitor has not explained why in our case one had continuous B_θ at the boundary of the charged shells. In addition to all above given arguments there was some distance between positively and negatively charged surfaces, whereas in our case the distance between the shells was zero. Thus, one had to consider one more alternative problem close to our case in order to carry out a cross check. This time two oppositely charged spherical layers with volume charge distribution have been considered in contrast with our case. Indeed this example was fortunate and the closest simple example. It explained all the common

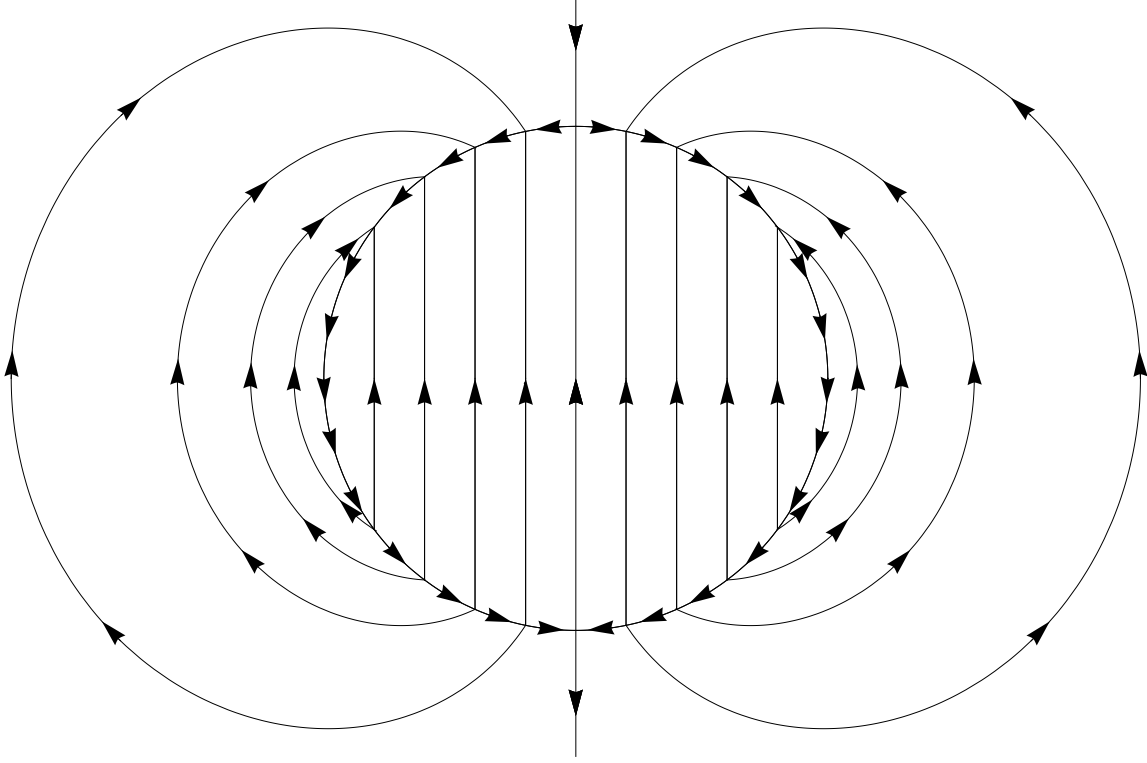


Figure 6.9: A schematic illustration of the magnetic lines of forces. Outside the star the magnetic field looks like a dipole field. Extra arrows along the surface of the star indicate an overcritical value of the field between positively and negatively charged shells.

electrodynamic properties of both systems. As a result, B_r and B_θ turned out to be functions of the thickness of the spherical layers. When these thickness is of order of λ_e one observes this huge difference and since the charge has been distributed in given volumes, with different signs, the electric field E and B_θ turned out to be continuous.

6.5 Stability of rotating nuclear matter cores of stellar dimensions

In the work [213] the gravitational stability against the Coulomb repulsion of a nuclear matter core of stellar dimensions has been analyzed. In particular since in this system the gravitational energy increases proportionally to $A^{4/3}$ and the Coulomb energy increases proportionally to $A^{2/3}$ the two cross at

$$A_R^{\omega=0} = 0.039 \left(\frac{m_{Planck}}{m_n} \right)^3 \left(\frac{N_p}{A} \right)^{1/2}, \quad (6.19)$$

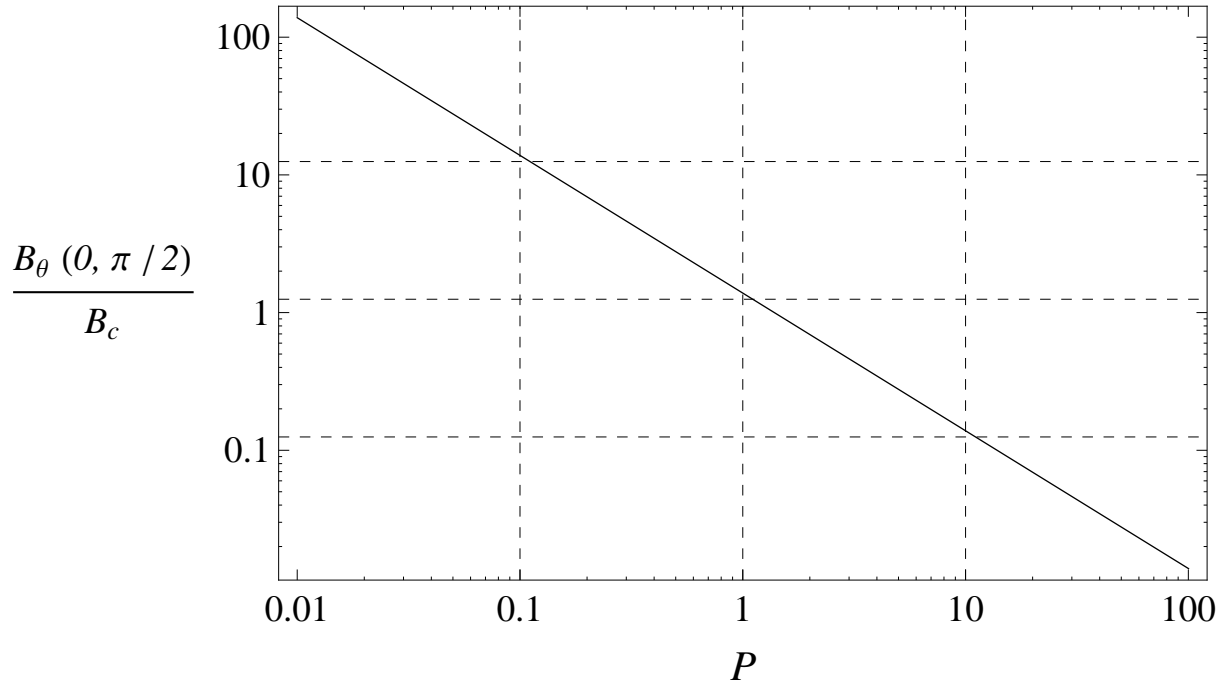


Figure 6.10: The magnitude of the magnetic field is plotted as a function of the period of the star P (in seconds) in the units of the critical field B_c at the surface of the core on the equator in the logarithmic scale. Here $R_c = 10 \text{ km}$ and $\Delta = 1$.

where m_{Planck} is the Planck mass and m_n is the neutron mass. This establishes a lower limit for the mass number A_R necessary for the existence of stable nuclear matter cores of stellar dimensions.

We consider now the analysis of the gravitational stability against the Coulomb repulsion of a nuclear matter core of stellar dimensions when the system is allowed to rotate as a whole rigid spherical object.

We know that the Coulomb energy, mainly distributed within a thin shell of width $\delta R_c \approx \hbar \Delta / (\sqrt{\alpha} m_\pi c)$ with a proton number $\delta N_p \approx 4\pi n_p R_c^2 \delta R_c$ at the surface, is given by

$$\mathcal{E}_{el} \approx 0.15 \frac{3(3\pi)^{1/2} \hbar c}{4\sqrt{\alpha}} \left(\frac{\Delta \hbar}{m_\pi c} \right)^{-1} \left(\frac{N_p}{A} \right)^{2/3} A^{2/3}, \quad (6.20)$$

while the magnetic energy evolving due to rotation is given by

$$\mathcal{E}_{mag} \approx 0.223 \frac{m_\pi c^2}{\Delta \sqrt{\alpha}} \left(\frac{N_p}{A} \right)^{4/3} A^{4/3} \left(\frac{\Delta \hbar}{m_\pi c} \right)^2 \frac{\omega^2}{c^2}. \quad (6.21)$$

and the rotational kinetic energy of that thin proton shell is given by

$$\mathcal{E}_{rot} \approx \frac{m_n c^2}{\sqrt{\alpha}} \left(\frac{N_p}{A} \right)^{4/3} A^{4/3} \left(\frac{\Delta \hbar}{m_\pi c} \right)^2 \frac{\omega^2}{c^2}. \quad (6.22)$$

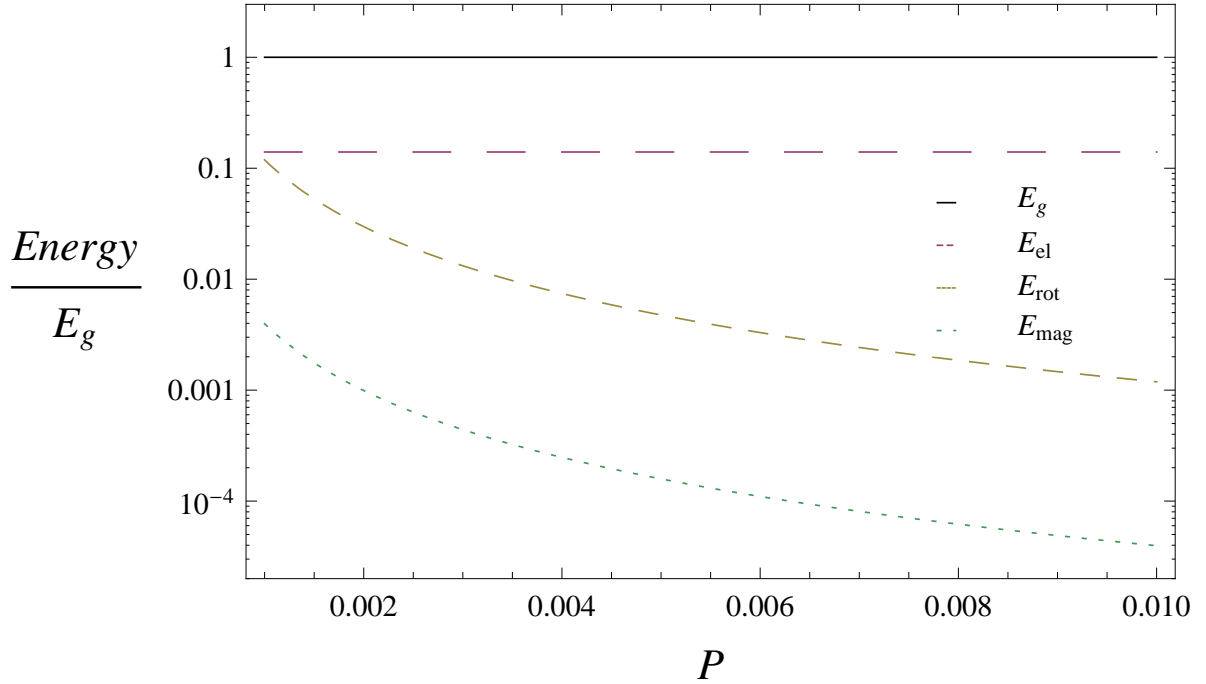


Figure 6.11: Energies of the system in the units of the gravitational energy of the thin shell plotted as a function of the period of the star P for $\Delta = 1$ in the range between $1ms$ and $10ms$ in logarithmic scale.

To ensure the stability of the system, the magnitude of the attractive gravitational energy of the thin proton shell

$$\mathcal{E}_g \approx \frac{3Gm_n^2}{\sqrt{\alpha}} \left(\frac{\Delta\hbar}{m_\pi c} \right)^{-1} \left(\frac{N_p}{A} \right)^{1/3} A^{4/3}, \quad (6.23)$$

must be larger than the repulsive Coulomb energy (6.20), the magnetic energy (6.21) and the repulsive rotational energy (6.22). Indeed, it is shown in the Fig. 6.11 that for the periods more than $1ms$, the condition $\mathcal{E}_g > \mathcal{E}_{el} + \mathcal{E}_{mag} + \mathcal{E}_{rot}$ is valid.

This leads to

$$A_R^{\omega \neq 0} \approx A_R^{\omega = 0} \left[1 + \left(0.112 + 0.5\Delta \frac{m_n}{m_\pi} \right) \left(\frac{m_{Planck}}{m_n} \right)^2 \frac{N_p}{A} \left(\frac{\Delta\hbar}{m_\pi c} \right)^2 \frac{\omega^2}{c^2} \right], \quad (6.24)$$

which generalizes the relation given by Eq.(6.19). We can see that the correction term $\left(0.112 + 0.5\Delta \frac{m_n}{m_\pi} \right) \left(\frac{m_{Planck}}{m_n} \right)^2 \frac{N_p}{A} \left(\frac{\Delta\hbar}{m_\pi c} \right)^2 \frac{\omega^2}{c^2}$ for the pulsars with the period more than $1ms$ is of the order of 10^{-3} , so in this case the system is stable.

6.6 Conclusions

We have investigated the behavior of the magnetic field induced by the rotation of a nuclear matter core of stellar dimensions on the basis of the research works considered in [222] and [213] using the technique developed by Marsh [158].

In particular, for such a rotating system with a period of $10ms$ we have obtained a magnetic field of order of the critical field near the surface and analyzed the magnetic lines of forces.

In addition we have investigated the stability of rotating nuclear matter cores of stellar dimensions against the rotational kinetic energy and induced magnetic energy. In fact the whole system is gravitationally bound and stable even for the $1ms$ period. However for the periods less than $1ms$ the centrifugal repulsive forces will prevail over the gravitational force. In that case the system can no longer be stable.

Since the electric field and the magnetic field are mainly concentrated in the very thin shell on the surface, compared to the radius of the object, we have considered the energies of the system only in that region. The magnetic energy has the order of one tenth of the rotational energy irrespective of the value of the period.

According to our results the magnetic field of a neutron star could be generated by its rotation as a whole rigid body leading to the formation of the constant magnetic field at the initial moments of neutron stars birth.

6.7 Perspectives

The results of the present work can be applied to the physics of compact objects; e.g. the emergence of critical electromagnetic fields in neutron stars and the process of gravitational collapse to a black hole.

We are currently investigating the effects of magnetic fields and the stability of a rotating self-gravitating system of degenerate fermions in β -equilibrium in general relativity, generalizing thus previous results of [211, 208, 218].

Chapter 7

Neutron star equilibrium configurations

7.1 Introduction

The fact that the Thomas-Fermi model originates from the realm of atomic physics has been known for a long time [97, 146]. It was proposed in 1973 that the Thomas-Fermi model could be useful to give an alternative derivation of a self-gravitating system of fermions within Newtonian gravity leading to a description of neutron stars and white dwarfs complementary to the traditional derivation in the perfect fluid approximation [221, 219]. This gravitational treatment needed the special relativistic generalization of the Thomas-Fermi model, which became also a necessity in order to describe the physics of heavy nuclei [164, 79, 223]. The Thomas-Fermi treatment from the original realm of atomic physics started so to be applied in its special relativistic extension to gravitational and nuclear physics.

It has been until [222, 220, 190, 213] that all these considerations have been extended to an heuristic simplified Thomas-Fermi model of a neutron star taking into account nuclear physics, Newtonian physics, and β -equilibrium. The evidence for the possible existence of overcritical electric fields at the core of neutron stars was there presented [220]. At this stage a basic theoretical progress in the description of neutron stars with a fully relativistic Thomas-Fermi model with all interactions became a *necessity*. It has been particularly important to use a Wigner Seitz cell: we first solved the relativistic Thomas-Fermi model for compressed atoms [210], generalizing the classical approach of Feynman, Metropolis and Teller [80]. This has given as a byproduct a new equation of state for white dwarfs duly expressed in general relativity [209]. We then proved the impossibility of imposing local charge neutrality on chemically equilibrated matter made of neutrons, protons, and electrons, in the simplified case where strong interactions are neglected [211]. This was a critical issue for neutron star matter calculations, since we demonstrated that the equations which describe baryonic matter need to be solved simultaneously in combination with the Einstein-Maxwell equations. The general formulation to the case of strong interactions have been recently achieved in [218]. The present work is the result of

the above multi year effort and summarizes and discusses the relevant equations for the description of neutron stars, i.e. relativistic mean field theory and the Einstein-Maxwell-Thomas-Fermi system of general relativistic equations, presenting a self-consistent neutron star model including all fundamental interactions: strong, weak, electromagnetic, and gravitational.

It is well-known that the classic works of Tolman [260] and Oppenheimer and Volkoff [175], for short TOV, address the problem of neutron star equilibrium configurations composed only of neutrons. For the more general case when protons and electrons are also considered, in all of the scientific literature on neutron stars it is assumed that the condition of local charge neutrality applies identically to all points of the equilibrium configuration (see e.g. [101]). Consequently, the corresponding solutions in this more general case of a non-rotating neutron star, are systematically obtained also on the base of the TOV equations.

In general, the formulation of the equilibrium of systems composed of different particle species must be established within the framework of statistical physics of multicomponent systems; see e.g. [76]. Thermodynamic equilibrium of these systems is warranted by demanding the constancy throughout the configuration of the generalized chemical potentials, often called “electro-chemical”, of each of the components of the system; see e.g. [125, 126, 174]. Such generalized potentials include not only the contribution due to kinetic energy but also the contribution due to the potential fields, e.g. gravitational and electromagnetic potential energies per particle, and in the case of rotating stars also the centrifugal potential. For such systems in presence of gravitational and Coulomb fields, global electric polarization effects at macroscopic scales occur. The balance of the gravitational and electric forces acting on ions and electrons in ideal electron-ion plasma leading to the occurrence of gravito-polarization was pointed out in the classic work of S. Rosseland [207].

If one turns to consider the gravito-polarization effects in neutron stars, the corresponding theoretical treatment acquires remarkable conceptual and theoretical complexity, since it must be necessarily formulated consistently within the Einstein-Maxwell system of equations. O. Klein, in [125], first introduced the constancy of the general relativistic chemical potential of particles, hereafter “Klein potentials”, in the study of the thermodynamic equilibrium of a self-gravitating one-component fluid of neutral particles throughout the configuration within the framework of general relativity. The extension of Klein’s work to the case of neutral multicomponent degenerate fluids can be found in [126] and to the case of multi-component degenerate fluid of charged particles in [174].

Using the concept of Klein potentials, we have recently proved the impossibility of imposing the condition of local charge neutrality in the simplest case of a self-gravitating system of degenerate neutrons, protons and electrons in β -equilibrium [211]: it has been shown that the consistent treatment of the above system implies the solution of the general relativistic Thomas-Fermi equations, coupled with the Einstein-Maxwell ones, being the TOV equations thus superseded.

We have recently formulated the theory of a system of neutrons, protons and electrons fulfilling strong, electromagnetic, weak and gravitational interactions [218]. The role of

the Klein first integrals has been again evidenced and their theoretical formulation in the Einstein-Maxwell background and in the most general case of finite temperature has been there presented, generalizing the previous results for the “non-interacting” case [211]. The strong interactions, modeled by a relativistic nuclear mean field theory, are there described by the introduction of the σ , ω and ρ virtual mesons (see Subsec. 7.2.1 for details).

In [18] for the first time the equilibrium configurations of non-rotating neutron stars have been constructed, following the new approach of [211, 218]. We calculate the properties of neutron star matter and neutron stars treated fully self-consistently with strong, weak, electromagnetic, and gravitational interactions. The full set of the Einstein-Maxwell-Thomas-Fermi equations is solved numerically for zero temperatures and for selected parameterizations of the nuclear model. We use units with $\hbar = c = 1$ throughout the chapter.

7.2 The Constitutive Relativistic Equations

7.2.1 Core Equations

It has been clearly recognized that, since neutron stars cores may reach density of order $\sim 10^{16}$ – 10^{17} g/cm³, much larger than the nuclear density $\rho_{\text{nuc}} = \rho_0 \sim 2.7 \times 10^{14}$ g/cm³, approaches for the nuclear interaction between nucleons based on phenomenological potentials and non-relativistic many-body theories become inapplicable (see [47, 46], for instance). Based on the pioneering work of Johnson and Teller [122], Duerr [68] and later on Miller and Green [165] formulated the basis of what is now known as Relativistic Mean Field Theory of nuclear matter. They constructed the simplest relativistic model that accounts for the binding of symmetric nuclear matter at saturation density by introducing the interaction of one scalar field and one vector field with nucleons through Yukawa couplings. A nuclear model with only the scalar field with a self-interacting potential up to quartic order based on the sigma-model was considered in [143, 141]. The repulsive contribution of nuclear force was there introduced by hand through a *hard-sphere* model that artificially increases the nucleon Fermi momentum emulating the effect of a massive vector field coupled to nucleons. The relevance of such interactions as well as relativistic effects in the determination of the equation of state and in the nuclear matter properties such as compressibility and the nucleon effective mass was clearly pointed out in [165, 37, 35]. The importance of allowing scalar meson self-interactions (cubic and quartic terms in the scalar field potential) as adjustable parameters to reproduce physical nuclear properties and not due to renormalization (see e.g. [267]) was stressed in [35, 38, 36, 34]. The necessity of introducing additional isovector fields to match the empirical symmetry energy of nuclear matter at saturation density was recognized in [35].

Assuming that the nucleons interact with σ , ω and ρ meson fields through Yukawa-like couplings and assuming flat spacetime the equation of state of nuclear matter can be determined. However, it has been clearly stated in [211, 218] that, when we turn into a neutron star configuration at nuclear and supranuclear densities, the global description of the Einstein-Maxwell-Thomas-Fermi equations is mandatory. Associated to this system

of equations there is a sophisticated eigenvalue problem, especially the one for the general relativistic Thomas-Fermi equation is necessary in order to fulfill the global charge neutrality of the system and to consistently describe the confinement of the ultrarelativistic electrons.

We here adopt the phenomenological relativistic mean field nuclear model of Boguta and Bodmer [35] by assuming nucleons interacting in minimal coupling approximation with a σ isoscalar meson field that provides the attractive long-range part of the nuclear force and a massive vector field ω that models the repulsive short range. The self-interacting scalar field potential $U(\sigma)$ is assumed as a quartic polynom with adjustable coefficients. In addition, a massive isovector field ρ is introduced to account for surface as well as isospin effects of nuclei.

The total Lagrangian density of the system is given by

$$\mathcal{L} = \mathcal{L}_g + \mathcal{L}_f + \mathcal{L}_\sigma + \mathcal{L}_\omega + \mathcal{L}_\rho + \mathcal{L}_\gamma + \mathcal{L}_{\text{int}}, \quad (7.1)$$

where the Lagrangian densities for the free-fields are

$$\mathcal{L}_g = -\frac{R}{16\pi G}, \quad (7.2)$$

$$\mathcal{L}_\gamma = -\frac{1}{16\pi} F_{\mu\nu} F^{\mu\nu}, \quad (7.3)$$

$$\mathcal{L}_\sigma = \frac{1}{2} \nabla_\mu \sigma \nabla^\mu \sigma - U(\sigma), \quad (7.4)$$

$$\mathcal{L}_\omega = -\frac{1}{4} \Omega_{\mu\nu} \Omega^{\mu\nu} + \frac{1}{2} m_\omega^2 \omega_\mu \omega^\mu, \quad (7.5)$$

$$\mathcal{L}_\rho = -\frac{1}{4} \mathcal{R}_{\mu\nu} \mathcal{R}^{\mu\nu} + \frac{1}{2} m_\rho^2 \rho_\mu \rho^\mu, \quad (7.6)$$

where $\Omega_{\mu\nu} \equiv \partial_\mu \omega_\nu - \partial_\nu \omega_\mu$, $\mathcal{R}_{\mu\nu} \equiv \partial_\mu \rho_\nu - \partial_\nu \rho_\mu$, $F_{\mu\nu} \equiv \partial_\mu A_\nu - \partial_\nu A_\mu$ are the field strength tensors for the ω^μ , ρ and A^μ fields respectively, ∇_μ stands for covariant derivative and R is the Ricci scalar. We adopt the Lorenz gauge for the fields A_μ , ω_μ , and ρ_μ .

The Lagrangian density for the three fermion species is

$$\mathcal{L}_f = \sum_{i=e,N} \bar{\psi}_i (i\gamma^\mu D_\mu - m_i) \psi_i, \quad (7.7)$$

where ψ_N is the nucleon isospin doublet, ψ_e is the electronic singlet, m_i states for the mass of each particle-specie and $D_\mu = \partial_\mu + \Gamma_\mu$, being Γ_μ the Dirac spin connections.

The interacting part of the Lagrangian density is, in the minimal coupling assumption, given by

$$\mathcal{L}_{\text{int}} = -g_\sigma \sigma \bar{\psi}_N \psi_N - g_\omega \omega_\mu J_\omega^\mu - g_\rho \rho_\mu J_\rho^\mu + e A_\mu J_{\gamma,e}^\mu - e A_\mu J_{\gamma,N}^\mu, \quad (7.8)$$

where the conserved currents are

$$J_\omega^\mu = \bar{\psi}_N \gamma^\mu \psi_N, \quad (7.9)$$

$$J_\rho^\mu = \bar{\psi}_N \tau_3 \gamma^\mu \psi_N, \quad (7.10)$$

$$J_{\gamma,e}^\mu = \bar{\psi}_e \gamma^\mu \psi_e, \quad (7.11)$$

$$J_{\gamma,N}^\mu = \bar{\psi}_N \left(\frac{1 + \tau_3}{2} \right) \gamma^\mu \psi_N. \quad (7.12)$$

The coupling constants of the σ , ω and ρ -fields are g_σ , g_ω and g_ρ , and e is the fundamental electric charge. The Dirac matrices γ^μ and the isospin Pauli matrices satisfy the Dirac algebra in curved spacetime (see e.g. [221, 142] for details).

We first introduce the non-rotating spherically symmetric spacetime metric

$$ds^2 = e^{\nu(r)} dt^2 - e^{\lambda(r)} dr^2 - r^2 d\theta^2 - r^2 \sin^2 \theta d\varphi^2, \quad (7.13)$$

where the $\nu(r)$ and $\lambda(r)$ are only functions of the radial coordinate r .

For very large number of fermions, we adopt the mean-field approximation in which fermion-field operators are replaced by their expectation values (see [221], for instance). Within this approximation, the full system of general relativistic equations can be written in the form

$$e^{-\lambda(r)} \left(\frac{1}{r^2} - \frac{1}{r} \frac{d\lambda}{dr} \right) - \frac{1}{r^2} = -8\pi G T_0^0, \quad (7.14)$$

$$e^{-\lambda(r)} \left(\frac{1}{r^2} + \frac{1}{r} \frac{d\nu}{dr} \right) - \frac{1}{r^2} = -8\pi G T_1^1, \quad (7.15)$$

$$V'' + \frac{2}{r} V' \left[1 - \frac{r(\nu' + \lambda')}{4} \right] = -4\pi e e^{\nu/2} e^\lambda (n_p - n_e), \quad (7.16)$$

$$\frac{d^2\sigma}{dr^2} + \frac{d\sigma}{dr} \left[\frac{2}{r} + \frac{1}{2} \left(\frac{d\nu}{dr} - \frac{d\lambda}{dr} \right) \right] = e^\lambda [\partial_\sigma U(\sigma) + g_s n_s], \quad (7.17)$$

$$\frac{d^2\omega}{dr^2} + \frac{d\omega}{dr} \left[\frac{2}{r} - \frac{1}{2} \left(\frac{d\nu}{dr} + \frac{d\lambda}{dr} \right) \right] = -e^\lambda (g_\omega J_0^\omega - m_\omega^2 \omega), \quad (7.18)$$

$$\frac{d^2\rho}{dr^2} + \frac{d\rho}{dr} \left[\frac{2}{r} - \frac{1}{2} \left(\frac{d\nu}{dr} + \frac{d\lambda}{dr} \right) \right] = -e^\lambda (g_\rho J_0^\rho - m_\rho^2 \rho), \quad (7.19)$$

$$E_e^F = e^{\nu/2} \mu_e - eV = \text{constant}, \quad (7.20)$$

$$E_p^F = e^{\nu/2} \mu_p + \mathcal{V}_p = \text{constant}, \quad (7.21)$$

$$E_n^F = e^{\nu/2} \mu_n + \mathcal{V}_n = \text{constant}, \quad (7.22)$$

where we have introduced the notation $\omega_0 = \omega$, $\rho_0 = \rho$, and $A_0 = V$ for the temporal components of the meson-fields. Here $\mu_i = \partial\mathcal{E}/\partial n_i = \sqrt{(P_i^F)^2 + \tilde{m}_i^2}$ and $n_i = (P_i^F)^3/(3\pi^2)$ are the free-chemical potential and number density of the i -specie with Fermi momentum P_i^F . The particle effective mass is $\tilde{m}_N = m_N + g_s \sigma$ and $\tilde{m}_e = m_e$ and the effective potentials

$\mathcal{V}_{p,n}$ are given by

$$\mathcal{V}_p = g_\omega\omega + g_\rho\rho + eV, \quad (7.23)$$

$$\mathcal{V}_n = g_\omega\omega - g_\rho\rho. \quad (7.24)$$

The constancy of the generalized Fermi energies E_n^F , E_p^F and E_e^F , the Klein potentials, derives from the thermodynamic equilibrium conditions given by the statistical physics of multicomponent systems, applied to a system of degenerate neutrons, protons, and electrons within the framework of general relativity (see [218] for details). These constants are linked by the β -equilibrium [33] between the matter constituents

$$E_n^F = E_p^F + E_e^F. \quad (7.25)$$

The electron density n_e is, via Eq. (7.20), given by

$$n_e = \frac{e^{-3\nu/2}}{3\pi^2} [\hat{V}^2 + 2m_e\hat{V} - m_e^2(e^\nu - 1)]^{3/2}, \quad (7.26)$$

where $\hat{V} \equiv eV + E_e^F$. Substituting Eq. (7.26) into Eq. (7.16) one obtains the general relativistic extension of the relativistic Thomas-Fermi equation recently introduced for the study of compressed atoms [210, 209]. This system of equations has to be solved with the boundary condition of global neutrality; see [211, 218] and below for details.

The scalar density n_s , within the mean-field approximation, is given by the following expectation value

$$n_s = \langle \bar{\psi}_N \psi_N \rangle = \frac{2}{(2\pi)^3} \sum_{i=n,p} \int d^3k \frac{\tilde{m}_N}{\epsilon_i(p)}, \quad (7.27)$$

where $\epsilon_i(p) = \sqrt{p^2 + \tilde{m}_i^2}$ is the single particle energy.

In the static case, only the temporal components of the covariant currents survive, i.e. $\langle \bar{\psi}(x)\gamma^i\psi(x) \rangle = 0$. Thus, by taking the expectation values of Eqs. (7.9)–(7.12), we obtain the non-vanishing components of the currents

$$J_0^{ch} = n_{ch}u_0 = (n_p - n_e)u_0, \quad (7.28)$$

$$J_0^\omega = n_b u_0 = (n_n + n_p)u_0, \quad (7.29)$$

$$J_0^\rho = n_3 u_0 = (n_p - n_n)u_0, \quad (7.30)$$

where $n_b = n_p + n_n$ is the baryon number density and $u_0 = \sqrt{g_{00}} = e^{\nu/2}$ is the covariant temporal component of the four-velocity of the fluid, which satisfies $u^\mu u_\mu = 1$.

The metric function λ is related to the mass $M(r)$ and the electric field $E(r) = -e^{-(\nu+\lambda)/2}V'$ through

$$e^{-\lambda(r)} = 1 - \frac{2GM(r)}{r} + \frac{GQ^2(r)}{r^2}, \quad (7.31)$$

being $Q(r)$ the conserved charge, related to the electric field by $Q(r) = r^2 E(r)$.

The energy-momentum tensor of free-fields and free-fermions $T^{\mu\nu}$ of the system is

$$T^{\mu\nu} = T_f^{\mu\nu} + T_\gamma^{\mu\nu} + T_\sigma^{\mu\nu} + T_\omega^{\mu\nu} + T_\rho^{\mu\nu}, \quad (7.32)$$

where

$$T_\gamma^{\mu\nu} = \frac{1}{4\pi} \left(F_\alpha^\mu F^{\alpha\nu} + \frac{1}{4} g^{\mu\nu} F_{\alpha\beta} F^{\alpha\beta} \right), \quad (7.33)$$

$$T_\sigma^{\mu\nu} = \nabla^\mu \sigma \nabla^\nu \sigma - g^{\mu\nu} \left[\frac{1}{2} \nabla_\sigma \sigma \nabla^\sigma \sigma - U(\sigma) \right], \quad (7.34)$$

$$T_\omega^{\mu\nu} = \Omega_\alpha^\mu \Omega^{\alpha\nu} + \frac{1}{4} g^{\mu\nu} \Omega_{\alpha\beta} \Omega^{\alpha\beta} + m_\omega^2 \left(\omega^\mu \omega^\nu - \frac{1}{2} g^{\mu\nu} \omega_\alpha \omega^\alpha \right), \quad (7.35)$$

$$T_\rho^{\mu\nu} = \mathcal{R}_\alpha^\mu \mathcal{R}^{\alpha\nu} + \frac{1}{4} g^{\mu\nu} \mathcal{R}_{\alpha\beta} \mathcal{R}^{\alpha\beta} + m_\rho^2 \left(\mathcal{R}^\mu \mathcal{R}^\nu - \frac{1}{2} g^{\mu\nu} \mathcal{R}_\alpha \omega^\alpha \right), \quad (7.36)$$

$$T_f^{\mu\nu} = (\mathcal{E} + \mathcal{P}) u^\mu u^\nu - \mathcal{P} g^{\mu\nu}, \quad (7.37)$$

where the energy-density \mathcal{E} and the pressure \mathcal{P} are given by

$$\mathcal{E} = \sum_{i=n,p,e} \mathcal{E}_i, \quad \mathcal{P} = \sum_{i=n,p,e} \mathcal{P}_i, \quad (7.38)$$

being \mathcal{E}_i and \mathcal{P}_i the single fermion fluid contributions

$$\mathcal{E}_i = \frac{2}{(2\pi)^3} \int_0^{P_i^F} \epsilon_i(p) 4\pi p^2 dp, \quad (7.39)$$

$$\mathcal{P}_i = \frac{1}{3} \frac{2}{(2\pi)^3} \int_0^{P_i^F} \frac{p^2}{\epsilon_i(p)} 4\pi p^2 dp. \quad (7.40)$$

It is worth recalling that the equation of state (7.38)–(7.40) satisfies the thermodynamic law

$$\mathcal{E} + \mathcal{P} = \sum_{i=n,p,e} n_i \mu_i. \quad (7.41)$$

The parameters of the nuclear model, namely the coupling constants g_s , g_ω and g_ρ , and the meson masses m_σ , m_ω and m_ρ are fixed by fitting experimental properties of nuclei, such as saturation density, binding energy per nucleon (or experimental masses), symmetry energy, surface energy, and nuclear incompressibility. In Table 7.1 we present selected fits of the nuclear parameters. In particular, we show the following parameter sets: NL3 [135], NL-SH [238], TM1 [248], and TM2 [115].

The constants g_2 and g_3 are the third and fourth order constants of the self-scalar interaction as given by the scalar self-interaction potential (see [35], for instance)

$$U(\sigma) = \frac{1}{2} m_\sigma^2 \sigma^2 + \frac{1}{3} g_2 \sigma^3 + \frac{1}{4} g_3 \sigma^4. \quad (7.42)$$

The non-zero constant c_3 that appears in the TM1 and TM2 models corresponds to the self-coupling constant of the non-linear vector self-coupling $\frac{1}{4} c_3 (\omega_\mu \omega^\mu)^2$. We have not

	NL3	NL-SH	TM1	TM2
m_σ (MeV)	508.194	526.059	511.198	526.443
m_ω (MeV)	782.501	783.000	783.000	783.000
m_ρ (MeV)	763.000	763.000	770.000	770.000
g_s	10.2170	10.4440	10.0289	11.4694
g_ω	12.8680	12.9450	12.6139	14.6377
g_ρ	4.4740	4.3830	4.6322	4.6783
g_2 (fm $^{-1}$)	-10.4310	-6.9099	-7.2325	-4.4440
g_3	-28.8850	-15.8337	0.6183	4.6076
c_3	0.0000	0.0000	71.3075	84.5318

Table 7.1: Selected parameter sets of the σ - ω - ρ model.

include such a self-coupling vector interaction in the general formulation presented above. However, we show also here the results of the integration when such a self-interaction is taken into account and we refer to [248, 115] for details about the motivations of including such a contribution.

The numerical integration of the core equations can be started with a given central density and the regularity conditions at the origin; see below Sec. 7.3 for details. At nuclear density the phase-transition to the “solid” crust takes place. Thus, the radius of the core R_{core} is given by $\mathcal{E}(r = R_{\text{core}})/c^2 = \rho_{\text{nuc}} = \rho_0$. These equations must be solved with the boundary conditions given by the fulfillment of the condition of global charge neutrality and the continuity of the Klein potentials of particles between the core and the crust.

7.2.2 Core-crust transition layer equations

In the core-crust interface, the mean-field approximation for the meson-fields is not valid any longer and thus a full numerical integration of the meson-field equations of motion, taking into account all gradient terms, must be performed. We expect the core-crust transition boundary-layer to be a region with characteristic length scale of the order of the electron Compton wavelength $\sim \lambda_e = \hbar/(m_e c) \sim 100$ fm corresponding to the electron screening scale. Then, in the core-crust transition layer, the system of equations (7.14)–(7.22) reduces to

$$V'' + \frac{2}{r}V' = -e^{\lambda_{\text{core}}} e J_{ch}^0, \quad (7.43)$$

$$\sigma'' + \frac{2}{r}\sigma' = e^{\lambda_{\text{core}}} [\partial_\sigma U(\sigma) + g_s n_s], \quad (7.44)$$

$$\omega'' + \frac{2}{r}\omega' = -e^{\lambda_{\text{core}}} [g_\omega J_0^\omega - m_\omega^2 \omega], \quad (7.45)$$

$$\rho'' + \frac{2}{r}\rho' = -e^{\lambda_{\text{core}}} [g_\rho J_0^\rho - m_\rho^2 \rho], \quad (7.46)$$

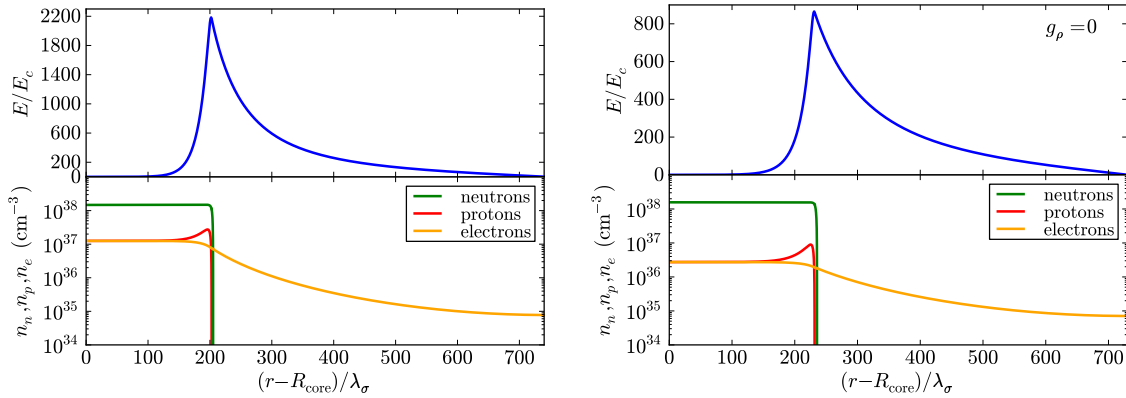


Figure 7.1: Left Fig. upper panel: electric field in the core-crust transition layer in units of the critical field E_c . Lower panel: particle density profiles in the core-crust boundary interface in units of cm^{-3} . Here we use the NL3-model of Table 7.1 and $\lambda_\sigma = \hbar/(m_\sigma c) \sim 0.4$ fm denotes the sigma-meson Compton wavelength. The density at the edge of the crust in this example is $\rho_{\text{crust}} = \rho_{\text{drip}} = 4.3 \times 10^{11}$ g/cm³. Right Fig. the same as Left Fig., but setting $g_\rho = 0$ in order to see the effects of the ρ -meson with respect to the case $g_\rho \neq 0$.

$$e^{\nu_{\text{core}}/2} \mu_e - eV = \text{constant}, \quad (7.47)$$

$$e^{\nu_{\text{core}}/2} \mu_p + eV + g_\omega \omega + g_\rho \rho = \text{constant}, \quad (7.48)$$

$$\mu_n = \mu_p + \mu_e + 2g_\rho \rho e^{-\nu_{\text{core}}/2}, \quad (7.49)$$

due to the fact that the metric functions are essentially constant on the core-crust transition layer and thus we can take their values at the core-radius $e^{\nu_{\text{core}}} \equiv e^{\nu(R_{\text{core}})}$ and $e^{\lambda_{\text{core}}} \equiv e^{\lambda(R_{\text{core}})}$.

The system of equations of the transition layer has a stiff nature due to the existence of two different scale lengths. The first one is associated with the nuclear interactions $\sim \lambda_\pi = \hbar/(m_\pi c) \sim 1.5$ fm and the second one is due to the aforementioned screening length $\sim \lambda_e = \hbar/(m_e c) \sim 100$ fm. Thus, the numerical integration of Eqs. (7.43)–(7.49) has been performed subdividing the core-crust transition layer in the following three regions: (I) a mean-field-like region where all the fields vary slowly with length scale $\sim \lambda_e$, (II) a strongly interacting region of scale $\sim \lambda_\pi$ where the surface tension due to nuclear interactions dominate producing a sudden decrease of the proton and the neutron densities and, (III) a Thomas-Fermi-like region of scale $\sim \lambda_e$ where only a layer of opposite charge made of electrons is present producing the total screening of the positively charged core. The results of the numerical integration of the equilibrium equations are shown in Figs. 7.1 for the NL3-model.

We have integrated numerically Eqs. (7.14)–(7.22) for the models listed in Table 7.1. The boundary conditions for the numerical integration are fixed through the following procedure. We start assuming a value for the central baryon number density $n_b(0) = n_n(0) + n_p(0)$. From the regularity conditions at the origin we have $e^{-\lambda(0)} = 1$ and

$$n_e(0) = n_p(0).$$

The metric function ν at the origin can be chosen arbitrarily, e.g. $\nu(0) = 0$, due to the fact that the system of equations remain invariant under the shift $\nu \rightarrow \nu + \text{constant}$. The right value of ν is obtained once the end of the integration of the core has been accomplished and duly matched to the crust, by fulfilling the following identity at the surface of the neutron star,

$$e^{\nu(R)} = e^{-\lambda(R)} = 1 - \frac{2GM(R)}{c^2 R}, \quad (7.50)$$

being $M(R)$ and R the total mass and radius of the star. Then, taking into account the above conditions, we solve the system (7.17)–(7.22) at the origin for the other unknowns $\sigma(0)$, $\omega(0)$, $\rho(0)$, $n_n(0)$, $n_p(0)$, $n_e(0)$.

The initial conditions for the numerical integration of the core-crust transition layer equations are determined through the final values given by the numerical integration of the core equations, i.e. we take the values of all the variables at the core-radius R_{core} .

In the region I the effect of the Coulomb interaction is clear: on the proton-profile we can see a bump due to Coulomb repulsion while the electron-profile decreases as expected. Such a Coulomb effect is indirectly felt also by the neutrons due to the coupled nature of the system of equations. However, the neutron-bump is much smaller than the one of protons and it is not appreciable in Figs. 7.1 due to the plot-scale. In the region II we see clearly the effect of the surface tension due to nuclear interaction which produces a sharp decrease of the neutron and proton profiles in a characteristic scale $\sim \lambda_\pi$. In addition, one can see a neutron skin effect, analogous to the one observed in heavy nuclei, which makes the scale of the neutron density falloff slightly larger with respect to the proton one, in close analogy to the neutron skin effect observed in neutron rich nuclei, see e.g. [251]. The region III is characterized by a smooth decreasing of the electron density which resembles the behavior of the electrons surrounding a nucleus in the Thomas-Fermi model.

The matching to the crust must be done at a radius $R_{\text{core}} + \delta R$ where full charge neutrality of the core is reached. Different thicknesses δR correspond to different electron Fermi energies E_e^F . The thickness of the core-crust transition boundary layer δR as well as the value of the electron density at the edge of the crust, $n_e^{\text{crust}} = n_e(R_{\text{core}} + \delta R)$, depend on the nuclear parameters, especially on the nuclear surface tension.

The equilibrium conditions given by the constancy of the Klein potentials (7.20)–(7.22) throughout the configuration, impose in the transition layer the following continuity condition

$$E_e^F = e^{\nu_{\text{core}}/2} \mu_e^{\text{core}} - eV^{\text{core}} = e^{\nu_{\text{crust}}/2} \mu_e^{\text{crust}}, \quad (7.51)$$

where $\mu_e^{\text{core}} = \mu_e(R_{\text{core}})$, $eV^{\text{core}} = eV(R_{\text{core}})$, and $\mu_e^{\text{crust}} = \mu_e(R_{\text{core}} + \delta R)$, and $e^{\nu_{\text{crust}}} \simeq e^{\nu_{\text{core}}}$.

In the boundary interface, the electron chemical potential and the density decrease: $\mu_e^{\text{crust}} < \mu_e^{\text{core}}$ and $\rho_{\text{crust}} < \rho_{\text{core}}$. For each central density, an entire family of core-crust interface boundaries exist each one with a specific value of δR : the larger the ρ_{crust} , the smaller the δR . Correspondingly, an entire family of crusts with different mass and thickness, exist. From the continuity of the electron Klein potential in the boundary interface given by Eq. (7.51), it follows that different values of $\rho_{\text{crust}} \geq 0$ correspond to different

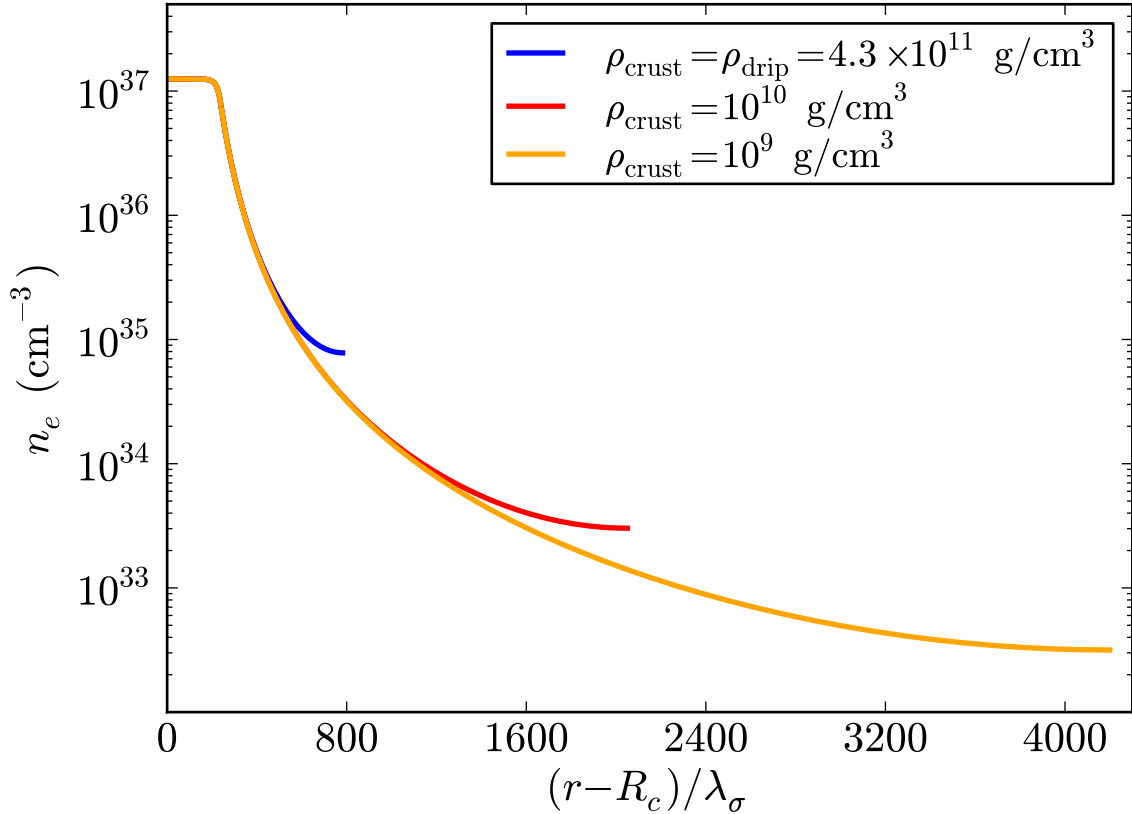


Figure 7.2: Distribution of electrons in the core-crust boundary interface for different densities at the edge of the crust, ρ_{crust} . The larger the ρ_{crust} , the smaller the electric field E and the smaller the thickness of the interface δR .

values of the electron Fermi energy $E_e^F \geq 0$. In close analogy to the compressed atoms studied in [210], the case $E_e^F = 0$ corresponds to the “free” (uncompressed) configuration, where $\delta R \rightarrow \infty$ and $\rho_{\text{crust}} = 0$, i.e. a bare core. In this configuration the electric field reaches its maximum value. The case $E_e^F > 0$ is analogous to the one of the compressed atom [210]. In Fig. 7.2 we have plotted the electron distribution in the core-crust boundary interface for selected densities at the edge of the crust $\rho_{\text{crust}} = [\rho_{\text{drip}}, 10^{10}, 10^9] \text{ g/cm}^3$, where $\rho_{\text{drip}} \sim 4.3 \times 10^{11} \text{ g/cm}^3$ is the neutron drip density.

The configuration with $\rho_{\text{crust}} = \rho_{\text{drip}}$ separates neutron stars with and without inner crust. In the so-called inner crust, the neutrons dripped from the nuclei in the crust form a fluid that coexist with the nuclei lattice and the degenerate electrons [15]. For definiteness, we present in this work the results for configurations $\rho_{\text{crust}} \leq \rho_{\text{drip}}$, i.e for neutron stars possessing only outer crust. The construction of configurations with $\rho_{\text{crust}} > \rho_{\text{drip}}$ needs to be studied in more detail and will be the subject of a forthcoming work. In Figs. 7.1, we show the core-crust transition layer for the NL3 model of Table 7.1 with and without the presence of the ρ -meson respectively. The presence of the ρ -meson is responsible for the nuclear asymmetry within this nuclear model. The relevance of the nuclear symmetry

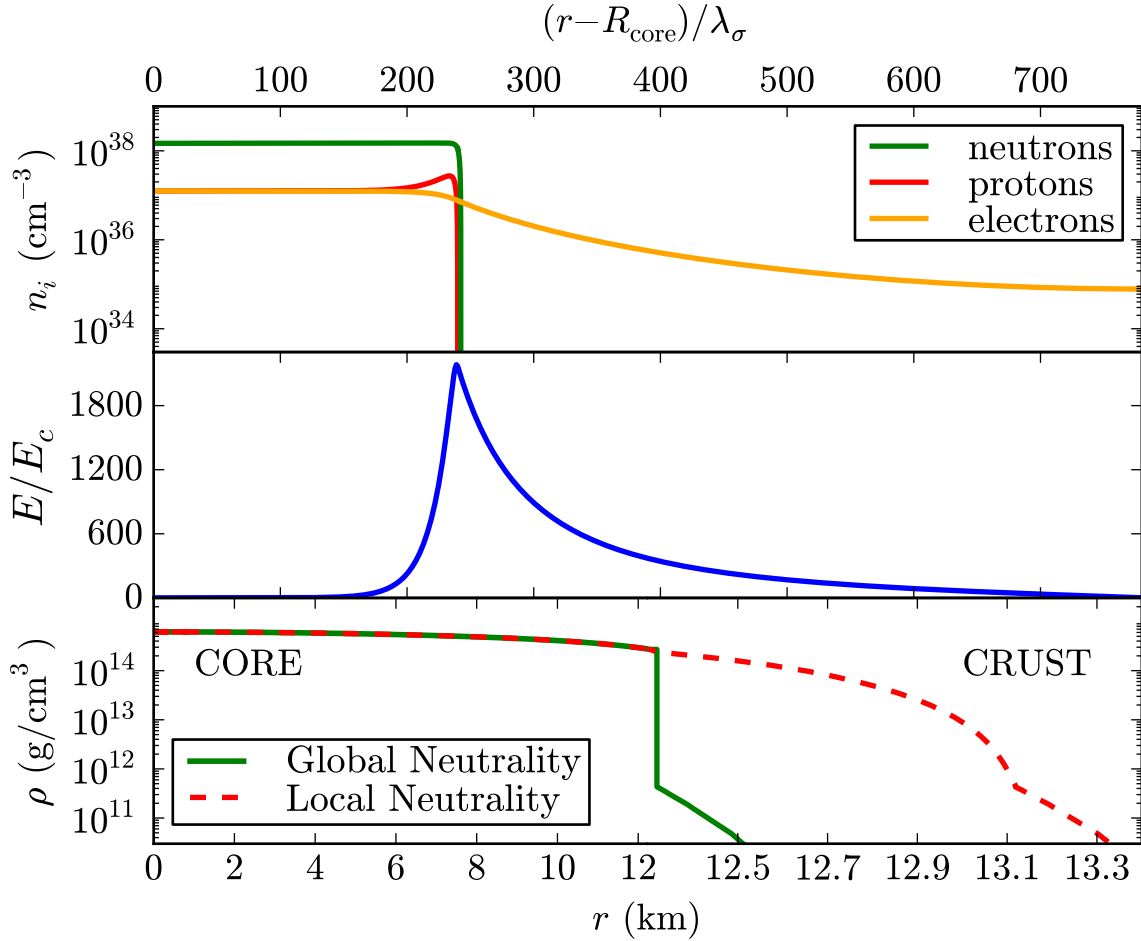


Figure 7.3: Upper panel: particle density profiles in the core-crust boundary interface, in units of cm^{-3} . Middle panel: electric field in the core-crust transition layer, in units of the critical field E_c . Lower panel: density profile inside a neutron star with central density $\rho(0) \sim 5\rho_{\text{nuc}}$. We compare and contrast the structural differences between the solution obtained from the traditional TOV equations (locally neutral case) and the globally neutral solution presented here. We use here the NL3 nuclear parametrization of Table 7.1 and $\lambda_\sigma = \hbar/(m_\sigma c) \sim 0.4$ fm, denotes the sigma-meson Compton wavelength. In this example the density at the edge of the crust is $\rho_{\text{crust}} = \rho_{\text{drip}} = 4.3 \times 10^{11}$ g/cm^3 .

energy on the structure of nuclei and neutron stars is continuously stressed in literature; see e.g. [171, 130, 237, 109, 151]. The precise value of the nuclear symmetry energy plays here a crucial role in determining the precise value of the ρ -meson coupling which, in the present case, is essential in the determination of the intensity of the electric field in the core-crust boundary interface; as can be seen from the comparison of Figs. 7.1.

7.2.3 Crust equations

Turning now to the crust, it is clear from our recent treatment of white dwarfs [209] that also this problem can be solved by the adoption of Wigner-Seitz cells and from the relativistic Feynman-Metropolis-Teller (RFMT) approach [210] it follows that the crust is clearly neutral. Thus, the structure equations to be integrated are the TOV equations

$$\frac{d\mathcal{P}}{dr} = -\frac{G(\mathcal{E} + \mathcal{P})(M + 4\pi r^3 \mathcal{P})}{r^2(1 - \frac{2GM}{r})}, \quad (7.52)$$

$$\frac{dM}{dr} = 4\pi r^2 \mathcal{E}, \quad (7.53)$$

where $M = M(r)$ is the mass enclosed at the radius r .

The effects of the Coulomb interaction in “solid”-like electron-ion systems appears only at the microscopic level e.g. Debye-Hueckel screening in classical systems [64] and Thomas-Fermi screening in the degenerate case [168]. In order to analyze the effects of the microscopic screening on the structure of the configuration we will consider two equations of state for the crust: the locally neutral case or uniform approximation (see e.g. [53]) and, for simplicity, instead of using the RFMT EoS [210], we use as second EoS the one due to Baym, Pethick and Sutherland (BPS) [15], which is by far the most used equation of state in literature for the description of the neutron star crust (see e.g. [101]).

In the uniform approximation, both the degenerate electrons and the nucleons distribution are considered constant inside each cell of volume V_{ws} . This kind of configuration can be obtained only imposing microscopically the condition of local charge neutrality

$$n_e = \frac{Z}{V_{\text{ws}}}. \quad (7.54)$$

The total pressure of the system is assumed to be entirely due to the electrons, i.e.

$$\mathcal{P} = \mathcal{P}_e = \frac{2}{3(2\pi\hbar)^3} \int_0^{P_e^F} \frac{c^2 p^2 4\pi p^2}{\sqrt{c^2 p^2 + m_e^2 c^4}} dp, \quad (7.55)$$

while the total energy-density of the system is due to the nuclei, i.e. $\mathcal{E} = (A/Z)m_N n_e$, where m_N is the nucleon mass.

We turn now to the BPS equation of state. The first correction to the uniform model, corresponds to abandon the assumption of the electron-nucleon fluid through the so-called “lattice” model which introduces the concept of Wigner-Seitz cell: each cell of radius R_{ws}

contains a point-like nucleus of charge $+Ze$ with A nucleons surrounded by a uniformly distributed cloud of Z fully-degenerate electrons.

The sequence of the equilibrium nuclides present at each density in the BPS equation of state is obtained by looking for the nuclear composition that minimizes the energy per nucleon for each fixed nuclear composition (Z, A) (see [15] for details). The pressure \mathcal{P} and the energy-density \mathcal{E} of the system are, within this model, given by

$$\mathcal{P} = \mathcal{P}_e + \frac{1}{3}W_L n_N, \quad (7.56)$$

$$\frac{\mathcal{E}}{n_b} = \frac{W_N + W_L}{A} + \frac{\mathcal{E}_e(n_b Z/A)}{n_b}, \quad (7.57)$$

where the electron energy-density is given by

$$\mathcal{E}_e = \frac{2}{(2\pi)^3} \int_0^{P_e^F} \sqrt{p^2 + m_e^2} 4\pi p^2 dp, \quad (7.58)$$

and $W_N(A, Z)$ is the total energy of an isolated nucleus given by the semi-empirical formula

$$W_N = m_n c^2 (A - Z) + m_p c^2 Z - bA, \quad (7.59)$$

with b being the Myers and Swiatecki binding energy per nucleon [172]. The lattice energy per nucleus W_L is given by

$$W_L = -\frac{1.819620Z^2 e^2}{a}, \quad (7.60)$$

where the lattice constant a is related to the nucleon density n_N by $n_N a^3 = 2$.

7.3 Neutron star structure

In the traditional TOV treatment the density and the pressure are a priori assumed to be continuous as well as the local charge neutrality of the system. The distinguishing feature of our new solution is that the Klein potentials are constant throughout the three regions; the core, the crust and the transition interface boundary. An overcritical electric field is formed and consequently a discontinuity in density is found with a continuous total pressure including the surface tension of the boundary. In Fig. 7.3, we compare and contrast the density profiles of configurations obtained from the traditional TOV treatment and with the treatment presented here.

It is worth noting that the inclusion of the Coulomb interaction and in particular the presence of the negative lattice energy W_L results in a decreasing of the pressure of the cells. Such an effect, leads to a decreasing of the mass and the thickness of the crust with respect to the uniform-approximation case where no Coulomb interactions are taken into account. Comparing the mass and the thickness of the crust obtained with these two different EoS, we obtain systematically crusts with smaller mass and larger thickness when Coulomb interactions are taken into account. This results are in line with the recent

results in [209], where the mass-radius relation of white-dwarfs has been calculated using an EoS based on the relativistic Feynman-Metropolis-Teller model for compressed atoms [210].

In the case of the BPS EoS, the average nuclear composition in the outer crust, namely the average charge to mass ratio of nuclei Z/A , is obtained by calculating the contribution of each nuclear composition present to the mass of the crust. We exemplified the analysis for two different cores: $M_{\text{core}} = 2.56M_{\odot}$, $R_{\text{core}} = 12.79$ km; $M_{\text{core}} = 1.35M_{\odot}$, $R_{\text{core}} = 11.76$ km. The relative abundance of each nuclide within the crust of the star can be obtained as

$$\text{R.A.} = \frac{1}{M_{\text{crust}}^{\text{BPS}}} \int_{\Delta r} 4\pi r^2 \mathcal{E} dr, \quad (7.61)$$

where the integration is carried out in the layer of thickness Δr where the particular nuclide is present; Our results are in agreement with the analysis on the neutron star crust composition obtained in [98, 188]. In both cases we obtain as average nuclear composition $^{105}_{35}\text{Br}$. The corresponding crusts with fixed nuclear composition $^{105}_{35}\text{Br}$ for the two chosen cores are calculated neglecting Coulomb interactions (i.e. using the first EoS). The mass and the thickness of these crusts with fixed $^{105}_{35}\text{Br}$ are different with respect to the ones obtained using the full BPS EoS, leading to such average nuclear composition. For the two selected examples we obtain that the mass and the thickness of the crust with average $^{105}_{35}\text{Br}$ are, respectively, 18% larger and 5% smaller with respect to the ones obtained with the corresponding BPS EoS. This result shows how small microscopic effects due to the Coulomb interaction in the crust of the neutron star leads to quantitative not negligible effects on the macroscopic structure of the configuration (see [18] for details).

7.4 Observational constraints on the mass-radius relation

It has been recently pointed out that the most up-to-date stringent constraints to the mass-radius relation of neutron stars are provided by the largest mass, the largest radius, the highest rotational frequency, and the maximum surface gravity, observed for pulsars [262].

So far, the highest neutron star mass measured with a high level of experimental confidence is the mass of the 3.15 millisecond pulsar PSR J1614-2230, $M = 1.97 \pm 0.04 M_{\odot}$, obtained from the Shapiro time delay and the Keplerian orbital parameters of the binary system [65]. The fitting of the thermonuclear burst oscillation light curves from the accreting millisecond pulsar XTE J1814-338 weakly constrain the mass-radius relation imposing an upper limit to the surface gravity of the neutron star, $GM/(c^2 R) < 0.24$ [22]. A lower limit of the radius of RX J1856-3754, as seen by an observer at infinity $R_{\infty} = R[1 - 2GM/(c^2 R)]^{-1/2} > 16.8$ km, has been obtained from the fit of the optical and X-ray spectra of the source [263]; it gives the constraint $2GM/c^2 > R - R^3/(R_{\infty}^{\text{min}})^2$, being $R_{\infty}^{\text{min}} = 16.8$ km. Assuming a neutron star of $M = 1.4M_{\odot}$ to fit the Chandra data of the low-mass X-ray binary X7, it turns out that the radius of the star satisfies

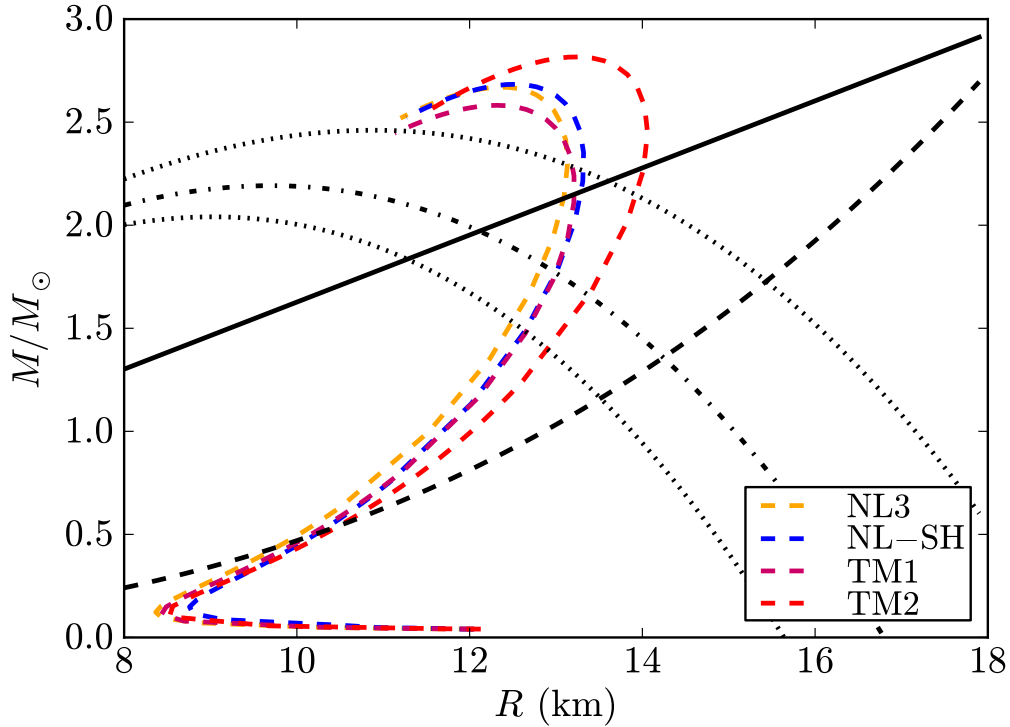


Figure 7.4: Constraints on the mass-radius relation given by J. E. Trümper in [262] and the theoretical mass-radius relation presented in this work. The solid line is the upper limit of the surface gravity of XTE J1814-338, the dotted-dashed curve corresponds to the lower limit to the radius of RX J1856-3754, the dashed line is the constraint imposed by the fastest spinning pulsar PSR J1748-2246ad, and the dotted curves are the 90% confidence level contours of constant R_∞ of the neutron star in the low-mass X-ray binary X7. Any mass-radius relation should pass through the area delimited by the solid, the dashed and the dotted lines and, in addition, it must have a maximum mass larger than the mass of PSR J1614-2230, $M = 1.97 \pm 0.04 M_\odot$.

$R = 14.5_{-1.6}^{+1.8}$ km, at 90% confidence level, corresponding to $R_\infty = [15.64, 18.86]$ km, respectively (see [110] for details). The maximum rotation rate of a neutron star taking into account both the effects of general relativity and deformations has been found to be $\nu_{\max} = 1045(M/M_\odot)^{1/2}(10 \text{ km}/R)^{3/2}$ Hz, largely independent of the equation of state [140]. The fastest observed pulsar is PSR J1748-2246ad with a rotation frequency of 716 Hz [112], which results in the constraint $M \geq 0.47(R/10 \text{ km})^3 M_\odot$. In Fig. 7.4 we show all these constraints and the mass-radius relation presented in this work.

As discussed by J. E. Trümper in [262], the above constraints strongly favor stiff equations of state which provide high maximum masses for neutron stars. In addition, putting all of them together, the radius of a canonical neutron star of mass $M = 1.4 M_\odot$ is highly constrained to the range $R \gtrsim 12$ km disfavoring, at the same time, the strange quark hypothesis for these specific objects. It is clear from Fig. 7.4 that the mass-radius

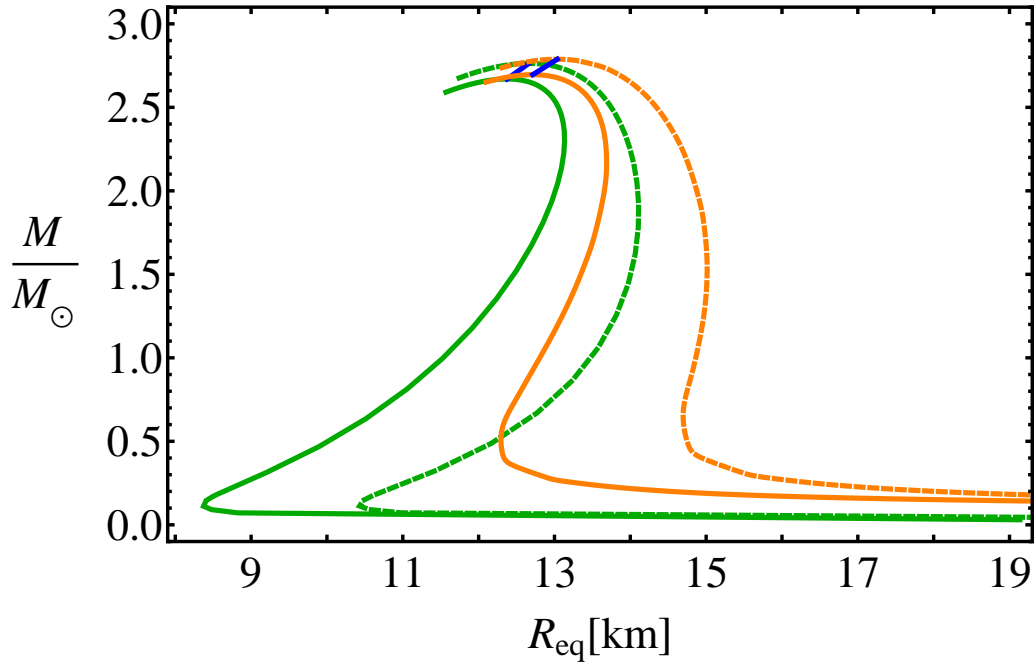


Figure 7.5: Mass-Radius relation obtained with the traditional locally neutral TOV treatment (orange lines) and with the new globally neutral equilibrium configurations (green lines) presented here. We use here the NL3 nuclear model, see Table 7.1. Solid blue lines show axisymmetric secular instability lines. Solid orange and green lines correspond to the static case and the dashed lines show corresponding Keplerian sequences.

relation presented here is consistent with all the observation constraints, for all the nuclear parametrizations of Table 7.1.

7.5 Comparison with the traditional TOV treatment

In the traditional TOV treatment local charge neutrality as well as the continuity of the pressure and the density in the core-crust transition are assumed. This leads to explicit violation of the constancy of the Klein potentials throughout the configuration (see e.g. [211]). In such a case there is a smooth transition from the core to the crust without any density discontinuity and therefore the density at the edge of the crust is $\sim \rho_{\text{nuc}} = \rho_0 \sim 2.7 \times 10^{14} \text{ g/cm}^3$. The so-called inner crust in those configurations extends in the range of densities $\rho_{\text{drip}} \lesssim \rho \lesssim \rho_{\text{nuc}}$ while, at densities $\rho \lesssim \rho_{\text{drip}}$, there is the so-called outer crust.

The markedly differences both in mass and thickness of the crusts (see [18] for details) obtained from the traditional Tolman-Oppenheimer-Volkoff approach and the new equilibrium configurations presented here, leads to a very different mass-radius relations which we compare and contrast in Fig. 7.5.

7.6 Rotating neutron stars

To rotate a static neutron star we make use of Hartle's formalism by analogy to what we have already performed in Chapter 5. From the conceptual point of view it is well-known that Hartle's formalism is valid only for neutral systems, when there is no any electric charge and the pressure is the function of the density only. As it has been pointed out in this and previous chapters we consider a globally neutral configuration. Moreover the critical electric field that emerges at the transition layer between core and crust does not affect the total mass of the configuration. In addition the thickness of the transition layer is negligible with respect to the size of the configuration. The critical magnetic field that is generated due to the rotation is also limited in the transition layer and outside it is very small, as it can be seen from the previous chapter. These facts allow us to neglect the electromagnetic field in these configurations and safely use Hartle's approach in order to analyze the stability of rotating configurations against axisymmetric secular instabilities discussed in [84] and estimate the maximum mass and minimum period of neutron stars.

The maximum mass of neutron stars plays an important role in determining the end point of the evolution of massive stars. In other words it sets the upper bound for the mass of neutron stars before undergoing a gravitational collapse. To this end, the maximum mass of non-rotating and rotating neutron stars has been intensively studied in the literature (see [205, 57, 106, 83, 191, 99, 244, 111, 123] for details). Depending on the model and the equation of state the maximum masses are different. In our case with the assumptions, the global or local charge neutrality, we have obtained $M_{max}^{rot} \sim 2.76M_{\odot}$ and $M_{max}^{rot} \sim 2.78M_{\odot}$ and the corresponding central densities $\rho_c = 6.12\rho_{nuc}$ and $\rho_c = 5.89\rho_{nuc}$, respectively. The maximum static masses are $M_{max}^{stat} \sim 2.67M_{\odot}$ and $M_{max}^{rot} \sim 2.69M_{\odot}$ and the corresponding central densities are $\rho_c = 6.32\rho_{nuc}$ and $\rho_c = 6.18\rho_{nuc}$, respectively. The larger masses of the locally neutral configurations with respect to the globally neutral one are the sequence of the presence of the inner crust (see Figs. 7.5, 7.6, 7.7, 7.8, 7.9 for details).

The minimum period has been studied in the literature intensively as well (see [269, 94, 100, 129] for details) since it determines the upper limits for the frequency of neutron stars close to the mass shedding. Before defining the minimum period we have analyzed the stability of the system against axisymmetric secular instabilities [84]. As we expected, it turned out that the turning points (the maximum masses) of the constant angular momentum (J) sequences were almost located along the line connecting the maximum static and rotating masses on the mass-central density, the mass-radius etc. planes (see Appendix E). We have obtained for the globally and locally neutral system the minimum periods $P_{min} \sim 0.51$ and ~ 0.53 ms with the corresponding central densities $\rho_c \sim 6.12\rho_{nuc}$ and $\sim 5.89\rho_{nuc}$, respectively. Since for the globally neutral configuration we have no inner crust, its size is smaller than the locally neutral one, though their masses are slightly different. As a result we have the smaller rotation period for the globally neutral configuration (see Figs. 7.5, 7.6, 7.7, 7.8, 7.9 and Appendix E for details).

The shape of these configurations becomes less oblate with the increasing central density (see Figs. 7.8, 7.9 for details). The size of the core initially increases then after

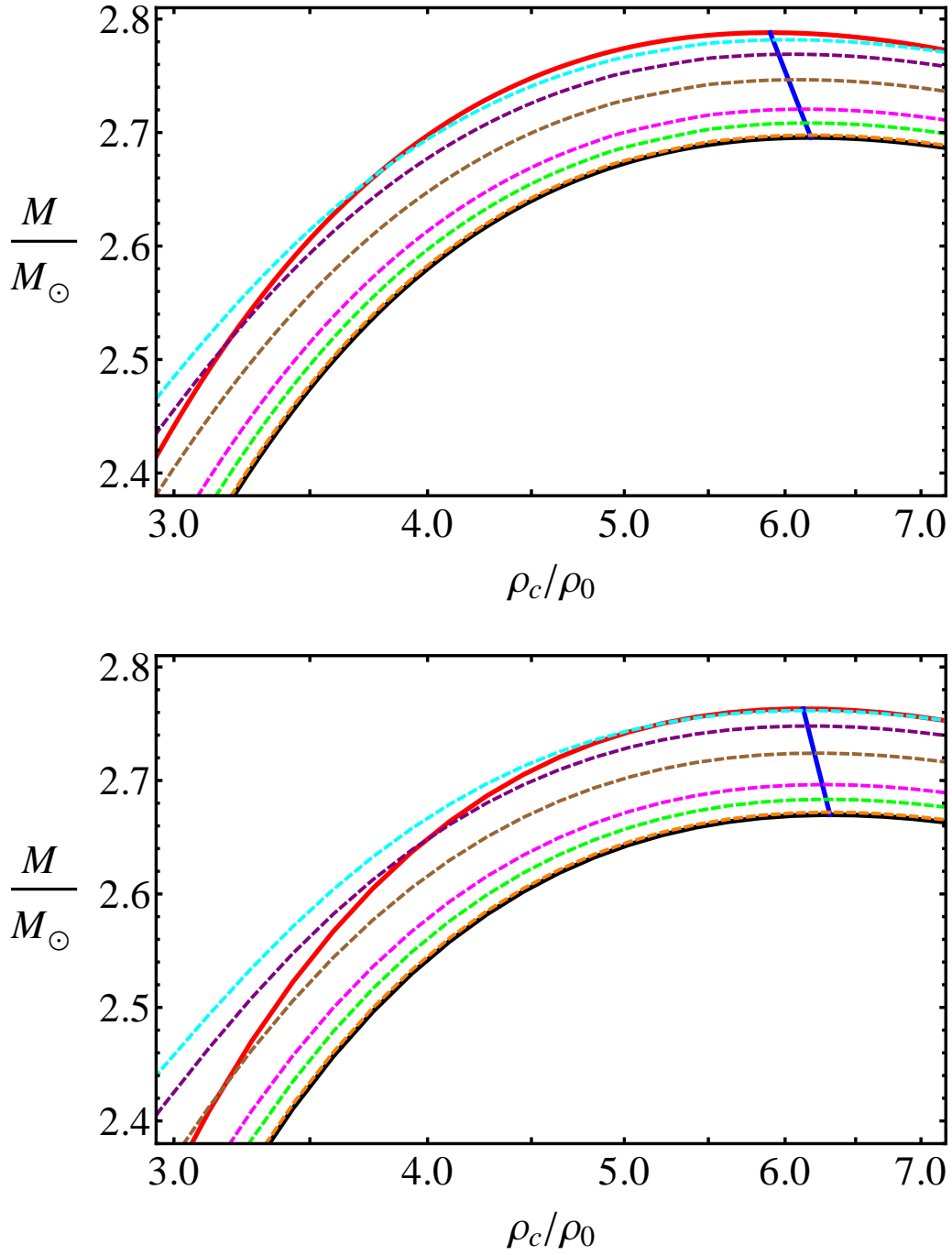


Figure 7.6: Mass-Central density relation obtained with the traditional locally neutral TOV treatment (top panel) and with the new globally neutral equilibrium configurations presented here (bottom panel). The black thick line is the static case, the red thick line is the Keplerian sequence, the blue thick line is the axisymmetric secular instability line and the rest dashed lines are $J = \text{constant}$ sequences. We use here the NL3 nuclear model, see Table 7.1.

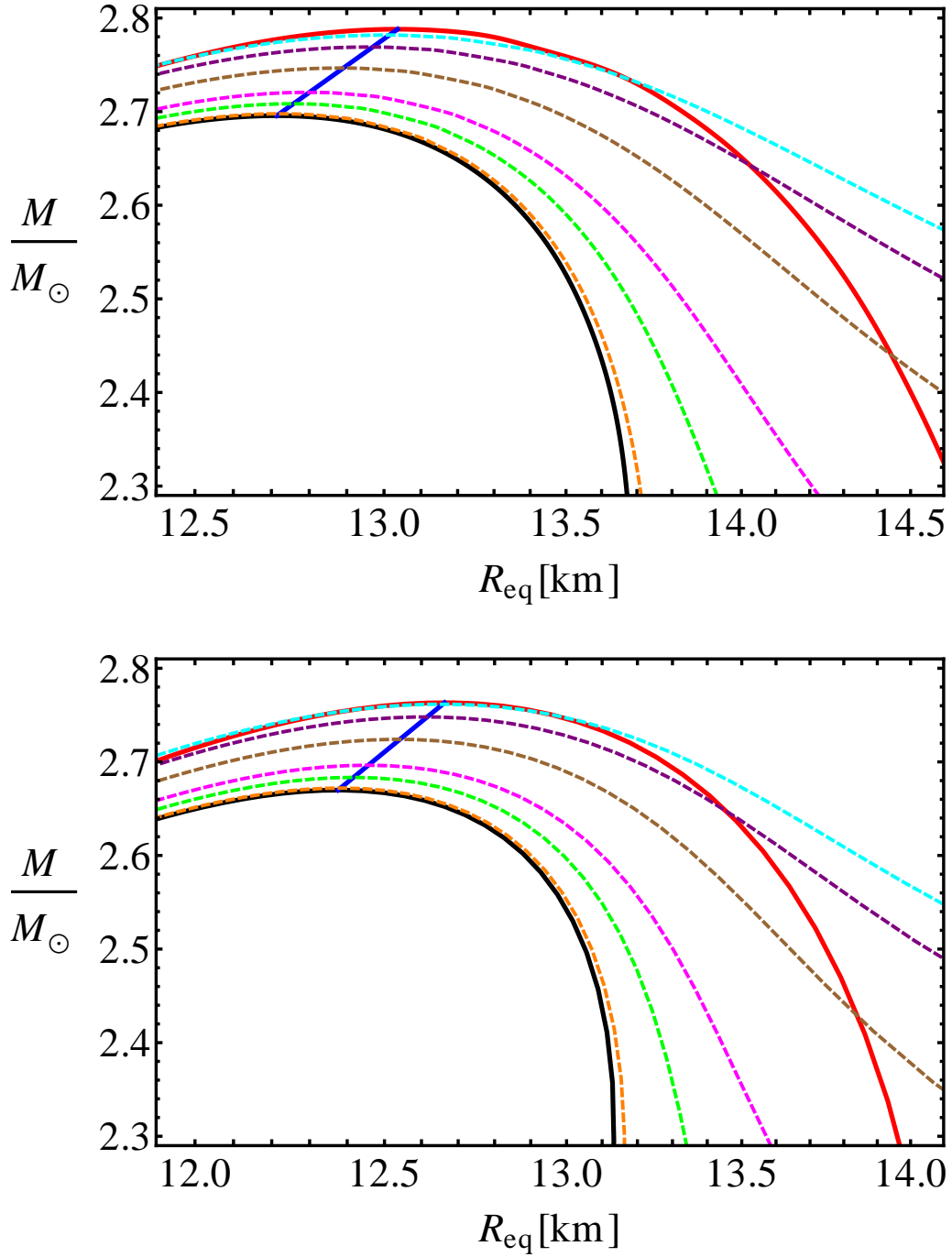


Figure 7.7: Mass-Radius relation obtained with the traditional locally neutral TOV treatment (top panel) and with the new globally neutral equilibrium configurations presented here (bottom panel). The black thick line is the static case, the red thick line is the Keplerian sequence, the blue thick line is the axisymmetric secular instability line and the rest dashed lines are $J = \text{constant}$ sequences. We use here the NL3 nuclear model, see Table 7.1.

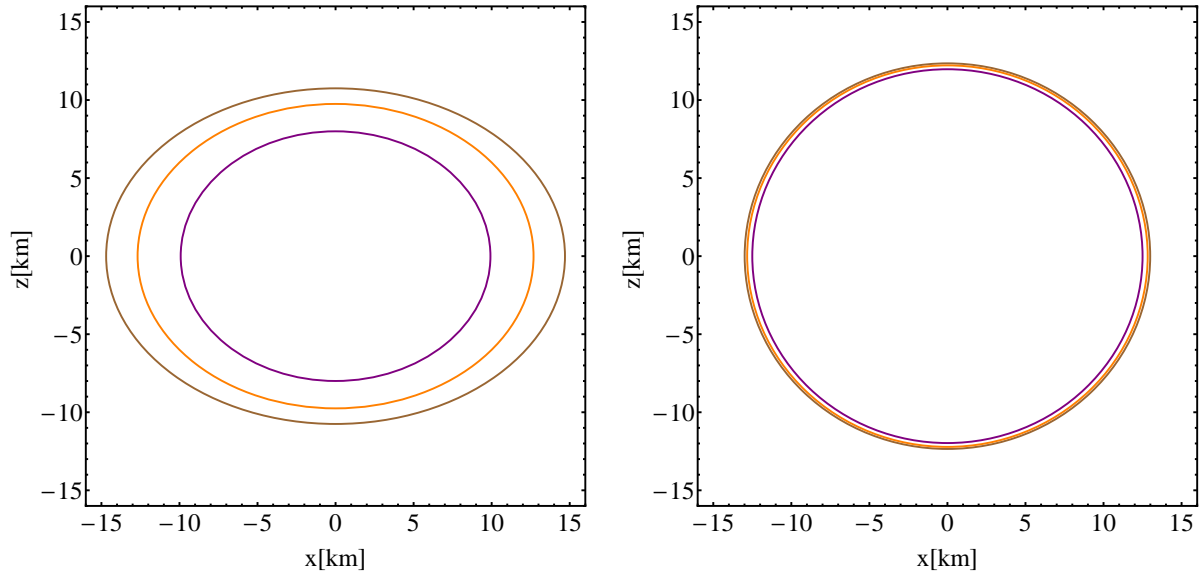


Figure 7.8: Cross section in the plane passing through the rotational axis of a neutron star with the traditional locally neutral TOV treatment at frequency $f = 852\text{Hz}$ and $f = 1900\text{Hz}$. The total rotating gravitational mass is $M = 0.67M_{\odot}$ and $M = 2.78M_{\odot}$, the central density $\rho_c = 1.445\rho_{nuc}$ and $\rho_c = 6\rho_{nuc}$ (left and right panels). The contours are the lines of constant density. The inner purple contour is the core-crust interface, corresponding to the nuclear density; the outer brown one is the stellar surface, and the intermediate orange contour corresponds to the neutron drip density. We use here the NL3 nuclear model, see Table 7.1.

reaching its maximum decreases with the increasing central density. The thickness of the crusts in both global and local neutrality cases gradually decreases with the increasing central density. However the radii of the crusts behave similarly to the radius of the core (for details see Appendix E). Close to the maximum rotating mass, even though the configurations rotate at the Keplerian rate, the shape becomes almost spherical, but still oblate (see the right panels of Figs. 7.8, 7.9 for details).

7.7 Conclusions

We have considered the equations of equilibrium of neutron stars based on the recent works [218, 18] and [210, 209, 211]. The strong, weak, electromagnetic, and gravitational interactions are taken into due account within the framework of general relativity. In particular, the strong interactions between nucleons is described by the exchange of the σ , ω , and ρ mesons. The equilibrium conditions are given by the set of Einstein-Maxwell-Thomas-Fermi equations and by the constancy of the general relativistic Fermi energies of particles, the Klein potentials, throughout the configuration.

We have solved these equilibrium equations numerically, in the case of zero tempera-

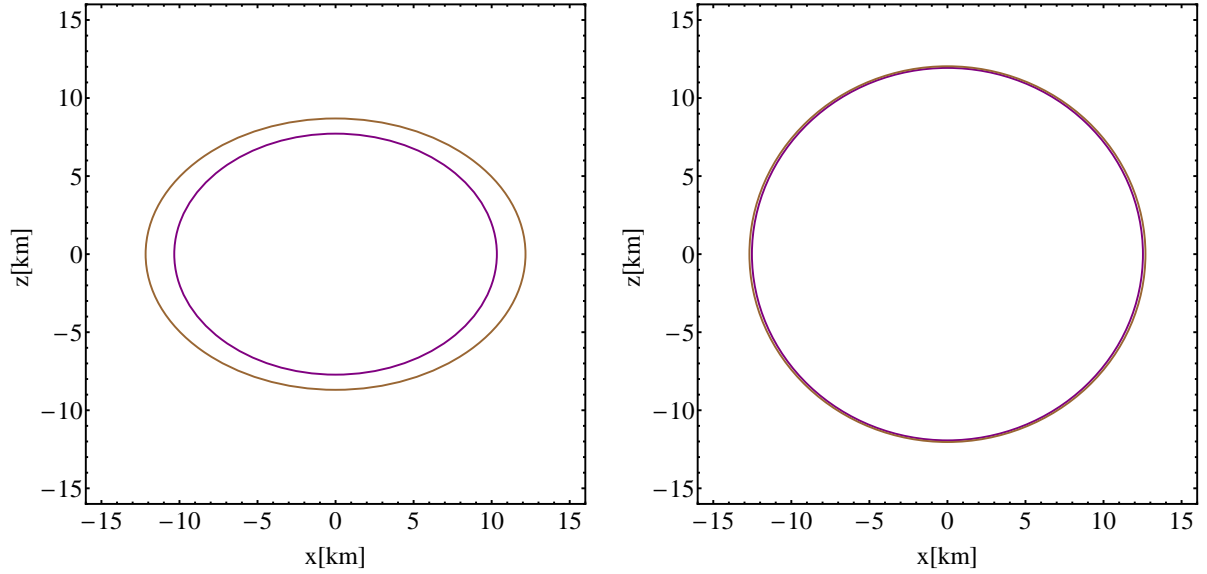


Figure 7.9: Cross section in the plane passing through the rotational axis of a neutron star with the new globally neutral equilibrium configurations presented here at frequency $f = 986\text{Hz}$ and $f = 1942\text{Hz}$. The total rotating gravitational mass is $M = 0.488M_\odot$ and $M = 2.763M_\odot$, the central baryon density $\rho_c = 1.445\rho_{nuc}$ and $\rho_c = 6\rho_{nuc}$ (left and right panels). The contours are the lines of constant density. The inner purple contour is the core-crust interface (corresponds to the nuclear and neutron drip density); the outer brown one is the stellar surface. We use here the NL3 nuclear model, see Table 7.1.

tures, for the nuclear parameter sets NL3 [135], NL-SH [238], TM1 [248], and TM2 [115]; see Table 7.1 for details.

A new structure of the star is found: the positively charged core at supranuclear densities is surrounded by an electronic distribution of thickness $\gtrsim \hbar/(m_e c) \sim 10^2 \hbar/(m_\pi c)$ of opposite charge and, at lower densities, a neutral ordinary crust.

In the core interior the Coulomb potential well is $\sim m_\pi c^2/e$ and correspondingly the electric field is $\sim (m_p/m_{\text{Planck}})(m_\pi/m_e)^2 E_c \sim 10^{-14} E_c$. Due to the equilibrium condition given by the constancy of the Klein potentials, there is a discontinuity in the density at the transition from the core to the crust, and correspondingly an overcritical electric field $\sim (m_\pi/m_e)^2 E_c$ develops in the boundary interface; see Figs. 7.1¹.

The continuity of the Klein potentials at the core-crust boundary interface leads to the decrease of the electron chemical potential and density, until values $\mu_e^{\text{crust}} < \mu_e^{\text{core}}$ and $\rho_{\text{crust}} < \rho_{\text{core}}$ at the edge of the crust, where the global charge neutrality is achieved. For each central density, an entire family of core-crust interface boundaries and, correspondingly, an entire family of crusts with different mass and thickness, exist. The larger ρ_{crust} , the smaller the thickness of the interface, the peak of the electric field, and the larger the mass and the thickness of the crust. The configuration with $\rho_{\text{crust}} = \rho_{\text{drip}} \sim 4.3 \times 10^{11}$

¹This strong electric field reminds the one studied in the stability of charged nuclear cores against vacuum polarization; see e.g. [170, 164, 212].

g/cm^3 separates neutron stars with and without inner crust. The neutron stars with $\rho_{\text{crust}} > \rho_{\text{drip}}$ deserve a further analysis in order to account for the reduction of the nuclear tension at the core-crust transition due to the presence of dripped neutrons from the nuclei in the crust.

All the above new features lead to crusts with masses and thickness smaller than the ones obtained from the traditional TOV treatment, and we have shown specifically neutron stars with $\rho_{\text{crust}} = \rho_{\text{drip}}$. The mass-radius relation obtained in this case have been compared and contrasted with the one obtained from the locally neutral TOV approach; see Fig. 7.5. We have shown that our mass-radius relation is in line with observations, based on the recent work by J. E. Trümper [262]; see Fig. 7.4 for details.

Furthermore we have analyzed the stability of rotating neutron stars, making use of Hartle's approach, against axisymmetric secular instabilities. We have estimated the maximum rotating mass and minimum period for both globally and locally neutral configurations.

7.8 Perspectives

The electromagnetic structure of the neutron star presented here is of clear astrophysical relevance. The process of gravitational collapse of a core endowed with electromagnetic structure leads to signatures and energetics markedly different from the ones of a core endowed uniquely of gravitational interactions; see e.g. [225, 226, 227, 224].

It is clear that the release of gravitational energy in the process of gravitational collapse of the core, following the classic work of Gamow and Schoenberg (see [86, 9]), is carried away by neutrinos. The additional nuclear and electromagnetic energy $\sim 10^{51}$ erg of the collapsing core introduced in [18] are expected to be carried away by electron-positron plasma created in the overcritical electromagnetic field in the collapsing core.

It would be interesting to investigate the spin-up and spin down effects of rotating neutron stars, losing angular momentum via electromagnetic radiation. To this end, it is appropriate to construct the constant rest mass (baryon mass) sequences.

To accurately reproduce the moment of inertia of a star which rotates at rates comparable to that of the fastest isolated pulsars, one needs to take into consideration the third order corrections.

To explore the induced magnetic field, Hartle's approach needs to be reformulated including the charge of the system. These tasks will be considered in the forthcoming works.

Appendix A

Derivation of the Fock extended metric

In this Appendix, we present a review of the derivation of a generalization of Fock's metric, based upon the approach formulated by Abdildin in [4]. The original approximate metric derived by Fock in [82] can be written as

$$ds^2 = (c^2 - 2U) dt^2 - \left(1 + \frac{2U}{c^2}\right) (dx_1^2 + dx_2^2 + dx_3^2) + \frac{8}{c^2} (U_1 dx_1 + U_2 dx_2 + U_3 dx_3) dt, \quad (\text{A.1})$$

where U is the Newtonian gravitational potential that satisfies the equation $\nabla^2 U = -4\pi G\rho$, where ρ represents the matter density of the gravitational source. Moreover, the gravitational vector potential \vec{U} satisfies the equation $\nabla^2 U_i = -4\pi G\rho v_i$, where v_i are the components of the 3-velocity of the particles inside the source. The coordinates x^μ are harmonic functions satisfying the D'Alembert equation $\square x^\mu = 0$.

As noticed by Abdildin, the metric (A.1) presents certain difficulties. First, the components g_{0i} and g_{ij} contain a relativistic contribution that is absent in the component g_{00} . Second, if we use the metric (A.1) to investigate the motion of test particles in a central potential, we obtain an expression for the perihelion shift that differs from the correct one by a factor of 1/2. Finally, in the case of a static field or for Gaussian-like coordinate systems $U dt^2 \sim dx_1^2 + dx_2^2 + dx_3^2$, i.e., the relativistic correction of g_{00} must be of the same order as that of g_{ij} .

From the above observations it follows that it is necessary to consider a more appropriate expression for the component

$$g^{00} = \frac{1}{c^2} + \frac{2U}{c^4} + \frac{\Phi}{c^6}, \quad (\text{A.2})$$

where Φ is an unknown function which must satisfy the corresponding approximate Einstein equation in harmonic coordinates

$$R^{00} = \frac{1}{2}\nabla^2 g^{00} - \frac{2U}{c^6}\nabla^2 U - \frac{2}{c^6}\sum_i \left(\frac{\partial U}{\partial x_i}\right)^2 = -\frac{8\pi G}{c^2}\left(T^{00} - \frac{1}{2}g^{00}T\right). \quad (\text{A.3})$$

As for the components of a energy-momentum tensor, in the case of an elastic source one can use the expressions

$$T^{00} = \frac{\rho}{c^2} \left[1 + \frac{1}{c^2} \left(\frac{v^2}{2} + \Pi - U \right) \right], \quad T^{0i} = \frac{\rho}{c^2} v^i, \quad T^{ij} = \frac{1}{c^2} (\rho v^i v^j + p \delta^{ij}), \quad (\text{A.4})$$

where Π is the elastic energy. It is then straightforward from Eqs.(A.3) and (A.4) to conclude that

$$\Phi = 2U^2 + 2G \int \frac{\rho \left(\frac{3}{2}v^2 + \Pi - U \right) + 3p}{|\vec{r} - \vec{r}'|} (dx')^3. \quad (\text{A.5})$$

Consequently, the generalized approximate metric is

$$ds^2 = \left[c^2 - 2U + \frac{2U^2}{c^2} - \frac{2G}{c^2} \int \frac{\rho \left(\frac{3}{2}v^2 + \Pi - U \right) + 3p}{|\vec{r} - \vec{r}'|} (dx')^3 \right] dt^2 - \left(1 + \frac{2U}{c^2} \right) (dx_1^2 + dx_2^2 + dx_3^2) + \frac{8}{c^2} (U_1 dx_1 + U_2 dx_2 + U_3 dx_3) dt. \quad (\text{A.6})$$

This form of the metric overcomes all the difficulties mentioned above for the original Fock metric (A.1), and is used everywhere in the present work to obtain the correct approximations.

Appendix B

Relevant frame components of tidal tensors

We list below the relevant nonvanishing ZAMO frame components of the electric and magnetic parts of the Riemann tensor:

$$\begin{aligned}
E(n)_{11} &= \frac{e^{-2\gamma}}{4T\sigma^2x^2} \left\{ \frac{X^2Sf_x^3}{2xf^2} + \frac{X}{x}f^2f\omega(X\omega_x + x\omega) - 2X(Sf_{xx} + 2f^3\omega\omega_{xx}) \right. \\
&\quad \left. - f_x \left[10Xf^2\omega\omega_x + \frac{2}{X}f^2\omega^2(X+2) + \frac{X}{2\sigma^2x}(4\sigma^4 + Sf^2\omega_x^2) \right] \right. \\
&\quad \left. - \frac{X}{x\sigma^2}f^3\omega\omega_x(f^2\omega_x^2 - 4\sigma^2) - \frac{f^3}{\sigma^2}\omega_x^2(S + f^2\omega^2) \right\} , \\
E(n)_{33} &= \frac{e^{-2\gamma}}{4\sigma^4fx^2} \left[\sigma^2f_x(2xf - Xf_x) + \omega_x^2f^4 \right] , \\
H(n)_{12} &= \frac{e^{-2\gamma}\sqrt{X}}{8Tx^3\sigma^5f} \left\{ 2\omega\sigma^4[Xf_x^2(f_xX + xf) - 6f^2f_x - 2Xf^2(f_x + 2xf_{xx})] - f^5\omega_x^3S \right. \\
&\quad \left. + f\sigma^2[-2f^3\omega\omega_x^2(Xf_x + 3xf) + 4Sf^2(\omega_x - x\omega_{xx}) \right. \\
&\quad \left. + Sf_x\omega_x(Xf_x - 10xf)] \right\} , \tag{B.1}
\end{aligned}$$

where $X = x^2 - 1$, $S = \sigma^2X + f^2\omega^2$ and $T = S - 2\sigma^2X$.

Furthermore, the Kretschmann invariant (3.33) of the QM spacetime evaluated on the

equatorial plane $y = 0$ is given by

$$\begin{aligned}
K = e^{-4\gamma} \frac{4X^2}{\sigma^4 x^4} & \left\{ f_{xx}^2 - \frac{f^4 \omega_{xx}^2}{X \sigma^2} + \frac{f^2 \omega_x \omega_{xx}}{2x X \sigma^4} [\sigma^2 f_x (X f_x - 10xf) - f^2 (f^2 \omega_x^2 - 4\sigma^2)] \right. \\
& + f_{xx} \left[(X+3) \frac{f_x}{Xx} - \frac{f_x^2}{2f^2 x} (X f_x + xf) + \frac{f^2 \omega_x^2}{2Xx\sigma^2} (X f_x + 3xf) \right] \\
& + \frac{f_x^3}{16\sigma^2 x^2 f^2} \left[\frac{X\sigma^2}{f^2} f_x^2 (X f_x + 2xf) - 3f^2 \omega_x^2 (X f_x - 4xf) - 8\sigma^2 f_x \right. \\
& \left. - \frac{8x\sigma^2 f}{X} (2X+3) \right] + \frac{f^3 f_x \omega_x^2}{2x X \sigma^2} \left(-\frac{7f^2 \omega_x^2}{4\sigma^2} + 13 + \frac{6}{X} \right) \\
& + f_x^2 \left[\frac{3f^4 \omega_x^4}{16\sigma^4 x^2} - \frac{f^2 \omega_x^2}{4X\sigma^2 x^2} (29X+25) + \frac{X^2+3X+3}{X^2 x^2} \right] \\
& \left. - \frac{f^4 \omega_x^2}{X\sigma^2 x^2} \left[\frac{f^4 \omega_x^4}{16\sigma^4} + 1 - \frac{f^2 \omega_x^2}{4X\sigma^2} (5X+3) \right] \right\}. \tag{B.2}
\end{aligned}$$

Appendix C

The Hartle-Thorne solution and equatorial circular orbits

C.0.1 The Hartle-Thorne vacuum solution

The HT metric given by Eq. (4.1) can be written in an analytic closed-form in the exterior vacuum case in terms of the total mass M , angular momentum J , and quadrupole moment Q of the rotating star. The angular velocity of local inertial frames $\omega(r)$, proportional to Ω , and the functions h_0 , h_2 , m_0 , m_2 , k_2 , proportional to Ω^2 , are derived from the Einstein equations [see 105, 108, for details]. Thus, the metric can be then written as

$$\begin{aligned}
 ds^2 = & \left(1 - \frac{2M}{r}\right) \left[1 + 2k_1 P_2(\cos \theta) + 2 \left(1 - \frac{2M}{r}\right)^{-1} \frac{J^2}{r^4} (2 \cos^2 \theta - 1)\right] dt^2 \\
 & - \left(1 - \frac{2M}{r}\right)^{-1} \left[1 - 2 \left(k_1 - \frac{6J^2}{r^4}\right) P_2(\cos \theta) - 2 \left(1 - \frac{2M}{r}\right)^{-1} \frac{J^2}{r^4}\right] dr^2 \\
 & - r^2 [1 - 2k_2 P_2(\cos \theta)] (d\theta^2 + \sin^2 \theta d\phi^2) + \frac{4J}{r} \sin^2 \theta dt d\phi
 \end{aligned} \tag{C.1}$$

where

$$\begin{aligned}
 k_1 &= \frac{J^2}{Mr^3} \left(1 + \frac{M}{r}\right) + \frac{5Q - J^2/M}{8M^3} Q_2^2 \left(\frac{r}{M} - 1\right), \\
 k_2 &= k_1 + \frac{J^2}{r^4} + \frac{5Q - J^2/M}{4M^2 r} \left(1 - \frac{2M}{r}\right)^{-1/2} Q_2^1 \left(\frac{r}{M} - 1\right),
 \end{aligned}$$

and

$$\begin{aligned}
 Q_2^1(x) &= (x^2 - 1)^{1/2} \left[\frac{3x}{2} \ln \frac{x+1}{x-1} - \frac{3x^2 - 2}{x^2 - 1} \right], \\
 Q_2^2(x) &= (x^2 - 1) \left[\frac{3}{2} \ln \frac{x+1}{x-1} - \frac{3x^3 - 5x}{(x^2 - 1)^2} \right],
 \end{aligned} \tag{C.2}$$

are the associated Legendre functions of the second kind, with $x = r/M - 1$, and $P_2(\cos\theta) = (1/2)(3\cos^2\theta - 1)$ is the Legendre polynomial. The constants M , J and Q the total mass, angular momentum and mass quadrupole moment of the rotating object, respectively. This form of the metric corrects some misprints of the original paper by [108] (see also [21] and [30]). The precise numerical values of M , J and Q are calculated from the matching procedure of the exterior and interior metrics at the surface of the star.

The total mass of a rotating configuration is defined as $M = M^{J \neq 0} = M^{J=0} + \delta M$, where $M^{J=0}$ is the mass of non-rotating configuration and δM is the change in mass of the rotating from the non-rotating configuration with the same central density. It should be stressed that in the terms involving J^2 and Q the total mass M can be substituted by $M^{J=0}$ since δM is already a second order term in the angular velocity.

C.0.2 Angular velocity of equatorial circular orbits

The four-velocity u of a test particle on a circular orbit in equatorial plane of axisymmetric stationary spacetime can be parametrized by the constant angular velocity Ω with respect to an observer at infinity

$$u = \Gamma[\partial_t + \Omega\partial_\phi], \quad (\text{C.3})$$

where Γ is a normalization factor which assures that $u^\alpha u_\alpha = 1$. From normalization and geodesics conditions we obtain the following expressions for Γ and $\Omega = u^\phi/u^t$

$$\Gamma = \pm(g_{tt} + 2\Omega g_{t\phi} + \Omega^2 g_{\phi\phi})^{-1/2}, \quad g_{tt,r} + 2\Omega g_{t\phi,r} + \Omega^2 g_{\phi\phi,r} = 0, \quad (\text{C.4})$$

hence, Ω , the solution of (C.4)₂, is given by

$$\Omega_{\pm orb}(r) = \frac{u^\phi}{u^t} = \frac{-g_{t\phi,r} \pm \sqrt{(g_{t\phi,r})^2 - g_{tt,r}g_{\phi\phi,r}}}{g_{\phi\phi,r}}, \quad (\text{C.5})$$

where (+/-) stands for co-rotating/counter-rotating orbits, u^ϕ and u^t are the angular and time components of the four-velocity, and a colon stands for partial derivative with respect to the corresponding coordinate. In our case one needs to consider only co-rotating orbits (omitting the plus sign in $\Omega_{+orb}(r) = \Omega_{orb}(r)$) to determine the mass shedding (Keplerian) angular velocity on the surface of the WD. For the Hartle-Thorne external solution Eq. (C.1) we have

$$\Omega_{orb}(r) = \sqrt{\frac{M}{r^3}} [1 - jF_1(r) + j^2F_2(r) + qF_3(r)], \quad (\text{C.6})$$

where $j = J/M^2$ and $q = Q/M^3$ are the dimensionless angular momentum and quadrupole moment,

$$\begin{aligned}
F_1 &= \left(\frac{M}{r}\right)^{3/2}, \\
F_2 &= [48M^7 - 80M^6r + 4M^5r^2 - 18M^4r^3 + 40M^3r^4 + 10M^2r^5 \\
&\quad + 15Mr^6 - 15r^7][16M^2r^4(r - 2M)]^{-1} + F, \\
F_3 &= \frac{6M^4 - 8M^3r - 2M^2r^2 - 3Mr^3 + 3r^4}{16M^2r(r - 2M)/5} - F, \\
F &= \frac{15(r^3 - 2M^3)}{32M^3} \ln \frac{r}{r - 2M}.
\end{aligned}$$

The mass shedding limiting angular velocity of a rotating star is the Keplerian angular velocity evaluated at the equator ($r = R_{eq}$), i.e.

$$\Omega_K^{J \neq 0} = \Omega_{orb}(r = R_{eq}). \quad (\text{C.7})$$

In the static case i.e. when $j = 0$ hence $q = 0$ and $\delta M = 0$ we have the well-known Schwarzschild solution and the orbital angular velocity for a test particle $\Omega_{ms}^{J=0}$ on the surface ($r = R$) of the WD is given by

$$\Omega_K^{J=0} = \sqrt{\frac{M^{J=0}}{R_{M^{J=0}}^3}}. \quad (\text{C.8})$$

C.0.3 Weak field limit

Let us estimate the values of j and q recovering physical units with c and G . The dimensionless angular momentum is

$$j = \frac{cJ}{GM^2} = \frac{c}{G} \frac{\alpha MR^2 \Omega}{M^2} = \alpha \left(\frac{\Omega R}{c}\right) \left(\frac{GM}{c^2 R}\right)^{-1}, \quad (\text{C.9})$$

where we have used the fact that $J = I\Omega$, with $I = \alpha MR^2$, and $\alpha \sim 0.1$ from our numerical integrations. For massive and fast rotating WDs we have $(\Omega R)/c \sim 10^{-2}$ and $(GM)/(c^2 R) \sim 10^{-3}$, so $j \sim 1$.

The dimensionless quadrupole moment q is

$$q = \frac{c^4 Q}{G^2 M^3} = \frac{c^4 \beta MR^2}{G^2 M^3} = \beta \left(\frac{GM}{c^2 R}\right)^{-2}, \quad (\text{C.10})$$

where we have expressed the mass quadrupole moment Q in terms of mass and radius of the WD, $Q = \beta MR^2$, where $\beta \sim 10^{-2}$, so we have $q \sim 10^4$.

The large values of j and q might arise some suspicion on the products jF_1 , j^2F_2 and qF_3 as real correction factors in Eq. (C.6). It is easy to check this in the weak field limit $M/r \ll 1$, where the functions F_i can be expanded as a power-series

$$\begin{aligned} F_1 &= \left(\frac{M}{r}\right)^{3/2}, \\ F_2 &\approx \frac{1}{2}\left(\frac{M}{r}\right)^3 - \frac{117}{28}\left(\frac{M}{r}\right)^4 - 6\left(\frac{M}{r}\right)^5 - \dots, \\ F_3 &\approx \frac{3}{4}\left(\frac{M}{r}\right)^2 + \frac{5}{4}\left(\frac{M}{r}\right)^3 + \frac{75}{28}\left(\frac{M}{r}\right)^4 + 6\left(\frac{M}{r}\right)^5 + \dots \end{aligned}$$

so evaluating at $r = R$

$$jF_1 = \alpha \left(\frac{\Omega R}{c}\right) \left(\frac{GM}{c^2 R}\right)^{1/2}, \quad j^2F_2 = \frac{\alpha}{2} \left(\frac{\Omega R}{c}\right) \left(\frac{GM}{c^2 R}\right)^2, \quad (\text{C.11})$$

so we finally have $jF_1 \sim 10^{-9/2}$, $j^2F_2 \sim 10^{-9}$, and $qF_3 \sim 10^{-2}$. We can therefore see that the products are indeed correction factors and, in addition, that effect due to the quadrupolar deformation is larger than the frame-dragging effect.

C.1 Pycnonuclear fusion reaction rates

The theoretical framework for the determination of the pycnonuclear reaction rates was developed by [230]. The number of reactions per unit volume per unit time can be written as

$$\begin{aligned} R_{pyc} &= Z^4 A \rho S(E_p) 3.90 \times 10^{46} \lambda^{7/4} \exp(-2.638/\sqrt{\lambda}) \text{ cm}^{-3} \text{ s}^{-1} \\ \lambda &= \frac{1}{Z^2 A^{4/3}} \left(\frac{\rho}{1.3574 \times 10^{11} \text{ g cm}^{-3}} \right)^{1/3}, \end{aligned} \quad (\text{C.12})$$

where S are astrophysical factors in units of Mev barns (1 barn = 10^{-24} cm²) that have to be evaluated at the energy E_p given by Eq. (4.4).

For the S -factors we adopt the results of [89] calculated with the NL2 nuclear model parameterization. For center of mass energies $E \geq 19.8$ MeV, the S -factors can be fitted by

$$S(E) = 5.15 \times 10^{16} \exp \left[-0.428E - \frac{3E^{0.308}}{1 + e^{0.613(8-E)}} \right] \text{ MeV barn}, \quad (\text{C.13})$$

which is appropriate for the ranges of the zero-point energies at high densities. For instance, ¹²C nuclei at $\rho = 10^{10}$ g cm⁻³ have a zero-point oscillation energy $E_p \sim 34$ keV.

All the nuclei (Z, A) at a given density ρ will fuse in a time τ_{pyc} given by

$$\tau_{pyc} = \frac{n_N}{R_{pyc}} = \frac{\rho}{AM_u R_{pyc}}, \quad (\text{C.14})$$

Treatment/EOS	$M_{max}^{J \neq 0}/M_{\odot}$	References
Newtonian/Chandrasekhar $\mu = 2$	1.474	[7]
Newtonian/Polytrope $n = 3$	1.487	[214]
Post-Newtonian/Chandrasekhar $\mu = 2$	1.482	[215]
GR/Chandrasekhar $\mu = 2$	1.478	[11]

Table C.1: Maximum rotating mass of WDs in literature.

where $n_N = \rho/(AM_u)$ is the ion-density. [89] estimated that the S -factors (C.13) are uncertain within a factor ~ 3.5 ; it is clear from the above equation that for a given lifetime τ_{pyc} such uncertainties reflect also in the determination of the density threshold.

C.2 Comparison with the Newtonian treatment and other works

We have constructed solutions of the Newtonian equilibrium equations for RWDs accurate up to order Ω^2 , following the procedure of [105]. In Fig. C.1 (left panel) we compare these Newtonian configurations with general relativistic RWDs for the Chandrasekhar EOS with $\mu = 2$. We can see clearly the differences between the two mass-density relations toward the high density region, as expected. A most remarkable difference is the existence of axisymmetric instability boundary in the general relativistic case, absent in its Newtonian counterpart.

Up to our knowledge, the only previous work on RWDs within GR is the one of [11]. A method to compute RWDs configurations accurate up to second order in Ω was developed by two of the authors [see 234, for details], independently of the work of [105]. In [11], RWDs were computed for the Chandrasekhar EOS with $\mu = 2$.

In Fig. C.1 (right panel) we show the mass-central density relation obtained with their method with the ones constructed in this work for the same EOS. We note here that the results are different even at the level of static configurations, and since the methods are based on construction of rotating configurations from seed static ones, those differences extrapolate to the corresponding rotating objects. This fact is to be added to the possible additional difference arising from the different way of approaching the order Ω^2 in the approximation scheme. The differences between the two equilibrium configurations are evident.

Turning now to the problem of the maximum mass of a RWD, in Table C.2 we present the previous results obtained in Newtonian, Post-Newtonian approach and GR by several authors. Depending on their method, approach, treatment, theory and numerical code the authors showed different results. These maximum mass of RWDs are to be compared with the ones found in this work and presented in Table 4.4 for the Chandrasekhar $\mu = 2$, Salpeter, and RFMT EOS.

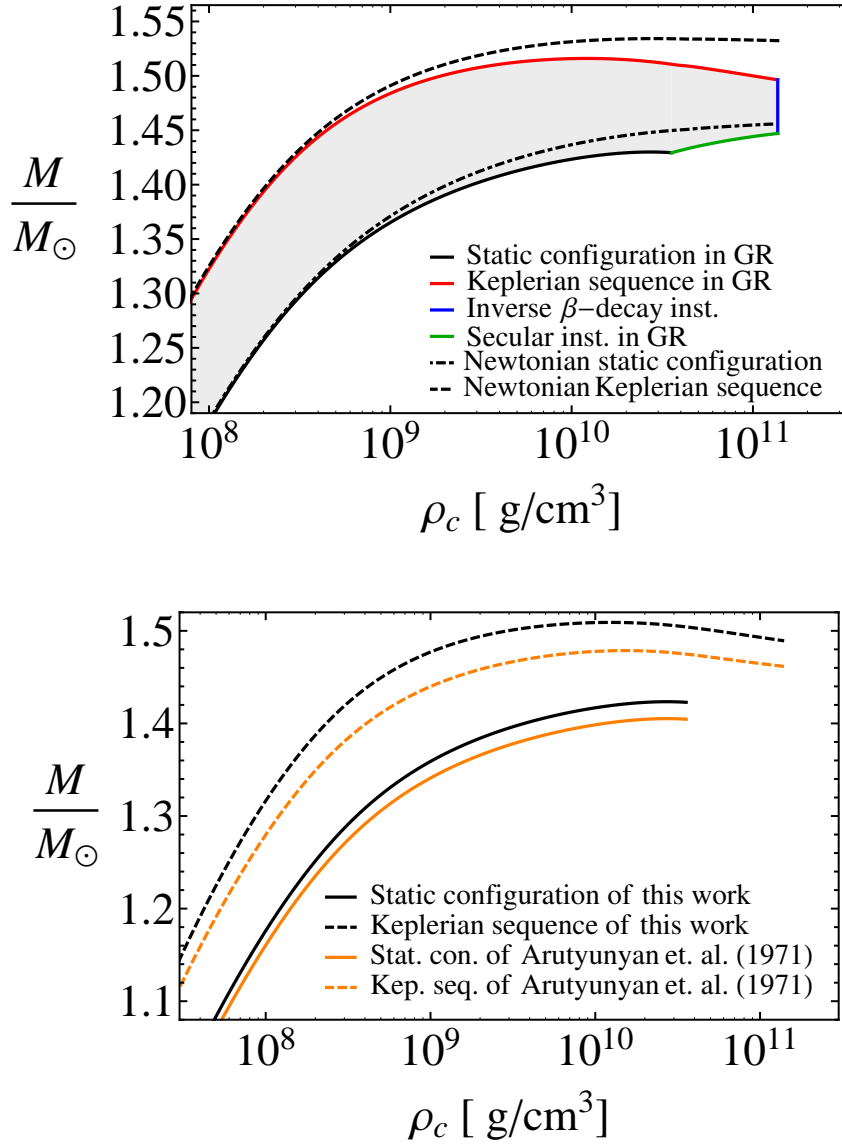


Figure C.1: Top panel: Mass versus central density of Newtonian and general relativistic WDs for the Chandrasekhar EOS with $\mu = 2$. Both the non-rotating case and the Keplerian sequence are shown. We have stopped the density, just for sake of comparison, at the critical density for the onset of inverse β -decay of ${}^4\text{He}$ $\rho = 1.39 \times 10^{11}$ g cm⁻³. Bottom panel: Mass versus central density relation for general relativistic WDs for the Chandrasekhar EOS with $\mu = 2$ for the static and the Keplerian sequence in this work and the one of [11].

C.3 Accuracy of the Hartle's approach

In his classic work, [105] described the slow rotation regime by requesting that fractional changes in pressure, energy density, and gravitational field due to the rotation of the star are all much smaller with respect to a non-rotating star with the same central density. From a dimensional analysis, such a condition implies

$$\Omega^2 \ll \left(\frac{c}{R}\right)^2 \frac{GM^{J=0}}{c^2 R}, \quad (\text{C.15})$$

where $M^{J=0}$ is the mass of the unperturbed configuration and R its radius. The expression on the right is the only multiplicative combination of M , R , G , and c , and in the Newtonian limit coincides with the critical Keplerian angular velocity $\Omega_K^{J=0}$ given by Eq. (C.8). For unperturbed configurations with $(GM)/(c^2 R) < 1$, the condition (C.15) implies $\Omega R/c \ll 1$. Namely, every particle must move at non-relativistic velocities if the perturbation to the original geometry have to be small in terms of percentage. Eq. (C.15) can be also written as

$$\Omega \ll \Omega_K^{J=0}, \quad (\text{C.16})$$

which is the reason why it is often believed that the slow rotation approximation is not suitable for the description of stars rotating at their mass-shedding value.

Let us discuss this point more carefully. It is clear that the request that the contribution of rotation to pressure, energy density, and gravitational field to be small can be summarized in a single expression, Eq. (C.15), since all of them are quantitatively given by the ratio between the rotational and the gravitational energy of the star. The rotational energy is $T \sim MR^2\Omega^2$ and the gravitational energy is $|W| \sim GM^2/R = (GM/c^2 R)Mc^2$, hence the condition $T/|W| \ll 1$ leads to Eq. (C.15) or (C.16). Now we will discuss the above condition for realistic values of the rotational and gravitational energy of a rotating star, abandoning the assumption of either fiducial or order of magnitude calculations. We show below that the actual limiting angular velocity on the right-hand-side of the condition (C.16) has to be higher than the Keplerian value.

We can write the gravitational binding energy of the star as $|W| = \gamma GM^2/R$ and the rotational kinetic energy as $T = (1/2)I\Omega^2 = (1/2)\alpha MR^2\Omega^2$, where the constants γ and α are structure constants that depends on the density and pressure distribution inside the star. According to the slow rotation approximation, $T/|W| \ll 1$, namely

$$\frac{T}{|W|} = \frac{\alpha MR^2\Omega^2/2}{\gamma GM^2/R} = \left(\frac{\alpha}{2\gamma}\right) \left(\frac{GM}{R^3}\right)^{-1} \Omega^2 = \left(\frac{\alpha}{2\gamma}\right) \left(\frac{\Omega}{\Omega_K^{J=0}}\right)^2 \ll 1, \quad (\text{C.17})$$

which can be rewritten in analogous form to Eq. C.16 as

$$\Omega \ll \sqrt{\frac{2\gamma}{\alpha}} \Omega_K^{J=0}. \quad (\text{C.18})$$

Now we check that the ratio of the structural constants is larger than unity. Let us first consider the simplest example of a constant density sphere. In this case $\alpha = 2/5$ and

$\gamma = 3/5$, so $\sqrt{2\gamma/\alpha} \approx 1.73$, and the condition (C.18) is $\Omega \ll 1.73\Omega_K^{J=0}$. If we consider now a more realistic density profile, for instance, a polytrope of index $n = 3$, we have [see e.g. 235]

$$|W| = \frac{3}{5-n} \frac{GM^2}{R} = \frac{3}{2} \frac{GM^2}{R}, \quad T = \frac{1}{2} I \Omega^2 = \frac{1}{2} \frac{2}{3} M \langle r^2 \rangle \Omega^2 \quad (\text{C.19})$$

where $\langle r^2 \rangle = 0.11303R^2$. Therefore we have in this case $\gamma = 3/2$ and $\alpha = 0.075$, and so Eq. (C.18) becomes $\Omega \ll 6.32\Omega_K^{J=0}$. This is not surprising since $T/|W| \rightarrow 0.025$ when $\Omega \rightarrow \Omega_K^{J=0}$.

The above analysis has been done assuming spherical symmetry. When deviations from the spherical shape are taken into account, the ratio $T/|W|$ turn to be even smaller than the previous estimates based on spherical polytropes. Since the equatorial radius satisfies $R_{eq} > R$, at mass-shedding we will have $\Omega < \Omega_K^{J=0}$. In fact, in the Roche model the mass-shedding angular velocity is $\Omega_K^{J \neq 0} = (2/3)^{3/2} \Omega_K^{J=0} \approx 0.544\Omega_K^{J=0}$, corresponding to a rotational to gravitational energy ratio $T/|W| \approx 0.0074$ [see e.g. 235].

In our RWDs we have obtained that the mass-shedding angular velocity satisfies $\Omega_K^{J \neq 0} \approx 0.75\Omega_K^{J=0}$ at any density; see Eq. (4.12). Accordingly to this, we show in the left panel of Fig. C.2 the ratio $T/|W|$ for RWDs as a function of the central density for the Keplerian sequence. For an increasing central density $T/|W|$ decreases. On the right panel we have plotted the eccentricity versus the central density. For increasing central density the eccentricity decreases, so RWDs become less oblate at higher densities.

Now we turn to evaluate more specifically the deviations from the spherical symmetry. The expansion of the radial coordinate of a rotating configuration $r(R, \theta)$ in powers of the angular velocity is written as [105]

$$r = R + \xi(R, \theta) + O(\Omega^4), \quad (\text{C.20})$$

where ξ is the difference in the radial coordinate, r , between a point located at the polar angle θ on the surface of constant density $\rho(R)$ in the rotating configuration, and the point located at the same polar angle on the same constant density surface in the non-rotating configuration. In the slow rotation regime, the fractional displacement of the surfaces of constant density due to the rotation have to be small, namely $\xi(R, \theta)/R \ll 1$, where $\xi(R, \theta) = \xi_0(R) + \xi_2(R)P_2(\cos \theta)$ and $\xi_0(R)$ and $\xi_2(R)$ are function of R proportional to Ω^2 . On the right panel of Fig. C.3 the difference in the radial coordinate over static radius versus the central density is shown. Here we see the same tendency as in the case of the eccentricity, that these differences are decreasing with an increasing central density. On the left panel the rotation parameter $\Omega R/c$ versus the central density is shown. Here, with an increasing central density the rotation parameter increases. Thus, for higher densities the system becomes less oblate, smaller in size with a larger rotation parameter i.e. higher angular velocity.

In order to estimate the accuracy of the slow rotation approximation for RWDs, based on the above results, it is useful to compare all the above numbers with the known results for NSs. For instance, we notice that in NSs $\Omega R/c \sim 10^{-1}$, $\xi(R, 0)/R \sim 10^{-2}$ and $\xi(R, \pi/2)/R \sim 10^{-1}$ [see e.g. 21], to be compared with the corresponding values of

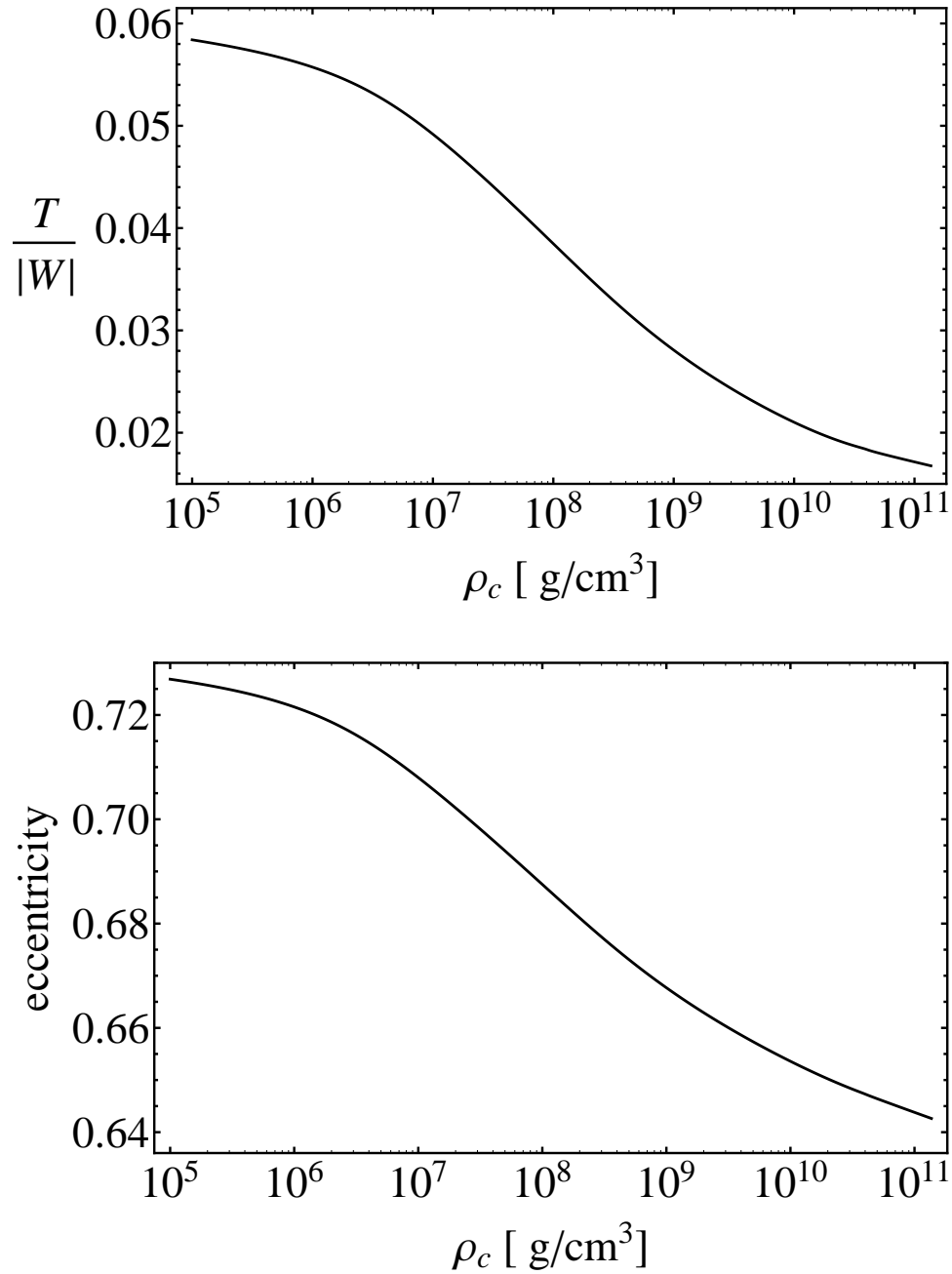


Figure C.2: Top panel: rotational to gravitational energy ratio versus the central density for maximally rotating RWDs, calculated with the Chandrasekhar EOS $\mu = 2$. Bottom panel: the eccentricity versus the central density for the same sequence of RWDs.

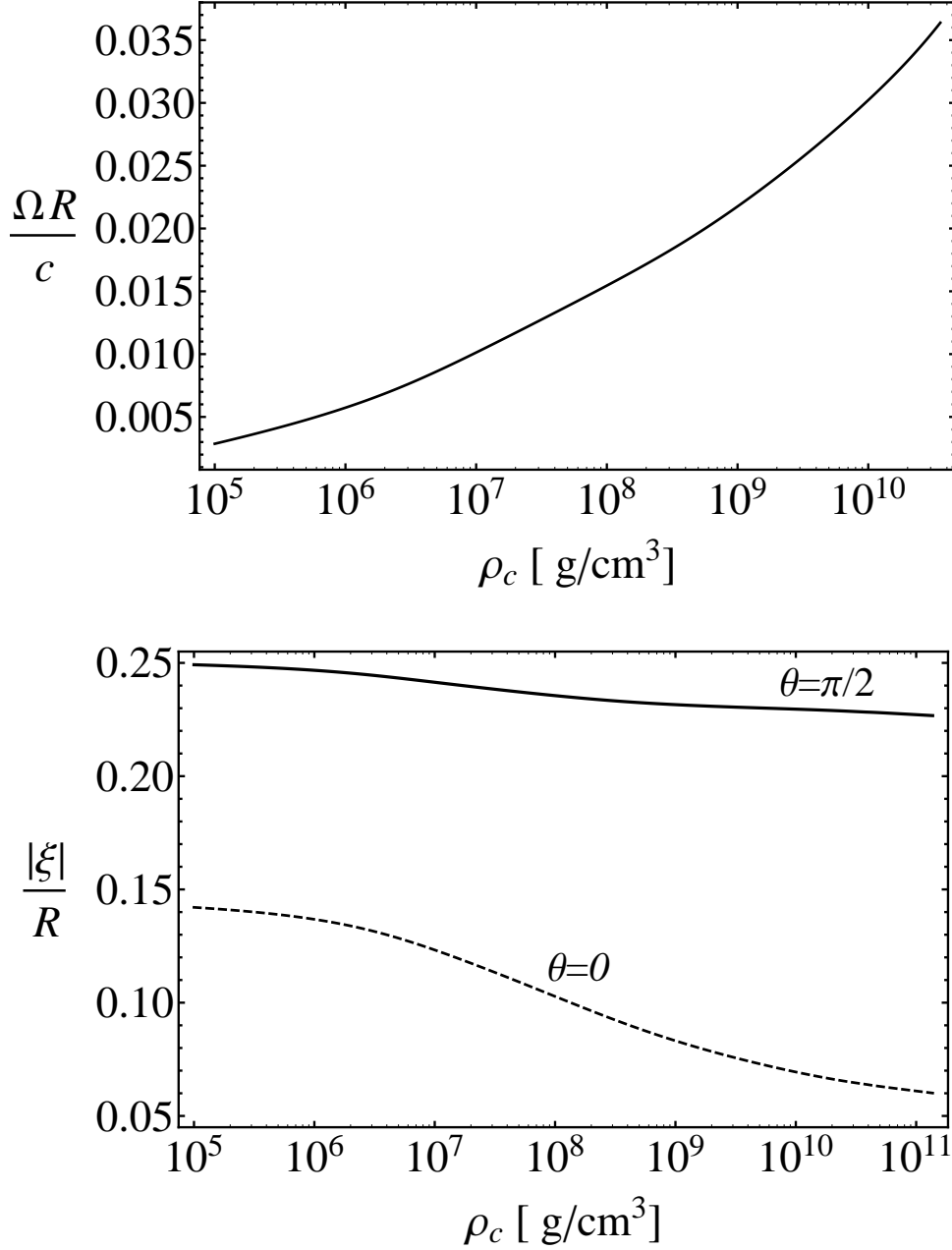


Figure C.3: Top panel: the rotation parameter normalized to the speed of light versus the central density. Bottom panel: the difference in the radial coordinate over the static radius versus the central density. The solid curve corresponds to the difference between equatorial ($\theta = \pi/2$) and static radii and the dashed curve corresponds to the difference between polar ($\theta = 0$) and static radii.

RWDs shown in Fig. C.3, $\Omega R/c \lesssim 10^{-2}$, $\xi(R, 0)/R \sim 10^{-2}$ and $\xi(R, \pi/2)/R \sim 10^{-1}$. [270] calculate the accuracy of the Hartle's second order approximation and found that the mass of maximally rotating NSs is accurate within an error $\lesssim 4\%$; [19] found that the inclusion of third order expansion Ω^3 improved the mass-shedding limit numerical values in less than 1% for NSs obeying different EOS. On the other-hand, it is known that the ratio $T/|W|$ in the case of NSs is as large as ~ 0.1 in the Keplerian sequence (see e.g. Tables 1–5 of [20]). Since RWDs have $T/|W|$ and $\Omega R/c$ smaller than NSs, and $\delta R/R = \xi/R$ at least of the same order (see left panel of Fig. C.2), we expect that the description of the structure of RWDs up to the mass-shedding limit within the Hartle's approach to have at least the same accuracy as in the case of NSs.

Appendix D

Spherical Capacitor

Consider a spherical capacitor with the internal R_1 and external R_2 radii having charges q_1 and q_2 correspondingly. The Coulomb potential in general has forms

$$V(r) = \begin{cases} k \left(\frac{q_1}{R_1} + \frac{q_2}{R_2} \right), & r < R_1, \\ k \left(\frac{q_1}{r} + \frac{q_2}{R_2} \right), & R_1 < r < R_2, \\ k \left(\frac{q_1}{r} + \frac{q_2}{r} \right), & r > R_2, \end{cases} \quad (\text{D.1})$$

where

$$k = \frac{1}{4\pi\epsilon_0}. \quad (\text{D.2})$$

Using the procedure developed by [158] for the computation of the magnetic field one has

$$B_r(r, \theta) = \begin{cases} \frac{2k\omega \cos \theta}{3c^2} \left(\frac{q_1}{R_1} + \frac{q_2}{R_2} \right), & r < R_1, \\ \frac{2k\omega \cos \theta}{3c^2} \left(\frac{q_1 R_1^2}{r^3} + \frac{q_2}{R_2} \right), & R_1 < r < R_2, \\ \frac{2k\omega \cos \theta}{3c^2} \left(\frac{q_1 R_1^2}{r^3} + \frac{q_2 R_2^2}{r^3} \right), & r > R_2, \end{cases} \quad (\text{D.3})$$

$$B_\theta(r, \theta) = \begin{cases} -\frac{2k\omega \sin \theta}{3c^2} \left(\frac{q_1}{R_1} + \frac{q_2}{R_2} \right), & r < R_1, \\ \frac{k\omega \sin \theta}{3c^2} \left(\frac{q_1 R_1^2}{r^3} - \frac{2q_2}{R_2} \right), & R_1 < r < R_2, \\ \frac{k\omega \sin \theta}{3c^2} \left(\frac{q_1 R_1^2}{r^3} + \frac{q_2 R_2^2}{r^3} \right), & r > R_2. \end{cases} \quad (\text{D.4})$$

Let us consider a limiting case analogous to ours when

$$q_1 = q, \quad q_2 = -q, \quad R_1 \approx R_2 - \lambda_e. \quad (\text{D.5})$$

This means that one may expand the expressions for both B_r and B_θ in λ_e . Retaining only the terms linear in λ_e one has

$$B_r(r, \theta) = \begin{cases} \frac{2k\omega q \lambda_e \cos \theta}{3c^2 R_2^2}, & r < R_1, \\ -\frac{4k\omega q \lambda_e R_2 \cos \theta}{3c^2 r^3} + \frac{2k\omega q (R_2^3 - r^3) \cos \theta}{3c^2 r^3 R_2}, & R_1 < r < R_2, \\ -\frac{4k\omega q \lambda_e R_2 \cos \theta}{3c^2 r^3}, & r > R_2, \end{cases} \quad (\text{D.6})$$

$$B_{\theta}(r, \theta) = \begin{cases} -\frac{2k\omega q\lambda_e \sin \theta}{3c^2 R_2^2}, & r < R_1, \\ -\frac{2k\omega q\lambda_e R_2 \sin \theta}{3c^2 r^3} + \frac{k\omega q(R_2^3 + 2r^3) \sin \theta}{3c^2 r^3 R_2}, & R_1 < r < R_2, \\ -\frac{2k\omega q\lambda_e R_2 \sin \theta}{3c^2 r^3}, & r > R_2. \end{cases} \quad (\text{D.7})$$

Note that when $r = R_2$ one will have a huge difference between B_r and B_{θ} in orders between the spherical shells.

Appendix E

Rotating neutron stars

In Fig. E.1 we show the mass-radius relation making use of the observations constraints for neutron stars given by Trümper in [262]. It can be seen that for both globally and locally neutral configurations, including static and rotating cases the mass-radius relation is in a good agreement with the constraints.

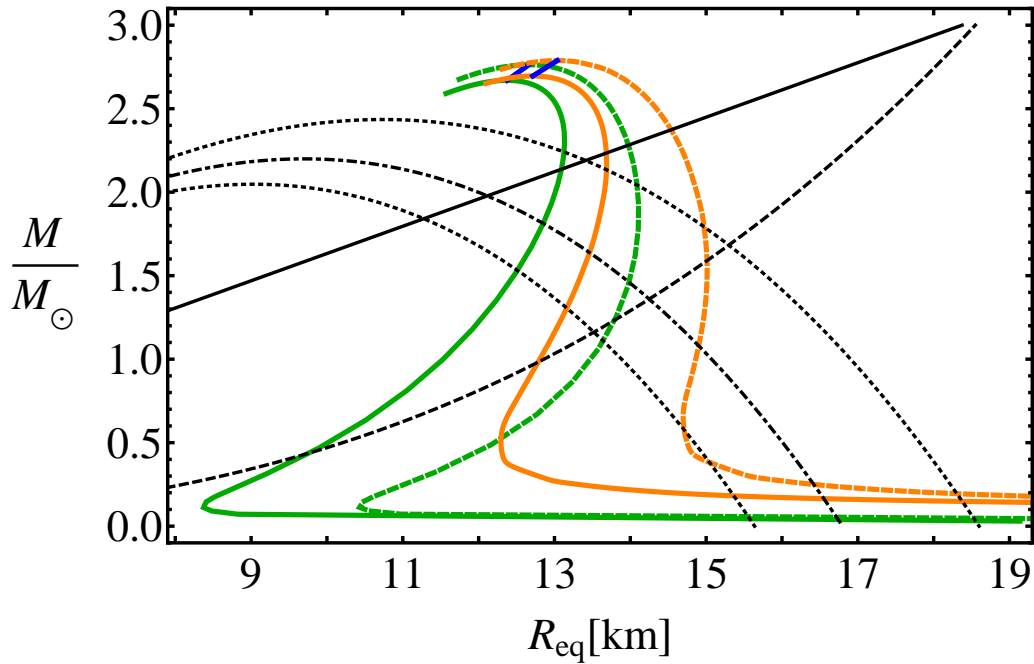


Figure E.1: Constraints on the mass-radius relation given by J.E. Trümper in [262] and the theoretical mass-radius relation presented in this work. Globally neutral configurations are in green and locally neutral ones are in orange. The solid lines correspond to the static case and dashed lines correspond to the Keplerian sequence. We use here the NL3 nuclear model.

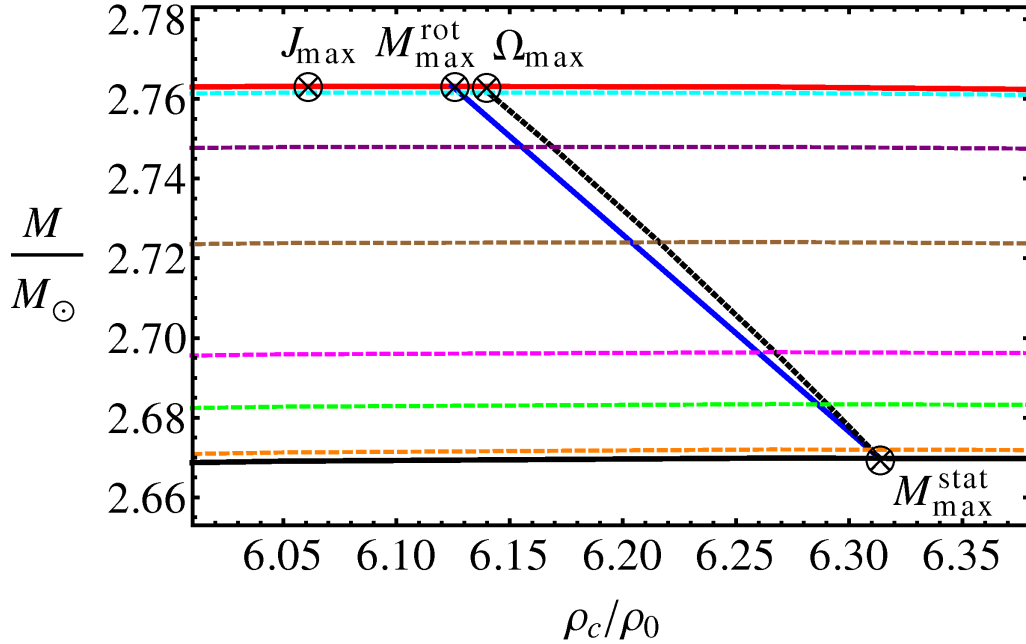


Figure E.2: Detail near the maximum mass versus central density, plot for globally neutral configuration. We use the NL3 nuclear model. Colored dashed lines are constant J sequences, the solid black line is the static case, the solid red line is the Keplerian sequence, the dotted black line is the axisymmetric secular instability line, the blue line is the line connecting M_{max}^{rot} and M_{max}^{stat} .

In Fig. E.2 we show the mass-central density relation for the globally neutral configuration. Here we focus on the definition of the maximum rotating mass M_{max}^{rot} , maximum static mass M_{max}^{stat} , maximum angular momentum J_{max} and maximum angular velocity (minimum rotation period) Ω_{max} (P_{min}). Note that Ω_{max} is defined along the turning points of constant J sequences (axisymmetric secular instability line) what is consistent with the results of Stergioulas and Friedman [247]. At large scales the difference between axisymmetric secular instability line and the line joining M_{max}^{rot} with M_{max}^{stat} can not be seen. For details see [20] and [101].

In Figs. E.3, E.4, and E.5 we show the eccentricity, moment of inertia, and angular momentum versus central density. For the globally neutral configurations the moment of inertia and eccentricity are smaller with respect to the one of the locally neutral configurations, since there is the inner crust in the locally neutral configurations and due to this fact these configurations will have larger radius and mass. Details are shown in Fig. E.7.

In Fig. E.6 we show nonlinear dependence of the angular momentum on the angular velocity.

In Figs. E.8 and E.9 we show the quadrupole moment and $T/|W|$ versus central density. Here we have larger values for locally neutral configurations.

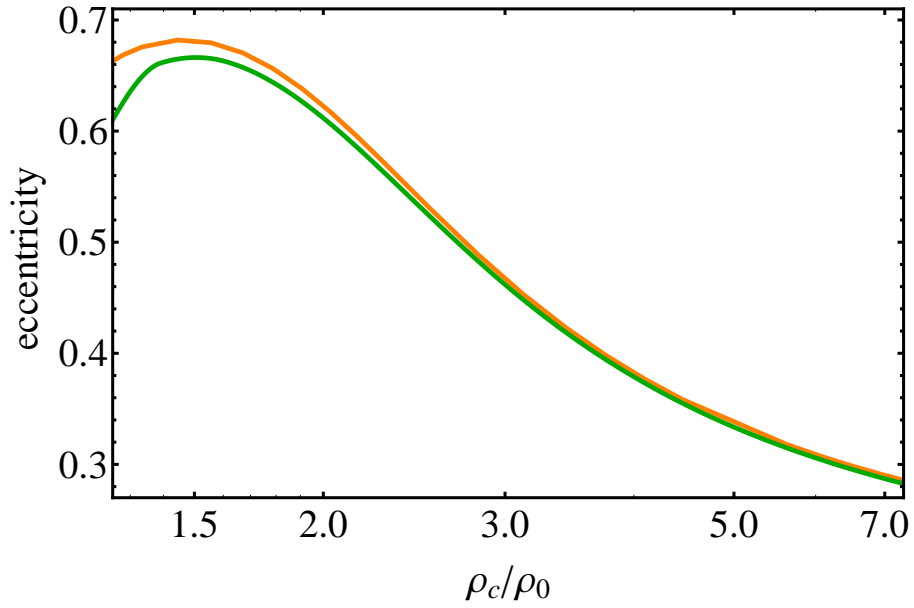


Figure E.3: Eccentricity versus central density. We use the NL3 nuclear model. The green line is globally neutral configuration and the orange line is locally neutral configuration.

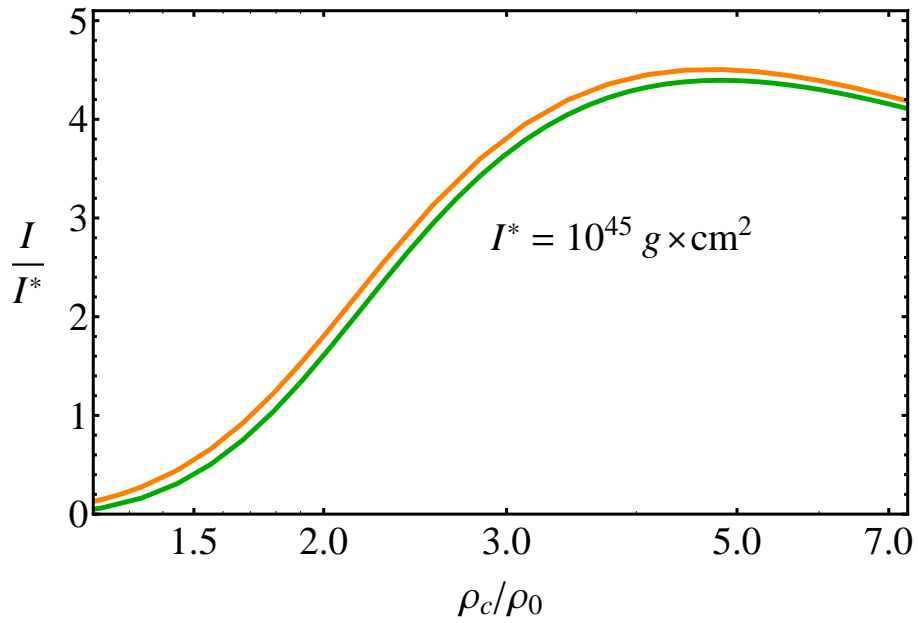


Figure E.4: Moment of inertia versus central density for static case. We use the NL3 nuclear model. The green line is globally neutral configuration and the orange line is locally neutral configuration.

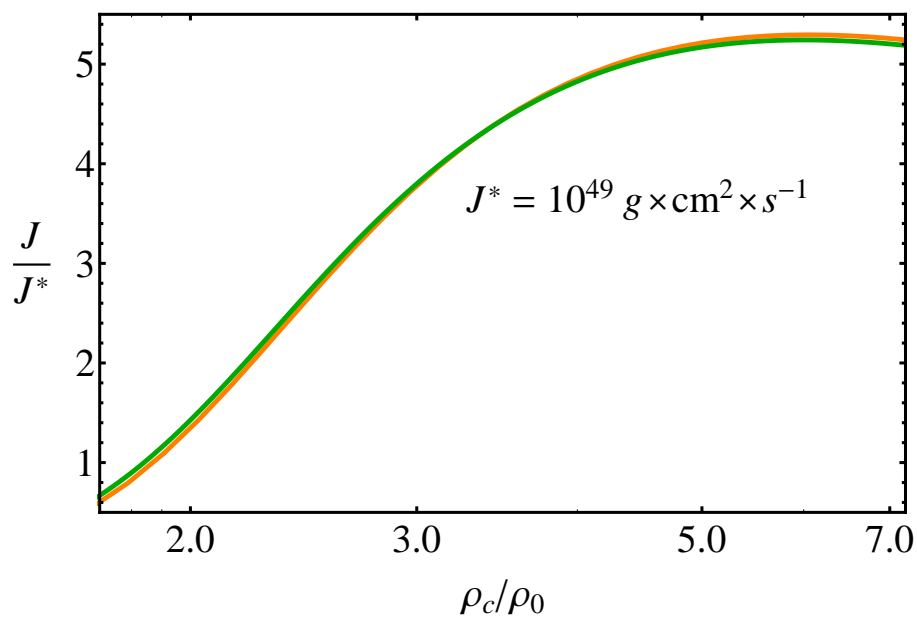


Figure E.5: Angular momentum versus central density. We use the NL3 nuclear model. The green line is the global charge neutrality and orange line is the local charge neutrality

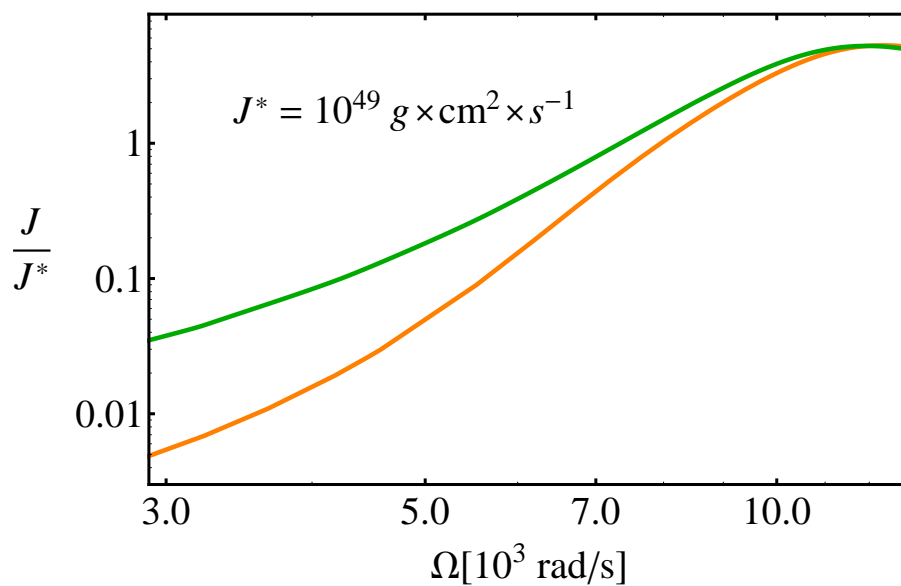


Figure E.6: Angular momentum versus angular velocity. We use the NL3 nuclear model. The green line is the globally neutral configuration and the orange line is the locally neutral configuration.

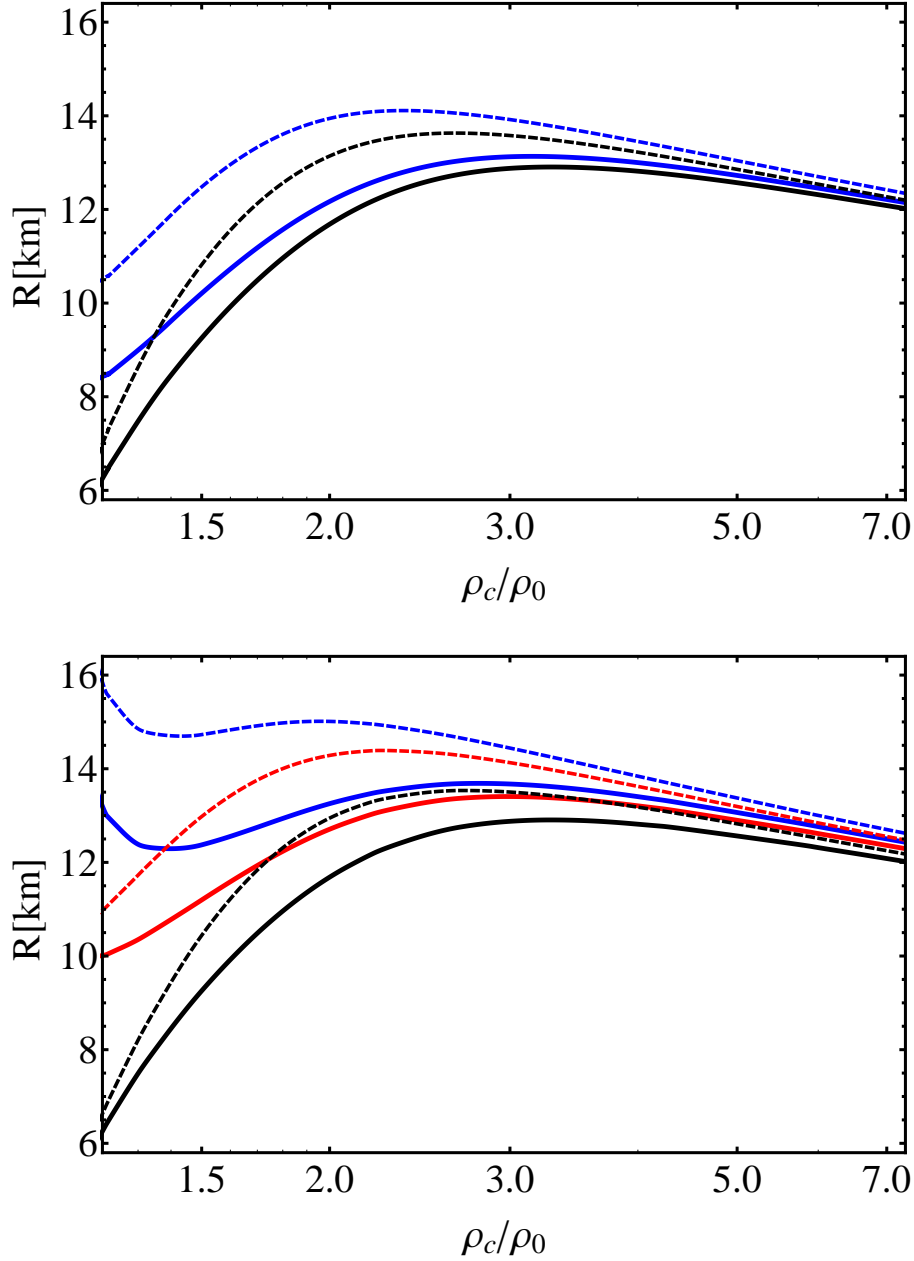


Figure E.7: Radius versus central density. We use the NL3 nuclear model. Top: globally neutral configuration. Bottom: locally neutral configuration. The black lines are the radii of the cores, the red lines are the radii of the inner crusts, the blue lines are the radii of the outer crusts. All solid lines are for the static configurations. All dashed lines are the equatorial radii for the Keplerian sequence.

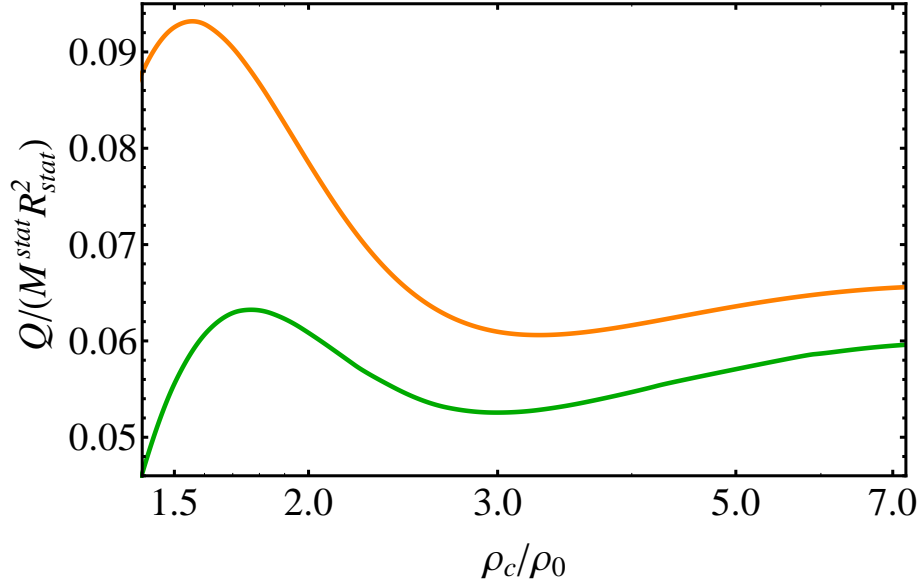


Figure E.8: Quadrupole moment versus central density. We use the NL3 nuclear model. The green line is global charge neutrality and orange line is local charge neutrality

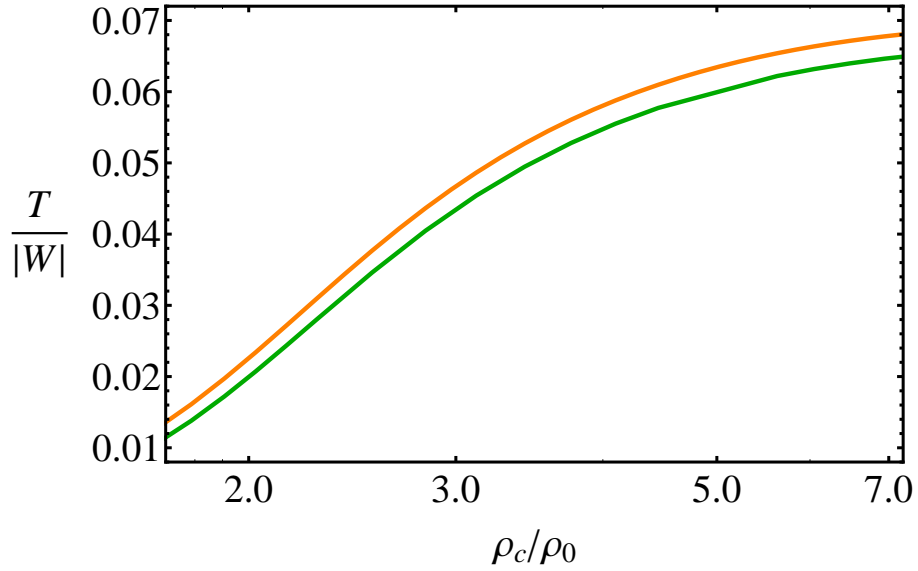


Figure E.9: Kinetic energy/binding energy ($T/|W|$) versus central density. We use the NL3 nuclear model. The green line is global charge neutrality and orange line is local charge neutrality

Bibliography

- [1] J. Abadie, B. P. Abbott, R. Abbott, M. Abernathy, T. Accadia, F. Acernese, C. Adams, R. Adhikari, P. Ajith, B. Allen, and et al. TOPICAL REVIEW: Predictions for the rates of compact binary coalescences observable by ground-based gravitational-wave detectors. *Classical and Quantum Gravity*, 27(17):173001, September 2010.
- [2] M. M. Abdil'Din. On the metrics of a rotating liquid sphere. In Problems of Field Theory, editor, *S. E. Ermatov et al*, pages 20–25, 1985.
- [3] M. M. Abdil'Din. *Mechanics of Einstein's gravitation theory*. Nauka Press, Alma-Ata, 1988.
- [4] M. M. Abdil'Din. *The problem of bodies motion in general relativity*. Kazakh University Press, Almaty, 2006.
- [5] M. M. Abdil'Din, M. E. Abishev, N. A. Beissen, and K. A. Boshkaev. On the uniqueness problem for the metric of the first approximation in general-relativistic mechanics. *Gravitation and Cosmology*, 15:1–4, March 2009.
- [6] M. M. Abdil'Din, M. E. Abishev, N. A. Beissen, and Z. N. Brisheva. On the uniqueness problem for the Lagrangian of two rotating bodies in general relativity. *Gravitation and Cosmology*, 15:141–143, June 2009.
- [7] S. P. S. Anand. On Chandrasekhar's Limiting Mass for Rotating White Dwarf Stars. *Proceedings of the National Academy of Science*, 54:23–26, July 1965.
- [8] N. Andersson and G. L. Comer. Slowly rotating general relativistic superfluid neutron stars. *Classical and Quantum Gravity*, 18:969–1002, March 2001.
- [9] D. Arnett. *Supernovae and Nucleosynthesis: An Investigation of the History of Matter from the Big Bang to the Present*. Princeton: Princeton University Press, 1996., 1996.
- [10] R. Arnowitt, S. Deser, and C. W. Misner. Interior Schwarzschild Solutions and Interpretation of Source Terms. *Physical Review*, 120:321–324, October 1960.

-
- [11] G. G. Arutyunyan, D. M. Sedrakyan, and É. V. Chubaryan. Rotating white dwarfs in the general relativity theory. *Astrophysics*, 7:274–280, July 1971.
- [12] G. Audi, A. H. Wapstra, and C. Thibault. The Ame2003 atomic mass evaluation (II). Tables, graphs and references. *Nuclear Physics A*, 729:337–676, December 2003.
- [13] J. M. Bardeen, W. H. Press, and S. A. Teukolsky. Rotating Black Holes: Locally Nonrotating Frames, Energy Extraction, and Scalar Synchrotron Radiation. *Astrophys. J.*, 178:347–370, December 1972.
- [14] M. A. Barstow, S. Jordan, D. O’Donoghue, M. R. Burleigh, R. Napiwotzki, and M. K. Harrop-Allin. RE J0317-853: the hottest known highly magnetic DA white dwarf. *Mon. Not. Roy. Astr. Soc.*, 277:971–985, December 1995.
- [15] G. Baym, H. A. Bethe, and C. J. Pethick. Neutron star matter. *Nuclear Physics A*, 175:225–271, November 1971.
- [16] G. Baym and D. Pines. Neutron starquakes and pulsar speedup. *Annals of Physics*, 66:816–835, 1971.
- [17] L. Bel. . *C.R. Acad. Sci., Paris*, 247:1094, 1958.
- [18] R. Belvedere, D. Pugliese, J. A. Rueda, R. Ruffini, and S.-S. Xue. Neutron star equilibrium configurations within a fully relativistic theory with strong, weak, electromagnetic, and gravitational interactions. *Nuclear Physics A*, 883:1–24, June 2012.
- [19] O. Benhar, V. Ferrari, L. Gualtieri, and S. Marassi. Perturbative approach to the structure of rapidly rotating neutron stars. *Phys. Rev. D*, 72(4):044028–+, August 2005.
- [20] E. Berti and N. Stergioulas. Approximate matching of analytic and numerical solutions for rapidly rotating neutron stars. *Mon. Not. Roy. Astr. Soc.*, 350:1416–1430, June 2004.
- [21] E. Berti, F. White, A. Maniopoulou, and M. Bruni. Rotating neutron stars: an invariant comparison of approximate and numerical space-time models. *Mon. Not. Roy. Astr. Soc.*, 358:923–938, April 2005.
- [22] S. Bhattacharyya, T. E. Strohmayer, M. C. Miller, and C. B. Markwardt. Constraints on Neutron Star Parameters from Burst Oscillation Light Curves of the Accreting Millisecond Pulsar XTE J1814-338. *Astrophys. J.*, 619:483–491, January 2005.
- [23] D. Bini, K. Boshkayev, and A. Geralico. Tidal indicators in the spacetime of a rotating deformed mass. *Classical and Quantum Gravity*, 29(14):145003, July 2012.

- [24] D. Bini, K. Boshkayev, R. Ruffini, and I. Siutsou. . *Nuovo Cimento B, in press*, 2012.
- [25] D. Bini, P. Carini, and R. T. Jantzen. The Intrinsic Derivative and Centrifugal Forces in General Relativity: I. Theoretical Foundations. *International Journal of Modern Physics D*, 6:1–38, 1997.
- [26] D. Bini, P. Carini, and R. T. Jantzen. The Intrinsic Derivative and Centrifugal Forces in General Relativity:. II. Applications to Circular Orbits in Some Familiar Stationary Axisymmetric Spacetimes. *International Journal of Modern Physics D*, 6:143–198, 1997.
- [27] D. Bini, T. Damour, and G. Faye. Effective action approach to higher-order relativistic tidal interactions in binary systems and their effective one body description. *Phys. Rev. D*, 85(12):124034, June 2012.
- [28] D. Bini, F. de Felice, and R. T. Jantzen. Absolute and relative Frenet-Serret frames and Fermi-Walker transport. *Classical and Quantum Gravity*, 16:2105–2124, June 1999.
- [29] D. Bini and A. Geralico. Observer-dependent tidal indicators in the Kerr spacetime. *Classical and Quantum Gravity*, 29(5):055005, March 2012.
- [30] D. Bini, A. Geralico, O. Luongo, and H. Quevedo. Generalized Kerr spacetime with an arbitrary mass quadrupole moment: geometric properties versus particle motion. *Classical and Quantum Gravity*, 26(22):225006, November 2009.
- [31] D. Bini, R. T. Jantzen, and B. Mashhoon. Gravitomagnetism and relative observer clock effects. *Classical and Quantum Gravity*, 18:653–670, February 2001.
- [32] T. Binnington and E. Poisson. Relativistic theory of tidal Love numbers. *Phys. Rev. D*, 80(8):084018, October 2009.
- [33] J. Boguta. Remarks on the beta stability in neutron stars. *Physics Letters B*, 106:255–258, November 1981.
- [34] J. Boguta. Chiral nuclear interactions. *Nuclear Physics A*, 501:637–652, October 1989.
- [35] J. Boguta and A. R. Bodmer. Relativistic calculation of nuclear matter and the nuclear surface. *Nuclear Physics A*, 292:413–428, December 1977.
- [36] J. Boguta and S. A. Moszkowski. Nonlinear mean field theory for nuclear matter and surface properties. *Nuclear Physics A*, 403:445–468, July 1983.
- [37] J. Boguta and J. Rafelski. Thomas Fermi model of finite nuclei. *Physics Letters B*, 71:22–26, November 1977.

- [38] J. Boguta and H. Stocker. Systematics of nuclear matter properties in a non-linear relativistic field theory. *Physics Letters B*, 120:289–293, January 1983.
- [39] M. A. G. Bonilla and J. M. M. Senovilla. Some Properties of the Bel and Bel-Robinson Tensors. *General Relativity and Gravitation*, 29:91–116, January 1997.
- [40] K. Boshkayev, L. Izzo, and R. Rueda, J. and Ruffini. In preparation. *ApJ*, 2012.
- [41] K. Boshkayev, H. Quevedo, and R. Ruffini. Gravitational field of compact objects in general relativity. *Phys. Rev. D*, 86(6):064043, September 2012.
- [42] K. Boshkayev, M. Rotondo, and R. Ruffini. On the Stability of Rotating Nuclear Matter Cores of Stellar Dimensions. In *25th Texas Symposium on Relativistic Astrophysics*, 2010.
- [43] K. Boshkayev, M. Rotondo, and R. Ruffini. On Magnetic Fields in Rotating Nuclear Matter Cores of Stellar Dimensions. *International Journal of Modern Physics Conference Series*, 12:58, 2012.
- [44] K. Boshkayev, J. Rueda, and R. Ruffini. On the Maximum Mass of General Relativistic Uniformly Rotating White Dwarfs. *International Journal of Modern Physics E*, 20:136–140, 2011.
- [45] K. Boshkayev, J. A. Rueda, R. Ruffini, and I. Siutsou. On general relativistic uniformly rotating white dwarfs. *in press ApJ*, April 2012.
- [46] R. L. Bowers, J. A. Campbell, and R. L. Zimmerman. Model Equation of State for Strongly Interacting Superdense Matter. *Phys. Rev. D*, 7:2289–2299, April 1973.
- [47] R. L. Bowers, J. A. Campbell, and R. L. Zimmerman. Relativistic Many-Body Theory for Strongly Interacting Matter. *Phys. Rev. D*, 7:2278–2288, April 1973.
- [48] R. H. Boyer and R. W. Lindquist. Maximal Analytic Extension of the Kerr Metric. *Journal of Mathematical Physics*, 8:265–281, February 1967.
- [49] V. A. Brumberg. *Essential relativistic celestial mechanics*. Bristol, England and New York, Adam Hilger, 1991.
- [50] A. G. W. Cameron. Pycnonuclear Reactions and Nova Explosions. *Astrophys. J.*, 130:916, November 1959.
- [51] J. A. Cardelli, G. C. Clayton, and J. S. Mathis. The relationship between infrared, optical, and ultraviolet extinction. *Astrophys. J.*, 345:245–256, October 1989.
- [52] J. Castejon-Amenedo and V. S. Manko. On a stationary rotating mass with an arbitrary multipole structure. *Classical and Quantum Gravity*, 7:779–785, May 1990.

-
- [53] S. Chandrasekhar. The Maximum Mass of Ideal White Dwarfs. *Astrophys. J.*, 74:81–+, July 1931.
- [54] S. Chandrasekhar. The Post-Newtonian Equations of Hydrodynamics in General Relativity. *Astrophys. J.*, 142:1488, November 1965.
- [55] S. Chandrasekhar. *Ellipsoidal figures of equilibrium*. New Haven: Yale University Press, 1969.
- [56] S. Chandrasekhar. The Evolution of the Jacobi Ellipsoid by Gravitational Radiation. *Astrophys. J.*, 161:571, August 1970.
- [57] D. M. Chitre and J. B. Hartle. Stationary configurations and the upper bound on the mass of nonrotating, causal neutron stars. *Astrophys. J.*, 207:592–600, July 1976.
- [58] T. Damour and O. M. Lecian. Gravitational polarizability of black holes. *Phys. Rev. D*, 80(4):044017, August 2009.
- [59] T. Damour and A. Nagar. Relativistic tidal properties of neutron stars. *Phys. Rev. D*, 80(8):084035, October 2009.
- [60] T. Damour and A. Nagar. Effective one body description of tidal effects in inspiralling compact binaries. *Phys. Rev. D*, 81(8):084016, April 2010.
- [61] T. Damour, M. Soffel, and C. Xu. General-relativistic celestial mechanics. II. Translational equations of motion. *Phys. Rev. D*, 45:1017–1044, February 1992.
- [62] T. De Donder. *La gravifique einsteinienne*. Gauthier-Villars, Paris, 1921.
- [63] F. de Felice and D. Bini. *Classical Measurements in Curved Space-times*. Cambridge, UK: Cambridge University Press., 2010.
- [64] P. Debye and E. Hueckerl. . *Phyz. Zeitschr.*, 24:185, 1923.
- [65] P. B. Demorest, T. Pennucci, S. M. Ransom, M. S. E. Roberts, and J. W. T. Hessels. A two-solar-mass neutron star measured using Shapiro delay. *Nature*, 467:1081–1083, October 2010.
- [66] W. Dietz and C. Hoenselaers. A new class of bipolar vacuum gravitational fields. *Royal Society of London Proceedings Series A*, 382:221–229, July 1982.
- [67] A. Doroshkevich, Ya. B. Zeldovich, and I. D. Novikov. . *Soviet Journal of Experimental and Theoretical Physics*, 22:122–+, 1965.
- [68] H.-P. Duerr. Relativistic Effects in Nuclear Forces. *Physical Review*, 103:469–480, July 1956.

- [69] M. D. Duez, F. Foucart, L. E. Kidder, H. P. Pfeiffer, M. A. Scheel, and S. A. Teukolsky. Evolving black hole-neutron star binaries in general relativity using pseudospectral and finite difference methods. *Phys. Rev. D*, 78(10):104015, November 2008.
- [70] R. C. Duncan and C. Thompson. Formation of very strongly magnetized neutron stars - Implications for gamma-ray bursts. *Astrophys. J. Lett.*, 392:L9–L13, June 1992.
- [71] M. Durant, O. Kargaltsev, and G. G. Pavlov. Search for the Optical Counterpart to SGR 0418+5729. *Astrophys. J.*, 742:77, December 2011.
- [72] R. H. Durisen. Viscous Effects in Rapidly Rotating Stars with Application to White-Dwarf Models. Theory and Techniques. *Astrophys. J.*, 183:205–214, July 1973.
- [73] R. H. Durisen. Upper mass limits for stable rotating white dwarfs. *Astrophys. J.*, 199:179–183, July 1975.
- [74] G. Erez and N. Rosen. . *Bull. Res. Council Israel*, 8:47, 1959.
- [75] F. J. Ernst. New Formulation of the Axially Symmetric Gravitational Field Problem. *Physical Review*, 167:1175–1177, March 1968.
- [76] R. Evans, editor. *Fundamentals of inhomogeneous fluids*, Decker, New York 1992, 1992.
- [77] A. Ferrari and R. Ruffini. Theoretical Implications of the Second Time Derivative of the Period of the Pulsar NP 0532. *Astrophys. J. Lett.*, 158:L71+, November 1969.
- [78] L. Ferrario, D. Wickramasinghe, J. Liebert, and K. A. Williams. The open-cluster initial-final mass relationship and the high-mass tail of the white dwarf distribution. *Mon. Not. Roy. Astr. Soc.*, 361:1131–1135, August 2005.
- [79] J. Ferreira, R. Ruffini, and L. Stella. On the relativistic Thomas-Fermi model. *Physics Letters B*, 91:314–316, April 1980.
- [80] R. P. Feynman, N. Metropolis, and E. Teller. Equations of State of Elements Based on the Generalized Fermi-Thomas Theory. *Phys. Rev.*, 75:1561–1573, May 1949.
- [81] É. É. Flanagan and T. Hinderer. Constraining neutron-star tidal Love numbers with gravitational-wave detectors. *Phys. Rev. D*, 77(2):021502, January 2008.
- [82] V. A. Fock. *Theory of space, time and gravitation*. Pergamon Press, London, U.K., 1959.
- [83] J. L. Friedman and J. R. Ipser. On the maximum mass of a uniformly rotating neutron star. *Astrophys. J.*, 314:594–597, March 1987.

- [84] J. L. Friedman, J. R. Ipser, and R. D. Sorkin. Turning-point method for axisymmetric stability of rotating relativistic stars. *Astrophys. J.*, 325:722–724, February 1988.
- [85] J. L. Friedman, L. Parker, and J. R. Ipser. Rapidly rotating neutron star models. *Astrophys. J.*, 304:115–139, May 1986.
- [86] G. Gamow and M. Schoenberg. Neutrino Theory of Stellar Collapse. *Physical Review*, 59:539–547, April 1941.
- [87] E. García-Berro, P. Lorén-Aguilar, G. Aznar-Siguán, S. Torres, J. Camacho, L. G. Althaus, A. H. Córscico, B. Külebi, and J. Isern. Double Degenerate Mergers as Progenitors of High-field Magnetic White Dwarfs. *Astrophys. J.*, 749:25, April 2012.
- [88] E. García-Berro, S. Torres, P. Lorén-Aguilar, G. Aznar-Siguán, J. Camacho, B. Külebi, J. Isern, L. G. Althaus, and A. H. Córscico. On the origin of high-field magnetic white dwarfs. *ArXiv e-prints*, September 2012.
- [89] L. R. Gasques, A. V. Afanasjev, M. Beard, L. C. Chamon, P. Ring, and M. Wiescher. Pycnonuclear reaction rates between neutron-rich nuclei. *Nuclear Physics A*, 758:134–137, July 2005.
- [90] R. Geroch. Multipole Moments. II. Curved Space. *Journal of Mathematical Physics*, 11:2580–2588, August 1970.
- [91] V. S. Geroyannis and A. A. Hadjopoulos. Models of white dwarfs under rapid uniform or differential rotation - Numerical results. *Astrophys. J. Suppl. Ser.*, 70:661–677, July 1989.
- [92] V. S. Geroyannis and P. J. Papasotiriou. Spin-up and Spin-down of Rotating Magnetic White Dwarfs: A Straightforward Numerical Approach. *Astrophys. J.*, 534:359–366, May 2000.
- [93] V. L. Ginzburg. The Magnetic Fields of Collapsing Masses and the Nature of Superstars. *Soviet Physics Doklady*, 9:329, November 1964.
- [94] N. K. Glendenning. Limiting rotational period of neutron stars. *Phys. Rev. D*, 46:4161–4168, November 1992.
- [95] N. K. Glendenning, editor. *Compact stars : nuclear physics, particle physics, and general relativity*, 2000.
- [96] N. K. Glendenning. *Special and General Relativity With Applications to White Dwarfs, Neutron Stars and Black Holes*. Springer Science+Business Media, 2007.
- [97] P. Gombás. *Die Statistische Theorie des Atoms und Ihre Anwendungen*. Wien : Springer-Verlag, 1949., 1949.

- [98] S. Goriely, N. Chamel, H.-T. Janka, and J. M. Pearson. The decompression of the outer neutron star crust and r-process nucleosynthesis. *Astron. Astrophys.*, 531:A78+, July 2011.
- [99] P. Haensel. Equation of State of Dense Matter and Maximum Mass of Neutron Stars. In C. Motch and J.-M. Hameury, editors, *EAS Publications Series*, volume 7 of *EAS Publications Series*, page 249, 2003.
- [100] P. Haensel, J. P. Lasota, and J. L. Zdunik. On the minimum period of uniformly rotating neutron stars. *Astron. Astrophys.*, 344:151–153, April 1999.
- [101] P. Haensel, A. Y. Potekhin, and D. G. Yakovlev, editors. *Neutron Stars 1 : Equation of State and Structure*, volume 326 of *Astrophysics and Space Science Library*, 2007.
- [102] T. Hamada and E. E. Salpeter. Models for Zero-Temperature Stars. *Astrophys. J.*, 134:683–+, November 1961.
- [103] R. O. Hansen. Multipole moments of stationary space-times. *Journal of Mathematical Physics*, 15:46–52, January 1974.
- [104] B. K. Harrison, M. Wakano, and J. A. Wheeler. La structure et l'évolution de l'univers. *Onzieme Conseil de Physique de Solvay*, 1958.
- [105] J. B. Hartle. Slowly Rotating Relativistic Stars. I. Equations of Structure. *Astrophys. J.*, 150:1005, December 1967.
- [106] J. B. Hartle and A. G. Sabbadini. The equation of state and bounds on the mass of nonrotating neutron stars. *Astrophys. J.*, 213:831–835, May 1977.
- [107] J. B. Hartle and D. H. Sharp. Variational Principle for the Equilibrium of a Relativistic, Rotating Star. *Astrophys. J.*, 147:317–+, January 1967.
- [108] J. B. Hartle and K. S. Thorne. Slowly Rotating Relativistic Stars. II. Models for Neutron Stars and Supermassive Stars. *Astrophys. J.*, 153:807, September 1968.
- [109] K. Hebeler, J. M. Lattimer, C. J. Pethick, and A. Schwenk. Constraints on Neutron Star Radii Based on Chiral Effective Field Theory Interactions. *Physical Review Letters*, 105(16):161102, October 2010.
- [110] C. O. Heinke, G. B. Rybicki, R. Narayan, and J. E. Grindlay. A Hydrogen Atmosphere Spectral Model Applied to the Neutron Star X7 in the Globular Cluster 47 Tucanae. *Astrophys. J.*, 644:1090–1103, June 2006.
- [111] H. Heiselberg and M. Hjorth-Jensen. Phase Transitions in Neutron Stars and Maximum Masses. *Astrophys. J. Lett.*, 525:L45–L48, November 1999.

- [112] J. W. T. Hessels, S. M. Ransom, I. H. Stairs, P. C. C. Freire, V. M. Kaspi, and F. Camilo. A Radio Pulsar Spinning at 716 Hz. *Science*, 311:1901–1904, March 2006.
- [113] T. Hinderer. Tidal Love Numbers of Neutron Stars. *Astrophys. J.*, 677:1216–1220, April 2008.
- [114] T. Hinderer. Erratum: "Tidal Love Numbers of Neutron Stars" (2008, ApJ, 677, 1216-1220). *Astrophys. J.*, 697:964, May 2009.
- [115] D. Hirata, H. Toki, and I. Tanihata. Relativistic mean-field theory on the xenon, cesium and barium isotopes. *Nuclear Physics A*, 589:239–248, February 1995.
- [116] F. Hulleman, M. H. van Kerkwijk, and S. R. Kulkarni. An optical counterpart to the anomalous X-ray pulsar 4U0142+61. *Nature*, 408:689–692, December 2000.
- [117] M. Ilkov and N. Soker. The number of progenitors in the core-degenerate scenario for Type Ia supernovae. *Mon. Not. Roy. Astr. Soc.*, page 30, September 2012.
- [118] M. Ilkov and N. Soker. Type Ia supernovae from very long delayed explosion of core-white dwarf merger. *Mon. Not. Roy. Astr. Soc.*, 419:1695–1700, January 2012.
- [119] M. Ishii, M. Shibata, and Y. Mino. Black hole tidal problem in the Fermi normal coordinates. *Phys. Rev. D*, 71(4):044017, February 2005.
- [120] J. N. Islam. *Rotating fields in general relativity*. Cambridge and New York, Cambridge University Press, 1985.
- [121] R. A. James. The Structure and Stability of Rotating Gas Masses. *Astrophys. J.*, 140:552, August 1964.
- [122] M. H. Johnson and E. Teller. Classical Field Theory of Nuclear Forces. *Physical Review*, 98:783–787, May 1955.
- [123] V. Kalogera and G. Baym. The Maximum Mass of a Neutron Star. *Astrophys. J. Lett.*, 470:L61, October 1996.
- [124] R. P. Kerr. Gravitational Field of a Spinning Mass as an Example of Algebraically Special Metrics. *Physical Review Letters*, 11:237–238, September 1963.
- [125] O. Klein. On the Thermodynamical Equilibrium of Fluids in Gravitational Fields. *Reviews of Modern Physics*, 21:531–533, July 1949.
- [126] T. Kodama and M. Yamada. Theory of Superdense Stars. *Progress of Theoretical Physics*, 47:444–459, February 1972.
- [127] H. Komatsu, Y. Eriguchi, and I. Hachisu. Rapidly rotating general relativistic stars. I - Numerical method and its application to uniformly rotating polytropes. *Mon. Not. Roy. Astr. Soc.*, 237:355–379, March 1989.

- [128] H. Komatsu, Y. Eriguchi, and I. Hachisu. Rapidly rotating general relativistic stars. II - Differentially rotating polytropes. *Mon. Not. Roy. Astr. Soc.*, 239:153–171, July 1989.
- [129] S. Koranda, N. Stergioulas, and J. L. Friedman. Upper Limits Set by Causality on the Rotation and Mass of Uniformly Rotating Relativistic Stars. *Astrophys. J.*, 488:799, October 1997.
- [130] S. Kubis. Nuclear symmetry energy and stability of matter in neutron stars. *Phys. Rev. C*, 76(2):025801, August 2007.
- [131] B. Külebi, S. Jordan, F. Euchner, B. T. Gänsicke, and H. Hirsch. Analysis of hydrogen-rich magnetic white dwarfs detected in the Sloan Digital Sky Survey. *Astron. Astrophys.*, 506:1341–1350, November 2009.
- [132] B. Külebi, S. Jordan, E. Nelan, U. Bastian, and M. Altmann. Constraints on the origin of the massive, hot, and rapidly rotating magnetic white dwarf RE J 0317-853 from an HST parallax measurement. *Astron. Astrophys.*, 524:A36+, December 2010.
- [133] W. G. Laarakkers and E. Poisson. Quadrupole Moments of Rotating Neutron Stars. *Astrophys. J.*, 512:282–287, February 1999.
- [134] K. Lake. Letter: Differential Invariants of the Kerr Vacuum. *General Relativity and Gravitation*, 36:1159–1169, May 2004.
- [135] G. A. Lalazissis, J. König, and P. Ring. New parametrization for the Lagrangian density of relativistic mean field theory. *Phys. Rev. C*, 55:540–543, January 1997.
- [136] K. Lanczos. . *Phys. ZS.*, 23:537, 1923.
- [137] L. D. Landau. On the theory of stars. *Phys. Z. Sowjetunion*, 1:285–288, 1932.
- [138] L. D. Landau and E. M. Lifshits. *The Classical Theory of Fields*. Reading, Mass.: Addison-Wesley Publishing Co., 1962.
- [139] A. F. Lanza and M. Rodonò. Orbital period modulation and quadrupole moment changes in magnetically active close binaries. *Astron. Astrophys.*, 349:887–897, September 1999.
- [140] J. M. Lattimer and M. Prakash. The Physics of Neutron Stars. *Science*, 304:536–542, April 2004.
- [141] T. D. Lee and M. Margulies. Interaction of a dense fermion medium with a scalar-meson field. *Phys. Rev. D*, 11:1591–1610, March 1975.
- [142] T. D. Lee and Y. Pang. Fermion soliton stars and black holes. *Phys. Rev. D*, 35:3678–3694, June 1987.

- [143] T. D. Lee and G. C. Wick. Vacuum stability and vacuum excitation in a spin-0 field theory. *Phys. Rev. D*, 9:2291–2316, April 1974.
- [144] J. Lense and H. Thirring. Über den Einfluß der Eigenrotation der Zentralkörper auf die Bewegung der Planeten und Monde nach der Einsteinschen Gravitationstheorie. *Physikalische Zeitschrift*, 19:156, 1918.
- [145] T. Lewis. Some Special Solutions of the Equations of Axially Symmetric Gravitational Fields. *Royal Society of London Proceedings Series A*, 136:176–192, May 1932.
- [146] E. H. Lieb. Thomas-fermi and related theories of atoms and molecules. *Reviews of Modern Physics*, 53:603–641, October 1981.
- [147] E. H. Lieb and B. Simon. Thomas-Fermi Theory Revisited. *Physical Review Letters*, 31:681–683, September 1973.
- [148] J. Liebert, G. D. Schmidt, R. F. Green, H. S. Stockman, and J. T. McGraw. Two hot, low-field magnetic DA white dwarfs. *Astrophys. J.*, 264:262–272, January 1983.
- [149] L. Lindblom. The role of the viscous secular instability in rotating neutron stars. *Astrophys. J.*, 317:325–332, June 1987.
- [150] K.-W. Lo and L.-M. Lin. The Spin Parameter of Uniformly Rotating Compact Stars. *Astrophys. J.*, 728:12, February 2011.
- [151] D. T. Loan, N. H. Tan, D. T. Khoa, and J. Margueron. Equation of state of neutron star matter, and the nuclear symmetry energy. *Phys. Rev. C*, 83(6):065809, June 2011.
- [152] A. E. H. Love. *Some Problems of Geodynamics*. Cambridge, UK: Cambridge University Press., 1911.
- [153] R. Maartens and B. A. Bassett. Gravito-electromagnetism. *Classical and Quantum Gravity*, 15:705–717, March 1998.
- [154] M. Malheiro, J. A. Rueda, and R. Ruffini. SGRs and AXPs as Rotation-Powered Massive White Dwarfs. *PASJ*, 64:56, June 2012.
- [155] V. S. Manko. LETTER TO THE EDITOR: On the description of the external field of a static deformed mass. *Classical and Quantum Gravity*, 7:L209–L211, September 1990.
- [156] V. S. Manko, E. W. Mielke, and J. D. Sanabria-Gómez. Exact solution for the exterior field of a rotating neutron star. *Phys. Rev. D*, 61(8):081501, April 2000.

- [157] V. S. Manko and I. D. Novikov. Generalizations of the Kerr and Kerr-Newman metrics possessing an arbitrary set of mass-multipole moments. *Classical and Quantum Gravity*, 9:2477–2487, November 1992.
- [158] J. S. Marsh. Magnetic and electric fields of rotating charge distributions. *American Journal of Physics*, 50:51–53, January 1982.
- [159] B. Mashhoon. On tidal phenomena in a strong gravitational field. *Astrophys. J.*, 197:705–716, May 1975.
- [160] B. Mashhoon. Tidal radiation. *Astrophys. J.*, 216:591–609, September 1977.
- [161] B. Mashhoon and D. S. Theiss. Relativistic lunar theory. *Nuovo Cimento B Serie*, 106:545–571, March 1991.
- [162] R. Meinel, M. Ansorg, A. Kleinwächter, G. Neugebauer, and D. Petroff. *Relativistic Figures of Equilibrium*. Cambridge University Press, June 2008.
- [163] S. Mereghetti. The strongest cosmic magnets: soft gamma-ray repeaters and anomalous X-ray pulsars. *Astron. Astrophys. Rev.*, 15:225–287, July 2008.
- [164] A. B. Migdal, V. S. Popov, and D. N. Voskresenskii. The vacuum charge distribution near super-charged nuclei. *Soviet Journal of Experimental and Theoretical Physics*, 45:436–+, March 1977.
- [165] L. D. Miller and A. E. Green. Relativistic Self-Consistent Meson Field Theory of Spherical Nuclei. *Phys. Rev. C*, 5:241–252, January 1972.
- [166] J. J. Monaghan. The structure of rapidly rotating white dwarfs. *Mon. Not. Roy. Astr. Soc.*, 132:305, 1966.
- [167] M. Morini, N. R. Robba, A. Smith, and M. van der Klis. EXOSAT observations of the supernova remnant G109.1-1.0 and the X-ray pulsar 1E 2259+586. *Astrophys. J.*, 333:777–787, October 1988.
- [168] N. F. Mott. The Electrical Resistance of Dilute Solid Solutions. *Proceedings of the Cambridge Philosophical Society*, 32:281, 1936.
- [169] M. Mukherjee, F. P. Esposito, and L. C. R. Wijewardhana. A scalar invariant and the local geometry of a class of static spacetimes. *Journal of High Energy Physics*, 10:38, October 2003.
- [170] B. Müller and J. Rafelski. Stabilization of the Charged Vacuum Created by Very Strong Electrical Fields in Nuclear Matter. *Physical Review Letters*, 34:349–352, February 1975.

- [171] H. Mütter, M. Prakash, and T. L. Ainsworth. The nuclear symmetry energy in relativistic Brueckner-Hartree-Fock calculations. *Physics Letters B*, 199:469–474, December 1987.
- [172] W. Myers. Nuclear masses and deformations. *Nucl. Phys.*, 81:1–60, June 1966.
- [173] G. Neugebauer and R. Meinel. The Einsteinian gravitational field of the rigidly rotating disk of dust. *Astrophys. J. Lett.*, 414:L97–L99, September 1993.
- [174] E. Olson and M. Bailyn. Internal structure of multicomponent static spherical gravitating fluids. *Phys. Rev. D*, 12:3030–3036, November 1975.
- [175] J. R. Oppenheimer and G. M. Volkoff. On Massive Neutron Cores. *Phys. Rev.*, 55:374–381, February 1939.
- [176] J. P. Ostriker and P. Bodenheimer. Rapidly Rotating Stars. II. Massive White Dwarfs. *Astrophys. J.*, 151:1089–+, March 1968.
- [177] J. P. Ostriker and J. L. Tassoul. On the Oscillations and Stability of Rotating Stellar Models. II. Rapidly Rotating White Dwarfs. *Astrophys. J.*, 155:987, March 1969.
- [178] R. Owen, J. Brink, Y. Chen, J. D. Kaplan, G. Lovelace, K. D. Matthews, D. A. Nichols, M. A. Scheel, F. Zhang, A. Zimmerman, and K. S. Thorne. Frame-Dragging Vortexes and Tidal Tendexes Attached to Colliding Black Holes: Visualizing the Curvature of Spacetime. *Physical Review Letters*, 106(15):151101, April 2011.
- [179] L. A. Pachón, J. A. Rueda, and J. D. Sanabria-Gómez. Realistic exact solution for the exterior field of a rotating neutron star. *Phys. Rev. D*, 73(10):104038, May 2006.
- [180] L. A. Pachón, J. A. Rueda, and C. A. Valenzuela-Toledo. On the Relativistic Precession and Oscillation Frequencies of Test Particles around Rapidly Rotating Compact Stars. *Astrophys. J.*, 756:82, September 2012.
- [181] B. Paczynski. X-ray pulsar 1E 2259 + 586 - A merged white dwarf with a 7 second rotation period? *Astrophys. J. Lett.*, 365:L9–L12, December 1990.
- [182] C. Pagani, A. P. Beardmore, and J. A. Kennea. Swift J1822.3-1606: Enhanced Swift-XRT position. *The Astronomer's Telegram*, 3493:1, July 2011.
- [183] A. Papapetrou. . *Ann. Inst. H. Poincaré A*, 4:83, 1966.
- [184] G. Pappas. Matching of analytical and numerical solutions for neutron stars of arbitrary rotation. *Journal of Physics Conference Series*, 189(1):012028, October 2009.

- [185] G. Pappas. What can quasi-periodic oscillations tell us about the structure of the corresponding compact objects? *Mon. Not. Roy. Astr. Soc.*, 422:2581–2589, May 2012.
- [186] G. Pappas and T. A. Apostolatos. COMMENTS, REPLIES AND NOTES: Faithful transformation of quasi-isotropic to Weyl Papapetrou coordinates: a prerequisite to compare metrics. *Classical and Quantum Gravity*, 25(22):228002, November 2008.
- [187] G. Pappas and T. A. Apostolatos. Revising the Multipole Moments of Numerical Spacetimes and its Consequences. *Physical Review Letters*, 108(23):231104, June 2012.
- [188] J. M. Pearson, S. Goriely, and N. Chamel. Properties of the outer crust of neutron stars from Hartree-Fock-Bogoliubov mass models. *Phys. Rev. C*, 83(6):065810–+, June 2011.
- [189] I. Pomeranchuk and Ya. Smorodinsky. . *Journal of Physics*, 9:97, 1945.
- [190] V. Popov. From super-charged nuclei to massive nuclear density cores. In R. Ruffini and G. Vereshchagin, editors, *American Institute of Physics Conference Series*, volume 1205 of *American Institute of Physics Conference Series*, pages 127–131, March 2010.
- [191] M. Prakash, J. M. Lattimer, and T. L. Ainsworth. Equation of state and the maximum mass of neutron stars. *Physical Review Letters*, 61:2518–2521, November 1988.
- [192] P. Predehl and J. H. M. M. Schmitt. X-raying the interstellar medium: ROSAT observations of dust scattering halos. *Astron. Astrophys.*, 293:889–905, January 1995.
- [193] D. Pugliese, J. A. Rueda, R. Ruffini, and S. S. Xue. a General Relativistic Thomas Fermi Treatment of Neutron Star Cores II: Generalized Fermi Energies and Beta Equilibrium. *International Journal of Modern Physics Conference Series*, 12:198–202, January 2012.
- [194] H. Quevedo. Class of stationary axisymmetric solutions of Einstein’s equations in empty space. *Phys. Rev. D*, 33:324–327, January 1986.
- [195] H. Quevedo. General static axisymmetric solution of Einstein’s vacuum field equations in prolate spheroidal coordinates. *Phys. Rev. D*, 39:2904–2911, May 1989.
- [196] H. Quevedo. Exterior and interior metrics with quadrupole moment. *General Relativity and Gravitation*, 43:1141–1152, April 2011.
- [197] H. Quevedo. Matching Conditions in Relativistic Astrophysics. In *Twelfth Marcel Grossmann Meeting on General Relativity*, page 35, 2012.

- [198] H. Quevedo and B. Mashhoon. Exterior gravitational field of a rotating deformed mass. *Physics Letters A*, 109:13–18, May 1985.
- [199] H. Quevedo and B. Mashhoon. Generalization of Kerr spacetime. *Phys. Rev. D*, 43:3902–3906, June 1991.
- [200] N. Rea, P. Esposito, R. Turolla, G. L. Israel, S. Zane, L. Stella, S. Mereghetti, A. Tiengo, D. Götz, E. Göğüş, and C. Kouveliotou. A Low-Magnetic-Field Soft Gamma Repeater. *Science*, 330:944–, November 2010.
- [201] N. Rea, G. L. Israel, P. Esposito, J. A. Pons, A. Camero-Arranz, R. P. Mignani, R. Turolla, S. Zane, M. Burgay, A. Possenti, S. Campana, T. Enoto, N. Gehrels, E. Göğüş, D. Götz, C. Kouveliotou, K. Makishima, S. Mereghetti, S. R. Oates, D. M. Palmer, R. Perna, L. Stella, and A. Tiengo. A New Low Magnetic Field Magnetar: The 2011 Outburst of Swift J1822.3-1606. *Astrophys. J.*, 754:27, July 2012.
- [202] A. Reisenegger. Chemical Equilibrium and Stable Stratification of a Multicomponent Fluid: Thermodynamics and Application to Neutron Stars. *Astrophys. J.*, 550:860–862, April 2001.
- [203] A. Reisenegger. Magnetic field evolution in neutron stars. *Astronomische Nachrichten*, 328:1173, December 2007.
- [204] A. Reisenegger, R. Benguria, J. P. Prieto, P. A. Araya, and D. Lai. Hall drift of axisymmetric magnetic fields in solid neutron-star matter. *Astron. Astrophys.*, 472:233–240, September 2007.
- [205] C. E. Rhoades and R. Ruffini. Maximum Mass of a Neutron Star. *Physical Review Letters*, 32:324–327, February 1974.
- [206] I. Robinson. On the Bel - Robinson tensor. *Classical and Quantum Gravity*, 14:A331–A333, January 1997.
- [207] S. Rosseland. Electrical state of a star. *Mon. Not. Roy. Astr. Soc.*, 84:720–728, June 1924.
- [208] M. Rotondo, J. A. Rueda, R. Ruffini, and S.-S. Xue. On the equilibrium of self-gravitating neutrons, protons and electrons in β -equilibrium. *ArXiv e-prints*, July 2011.
- [209] M. Rotondo, J. A. Rueda, R. Ruffini, and S.-S. Xue. Relativistic Feynman-Metropolis-Teller theory for white dwarfs in general relativity. *Phys. Rev. D*, 84(8):084007–+, October 2011.
- [210] M. Rotondo, J. A. Rueda, R. Ruffini, and S.-S. Xue. Relativistic Thomas-Fermi treatment of compressed atoms and compressed nuclear matter cores of stellar dimensions. *Phys. Rev. C*, 83(4):045805–+, April 2011.

- [211] M. Rotondo, J. A. Rueda, R. Ruffini, and S.-S. Xue. The self-consistent general relativistic solution for a system of degenerate neutrons, protons and electrons in β -equilibrium. *Physics Letters B*, 701:667–671, July 2011.
- [212] M. Rotondo, R. Ruffini, and S.-S. Xue. Neutral Nuclear Core VS Super Charged One. In H. Kleinert, R. T. Jantzen, and R. Ruffini, editors, *The Eleventh Marcel Grossmann Meeting On Recent Developments in Theoretical and Experimental General Relativity, Gravitation and Relativistic Field Theories*, pages 1352–1355, September 2008.
- [213] M. Rotondo, R. Ruffini, S.-S. Xue, and V. Popov. On Gravitationally and Electrodynamically Bound Nuclear Matter Cores of Stellar Dimensions. *International Journal of Modern Physics D*, 20:1995–2002, 2011.
- [214] I. W. Roxburgh. On Models of Non Spherical Stars. II. Rotating White Dwarfs. With 2 Figures in the Text. *Zeitschrift für Astrophysik*, 62:134, 1965.
- [215] I. W. Roxburgh and B. R. Durney. Structure, Oscillations and Stability of Rotating White Dwarfs. *Zeitschrift für Astrophysik*, 64:504–+, 1966.
- [216] M. Ruderman. Pulsars: Structure and Dynamics. *Annual Rev. of Astron. Astrophys.*, 10:427, 1972.
- [217] M. Ruderman. Spin-Driven Changes in Neutron Star Magnetic Fields. *Journal of Astrophysics and Astronomy*, 16:207, June 1995.
- [218] J. A. Rueda, R. Ruffini, and S.-S. Xue. The Klein first integrals in an equilibrium system with electromagnetic, weak, strong and gravitational interactions. *Nuclear Physics A*, 872:286–295, December 2011.
- [219] R. Ruffini. On the energetics of black holes. In Black Holes (Les Astres Occlus), editor, A. Giannaras, pages 451–546, 1973.
- [220] R. Ruffini. The Role of Thomas-Fermi Approach in Neutron Star Matter. In *Path Integrals - New Trends and Perspectives*, pages 207–218, November 2008.
- [221] R. Ruffini and S. Bonazzola. Systems of Self-Gravitating Particles in General Relativity and the Concept of an Equation of State. *Physical Review*, 187:1767–1783, November 1969.
- [222] R. Ruffini, M. Rotondo, and S.-S. Xue. Electrodynamics for Nuclear Matter in Bulk. *International Journal of Modern Physics D*, 16:1–9, 2007.
- [223] R. Ruffini and L. Stella. Some comments on the relativistic Thomas-Fermi model and the Vallarta-Rosen equation. *Physics Letters B*, 102:442–444, July 1981.

- [224] R. Ruffini, G. Vereshchagin, and S.-S. Xue. Electron-positron pairs in physics and astrophysics: From heavy nuclei to black holes. *Phys. Rep.*, 487:1–140, February 2010.
- [225] R. Ruffini, L. Vitagliano, and S.-S. Xue. On a separatrix in the gravitational collapse to an overcritical electromagnetic black hole. *Physics Letters B*, 573:33–38, October 2003.
- [226] R. Ruffini, L. Vitagliano, and S.-S. Xue. On plasma oscillations in strong electric fields. *Physics Letters B*, 559:12–19, April 2003.
- [227] R. Ruffini and S.-S. Xue. Dyadosphere formed in gravitational collapse. In D.-S. Lee and W. Lee, editors, *American Institute of Physics Conference Series*, volume 1059 of *American Institute of Physics Conference Series*, pages 72–100, October 2008.
- [228] A. Saa. A third-order curvature invariant in static spacetimes. *Classical and Quantum Gravity*, 24:2929–2934, June 2007.
- [229] E. E. Salpeter. Energy and Pressure of a Zero-Temperature Plasma. *Astrophys. J.*, 134:669–+, November 1961.
- [230] E. E. Salpeter and H. M. van Horn. Nuclear Reaction Rates at High Densities. *Astrophys. J.*, 155:183, January 1969.
- [231] G. D. Schmidt, P. Bergeron, J. Liebert, and R. A. Saffer. Two ultramassive white dwarfs found among candidates for magnetic fields. *Astrophys. J.*, 394:603–608, August 1992.
- [232] G. D. Schmidt, S. C. West, J. Liebert, R. F. Green, and H. S. Stockman. The new magnetic white dwarf PG 1031 + 234 - Polarization and field structure at more than 500 milion Gauss. *Astrophys. J.*, 309:218–229, October 1986.
- [233] K. Schwarzschild. On the Gravitational Field of a Mass Point According to Einstein's Theory. *Abh. Konigl. Preuss. Akad. Wissenschaften Jahre*, 1:189–196, 1916.
- [234] D. M. Sedrakyan and E. V. Chubaryan. Internal solution for stationary axially symmetric gravitational fields. *Astrophysics*, 4:227–233, December 1968.
- [235] S. L. Shapiro and S. A. Teukolsky. *Black holes, white dwarfs, and neutron stars: The physics of compact objects*. New York, Wiley-Interscience, 1983.
- [236] S. L. Shapiro, S. A. Teukolsky, and T. Nakamura. Spin-up of a rapidly rotating star by angular momentum loss. *Astrophys. J. Lett.*, 357:L17–L20, July 1990.
- [237] B. K. Sharma and S. Pal. Nuclear symmetry energy effects in finite nuclei and neutron star. *Physics Letters B*, 682:23–26, November 2009.

- [238] M. M. Sharma, M. A. Nagarajan, and P. Ring. Rho meson coupling in the relativistic mean field theory and description of exotic nuclei. *Physics Letters B*, 312:377–381, August 1993.
- [239] M. Shibata, K. Kyutoku, T. Yamamoto, and K. Taniguchi. Gravitational waves from black hole-neutron star binaries: Classification of waveforms. *Phys. Rev. D*, 79(4):044030, February 2009.
- [240] M. Shibata and K. Uryu. Merger of black hole neutron star binaries in full general relativity. *Classical and Quantum Gravity*, 24:125, June 2007.
- [241] R. Sorkin. A Criterion for the Onset of Instability at a Turning Point. *Astrophys. J.*, 249:254, October 1981.
- [242] R. D. Sorkin. A Stability Criterion for Many Parameter Equilibrium Families. *Astrophys. J.*, 257:847, June 1982.
- [243] H. C. Spruit. Dynamo action by differential rotation in a stably stratified stellar interior. *Astron. Astrophys.*, 381:923–932, January 2002.
- [244] G. Srinivasan. The maximum mass of neutron stars. *Astron. Astrophys. Rev.*, 11:67–96, 2002.
- [245] H. Stephani, D. Kramer, M. MacCallum, C. Hoenselaers, and E. Herlt. *Exact solutions of Einstein's field equations*. Cambridge, UK: Cambridge University Press., 2003.
- [246] N. Stergioulas. Rotating Stars in Relativity. *Living Reviews in Relativity*, 6:3–+, June 2003.
- [247] N. Stergioulas and J. L. Friedman. Comparing models of rapidly rotating relativistic stars constructed by two numerical methods. *Astrophys. J.*, 444:306–311, May 1995.
- [248] Y. Sugahara and H. Toki. Relativistic mean-field theory for unstable nuclei with non-linear σ and ω terms. *Nuclear Physics A*, 579:557–572, October 1994.
- [249] J. L. Synge. *Relativity: The general theory*. Amsterdam: North-Holland Publication Co., 1964.
- [250] K. Takami, L. Rezzolla, and S. Yoshida. A quasi-radial stability criterion for rotating relativistic stars. *Mon. Not. Roy. Astr. Soc.*, 416:L1–L5, September 2011.
- [251] A. Tamii, I. Poltoratska, P. von Neumann-Cosel, Y. Fujita, T. Adachi, C. A. Bertulani, J. Carter, M. Dozono, H. Fujita, K. Fujita, K. Hatanaka, D. Ishikawa, M. Itoh, T. Kawabata, Y. Kalmykov, A. M. Krumbholz, E. Litvinova, H. Matsubara, K. Nakanishi, R. Neveling, H. Okamura, H. J. Ong, B. Özel-Tashenov, V. Y.

- Ponomarev, A. Richter, B. Rubio, H. Sakaguchi, Y. Sakemi, Y. Sasamoto, Y. Shimbara, Y. Shimizu, F. D. Smit, T. Suzuki, Y. Tameshige, J. Wambach, R. Yamada, M. Yosoi, and J. Zenihiro. Complete Electric Dipole Response and the Neutron Skin in Pb208. *Physical Review Letters*, 107(6):062502, August 2011.
- [252] J.-L. Tassoul and J. P. Ostriker. Secular Stability of Uniformly Rotating Polytropes. *Astron. Astrophys.*, 4:423, March 1970.
- [253] R. J. Tayler. The adiabatic stability of stars containing magnetic fields-I. Toroidal fields. *Mon. Not. Roy. Astr. Soc.*, 161:365, 1973.
- [254] C. Thompson and R. C. Duncan. Neutron star dynamos and the origins of pulsar magnetism. *Astrophys. J.*, 408:194–217, May 1993.
- [255] C. Thompson and R. C. Duncan. The soft gamma repeaters as very strongly magnetized neutron stars - I. Radiative mechanism for outbursts. *Mon. Not. Roy. Astr. Soc.*, 275:255–300, July 1995.
- [256] C. Thompson and R. C. Duncan. The Soft Gamma Repeater as Very Strongly Magnetized Neutron Stars. II. Quiescent Neutrino, X-Ray, and Alfvén Wave Emission. *Astrophys. J.*, 473:322, December 1996.
- [257] K. S. Thorne. The General Relativistic Theory of Stellar Structure and Dynamics. In C. Dewitt, E. Schatzman, & P. Véron, editor, *High Energy Astrophysics, Volume 3*, pages 259–+, 1967.
- [258] K. S. Thorne. Multipole expansions of gravitational radiation. *Reviews of Modern Physics*, 52:299–340, April 1980.
- [259] K. S. Thorne. Tidal stabilization of rigidly rotating, fully relativistic neutron stars. *Phys. Rev. D*, 58(12):124031, December 1998.
- [260] R. C. Tolman. Static Solutions of Einstein’s Field Equations for Spheres of Fluid. *Physical Review*, 55:364–373, February 1939.
- [261] G. Torok, P. Bakala, Z. Stuchlik, and P. Cech. Modeling the Twin Peak QPO Distribution in the Atoll Source 4U 1636-53. *Acta Astronomica*, 58:1–14, March 2008.
- [262] J. E. Trümper. Observations of neutron stars and the equation of state of matter at high densities. *Progress in Particle and Nuclear Physics*, 66:674–680, July 2011.
- [263] J. E. Trümper, V. Burwitz, F. Haberl, and V. E. Zavlin. The puzzles of RX J1856.5-3754: neutron star or quark star? *Nuclear Physics B Proceedings Supplements*, 132:560–565, June 2004.
- [264] V. V. Usov. Glitches in the X-ray pulsar 1E 2259+586. *Astrophys. J.*, 427:984–986, June 1994.

- [265] H. M. van Horn. *Low-Luminosity Stars*. ed. Kumar, S. S., 1969.
- [266] B. H. Voorhees. Static Axially Symmetric Gravitational Fields. *Phys. Rev. D*, 2:2119–2122, November 1970.
- [267] J. D. Walecka. A theory of highly condensed matter. *Annals of Physics*, 83:491–529, 1974.
- [268] A. H. Wapstra and K. Bos. The 1977 Atomic Mass Evaluation: Parts I through III. *Atomic Data and Nuclear Data Tables*, 19:175–+, 1977.
- [269] F. Weber and N. K. Glendenning. Limiting angular velocity of realistic relativistic neutron star models. *Zeitschrift für Physik A Hadrons and Nuclei*, 339:211–215, March 1991.
- [270] F. Weber and N. K. Glendenning. Application of the improved Hartle method for the construction of general relativistic rotating neutron star models. *Astrophys. J.*, 390:541–549, May 1992.
- [271] H. Weyl. Zur Gravitationstheorie. *Annalen der Physik*, 359:117–145, 1917.
- [272] D. T. Wickramasinghe and L. Ferrario. Magnetism in Isolated and Binary White Dwarfs. *PASP*, 112:873–924, July 2000.
- [273] L. Woltjer. X-Rays and Type i Supernova Remnants. *Astrophys. J.*, 140:1309–1313, October 1964.
- [274] D. G. Yakovlev, L. R. Gasques, A. V. Afanasjev, M. Beard, and M. Wiescher. Fusion reactions in multicomponent dense matter. *Phys. Rev. C*, 74(3):035803, September 2006.
- [275] J. H. Young and C. A. Coulter. Exact Metric for a Nonrotating Mass with a Quadrupole Moment. *Physical Review*, 184:1313–1315, August 1969.
- [276] I. B. Zel'Dovich. Nuclear Reactions in Super-Dense Cold Hydrogen. *Soviet Journal of Experimental and Theoretical Physics*, 6:760, 1958.
- [277] D. M. Zipoy. Topology of Some Spheroidal Metrics. *Journal of Mathematical Physics*, 7:1137–1143, June 1966.